

## The Comparison between Single Atom Catalysis and Surface Organometallic Catalysis

Manoja K. Samantaray,<sup>†</sup> Valerio D'Elia,<sup>‡</sup> Eva Pump,<sup>†</sup> Laura Falivene,<sup>†</sup> Moussab Harb,<sup>†</sup> Samy Ould Chikh,<sup>†</sup> Luigi Cavallo,<sup>†</sup> and Jean-Marie Basset\*,<sup>†</sup>

<sup>†</sup>King Abdullah University of Science and Technology (KAUST), Thuwal 23955-6900, Saudi Arabia

<sup>‡</sup>School of Molecular Science and Engineering (MSE), Vidyasirimedhi Institute of Science and Technology (VISTEC), Wang Chan, Payupnai, 21210 Rayong, Thailand

**ABSTRACT:** Single atom catalysis (SAC) is a recent discipline of heterogeneous catalysis for which a single atom on a surface is able to carry out various catalytic reactions. A kind of revolution in heterogeneous catalysis by metals for which it was assumed that specific sites or defects of a nanoparticle were necessary to activate substrates in catalytic reactions. In another extreme of the spectrum, surface organometallic chemistry (SOMC), and, by extension, surface organometallic catalysis (SOMCat), have demonstrated that single atoms on a surface, but this time with specific ligands, could lead to a more predictive approach in heterogeneous catalysis. The predictive character of SOMCat was just the result of intuitive mechanisms derived from the elementary steps of molecular chemistry. This review article will compare the aspects of single atom catalysis and surface organometallic catalysis by considering several specific catalytic reactions, some of which exist for both fields, whereas others might see mutual overlap in the future. After a definition of both domains, a detailed approach of the methods, mostly modeling and spectroscopy, will be followed by a detailed analysis of catalytic reactions: hydrogenation, dehydrogenation, hydrogenolysis, oxidative dehydrogenation, alkane and cycloalkane metathesis, methane activation, metathetic oxidation, CO<sub>2</sub> activation to cyclic carbonates, imine metathesis, and selective catalytic reduction (SCR) reactions. A prospective resulting from present knowledge is showing the emergence of a new discipline from the overlap between the two areas.



### CONTENTS

|  |   |  |    |
|--|---|--|----|
| 1. Introduction  |   |  |    |
| 1.1. The Comparison between Single Atom Catalysis and Surface Organometallic Catalysis | B |  |    |
| 1.2. Remarks on Heterogeneous Catalysis by Single Atoms                                | B |  |    |
| 1.3. Definitions of SOMC, SOMF, and SCF  | C |  |    |
| 1.4. Definition of Single Atom Catalysis (SAC) and Single Alloy Atom Catalysis (SAAC)  | D |  |    |
| 1.5. Analogies and Differences between SOMCat and SAC                                  | D |  |    |
| 2. Physicochemical Tools for Structure Determination                                   | E |  |    |
| 2.1. Scanning Transmission Electron Microscopy (STEM)                                  | E |  |    |
| 2.2. X-ray Spectroscopy  | E |  |    |
| 2.2.1. EXAFS Spectroscopy  | H |  |    |
| 2.2.2. XANES and HERFD-XAS Spectroscopies  | J |  |    |
| 2.2.3. Valence-to-Core X-ray Emission Spectroscopy (XES)                               | M |  |    |
| 2.3. Solid-State NMR Spectroscopy  | N |  |    |
| 2.3.1. Standard Characterization of SOMC Complexes                                     | O |  |    |
|  |   | 2.3.2. Characterization of SOMCat through Heteroatoms                  | Q  |
|  |   | 2.3.3. Characterization of SOMC Complexes through Quadrupolar Nuclei   | R  |
|  |   | 3. Computational Tools   | S  |
|  |   | 3.1. Models  | S  |
|  |   | 3.2. Methods   | U  |
|  |   | 4. Classification by Types of Reaction and/or Activation               | U  |
|  |   | 4.1. Hydrogenation   | U  |
|  |   | 4.1.1. Via SOMC  | V  |
|  |   | 4.1.2. Via SAAC  | W  |
|  |   | 4.1.3. Via SAC   | Y  |
|  |   | 4.2. Hydrogenolysis, Alkane Metathesis via C–H and C–C Bond Activation | Z  |
|  |   | 4.2.1. Via SOMC  | Z  |
|  |   | 4.2.2. Via SAAC  | AG |
|  |   | 4.2.3. Via SAC   | AH |
|  |   | 4.3. Light Alkanes Dehydrogenation                                     | AH |
|  |   | 4.3.1. Via SOMC  | AH |
|  |   | <b>Special Issue:</b> Nanoparticles in Catalysis                       |    |
|  |   | <b>Received:</b> April 16, 2019  |    |

|   |    |
|---|----|
| 4.3.2. Via SAC  | AO |
| 4.4. Methane Activation   | AQ |
| 4.4.1. Via SOMC   | AR |
| 4.4.2. Via SAC  | AT |
| 4.4.3. Via SAAC   | AZ |
| 4.5. Emerging Reactions in SOMCat and SAC Chemistry                                       | AZ |
| 4.5.1. Imine Metathesis   | AZ |
| 4.5.2. Metathetic Oxidation of Olefins  | BB |
| 4.5.3. Catalytic Hydrogenation of N <sub>2</sub> into NH <sub>3</sub>                     | BC |
| 4.5.4. Selective Catalytic Reduction of NO <sub>x</sub> by Ammonia (NH <sub>3</sub> -SCR) | BE |
| 4.5.5. CO <sub>2</sub> Conversion for the Synthesis of Organic Compounds                  | BF |
| 5. Conclusions and Perspectives   | BI |
| 5.1. Hydrogenation  | BI |
| 5.2. Hydrogenolysis   | BJ |
| 5.3. Dehydrogenation  | BJ |
| 5.4. Methane Activation   | BJ |
| 5.5. Metathetic Oxidation   | BJ |
| 5.6. Imine Metathesis   | BJ |
| 5.7. Emission Control for SCR Catalysts for Automotive Diesel NO <sub>x</sub>             | BJ |
| 5.8. CO <sub>2</sub> Conversion to Organic Compounds                                      | BK |
| 5.9. Affinities   | BK |
| 5.10. Differences   | BK |
| 5.11. Concluding Remarks and Future Development   | BL |
| Author Information  | BL |
| Corresponding Author  | BL |
| ORCID   | BL |
| Notes   | BL |
| Biographies   | BL |
| Acknowledgments   | BM |
| Abbreviations Used  | BM |
| References  | BM |

## 1. INTRODUCTION

### 1.1. The Comparison between Single Atom Catalysis and Surface Organometallic Catalysis

Since the last century, there has been a considerable amount of work dedicated to catalysis by supported metals, a classical field in heterogeneous catalysis. Among the emerging concepts, several parameters were identified as crucial for activity, selectivity, and lifetime of heterogeneous catalysts based on supported nanoparticles. Among these parameters, (i) metal particle size, (ii) nature of exposed faces, (iii) defects sites, corners, step sites, (iv) (strong) metal support interactions, and (v) bimetallic effects (electronic or steric) can be mentioned. Recently, a huge effort has been devoted to catalysis on smaller and smaller supported nanoparticles.<sup>1–5</sup> Besides the crucial factors responsible for catalytic activity/selectivity/lifetime already mentioned in (i–v), there is a limit situation where **the nanoparticle size is restricted to a single metal atom on a surface**. After several experimental observations, it became evident to the catalytic community that a single atom is able to achieve what, in the last, century was believed to be the “privileged property” of an ensemble of atoms.<sup>6–14</sup> Even now, the discovery of single atom catalysis (SAC) is limited to a rather restricted, but growing, range of catalytic reactions.<sup>3,5,15–19</sup> This new area describes single metal

atoms “supported” or “embedded” on a solid support (oxide, nitride, sulfide, etc.) or even at the periphery of a metal nanoparticle.<sup>20,21</sup> The interaction between the single atom and the surface can be of a different nature involving covalent, coordination, or ionic bonds. Considering heterogeneous catalysts involving single atoms, the rules of molecular chemistry (whether it is coordination or organometallic chemistry) apply, and help to rationalize the structure and the reactivity of this grafted, “deposited” atom.

In parallel to SAC, but mostly earlier than its recent explosion, the discipline of surface organometallic chemistry (SOMC), which progressively developed into surface organometallic catalysis (SOMCat), emerged, involving single metal atoms covalently or ionically bound to a solid support.<sup>22–26</sup> In SOMCat, the catalytically active sites are formed by reacting organometallic complexes or coordination compounds with well-defined surfaces (oxides, metal nanoparticles, carbon, or graphene) to achieve the target functionalities on the surface.<sup>26</sup> The situation is different from the previous case (SAC) because the supported organometallic compounds keep at least part of their ligands after grafting (Scheme 1 for metal oxide

**Scheme 1.** Link between Single Atom Catalysts (SAC) on Oxide and Catalysts Prepared by SOMC on Oxides<sup>a</sup>



<sup>a</sup>M = catalytically active metal; M<sub>s</sub> = metal atom of the oxide support.

support). The latter aspect is crucial for catalysis. In *catalysis by design*,<sup>27</sup> the supported complex contains moieties (fragments A and B of Scheme 1) that are selected based on the proposed mechanism derived from well-established steps in molecular chemistry. Other ligands (spectator ligand X of Scheme 1) serve to control oxidation state, geometry, and d<sup>n</sup> configuration of the metal within the catalytic cycle.

Besides the evident differences discussed above, both disciplines present similarities and chances for mutual enrichment. SAC and SOMCat both deal with isolated metal atoms on surfaces, some with preexisting ligands and some without ligands. In both cases, applying isolated single atoms in heterogeneous catalysis helps in understanding elementary steps as they resemble elementary steps in molecular catalysis or coordination chemistry, where single atoms are surrounded by ligands. This suggests that both methodologies are not mutually exclusive. For example, one can consider that SAC adopts a coordination sphere already present in SOMC-prepared catalysts in the presence of reactants A and B and component X (Scheme 1).

Furthermore, the SOMC methodology can be employed to prepare single atoms. By combining grafting of precursors on surfaces via SOMC with a thermolytic, nonoxidative procedure that removes all organic ligands, isolated atoms may be produced on the surface.<sup>28</sup> Several alkane dehydrogenation catalysts (vide infra) have been prepared by this strategy having a proposed M–O<sub>s</sub> structure (O<sub>s</sub>: oxygen atom of the oxide support) without coordinated ligands on the metal.<sup>29</sup>

Many reviews have already appeared recently both in SAC<sup>1</sup> and SOMCat;<sup>26</sup> the target of this review article is, in the first place, to provide a critical and comprehensive overview about similarities and differences between SOMCat and SAC, and, additionally, to identify emerging reactions, areas of possible overlap, and how the two disciplines could mutually benefit each other. The comparison will be in terms of tools, structure, reactivity, and mechanistic understanding of elementary steps when they are known or proposed. Several types of “classical” heterogeneous chemistry reactions have been selected as a result of their relative importance either in both fields or in each field separately: hydrogenation, dehydrogenations, reactions involving C–C bond formation and breakage like hydrogenolysis or alkane metathesis, methane activation, transformation, and functionalization. Furthermore, to complete our overview, we will discuss emerging reactions in both fields such as imine metathesis, metathetic oxidation or selective catalytic reduction, and CO<sub>2</sub> conversion for organic synthesis. Preference will be given to publications where a tentative mechanistic interpretation has been proposed.

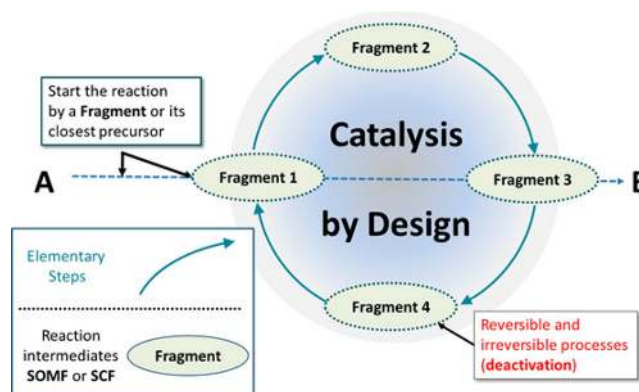
Several aspects will be considered in this review article: (i) single atom catalysis on support (SAC), (ii) single atoms on mono or plurimetallc nanoparticles or single atom alloy catalysis (SAAC) and (iii) single atoms in SOMCat. In the first case (i), the single atoms are located either at the periphery or on the surface of an oxide, nitride, carbon nitrides, sulfide, graphene, and microporous material including zeolites, MOF. In some particular cases (ii), the single metal atom has been isolated at the periphery of a metal nanoparticle, but it is the only species which exhibits catalytic activity (e.g., Pt/Sn). This situation is at the limit when an “ensemble of metal atoms” in a nanocluster decreases to such an extent that only one single metal atom is involved in the catalysis. In the third case (iii), the single metal atoms are covalently linked mostly to the surface of the oxide support but display ligands (spectator or functional) inherited by the organometallic or coordination compound precursors.

## 1.2. Remarks on Heterogeneous Catalysis by Single Atoms

In heterogeneous catalysis, catalysts transform molecules into new molecules, macromolecules, or solids. These transformations typically (except for electron transfer reactions) involve creation of covalent bonds between one or several surface atoms with one or several atoms of the substrate. The thus formed reaction intermediate has been named surface organometallic fragment (SOMF) or surface coordination fragment (SCF) and can be prepared on purpose.<sup>26,27</sup> This very simple concept was at the origin of the development of SOMC and later SOMCat.<sup>23–26</sup> SOMFs can be characterized with specific tools of molecular chemistry as well as surface science. In several cases, the rules of molecular chemistry (regarding structure or reactivity) apply to these surface organometallic fragments. This enables rationalization of the elementary steps of heterogeneous catalysis by understanding the way bonds are broken or made. These elementary steps are very different from the well-known and accepted classical elementary steps of adsorption, desorption, diffusion, etc.

SOMFs or SCFs are unparalleled tools to design catalysts, mimic and understand reaction intermediates and mechanisms in heterogeneous catalysis, or even discover new reactions yet unknown in homogeneous or heterogeneous catalysis (Scheme 2).<sup>27</sup> There are also more and more examples showing that single metal atoms with appropriate ligands (SOMFs and

**Scheme 2. Definition of Catalysis by Design: The Catalytic Cycle Is Entered by a Presumed Reaction Intermediate Called Surface Organometallic Fragment (SOMF) or Surface Coordination Fragment (SCF) or One of Its Closest Precursors<sup>a</sup>**



<sup>a</sup>Reproduced with permission from ref 32. Copyright 2018 Oxford University Press.

SCFs) are able to achieve new catalytic reactions.<sup>27</sup> In most cases, the choice of appropriate ligands was a pure direct prediction of a catalytic reaction. The most relevant examples are Ziegler–Natta depolymerization, alkane metathesis, or metathetic oxidation of olefins.<sup>30,31</sup>

There are more and more examples showing that a single metal atom on the metallic surface of a nanoparticle (SAAC) can achieve multistep reactions which were previously believed to occur only on a large number of atoms assumed to be the “active sites” of classical heterogeneous catalysis. The term “ensemble effect” was advanced to explain this phenomenon.<sup>6</sup>

The main difference between catalysis by single atoms and homogeneous catalysis is the presence of a surface which plays the role of a solid, rigid ligand with redox, acid–base, as well as physical properties (e.g., porosity, hydrophilicity, hydrophobicity, semiconducting properties, etc.). With oxide supports, the electron count of SOMFs and SCFs (including support and spectator ligands) are easily rationalized by the classical electron counts, oxidation state, and *d*<sup>n</sup> configurations of molecular chemistry.<sup>32</sup> The oxide surface can be regarded as an infinite “pool” of oxygens, or oxygen containing species, which plays the role of X or L ligands in the MLH Green formalism.<sup>33</sup> The composition of the surface in terms of adsorbed water molecules, surface hydroxyls, or metal oxides (M–O–M; M: metal, e.g., ≡Si–O–Si≡ on silica) is mostly governed by the temperature of dehydroxylation of the support. These M–O–M surface species may also coordinate the grafted metals via an oxygen lone pair, contributing to the global metal electron count (L ligand).

Besides the contribution of the surface to the electron count of the grafted metal, spectator ligands, which do not appear as participating directly in the elementary steps of the mechanism, are sometimes crucial ligands in the control of the electron density of the metal and also of its oxidation state, *d*<sup>n</sup> configuration and geometry.

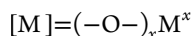
In this review article, we will focus mostly on the role of SOMF, SCF, and spectator ligands without entering into the complex situation of the interaction between a metal fragment and its support. The role of metal/support interaction will be considered in a separate article.



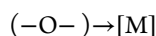
### 1.3. Definitions of SOMC, SOMF, and SCF

When a metal is grafted directly at the surface of an oxide (silica, alumina, ceria, silica–alumina, mesoporous materials, etc.) by classical methods of SOMC, the following bonds and interactions are possible (Scheme 2):

- **Metal–surface bond:**  $\sigma$ -bond between a surface oxygen (which behaves as an X-ligand, Scheme 1) and a metal (M). It formally oxidizes the metal by one unit. In the following, the metal grafted on a support will be written as “[M]”.

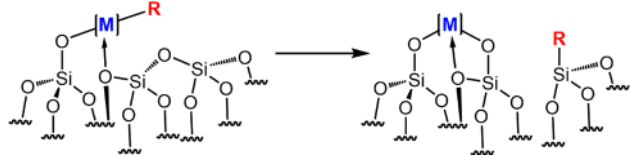


- **Metal–surface interaction:**  $\pi$ -bond or coordination bond between a surface oxygen (L-ligand) and the grafted metal [M]. This interaction formally does not oxidize the metal. It is also represented by



A surface oxygen which is covalently linked to a metal is not only an X-ligand but can also act as an L-ligand because its lone pair overlaps to a certain extent with the  $\pi$ -orbitals of the metal. Besides direct reaction with the precursor, there are many examples where a [M]–R or [M]–H group can open an adjacent  $\equiv Si-O-Si \equiv$  moiety with formation of [M]–O–Si $\equiv$  and, respectively,  $\equiv Si-R$  or  $\equiv Si-H$  via classical  $\sigma$ -bond metathesis mechanism (Scheme 3).<sup>34,35</sup>

**Scheme 3.** Example for [M]–Surface Bond and [M]–Surface Interaction and Opening of Siloxane Bridge through [M]–R Ligand



- **Metal–functional fragment bond:**  $\sigma$ -bond between the grafted metal [M] and the functional fragment “R” which formally oxidizes the metal by one unit. This fragment “R” is supposed to be an intermediate among all the elementary steps of a catalytic cycle (in contrast to the SSP and the support). The fragment “R” allows focusing on reactivity or interconversions of surface moieties. One SOMF can convert into another SOMF: [M]–R  $\rightarrow$  [M]–R’. This conversion can be linked to the reactivity of “R” and might influence the elementary

steps of heterogeneous catalysis (e.g., a metal alkyl giving a metal (carbene)(hydride)). The fragment “R” can have several functions (mono, bis, tris, tetra). This means that a single metal atom can possess simultaneously several different/or identical fragments (e.g., R can be a hydride or an alkyl).

- **Metal–spectator bond:** Typically, the spectator ligand (X-ligand in Scheme 1) does not directly take part to reactions but plays a crucial role in fine-tuning the electronic or steric effects of [M] and in defining the oxidation states. In rare cases, the same kind of ligand can serve as spectator or as catalytically active moiety according to the reaction (for instance metal oxo functionalities in olefin metathesis reactions<sup>36</sup> or in oxidative dehydrogenation of propane).<sup>37</sup>

A model of chemical environment of a single atom prepared via SOMC methodology is represented in Figure 1. To note, SOMC complexes that are directly bound to the surface, and where the surface acts as rigid ligand, are evidently different from supported homogeneous catalysts where the metal atom is tethered to the support surface via flexible linkers that generally coordinate the metal via noncovalent interactions.<sup>38</sup>

### 1.4. Definition of Single Atom Catalysis (SAC) and Single Alloy Atom Catalysis (SAAC)

Many reviews have been written recently on SAC.<sup>3,15–18</sup> Behind this acronym, there is a proliferation of examples in which single atoms are found or claimed to be involved in several catalytic reactions.<sup>18</sup> This makes it difficult to give a precise definition of single atom catalysis. The most frequently accepted concept, evolving with the progress of synthesis and characterization tools, is that “isolated” atoms “adsorbed,” “chemisorbed,” “embedded,” and “immobilized” on a “support,” exhibit catalytic properties in a still limited number of reactions.

The fact that a single supported metal atom displays catalytic properties has been considered as a kind of revolutionary concept in the heterogeneous catalysis community. There was a general belief that metal nanoparticles were responsible for the catalytic activity of metal containing catalysts. The contradiction came from the research of size effects or of the crystallographic position necessary to achieve a given reaction. The activities were usually divided by the number of surface atoms (TOF) in the particles. Some reactions were claimed to be “facile” and the TOF was just depending on the number of surface atoms irrespective of their position at the surface of the particle. Others were qualified as “demanding” because many parameters were playing a role on the measured TOF, in particular, the particle size. For those “demanding” reactions, the activity was found to depend on metal particle size, but nobody was expecting the extreme situation where only a

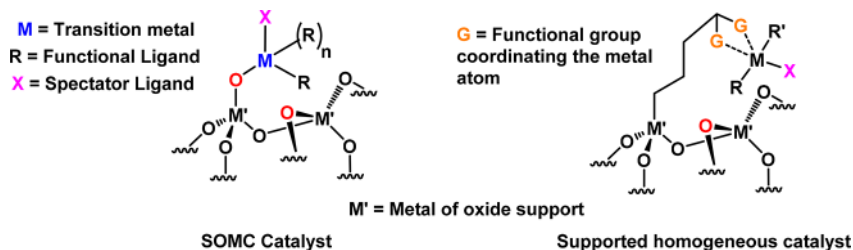


**Figure 1.** Representation of a typical SOMF or SCF containing oxide support, transition metal, spectator ligands, and functional ligands and comparison with supported homogeneous catalyst.

single metal atom could achieve catalytic reactions by itself and be recovered intact at the end of a catalytic run.

In addition, it is known that single atoms existing in the gas phase possess catalytic properties,<sup>39,40</sup> there are also disciplines, such as homogeneous catalysis, where single metal atoms catalyze many reactions in the presence of ligands. Also, in biocatalysis, a single metal atom surrounded by appropriate ligands could achieve difficult reactions (such as for example ammonia synthesis).<sup>41,42</sup> For a single atom which is “adsorbed,” “chemisorbed,” “embedded,” “immobilized,” or “grafted” on (or in) a support, the type of bonding between this atom and the surface, the bulk, the periphery of this support is crucial for the reactivity of the catalyst. The basic rules of chemistry apply to this so-called interfacial situation defining the interaction between surface and single atom as covalent, ionic, coordination, electron transfer, etc. The direct consequence is the precise definition of the oxidation state by rationalizing the electron count of this single atom “attached” to the surface or embedded in the bulk of the support.

The following examples of SACs have been reported:

- Single metal atoms may be linked to “unusual” (with respect to SOMC) or innovative materials such as carbon,<sup>43</sup> carbon nanotubes,<sup>44</sup> carbon nitrides,<sup>17</sup> MOFs-derived matrices,<sup>45</sup> silica layers grown by ultrahigh vacuum techniques,<sup>14,46</sup> etc., which possess chemical or physical functionalities. It was appealing to ascribe some catalytic properties to the site isolation concept.
- Single atom catalysis was also claimed to occur when the isolation of the single site occurs in a metallic nanoparticle for which the “active metal atom” was dispersed in a kind of matrix of inactive metal (SAAC). In classical heterogeneous catalysis, a so-called “dilution effect, at the opposite of ensemble effect,”<sup>47</sup> was observed.
- Another example of single atom catalysis is related to isolated metal atoms in semiconductors. It was discovered that the electronic properties of such semiconductors change with the incorporation of single metal atoms. Single atoms were proposed to participate in the energy level of the electron transfer process (e.g., photocatalytic water splitting).<sup>48</sup>

The consequence of this ambiguity is the difficulty to propose a unifying definition and theory behind SAC.

### 1.5. Analogies and Differences between SOMCat and SAC

SAC and SOMCat are both domains dealing with a **single atom** “attached,” “chemisorbed,” “embedded,” “immobilized,” and “grafted” to/in/on a support. In SOMCat, the support is mostly an oxide or an oxygen containing material (e.g., silica, MOF, zeolites). In SAC, a lot of supports have been tested including carbon, carbon nanotubes, carbon nitrides, MOF, semiconductors, and metal particles.

Both domains have studied various catalytic reactions that occur exclusively on single atoms. Some of these reactions are identical, some are different. Some transformations exist in SOMCat but not in SAC and vice versa. This difference is because in SOMCat efforts were, initially, mainly concerned with hydrogenolysis and alkane metathesis using early transition metals,<sup>25,27</sup> whereas SAC has only recently risen to wide popularity<sup>1</sup> and has not yet covered many existing processes. Additionally, SOMCat has been mainly focused on early transition metals, whereas most works on SAC use late transition or noble metals. Nevertheless, these gaps are due to

be filled in next few years because (a) the field of application of both domains is progressively being expanded; for instance, SOMCat has been recently applied to reactions such as oxidative<sup>37</sup> and nonoxidative dehydrogenation of propane,<sup>49</sup> CO<sub>2</sub> conversion to carbonates,<sup>50</sup> and imine metathesis,<sup>51</sup> just to cite some. Along with continued growth of SAC, it is expected that the number of transformations available for both techniques will strongly increase. (b) There is no specific reason, if not because of tradition, why SAC should not involve early transition metals. It has been shown that single atoms of tantalum can be synthesized on silica support using a cluster source and used in catalysis.<sup>46</sup> Similarly, SOMC syntheses of late transition metals<sup>52</sup> and noble metal<sup>53</sup> complexes have been reported although they were generally not used in catalysis as such but for the synthesis of supported single-site metal–oxo complexes or nanoparticles.

Therefore, whereas the gaps discussed above will eventually be bridged, the fundamental difference between the methodologies is the approach behind each specific domain:

In simple terms, we should say that single atom catalysis is the discovery that many catalytic reactions can occur on an isolated metal atom embedded on an inert support. This was a kind of revolution in heterogeneous catalysis. However, in the absence of a well-defined coordination sphere on the metal atom, prediction and tuning of catalytic activity are generally very challenging with SAC.

In SOMCat, the concept at the origin of the field was a kind of **predictive concept of catalysis by design**<sup>30</sup> for which the elementary steps of molecular chemistry can be applied to discover (or improve) reactions. This was made possible by **starting a catalytic reaction from a well-defined supported reaction intermediate** (SOMF or SCF), which means that the SOMCat strategy is predictive, provided a presumed mechanism at the origin of the catalyst synthesis.

## 2. PHYSICOCHEMICAL TOOLS FOR STRUCTURE DETERMINATION

### 2.1. Scanning Transmission Electron Microscopy (STEM)

The most convincing evidence of a full atomic dispersion is given simply by imaging the SACs or SOMC-prepared complexes. During the two last decades, electron microscopy science has benefited from a huge improvement in the lateral resolution of scanning transmission electron microscopes.<sup>54</sup> This is because the spherical aberration induced by the used electromagnetic round lenses are now compensated mostly by the integration of aberration correction devices.<sup>55</sup> Those past developments allowed new possibilities for the analysis at the atomic scale, which coincided with the emergence of synthesis protocols for the immobilization of single atoms.

Hence, the technique which is the most successful is the aberration corrected scanning transmission electron microscopy (STEM) coupled to a high-angle annular dark field (HAADF) detection. By using a combination of detector and camera length allowing a large collection angles ( $\beta > 70$ –200 mrad), electrons arising from Rutherford scattering are collected while electrons deviated by coherent elastic scattering are mostly excluded (removing the phase contrast). The intensity  $I$  in the resulting images is then, in first approximation, given by  $I \propto t \cdot Z^\alpha$  ( $\alpha = 1.5$ –2) with a thickness  $t$  and an average atomic number  $Z$ .<sup>56</sup> As a direct consequence, the contrast in HAADF-STEM images is sharpened when the difference between atomic number of

the single atoms and the atoms in the support is enhanced. Thus, the technique is best used for the observation of “heavy” single atoms on “light” supports ( $\text{C}_3\text{N}_4$ , graphite/C,  $\text{SiO}_2$ ,  $\text{Al}_2\text{O}_3$ , NiO, and zeolites). There are now a large number of examples in the literature imaging supporting metals atoms well separated from each other.<sup>57–62</sup> Some selected examples are shown in Figures 2–4.

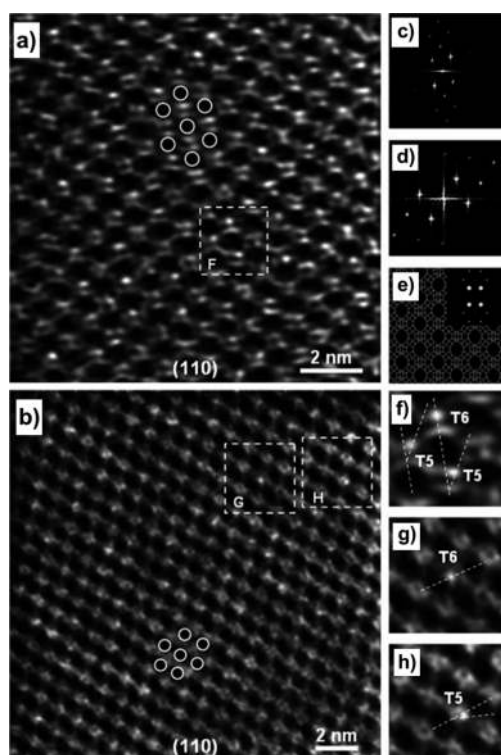


**Figure 2.** Aberration-corrected HAADF-STEM images of the sample prepared by adsorption of  $\text{Au}(\text{CH}_3)_2(\text{acac})$  in zeolite NaY. (a) Initially prepared sample. (b) Sample after treatment in flowing CO +  $\text{O}_2$  (during CO oxidation catalysis) for 30 min. (c) FFT of the experimental image shown in (a). (d) FFT of the experimental image shown in (b). (e) Simulated framework and theoretical diffraction pattern of zeolite Y in the  $[110]$  projection. (f–h) Zoomed-in views of the regions shown in rectangles in (a) and (b). Reproduced with permission from ref 57. Copyright 2012 John Wiley and Sons.

There are also several limitations to the technique, which are all important to mention. The first one, which is intrinsic to all

microscopies, is the number of single observations required to establish that an efficient metal dispersion has been achieved. Very often, single atoms in SACs are mixed with clusters, and thus it is best practice to provide some statistical evidence that single atoms are indeed the major species (Figure 4). The second is related to the previous explanation about the observed intensity in HAADF-STEM imaging: it is extremely difficult, not to say impossible, to observe light single atoms on heavy supports.<sup>64</sup> The third limitation is the sensitivity of the single atoms to the electron beam, which can modify their position, and distribution even before a single frame can be recorded (Figure 5).<sup>65</sup>

The stability of the support under the incident beam can also be a problem. Knock-on (e.g., graphene) or ionization damage (e.g., zeolite/nonconducting specimens) are both classically reported.<sup>66</sup> Knock-on damage occurs by transfer of kinetic energy above a given threshold value. For example, the threshold for such type of damage was calculated to be on the order of 80 keV for C nanotubes and of 70 keV for BN nanotubes.<sup>67</sup> Thus, imaging single atoms dispersed on such support requires an accelerating voltage of 20–60 kV and also a  $\text{C}_s$  aberration correction device to maintain a sufficient lateral resolution. On the other hand, reducing ionization damage demands the highest acceleration voltage to weaken the interaction between the electron beam and the support.<sup>68</sup> Imaging becomes even more complex when different types of single atoms are immobilized. How do we identify the nature of each bright dots in STEM images? Quantitative STEM simulation by multislice algorithm has to be undertaken to perform correct assignments by comparing the intensities in the experimental image with the simulated one.<sup>69</sup> For example, the group of B. Gates have reported a study, which demonstrates frame by frame, the reorganization under the electron beam of a bimetallic Rh–Ir system supported on MgO (Figure 6).<sup>70</sup> However, this is only possible when the support is crystalline and properly aligned along a zone axis and single atoms have significantly different atomic numbers.

To circumvent the limited discriminating power of the HAADF signal, spectroscopies are also used in combination with STEM imaging to perform a clear-cut identification. However, those developments associated with electron energy loss spectroscopy (EELS) and energy dispersive X-ray fluorescence spectroscopy (EDX) are relatively recent, and few examples are reported so far in the literature.<sup>71–77</sup>

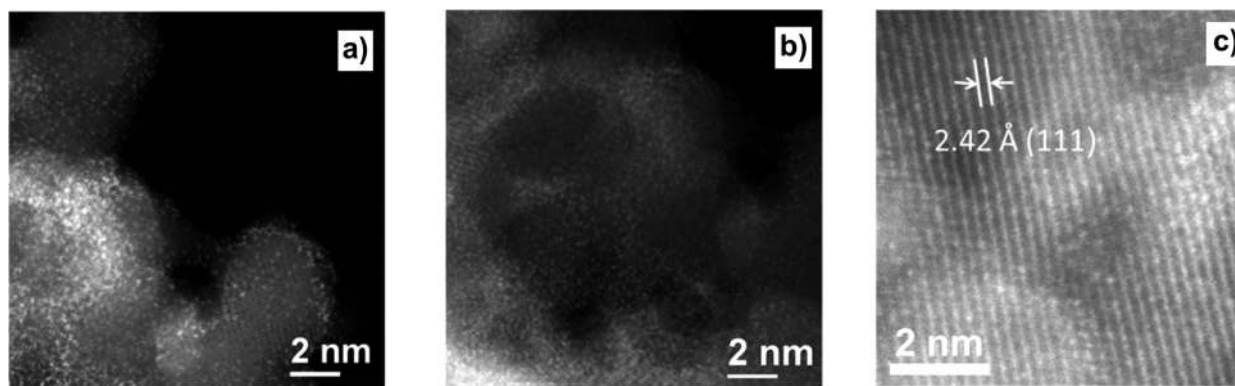


**Figure 3.** HAADF-STEM imaging of randomly selected areas of a Ta/NiO catalyst (a,b). High-resolution HAADF-STEM showing the single Ta atoms at lattice sites on NiO crystal surface (c). Adapted with permission from ref 58. Copyright 2015 Elsevier.



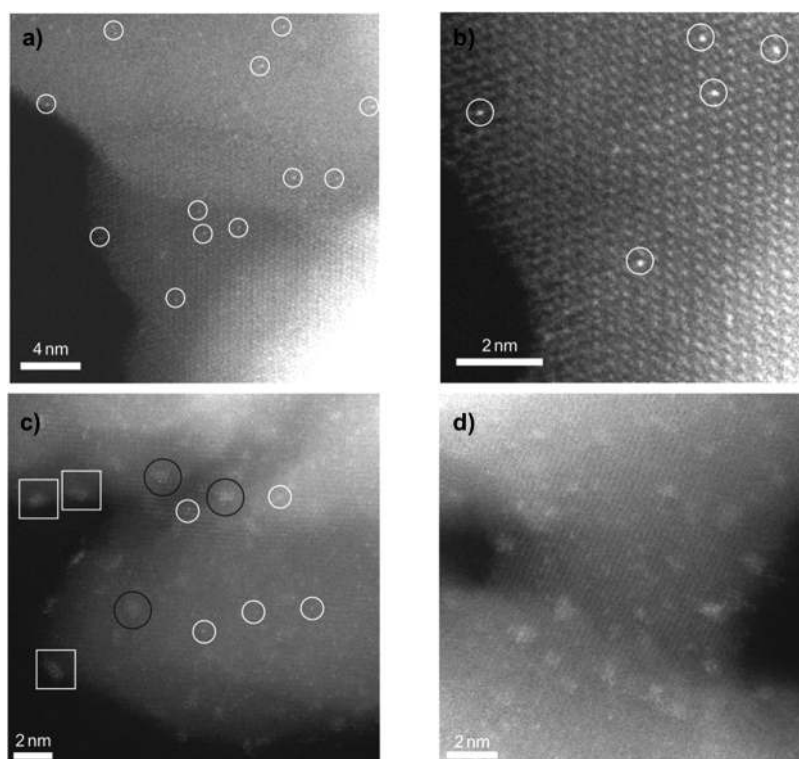


**Figure 4.** In sample A, Pt single atoms (white circles) are seen to be uniformly dispersed on the  $\text{FeO}_x$  support (a) and occupy exactly the positions of the Fe atoms (b). Examination of different regions shows that only Pt single atoms are present in sample A. (c,d) In sample B, a mixture of single atoms (white circles), two-dimensional Pt rafts consisting of fewer than 10 Pt atoms (black circles), and three-dimensional Pt clusters of size about 1 nm or less (white squares) are clearly observed. Reproduced with permission from ref 63. Copyright 2011 Springer Nature.

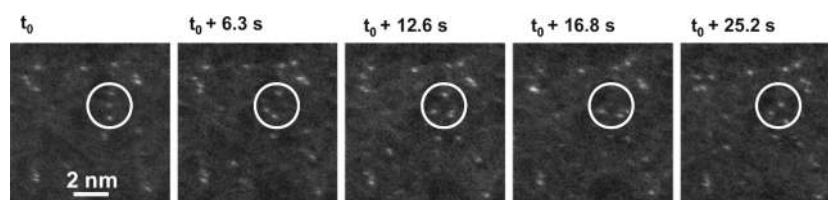


**Figure 5.** Examples of dynamic instabilities of atomic specimens: movement of individual atoms monitored by successive HAADF images in the Nion UltraSTEM operated at 60 keV. Reproduced with permission from ref 65. Copyright 2012 Elsevier.

With EEL spectroscopy, the spatial resolution is lowered compared to HAADF-STEM imaging. This is due to the inevitable delocalization of the inelastic signal.<sup>78</sup> The degree of delocalization varies roughly as  $v/E_l$  with  $v$  as the speed of the incident electrons and  $E_l$  the threshold energy of an atomic absorption edge. Practically, it implies that working with low acceleration voltage and high-energy ionization improves the spatial resolution. As an outstanding illustration of EEL single-atom spectroscopy, we present below the work of Suenaga et al.,<sup>79</sup> who performed the elemental analyses of various metallofullerene-doped single-wall nanotubes using an incident electron probe with a low accelerating voltage (60 kV). With La ( $Z = 57$ ) and Er ( $Z = 68$ ) atoms in a codoped peapod ( $\text{La}@\text{C}_{82}$  and  $\text{Er}@\text{C}_{82}$ ), there are no contrast difference on the ADF image (Figure 7a). However, the EELS chemical maps as shown on Figure 7b,c, clearly assign the La and Er atoms. The absorption edge energies of the La N-edge (99 eV) and Er N-edge (168 eV) are well separated, and the assignment is thus straightforward.

With close atomic numbers, overlaps between absorption edges require a careful analysis of the recorded EEL spectra.

For example, La and Ce atoms have the smallest atomic number difference ( $\Delta Z = 1$ ) and their  $N_{4,5}$ -edges have onset energies near each other (99 eV for  $\text{La}^{3+}$  and 109 eV for  $\text{Ce}^{4+}$ , Figure 8d). The position of the absorption edge is also subject to chemical shifts due to different valence states of the atom. With reduced  $\text{Ce}^{3+}$  cations, the 4d core-levels are located at higher energy, bringing the N-edges of  $\text{La}^{3+}$  and  $\text{Ce}^{3+}$  even closer (Figure 8d). By comparison of the EEL spectra with well-chosen references, Suenaga et al. succeeded in the unambiguous assignment of the single atoms shown on the ADF image (Figure 8a–c) and their respective valence state, namely  $\text{La}^{3+}$  and  $\text{Ce}^{3+}$  (Figure 8b–d).<sup>79</sup> Note also that in the same work, single calcium atoms inside the peapods were identified using EELS although invisible on the ADF images. The set of “light” atoms was expanded in 2015 to other elements such as Li, F, Na, and Cl.<sup>80</sup>

Only a few attempts are reported involving the use energy dispersive X-ray fluorescence spectroscopy (EDX) in order to detect single atoms.<sup>81–83</sup> EDX spectroscopy has always been regarded as more challenging compared to EEL spectroscopy. On the one hand, EELS collects most of the forward-scattered

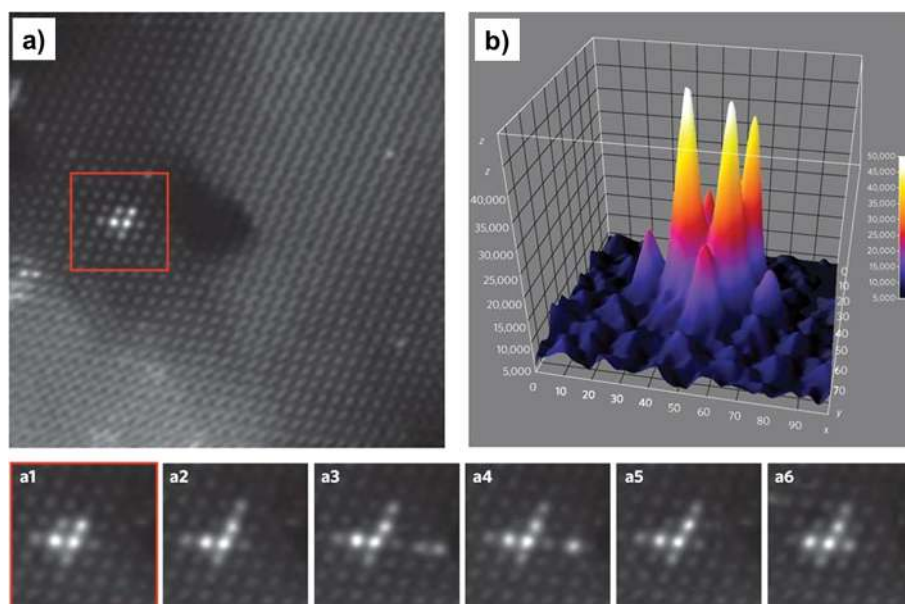


**Figure 6.** Sequentially taken STEM Z-contrast images and intensity surface plot of a rhodium–iridium cluster. (a) HAADF (Z-contrast) image of a rhodium–iridium cluster adsorbed on a MgO(110) surface. Panels a1–a6: sequentially taken Z-contrast images of the cluster in the square frame indicated in the main panel. The images show rhodium and iridium atoms in brighter contrast than the magnesium and oxygen columns of the MgO surface. The image in panel a1 corresponds to the area shown in the square frame in the main panel. (b) Intensity surface plots of the part of the image outlined in a. The surface plot and the Z-contrast images are smoothed for better visualization. Intensity measurement and quantification were performed using original images. Reproduced with permission from ref 70. Copyright 2010 Springer Nature.

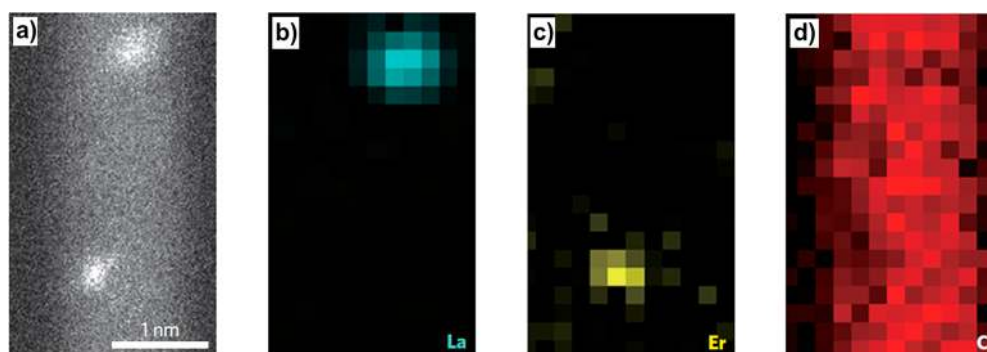


**Figure 7.** Element-selective imaging of single La and Er atoms. (a) ADF image of a peapod co-doped with La@C82 and Er@C82. Two atoms are visible, but elemental identification is not possible. (b–d) EELS maps for La (blue) (b), Er (yellow) (c), and C (red) (d). La and Er atoms are clearly visible and discriminated in each EELS chemical map. Reproduced with permission from ref 79. Copyright 2009 Springer Nature.

electrons that have lost energy upon photoionization of the absorber atom. On the other hand, the relaxation of the core-hole follows as a secondary process and can trigger an isotropic emission of X-ray photons. However, the EDX spectrometer collects only a fraction of those photons due to its limited collection angle ( $\approx 0.7$ – $1.0$  sr, providing less than 10% detection efficiency). Furthermore, not all ionization events lead to X-ray fluorescence. Specific fluorescence yield are tabulated for each transition and the general trend indicates that lighter atoms are more difficult to detect.<sup>84</sup> This constitutes the main drawback of X-ray fluorescence when compared to EEL spectroscopy. For example, Suegana proposed an estimation of the counting efficiencies of single-atom detection using EDX and EELS chemical analyses.<sup>82</sup> Simultaneous acquisition of the EELS N-edge and L or M fluorescence lines for single Er atoms highlights 4–5 orders of magnitude difference in terms of signal counts (Figure 9). However, STEM-EDX also has a few advantages over STEM-EELS. EDX detection is more efficient for deep inner-shell

ionizations above 2 keV, while it is practically marginal for EELS. Also in the collected X-ray fluorescence spectra, the signal intensity and background levels remain relatively constant over the typical collection range of 0–20 keV. Thus, few adjustments to analysis conditions are required, allowing EDX to detect small amount of unforeseen elements, such as impurities or contaminants. Finally, the possibility to work with high-energy emission lines is supposedly beneficial to the reduction of the delocalization in the inelastic signal.<sup>82</sup> This property, although predicted by the theory, has not yet been clearly demonstrated experimentally (Figure 9), probably due to the parasitic atomic motion of the single atoms under the beam.<sup>81</sup>

## 2.2. X-ray Spectroscopy

X-ray absorption spectroscopy (XAS) is a state-of-the-art spectroscopy to characterize the local environment of the catalytic metal centers. A typical XAS experiment consists of measuring the absorption signal directly or indirectly



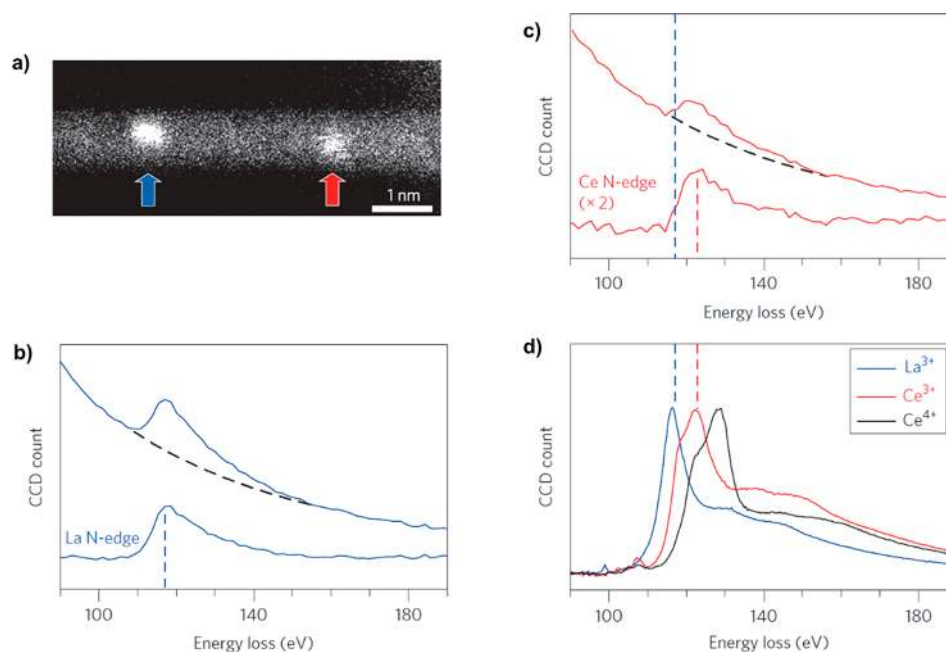


**Figure 8.** Single-atom spectroscopy for La and Ce. (a) ADF image of a peapod co-doped with La@C82 and Ce@C82. La is indicated by the blue arrow and Ce by the red arrow. (b,c) EELS spectra taken from La@C82 (b) and Ce@C82 (c) shown in (a). (d) Reference EELS spectra of La<sup>3+</sup> (in LaCl<sub>3</sub>, blue), Ce<sup>3+</sup> (in CeCl<sub>3</sub>, red), and Ce<sup>4+</sup> (in CeO<sub>2</sub>, black). The atom on the left in (a) is assigned as La and the atom on the right in (a) as Ce in the trivalent state (Ce<sup>3+</sup>). Reproduced with permission from ref 79. Copyright 2009 Springer Nature.

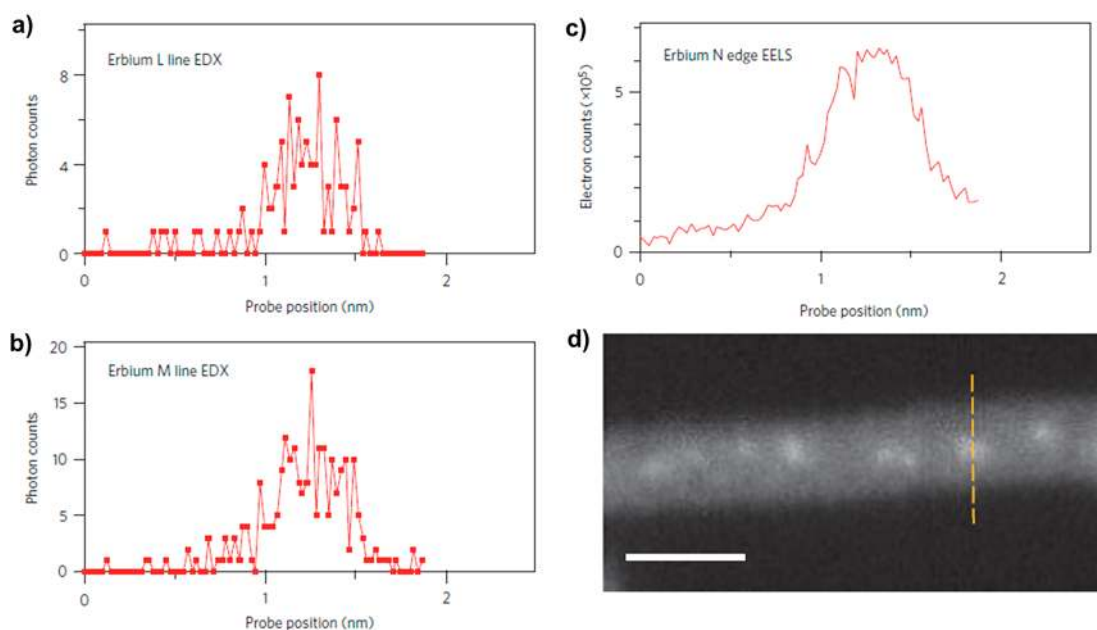


**Figure 9.** Line profiles of EDX and EELS. (a–c) Line profiles from the line scan across a single erbium atom for erbium L (EDX, a), M (EDX, b), N (EELS, c), respectively. (d) ADF image of the specimen. Brighter spots correspond to single erbium atoms and are well distributed at intervals of 1 nm, on average. The yellow dotted line shows where a typical line spectrum is recorded. Scale bar, 2 nm. The photon counts for erbium L and M EDX signals are  $\approx 8$  and 18 at maximum. Note that the transmission EELS can provide much better signals. There is a larger tail for the erbium N EELS signal than for EDX, which may reflect the different delocalization effects. Reproduced with permission from ref 82. Copyright 2012 Springer Nature.

(fluorescence, Auger electrons, total electron yield) while increasing the energy of the incoming X-rays. At a certain threshold energy, a sharp increase in the absorption signal occurs. This energy is referred to as the absorption edge, and its value is specific to the core-levels of each atoms. The physical phenomena at stake for both XAS and XPS is the photoelectric effect, where an electron from a core-level is

excited by an X-ray photon above the Fermi level. The latter is named a photoelectron, and its kinetic energy is equal to the difference in the energy of the incoming X-ray and its initial bonding energy. Hence, one of the main advantages of XAS is to be an element specific spectroscopy. XAS is also applicable to a broad range of elemental concentrations and therefore is applied to a broad range of single atoms distributed on various

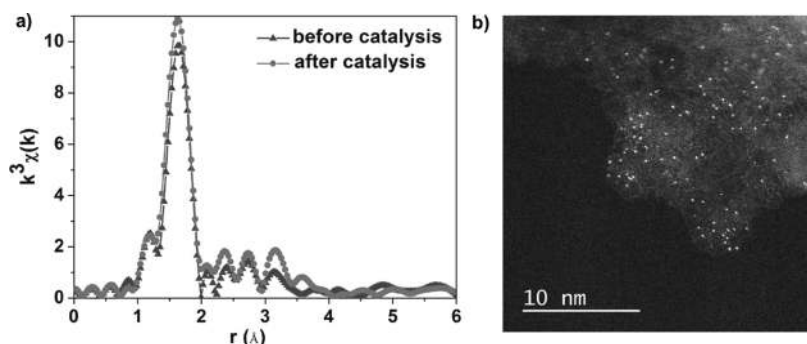


**Figure 10.** (a) Comparison of FT-EXAFS curves of the Pt single atoms isolated on g-C<sub>3</sub>N<sub>4</sub> before and after the photocatalytic reaction. (b) HAADF-STEM image of the photocatalyst after the photocatalytic reaction for hydrogen production. Reproduced with permission from ref 93. Copyright 2016 John Wiley and Sons.

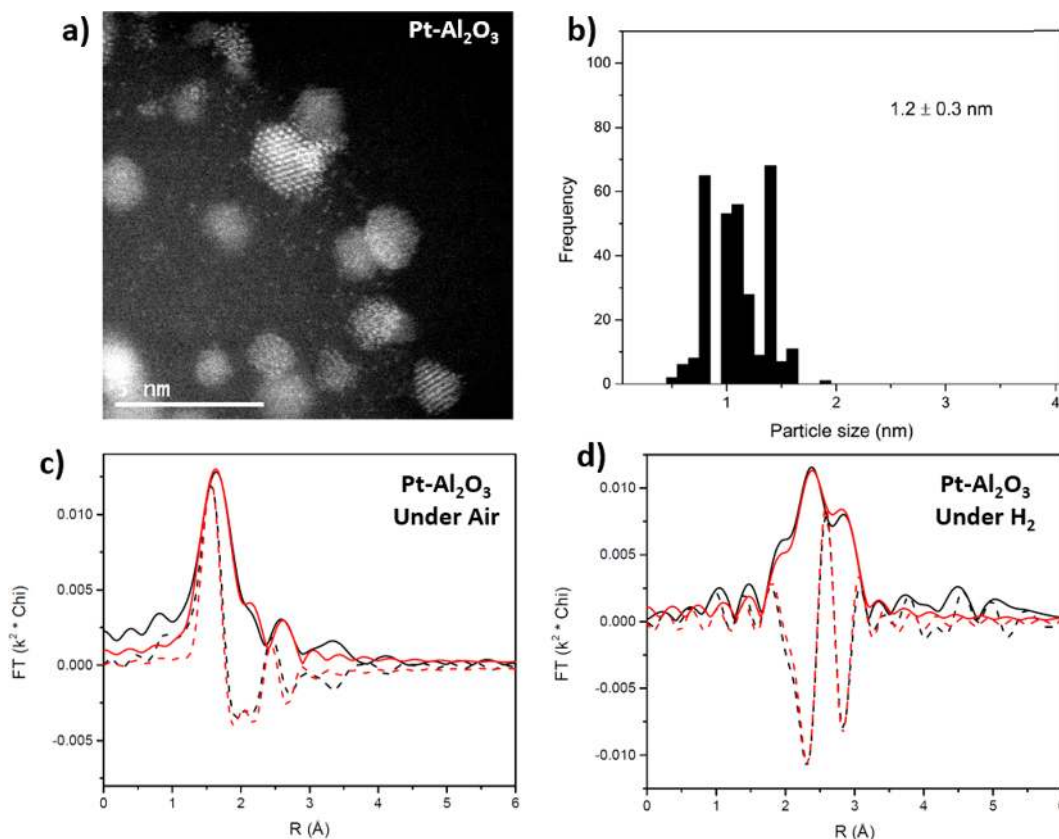


**Figure 11.** TEM micrographs and the corresponding particle size (number) distributions with mean and associated error ( $\pm 1\sigma$ ) of (a,b) 2 wt % Pt-Al<sub>2</sub>O<sub>3</sub>; EXAFS spectrum of prerduced 2 wt % Pt-Al<sub>2</sub>O<sub>3</sub> in air (c) and measure under H<sub>2</sub> (d). The solid black line represents the FT magnitude, the dashed black line represents the imaginary part of the FT, while the red solid and dashed lines are the fits of the magnitude and the imaginary part, respectively. Reproduced with permission from ref 94. Copyright 2014 Royal Society of Chemistry.

supports. A XAS spectrum can be divided into three regions, namely the pre-edge, the X-ray absorption near edge structure (XANES), and the extended X-ray absorption fine structure (EXAFS). XANES, due to its sensitivity to the oxidation states of metals, ligand field, and support materials, is a premier tool to study electronic properties. EXAFS, due to its local excellent spatial resolution, is a preferred technique for investigating structural properties. Although probing different information, these two spectroscopies are part of the same acquired spectrum and are complementary in the analysis and interpretation of the results. The inherent advantage of X-ray spectroscopies is their application under working conditions of

the catalysts (i.e., in operando) due to the extended penetration depth of hard X-rays.

**2.2.1. EXAFS Spectroscopy.** The EXAFS spectra present characteristic oscillations in the measured linear absorption coefficient in the energy region starting roughly at 50 eV above the absorption edge. The EXAFS region is classically understood by treating the ejected photoelectron as a spherical wave which expands in the lattice and is partially scattered by neighbors of the absorbing atom. The neighboring atoms are treated as point scatterers, and the total scattered wave is summed from the waves scattered by each atom. The resulting interference pattern leads to the modulation of the measured absorption coefficient, thereby causing the oscillation in the

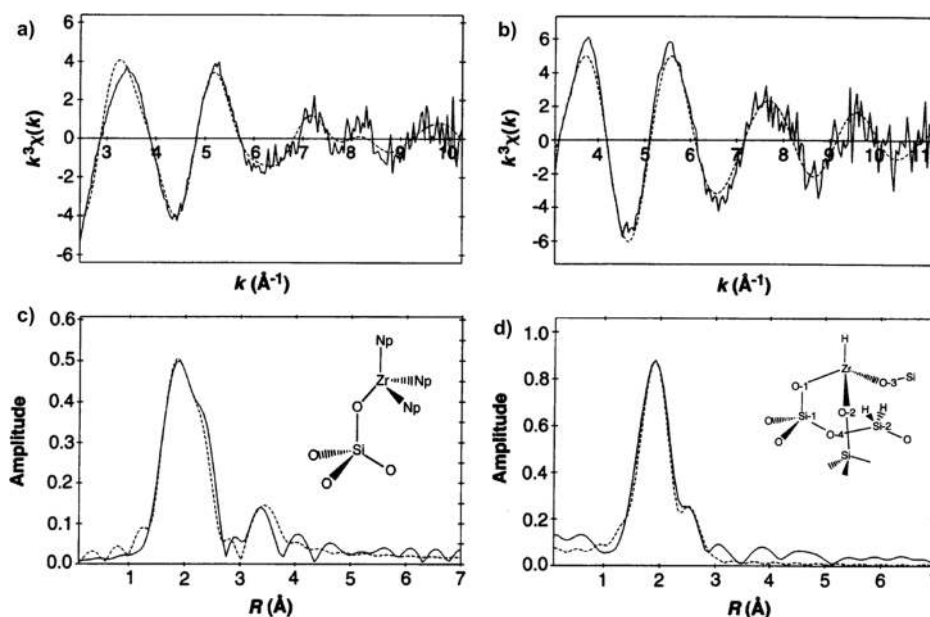


**Figure 12.** (a,b) Zr K-edge  $k^3$ -weighted EXAFS and (c,d) Fourier transform, phase-shift corrected for oxygen, of (a,c)  $(\equiv\text{Si}-\text{O})-\text{ZrNp}_3$  and (b,d)  $(\equiv\text{Si}-\text{O})-\text{ZrH}$  from experiment (solid lines) and spherical wave theory (dotted lines). Reproduced with permission from ref 97. Copyright 1996 The American Association for the Advancement of Science.

EXAFS spectra. With the majority of studied single atoms, the treatment of EXAFS spectroscopy data is performed with a single scattering approximation.<sup>85</sup> At the end, a pseudoradial distribution function is determined by calculating the bond lengths (with an accuracy of about 0.01 Å), the number of neighboring atoms, and in some favorable cases, by identifying the type of atoms bonded to the metal center. EXAFS spectroscopy in the context of single atoms characterization aims primarily at showing the absence of metal–metal shells in the Fourier transformed EXAFS spectra. This property supports the hypothesis of mononuclearity for the main body of the published studies.<sup>63,86–92</sup> For example, Li et al. reported the isolation of single Pt atoms as hydrogen evolution cocatalysts anchored on  $\text{g-C}_3\text{N}_4$ .<sup>93</sup> The FT-EXAFS spectra of the photocatalyst before and after the reaction (Figure 10a) gives a single sharp peak centered at about 1.5 Å and do not present any Pt–Pt shell (expected at 2.3 Å, without phase correction). This feature demonstrates the stability of the platinum dispersion and was further confirmed in parallel by HAADF-STEM (Figure 10b).

However, our own experience with this technique has pointed that the absence of metal–metal scattering on the Fourier transformed EXAFS spectrum is a necessary condition but not sufficient. To illustrate that point, we propose to consider the work of Gallagher et al. in Figure 11, which presents the FT-EXAFS spectra of  $\approx 1$  nm platinum nanoparticles supported on alumina (Figure 11a,b) measured in air (Figure 11c) and under hydrogen atmosphere (Figure 11d).<sup>94</sup> The Pt– $\text{Al}_2\text{O}_3$  catalyst measured under  $\text{H}_2$  clearly highlights, as expected, a Pt–Pt scattering with the typical 2.75 Å bond length distance of the metallic fcc structure. With the same material measured in air, the Pt–Pt contribution almost vanishes while a new shell appears with shorter bond distance ( $\approx 2.0$ – $2.1$  Å) typical of a Pt–O shell. Note that the latter spectrum (Figure 9c) looks similar to any spectrum measured for supported single atoms, although TEM imaging clearly shows an overwhelming presence of nanoparticles. Gallagher et

al. have demonstrated by a combination of X-ray synchrotron techniques (SAXS, PXRD, and PDF analysis) that upon exposure to air, the metallic particles were partially oxidized and the fraction of the remaining metallic core was dependent on the original size of the nanoparticles. For the smallest nanoparticles/clusters, it can reach a point where almost all platinum atoms are oxidized and thus the nanoparticles undergo large disorder within their crystalline structure. This has a direct influence on the possibility to detect metal–metal shell by EXAFS spectroscopy. Indeed, part of the attenuation of the EXAFS oscillations is modeled by an EXAFS Debye–Waller factor, which depends on the structural disorder around the metallic center, either due to thermal motion of atoms (dynamic disorder) or structural disorder (static disorder).<sup>95,96</sup> The net result is a damping of the EXAFS amplitude, especially at high wave vector value. Thus, an amorphous nanoparticle may not show any significant metal–metal contribution for this reason. Also, due to the limited accuracy of the technique, one can miss minor clusters incorporating metal–metal bonds depending on the sample and data quality. Practically, it means the evidence of atomically dispersed metals by EXAFS spectroscopy is only indisputable when complemented by atomic-resolution microscopic images with sufficient statistic.

Once the atomic dispersion is properly highlighted, one would like to go further in the EXAFS analysis in order to pinpoint the coordination geometry of the single atoms. Since EXAFS spectroscopy is an average technique, the structures deduced from EXAFS spectra are most relevant when the single atoms are actually single sites. By definition, a single site catalyst has a uniform structure through the sample. In practice, this is rarely achieved because most of the supports for SACs display surface structures with substantial complexity. Consequently, EXAFS spectroscopy will only provide an average of the local order around the metal center, knowing that the average can be a patchwork of various geometries. One strategy to reduce the surface complexity is to use high surface specific silica as an amorphous support but heat-treated up to



500–700 °C to create isolated and quasi-identical Si–OH surface groups. Those surface silanols are used as uniform anchoring point for the metal atoms. Some examples of EXAFS spectroscopy applied for those systems can be found from Basset, Scott, Gates, Marks, Taoufik, and Coperet research groups.<sup>31,35,37,97–109</sup> An example of such successful EXAFS characterization of SOMC is given in Figure 12 and Table 1.

**Table 1.** Zr K-Edge EXAFS-Derived Structural Parameters for the Grafted Zr Complexes on Silica Dehydroxylated at 500 °C<sup>a</sup>

| shell                    | coordination no. | distance <i>R</i> (Å) | 2σ <sup>2</sup> (Å <sup>2</sup> ) |
|--------------------------|------------------|-----------------------|-----------------------------------|
| (≡Si–O)ZrNp <sub>3</sub> |                  |                       |                                   |
| O                        | 1.1(1)           | 1.956(3)              | 0.0066(8)                         |
| C                        | 3.2(1)           | 2.219(4)              | 0.0163(9)                         |
| C                        | 2.8(3)           | 3.42(1)               | 0.026(3)                          |
| (≡Si–O) <sub>3</sub> ZrH |                  |                       |                                   |
| O                        | 3.1(1)           | 1.945(3)              | 0.0170(5)                         |
| O                        | 1.1(2)           | 2.61(1)               | 0.018(3)                          |

<sup>a</sup>Reproduced with permission from reference 97. Copyright 1996 The American Association for the Advancement of Science.

Corker et al. established the accurate coordination geometry of a SOMC-based zirconium hydride ((≡SiO)<sub>3</sub>Zr–H) resulting from hydrogenolysis of (≡Si–O)Zr(Np)<sub>3</sub> (Np, neopentyl).<sup>97</sup> A clear advantage of SOMC regarding the characterization by EXAFS spectroscopy is that they allow the determination of subtle changes in the metal coordination sphere depending on the temperature and/or the reactive atmosphere.

A well-known limitation of EXAFS spectroscopy is related to the difficulty of identifying atoms with close atomic number. There is in principle no reason to attribute a light backscatterer atom (e.g., O) over another (e.g., C) (Table 1). This is why the assignment of the scattering paths always needs to be supported by other characterization techniques such as elemental analysis, solid-state nuclear magnetic resonance, and infrared (IR) spectroscopies.<sup>97,98</sup>

EXAFS analysis can be challenging even with structurally uniform materials unless all the contributing paths are hinted by other characterization techniques. Indeed, the identification of scatterer is further complicated when two or more paths (single- and/or multiple-scattering) have similar path lengths with opposite phase, canceling each other in the Fourier transform (FT). Data treatment of EXAFS spectroscopy by wavelet transform (WT) was developed to resolve overlapping EXAFS paths based on the atomic numbers of the scattering atoms.<sup>110,111</sup> As an example, Scott et al. reported a study dedicated to the characterization of molybdates dispersed at low loading in the zeolite ZSM-5.<sup>112</sup> WT EXAFS was used to resolve a controversy on the presence of monomeric molybdate species or dimolybdate/oligomeric sites inside the zeolite channels (Figure 13). The utility of such an approach was demonstrated using EXAFS data of crystalline MgMoO<sub>4</sub> and MgMo<sub>2</sub>O<sub>7</sub>, in which single- and multiple-scattering paths (Mo–O, Mo–Mg, Mo–Mo, Mo–O–O, Mo–Mg–O, and Mo–Mo–O) were all found to contribute to the EXAFS signal over a narrow *R*-range. By comparing the WT-EXAFS features of the Mo/ZSM5 catalyst with the previous model compounds, the authors concluded that Mo/HZSM-5 catalyst mostly

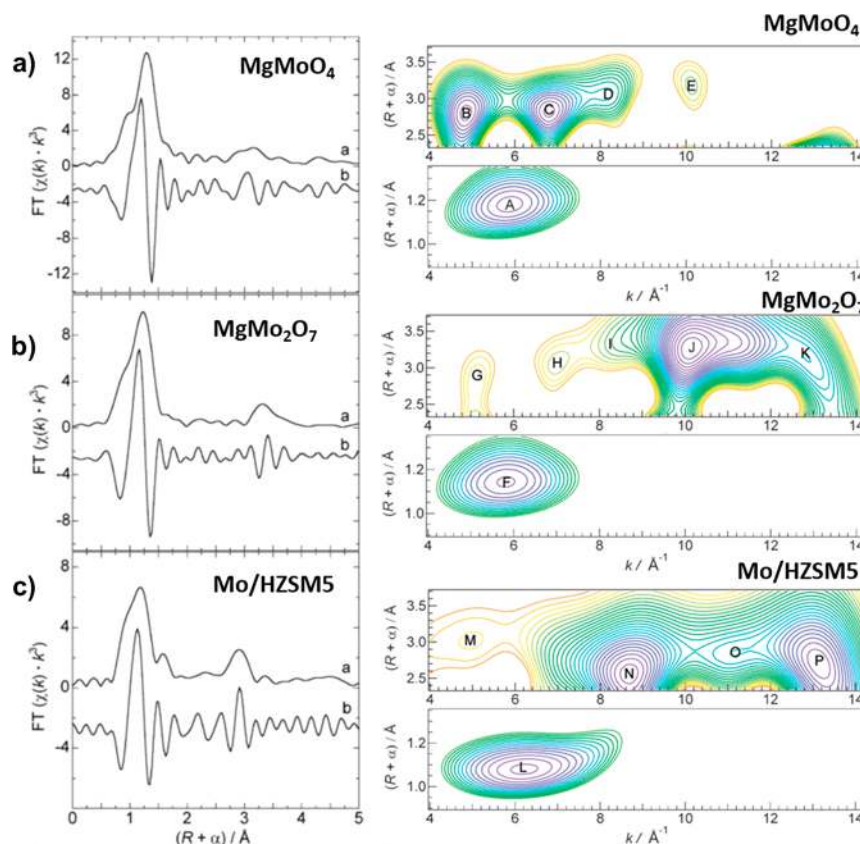


**Figure 13.** Comparison of *k*<sup>3</sup>-weighted EXAFS in *R*-space and Wavelet transform plots for MgMoO<sub>4</sub> (a), MgMo<sub>2</sub>O<sub>7</sub> (b), and Mo/HZSM-5 (c). High contour elevations are indicated in purple. Adapted with permission from ref 112. Copyright 2010 Royal Society of Chemistry.

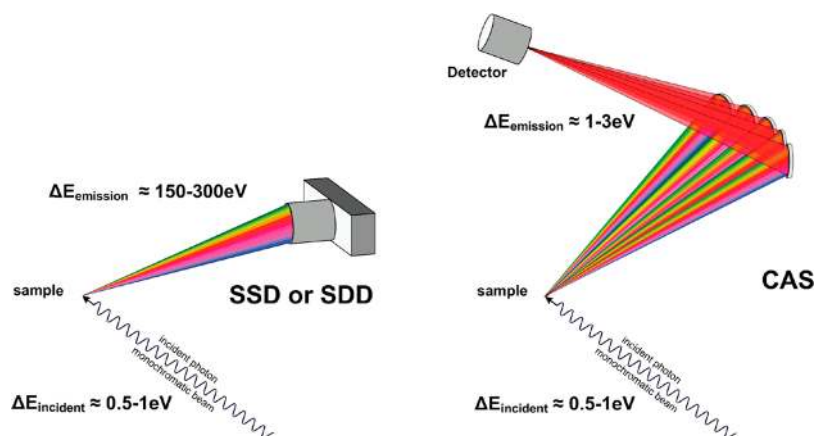


**Figure 14.** Principle of X-ray absorption spectroscopy (XAS)-fluorescence measurement using solid-state detector (SSD) and crystal analyzer spectrometer (CAS). Produced with permission from ref 137. Copyright 2017 Soil Science Society of America, Crop Science Society of America, American Society of Agronomy.

contains dimolybdate ions. WT analysis was also recently applied by the same group to characterize the structure of  $\text{Ga}(\text{i-Bu})_3$  grafted on silica and alumina. Here, the WT analysis was used as a straightforward assistance to pinpoint the Ga–Ga scattering in order to perform the final curve fitting of the EXAFS data. It was found that grafting on alumina occurs mostly as in mononuclear gallium sites while grafting on silica results in dinuclear species.<sup>113</sup>

SOMC and EXAFS spectroscopy also shine when crystalline supports with well-defined surface chemistry are used to isolate single atoms. Gates et al. have notably investigated two types of supports: nonporous nanoparticles with preferentially exposed facets (e.g.,  $\text{MgO}$ ,  $\text{TiO}_2$ ) and crystalline microporous solids (zeolite and metal organic framework).<sup>114–125</sup> Another group that is particularly active in this field is from the University of Torino (Bordiga, Lamberti et al.), and the reader is directed to their extensive review including their own work.<sup>126</sup>

**2.2.2. XANES and HERFD-XAS Spectroscopies.** In the XANES energy range, where the kinetic energy of the photoelectron is slightly positive (or the incident photon energy is just higher than the core level energy), modulation of the absorption cross-section will occur through multiple scattering events. This effect, although harder to understand and predict from the theoretical point of view, unlike EXAFS spectroscopy, is a unique chance to grasp the three-dimensional structure around the absorber atom. X-ray absorption near-edge structure also reflects the distribution in energy of the virtual orbitals located on the single metal atoms.<sup>126</sup> The principal type of probed virtual orbitals depends on the chosen absorption edge (assuming a dipolar selection rule): The K-edge probes the transition of a 1s electron to np level and the  $L_{2,3}$  edges, a transition from a 2p electron to d level. Consequently, the  $L_{2,3}$ -edges are particularly useful to monitor the oxidation state of a transition metal and to observe the interactions with adsorbates. For K-edges, another interesting energy region is the lower side of the XANES, the so-called pre-edge region. Resonant structures may appear in this region due to  $(1s) \rightarrow (nd)$  transitions. These transitions gain their intensity via quadrupolar coupling or by 3d-4p mixing in a noncentrosymmetric environment. The analysis of such features permits the extraction of information on the spin or oxidation state, geometry, and type of ligand/adsorbate. The pre-edge features for K-edge XANES of 3d transition metals have been studied in detail.<sup>127–129</sup> The standard analysis of the

XANES spectra is traditionally accomplished either by comparing the unknown spectrum with the spectra of model compounds and/or by calculating the theoretical spectra of hypothetical structures which are believed to match the experimental data.<sup>127,130–134</sup>

An intrinsic limitation of XANES spectroscopy arises from the natural width of the core–hole. The latter affect the apparent energy resolution and can hide relevant spectral features in the spectrum. To overcome this broadening, XANES can be measured by monitoring fluorescence line intensity with an energy resolution below the core–hole lifetime broadening of the absorption edge.<sup>135,136</sup> On the instrumentation side, this is achieved with a crystal analyzer spectrometer. A common geometry found on beamline is the Rowland geometry where spherically bent crystal wafers are arranged in the Rowland circle with respect to the sample and to the photon detector (Figure 14).<sup>137</sup> Thus, Bragg reflections are used to monochromatize the incident beam energy as well as to analyze the fluorescence emission, providing similar energy resolutions. The high experimental resolving power also ensures an optimal separation of all fluorescence lines that may potentially overlap depending on the sample and when using an SSD or SDD fluorescence detector (energy resolution of 150–300 eV). The fluorescence intensity is recorded as a function of the incident energy and the measurement is then called high-energy resolution fluorescence-detected X-ray absorption spectroscopy (HERFD-XAS).

A recent example of the application of HERFD-XAS for the characterization of SOMC-based complexes was reported by Hoffman et al.<sup>138</sup> The author investigated the exchange of ethylene and CO on single-site iridium supported on crystalline porous HY zeolite and on crystalline  $\text{MgO}$  powder. The interpretation of the spectral features in the HERFD-XANES spectra recorded at Ir  $L_{3\text{-edge}}$  were unraveled by electronic structure calculations and the simulation of the theoretical XANES spectra.<sup>139</sup> The study demonstrates that high-energy-resolution XANES is a sensitive method for characterization of single atoms in reactive atmospheres (Figure 15).

Even if HERFD-XANES has so far found more applications in the field of solid state chemistry and the number of works for the characterization of single atoms is rather scarce, we believe that the technique will emerge in the future for

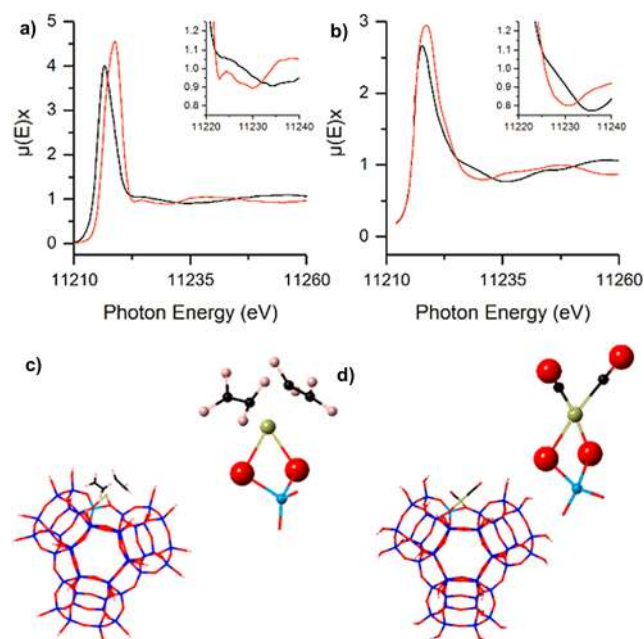


**Figure 15.** Comparison of (a) high-energy-resolution XANES and (b) FEFF-simulated XANES characterizing zeolite-supported  $\text{Ir}(\text{C}_2\text{H}_4)_2$  (black line) and  $\text{Ir}(\text{CO})_2$  (red line) species. Spectra were measured at the Ir  $L_3$ -edge with HERFD, and FEFF simulations were done with a 48-T atom HY zeolite structure. Insets: spectra between 11220 and 11240 eV highlighting the presence or lack of the feature at 11225 eV. (c) 48-T atom HY zeolite structure containing  $\text{Ir}(\text{C}_2\text{H}_4)_2$  and (d) 48-T atom HY zeolite structure containing  $\text{Ir}(\text{CO})_2$ . Atom colors: oxygen, red; silicon, dark blue; aluminum, light blue; iridium, yellow; carbon, black; hydrogen, pink. Reproduced with permission from ref 138. Copyright 2017 John Wiley and Sons.

characterization of ligands on metals dispersed on surfaces.<sup>140–143</sup>

### 2.2.3. Valence-to-Core X-ray Emission Spectroscopy (XES).

X-ray emission spectroscopy (XES), a relatively old technique, has been strongly developed in recent years. The required instrumentation for the measurement of an emission spectrum is similar to the one presented above for the HERFD-XAS measurement (Figure 14), although other types of set-ups are also developed for enhanced time resolution.<sup>144</sup>

For X-ray emission spectroscopy, the incident X-ray energy is maintained constant while the intensity of the fluorescence is scanned by varying the Bragg angle of the analyzer crystals. The spectroscopy relies on the ionization of a core electron on the absorber atom by incident X-ray photons with energies well-above the K-edge energy threshold. Then, an electron decays to fill the 1s core-hole with a simultaneous emission of photons.<sup>145</sup> For the particular case of valence-to-core X-ray emission (VTC-XES) spectrum, the peaks observed in the spectrum arise from transitions from occupied orbitals a few eV below the Fermi level (the valence band for solids or the highest occupied molecular orbitals for complexes). With first row transition metals, this valence-to-core region is traditionally divided into two emission lines: the  $K\beta''$  and  $K\beta_{2,5}$  transitions which are respectively attributed to orbitals mixed metal–ligand ns and np states. One of the first application of VTC-XES for chemistry is related to the sensitivity in energy position of the  $K\beta''$  peak which depends on the identity of the ligand (e.g., C, N, O, S).<sup>146–149</sup> This is why VTC-XES is a useful technique and complementary to XAS due to the impossibility of EXAFS spectroscopy to distinguish between neighboring atoms of similar atomic number such as C, O, and N. Furthermore, both the excited and emitted X-rays are hard

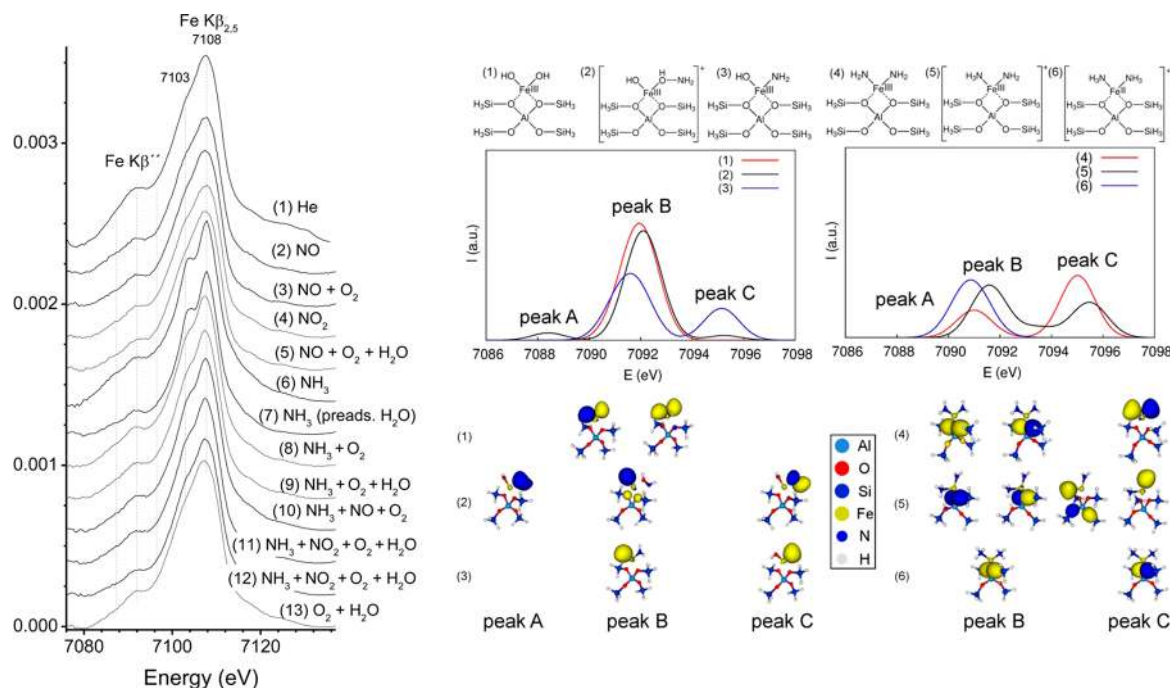


**Figure 16.** Comparison of measured VTC-XES spectra of Fe-ZSM-5 in different gas media (left). (right top) Lewis structures of molecular models (1–6) considered in DFT calculations. (right middle) Calculated V2C XES  $K\beta''$  spectra for these models. (right bottom) The orbitals from which the main contribution to peaks A–C originates, shown as isosurface plots. Reproduced with permission from ref 140. Copyright 2014 American Chemical Society.



X-rays, which means that the electronic structure of the single atoms can be investigated in reactive atmosphere.<sup>142,150–153</sup>

An exceptional example was reported by Boubnov et al., where VTC-XES was applied to unravel the mechanism of the selective catalytic reduction of NO over Fe-ZSM-5.<sup>140</sup> VTC-XES spectra of iron were recorded sequentially in different gas atmospheres aiming at stabilizing various intermediate iron states during the reaction mechanism (Figure 16, left). Their interpretation of the XES spectra has benefited from the recent theoretical development implemented in the ORCA program package.<sup>154–159</sup> By simulating the VTC-XES spectra corresponding to structures of molecular models expected during the reaction, the authors were able to assign most of the observed spectral features (Figure 16, right). Notably, VTC-XES K $\beta$ '' spectroscopy provided evidence of the adsorption of ammonia in the presence of large amount of water, which is difficult with vibrational spectroscopy. Combining the results of HERFD-XANES measured in the same operating conditions, the authors concluded that the key reactions in the NH<sub>3</sub>–SCR mechanism over Fe–ZSM-5 involved: (a) the adsorption of NO and ammonia via oxygen atom on a Fe<sup>3+</sup> site leading to a partial reduction of the site with (b) subsequent release of Fe<sup>2+</sup>, nitrogen, and water, (c) reoxidation of Fe<sup>2+</sup> as the rate-limiting step, and (d) water inhibition by coordination to the active center.

### 2.3. Solid-State NMR Spectroscopy

Solid-state NMR spectroscopy (SS NMR) is a powerful tool for the investigation of heterogeneous catalysts prepared from molecular precursors, especially those synthesized by SOMC<sup>160–163</sup> or catalysts connected through a tether to the surface.<sup>164</sup>

Generally, nuclei with spin number  $I = 1/2$ , such as <sup>1</sup>H, <sup>13</sup>C, <sup>19</sup>F, <sup>29</sup>Si, <sup>15</sup>N, or <sup>31</sup>P are commonly studied by SS NMR spectroscopy because the resolution is reasonably good, and the interpretation of results straightforward. Study of quadrupolar NMR nuclei with  $I > 1$ , such as <sup>11</sup>B ( $I = 3/2$ ),<sup>165</sup> <sup>27</sup>Al ( $I = 5/2$ ),<sup>166,167</sup> <sup>17</sup>O ( $I = 5/2$ ),<sup>168</sup> <sup>93</sup>Nb ( $I = 9/2$ ),<sup>50</sup> etc.,<sup>169</sup> is yet rarely reported in literature because SS NMR signals are typically wider due to rapid quadrupolar relaxation.<sup>50,162,163</sup> Nevertheless, many works in SOMC involve nuclei with spin number  $Z > 1$ . Hence, analysis of those nuclei is crucial to unravel structural information. In addition, two-dimensional methods often facilitated the determination of the structures of SOMC catalysts at a molecular level. 2D SS NMR experiments correlate proton spins, e.g., proton–proton double quantum (DQ),<sup>170</sup> triple quantum (TQ),<sup>171</sup> and combined rotation and multiple sequence (CRAMPS)<sup>172</sup> or spins of protons and other heteroatoms such as hetero nuclear correlation spectroscopy (HETCOR).<sup>173</sup>

The challenge of SS NMR spectroscopy remains the low signal-to-noise ratio per scan which depends on the following parameters: (i) the gyromagnetic ratio of the observed nuclei  $\gamma_{\text{obs}}$ , (ii) the strength of the static magnetic field  $B_0$ , (iii) the temperature, and (iv) the apparent transverse relaxation time  $T_2^*$ . Furthermore, detection limits in SS NMR are affected by inhomogeneous line broadening, which can reduce  $T_2^*$  by several orders of magnitude. The discovery of cross-polarization magic angle spinning (CP MAS)<sup>174</sup> solid-state NMR experiments improved the accurate determination of SOMC structures. Cross-polarization transfers polarization from nuclei with high gyromagnetic moment (for instance <sup>1</sup>H) to nuclei

with low gyromagnetic moment (for instance <sup>13</sup>C, <sup>15</sup>N, <sup>29</sup>Si, etc.). This, combined with magic angle spin at 5–20 kHz, yields high-resolution spectra. Dynamic nuclear polarization surface enhanced NMR spectroscopy (DNP-SENS) is another tool for better and faster characterization of heterogeneous catalysts.<sup>175,176</sup> Indeed, SOMC-prepared complexes typically display low loadings (<10 wt %, and generally on the order of 2 wt %), implying that it is even more challenging to obtain high quality SS NMR spectra. DNP-SENS requires the addition of a radical as exogenous source of polarization and solvent. Typically, the solid sample is prepared by incipient wetness impregnation (IWI) by mixing it with just enough radical containing solution to uniformly impregnate the whole surface of the investigated material. During a DNP SENS experiment, the sample is irradiated by microwaves which lead to a transfer of polarization from the radical through the solvent (proton spin diffusion) to the nucleus of interest. Such effect leads to the desired enhancement of the NMR signal within a very short time compared to conventional SS NMR spectroscopy (Figure 17).<sup>175</sup>

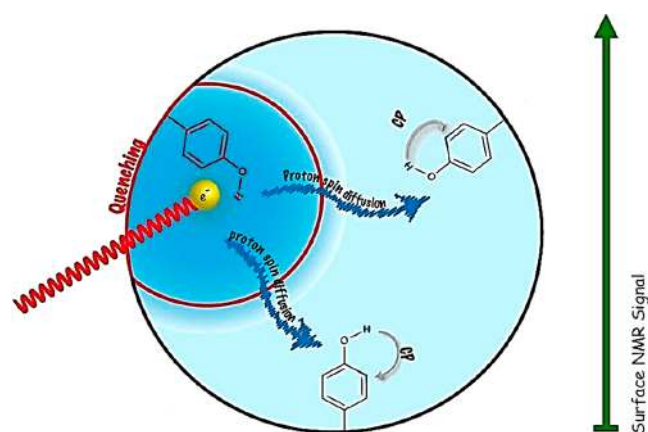


**Figure 17.** Schematic model of DNP SENS for porous materials. A stable radical is introduced into the pores by impregnation. Enhanced polarization is transferred to the protons of the solvent and organic functionalities. CP is used to transfer the enhanced polarization to dilute spin such as <sup>13</sup>C. Adapted with permission from ref 175. Copyright 2013 American Chemical Society.

In literature, there are many applications where DNP SENS is used to gain structural understanding of very complex molecules<sup>175,177,178</sup> on the surface materials such as silica,<sup>179</sup> alumina,<sup>180–182</sup> or zeolites<sup>183,184</sup> to functionalized heterogeneous catalysts.<sup>183,185–194</sup>

In the following, we will discuss some illustrative examples on how SS NMR spectroscopy and DNP SENS help to understand the structure of SOMC-prepared catalyst and, consequently, support the development of more efficient catalysts.

**2.3.1. Standard Characterization of SOMC Complexes.** **2.3.1.1. <sup>1</sup>H, <sup>13</sup>C MAS, and 2D SS NMR.** <sup>1</sup>H, <sup>13</sup>C MAS, and two-dimensional SS NMR techniques have become crucial tools for surface sciences, nanotechnology, and heterogeneous catalysis enabling the characterization of well-defined solids, as hybrid materials, grafted linkers, and heterogeneous catalysts. The applications of these techniques in SOMC are numerous. We have selected here some examples to deepen the understanding of SS NMR in SOMC.

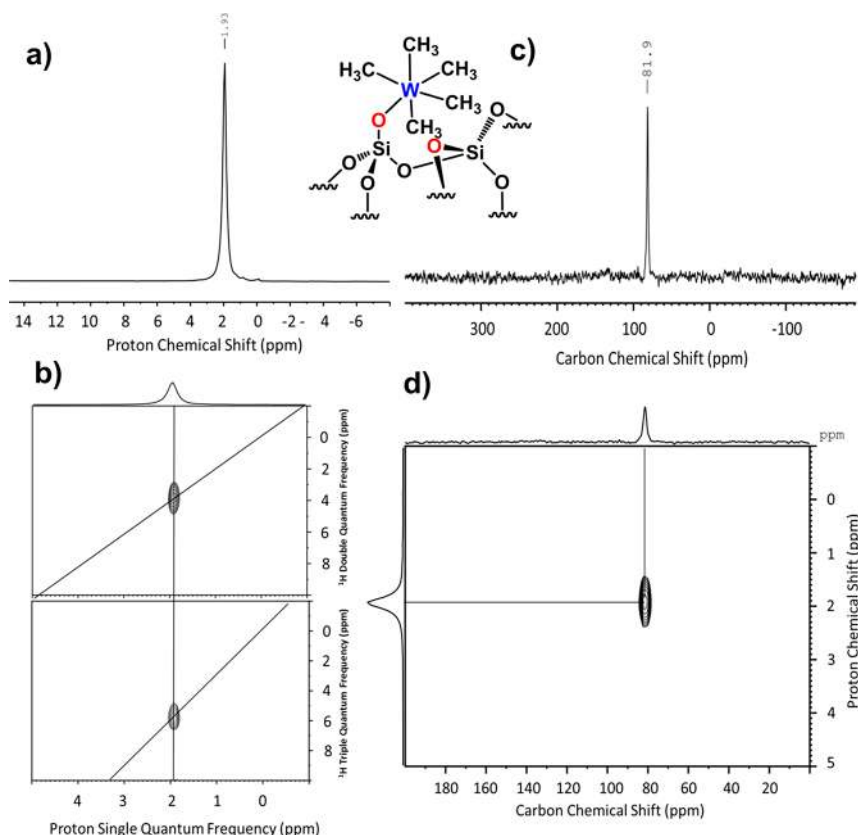


**Figure 18.** (a) One-dimensional  $^1\text{H}$  MAS solid-state NMR spectrum of  $[(\equiv\text{Si}-\text{O})\text{W}(\text{CH}_3)_5]$ . (b) Two-dimensional 2D  $^1\text{H}$ - $^1\text{H}$  double quantum (DQ)/single quantum and triple quantum (TQ)/single quantum NMR. (c)  $^{13}\text{C}$  CP-MAS NMR of  $[(\equiv\text{Si}-\text{O})\text{W}(\text{CH}_3)_5]$ . (d) 2D  $^1\text{H}$ - $^{13}\text{C}$  CP-MAS dipolar HETCOR spectrum of  $[(\equiv\text{Si}-\text{O})\text{WMe}_5]$ . Reproduced with permission from ref 196. Copyright 2014 American Chemical Society.

A breakthrough of SOMC was grafting  $\text{WMe}_6$  on partially dehydroxylated silica, a very sensitive molecule under standard conditions. The homogeneous structure of the complex was confirmed in 1996 by Seppelt et al.<sup>195</sup> It took 18 years, until 2014, before the complex was grafted on dehydroxylated silica  $\text{SiO}_{2-700}$ , which turned out to have powerful implications in catalysis.<sup>196</sup> The solid-state  $^1\text{H}$  MAS NMR and  $^{13}\text{C}$  CP/MAS NMR of  $[(\equiv\text{Si}-\text{O})\text{W}(\text{Me})_5]$  gave very sharp signals comparable to that of liquid NMR spectrum of homogeneous complex (Figure 18a,c). The development of CP/MAS NMR experiments helps determine the precise chemical shift of the grafted organometallic complex on oxide support.<sup>196</sup> With low temperature SS NMR experiments, the pseudo trigonal-prismatic arrangement of  $[(\equiv\text{Si}-\text{O})\text{WMe}_5]$  was proven by finding two nonequivalent types of methyl groups possessing a 2:3 stoichiometry instead than just one signal observed at room temperature because of coalescence.<sup>196</sup>

Additional two-dimensional experiments on  $[(\equiv\text{Si}-\text{O})\text{WMe}_5]$  confirmed (i) the spatial proximity of two protons observed as a peak which corresponds to the sum of two individual single-quantum frequencies ( $^1\text{H}$ - $^1\text{H}$  double quantum (DQ), Figure 18b, top), (ii) the proximity of three protons appearing as a signal, which equals thrice the individual single-quantum frequency (TQ spectrum, Figure 18b, bottom), and (iii) the structure of the complex as well as the well-defined nature of the surface complex ( $^1\text{H}$ - $^{13}\text{C}$ -HETCOR, Figure 18d).

DQ and TQ experiments, not only allow structural determination of a solid catalyst but also the spatial distance

between protons of different functional groups if they are close enough. For example, the DQ and TQ spectra of a bimetallic surface complex  $[(\equiv\text{Si}-\text{O})\text{W}(\text{CH}_3)_5/(\equiv\text{Si}-\text{O})\text{Zr}(\text{Np})_3]$  ( $\text{Np} = \text{CH}_2-\text{C}-(\text{CH}_3)_3$ ) show self-correlation corresponding to  $-\text{CH}_3$  (of  $-\text{W}(\text{CH}_3)_5$  at 2 ppm, and  $-\text{CH}_2$  of  $\text{ZrNp}_3$  at 1.2 ppm in the diagonal of the spectra (Figure 19). Additional peaks related to  $^1\text{H}$ - $^1\text{H}$  intercorrelation between both complexes are observed as extra peaks outside the diagonal (Figure 19). This observation confirms that both grafted complexes ( $-\text{WMe}_5$  and  $-\text{ZrNp}_3$ ) were placed in proximity with distance of  $\approx 5$  Å (Figure 19).<sup>197</sup>

Multiple quantum (MQ) experiments are helpful to distinguish different metal hydrides on solid surfaces. For example, after treating  $(\equiv\text{Si}-\text{O})\text{Zr}(\text{Np})_3$  with  $\text{H}_2$  at  $150^\circ\text{C}$ , the formation of zirconium hydride was identified by  $^1\text{H}$  MAS NMR spectroscopy showing two distinct hydride peaks at 10.1 and 12.1 ppm.<sup>170</sup> Nevertheless, it was not clear how many protons were present in the  $[\text{Zr}-\text{H}_x]$  metal complex. By closer analysis, it was observed that the two hydride species displayed very different relaxation times ( $T_1$ ). The signal at 12.1 ppm displayed a very short relaxation delay ( $\leq 2$  s), whereas it was much harder to obtain a constant signal at 10.1 ppm (relaxation delay was about 30 s). This observation confirmed the presence of two electronically different types of protons on  $[\text{Zr}-\text{H}_x]$ . To assign these species,  $^1\text{H}$ - $^1\text{H}$  MQ-MAS NMR was carried out. For the zirconium-hydride species at 12.1 ppm, the 2D spectrum showed a strong autocorrelation peak at 24.2 ppm in the  $\omega_1$  dimension on the diagonal (Figure 20). This indicated correlation between two protons indicating the

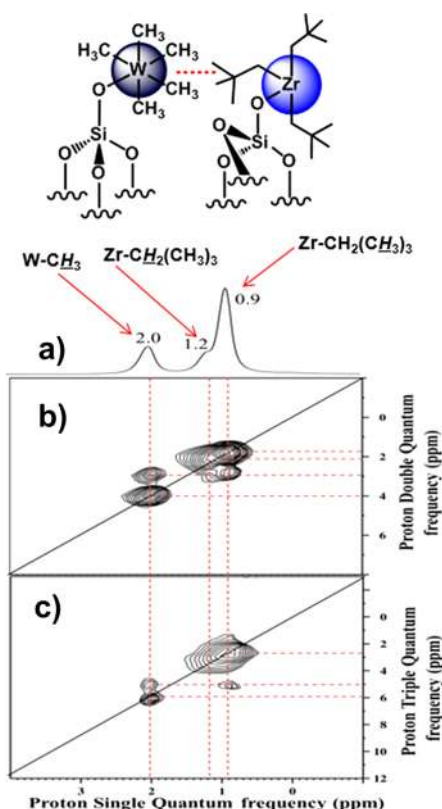


**Figure 19.** (a) One-dimensional  $^1\text{H}$  MAS solid-state spectrum of  $[(\equiv\text{Si}-\text{O})-\text{W}(\text{CH}_3)_5]/[(\equiv\text{Si}-\text{O})-\text{Zr}(\text{Np})_3]$  and (b) two-dimensional 2D  $^1\text{H}$ - $^1\text{H}$  double quantum (DQ)/single quantum (c) triple quantum (TQ)/single quantum NMR of surface complex  $[(\equiv\text{Si}-\text{O})-\text{W}(\text{CH}_3)_5]/[(\equiv\text{Si}-\text{O})-\text{Zr}(\text{Np})_3]$ . Reproduced with permission from ref 197. Copyright 2016 American Chemical Society.

presence of zirconium-bis-hydride  $[\text{Zr}-\text{H}_2]$ . The MQ MAS NMR for the proton resonance at 10.1 ppm showed a weak signal at 14.5 ppm in the  $\omega_1$  dimension outside the diagonal (Figure 20) which indicated correlation between  $\text{Zr}-\text{H}$  (10.1 ppm) with  $\text{Si}-\text{H}$  (4.4 ppm) from the surface. These species are therefore close to each other.

**2.3.1.2.  $^1\text{H}$ ,  $^{13}\text{C}$  DNP SENS.** To improve the sensitivity of the spectrum, DNP SENS can be applied to structural determination of heterogeneous catalysts<sup>176</sup> (i) if they are not sensitive to the radical,<sup>198–200</sup> or (ii) if the active site is protected from reacting with the radical.<sup>183,185–194</sup> The limitation of DNP SENS, when it comes to SOMC species, is that most surface organometallic complexes are highly sensitive and prone to react with the added radicals.<sup>186,194</sup> Strategies have been developed to overcome the challenge by protecting the complex from reacting with the added radical; herein, we discuss one strategy, namely confinement, and how it enables characterization of highly sensitive SOMC-prepared catalyst by SS NMR spectroscopy with high resolution.

DNP SENS was applied to  $[(\equiv\text{Si}-\text{O})-\text{W}(\equiv\text{C}^t\text{Bu})-(\text{CH}_2^t\text{Bu})_2]$  supported on mesoporous silica with various pore sizes ( $d_{\text{pore}} = 6.0, 3.0,$  and  $2.5$  nm).<sup>194</sup> Mesoporous supports were used to prevent direct contact of the large biradical nitroxide radical TEKPol<sup>201</sup> ( $d_{\text{radical}} \sim 2$  nm) and the surface complex. The sample was prepared by incipient wetness impregnation of the SOMC complex with a solution of TEKPol in dichlorobenzene (DCB) or tetrachloroethane (TCE). On SBA15 support (displaying large pore diameter),

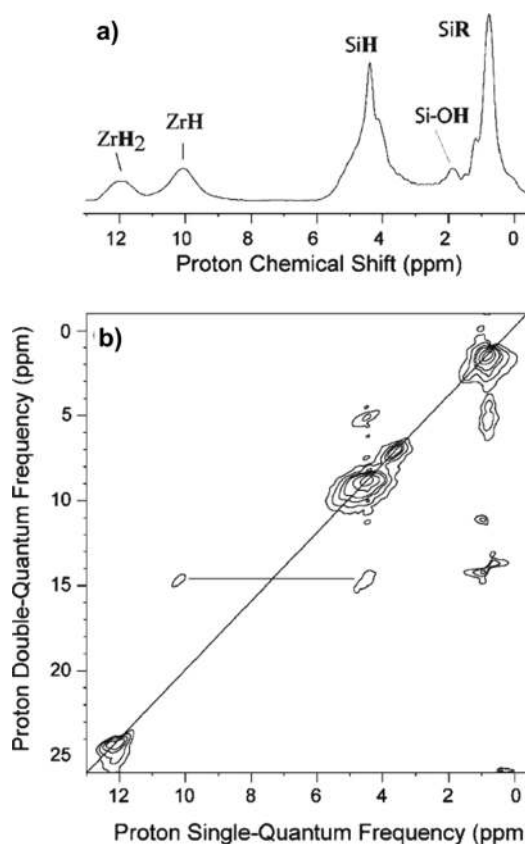


**Figure 20.** (a)  $^1\text{H}$  MAS NMR spectrum of  $[\text{Zr}-\text{H}_x]$  species obtained during the hydrolysis of  $(\equiv\text{Si}-\text{O})-\text{Zr}(\text{Np})_3$ . (b) DQ rotor-synchronized 2D  $^1\text{H}$  MAS spectrum of  $[\text{Zr}-\text{H}_x]$  species. Reproduced with permission from ref 170. Copyright 2004 American Chemical Society.

no surface signals were observed by  $^{13}\text{C}$  CP-MAS DNP SENS, most likely because TEKPol reacted with the surface. Using MCM41 as support with pore diameter of 3.0 nm, the  $^{13}\text{C}$  CP-MAS DNP SENS of  $[(\equiv\text{Si}-\text{O})-\text{W}(\equiv\text{C}^t\text{Bu})(\text{CH}_2^t\text{Bu})_2]$  showed all expected peaks of the surface complex at 33 ppm ( $\text{CH}_3$ ), 52 ppm ( $-\text{C}(\text{CH}_3)_3$ ) and 95 ppm ( $[\text{W}]-\text{CH}_2-\text{C}\equiv$ ). Even the carbyne signal at 317 ppm ( $[\text{W}]\equiv\text{C}-$ ) was detected after only 8000 scans, while conventional SS NMR spectroscopy typically needs at least 70000 scans to only observe alkyl fragments (32, 52, and 95 ppm) but not the carbyne fragment at 317 ppm (Figure 21).<sup>194</sup> This example illustrates how DNP is a powerful tool for characterization of samples in limited time frame as compared to conventional NMR.

It turned out that use of DNP SENS is even possible when the SOMF is grafted on spherical silica, if the SOMF is small enough and the concentration is moderate.<sup>194</sup> This condition allows silica particles to aggregate which (partially) prevents the direct contact of the radical and the sensitive SOMF.

**2.3.2. Characterization of SOMCat through Heteroatoms.** **2.3.2.1.  $^{15}\text{N}$  SS NMR Spectroscopy.**  $^{15}\text{N}$  has spin 1/2, however, the natural abundance of  $^{15}\text{N}$  is very low (0.37%). Particularly, for SS NMR, this means that it is very challenging to record a reasonable spectrum. Because the discovery of DNP enhanced SS NMR spectroscopy, the characterization of these materials became more accessible. Several heterogeneous catalysts (hybrid materials, SOMCats, etc.) bearing nitrogen-based moieties as attractive functionalization were investigated.



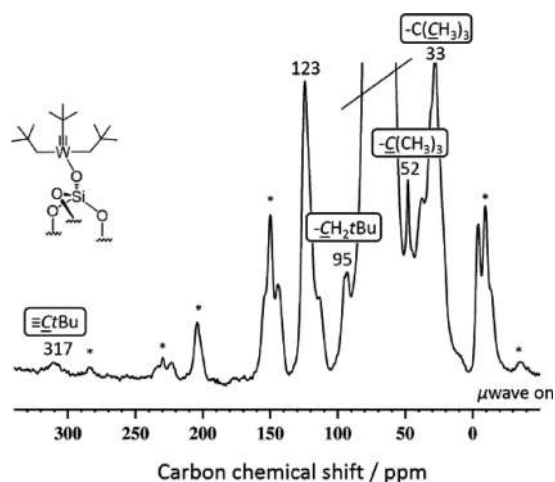


**Figure 21.**  $^{13}\text{C}$  CP-MAS DNP SENS spectra (100 K, 400 MHz/263 GHz) for  $[(\equiv\text{Si}-\text{O}-)\text{W}(\equiv\text{CtBu})(\text{CH}_2\text{tBu})_2]$  in a 16 mM TEKPol solution in TCE. Reproduced with permission from ref 194. Copyright 2018 Royal Society of Chemistry.

Examples described in literature include peptide-<sup>202</sup> or aniline-functionalized<sup>203</sup> silica and nitrated silica surfaces.<sup>204</sup>

**2.3.2.2.  $^{29}\text{Si}$  CP/MAS NMR Spectroscopy.** Besides structural determination of SOMC complexes, SS NMR serves also for the precise characterization of unfunctionalized support materials (silica, alumina, silica–alumina, etc.) used for SOMC. The most common support in SOMC is dehydroxylated silica;  $^{29}\text{Si}$  CP/MAS NMR spectroscopy<sup>160,205,206</sup> can be applied to distinguish silicon–oxygen bonds (Q-sites) in order to resolve silanols ( $\equiv\text{Si}-\text{OH}$ ) from bulk silicon atoms. The following terminology is used: (i)  $\text{Q}^4$  sites appear in the range between  $-115$  to  $-105$  ppm and describe bulk silica ( $\text{SiO}_2$ ), where silicon is only connected via siloxane bridges to other silicon atoms. (ii)  $\text{Q}^3$ -sites are found around  $-100$  ppm and are related to single surface silanols ( $\equiv\text{Si}-\text{OH}$ ). (iii)  $\text{Q}^2$ -sites describe adjacent bis-silanols [ $(\equiv\text{Si}(\text{OH})_2)$ ] and appear in the range between  $-85$  and  $-95$  ppm.<sup>206</sup>

After thermal treatment of SBA-15 at  $700^\circ\text{C}$ , the  $^{29}\text{Si}$  CP/MAS NMR spectrum of SBA-15<sub>700</sub> showed three peaks at  $-101$ ,  $-92$ , and  $-110$  ppm. The main peak at  $-101$  ppm was assigned to  $\text{Q}^3$ -sites, indicating that mainly surface silanols were observed. The peak at  $-92$  ppm relates to  $\text{Q}^2$ -sites (adjacent silanols) and the signal at  $-110$  ppm refers to bulk silica  $\text{Q}^4$ -sites.<sup>205,206</sup>

Apart from Q-sites, silicon NMR spectroscopy is also capable of distinguishing T-sites which describe Si–C bonds (following the same systematic). Those sites typically appear following alkyl migration from metal complexes to surface silicon atoms (Scheme 3).<sup>196,207</sup> Similar to  $^{13}\text{C}$  SS NMR spectroscopy, the drawback of  $^{29}\text{Si}$  SS NMR spectroscopy is the low natural abundance (4.7%) and the low gyromagnetic momentum which leads to extremely long experimental times. DNP enhance SS NMR spectroscopy helps overcome this problem, and spectra can be recorded in reasonable experimental times by indirect (with cross-polarization) or direct DNP.<sup>179</sup>

**2.3.3. Characterization of SOMC Complexes through Quadrupolar Nuclei.** **2.3.3.1.  $^{27}\text{Al}$  SS NMR Spectroscopy.** Quadrupolar nuclei, such as  $^{27}\text{Al}$  are less commonly encountered in SS NMR spectroscopy than dipolar nuclei<sup>162</sup> because of their intricate spin dynamics in the presence of

radiofrequency fields and magic angle spin (MAS). These dynamics lead to spectral broadening resulting from the residual quadrupolar interaction that cannot be completely removed by MAS leading to S/N-ratios close to detection limit. However, application of  $^{27}\text{Al}$  NMR spectroscopy in solid-state chemistry is very promising for the heterogeneous catalysis community,<sup>162</sup> especially when working with single atom catalysts, zeolites, or with well-defined SOMC-catalysts.<sup>208–211</sup> Generally, three types of aluminum atoms can be distinguished: tetracoordinated  $\text{Al}^{\text{IV}}$  or  $\text{Al}_\text{T}$  appearing at around 70 ppm, pentacoordinated  $\text{Al}^{\text{V}}$  or  $\text{Al}_\text{P}$  at 35 ppm and hexacoordinated  $\text{Al}^{\text{VI}}$  or  $\text{Al}_\text{H}$  at 8 ppm. In 2016, a unique type of mesoporous silica material with well-defined single-site and selective formation of terminal Al–H was designed.<sup>208</sup> The starting aluminum *iso*-butyl complex and the final aluminum hydride were fully characterized by advanced SS NMR spectroscopy ( $^1\text{H}$ ,  $^{13}\text{C}$ , multiple quanta (MQ) 2D  $^1\text{H}$ – $^1\text{H}$ , and  $^{27}\text{Al}$ ). Trimeric *iso*- $\text{Bu}_2\text{AlH}$  reacted selectively with surface silanols without affecting the siloxane bridges. The  $^{27}\text{Al}$  SS NMR spectrum exhibited an intense signal at 68 ppm, corresponding to a tetrahedral aluminum-hydride ( $\text{Al}^{\text{IV}}$ ), the characteristic resonances of  $\text{Al}^{\text{V}}$  (31 ppm) and  $\text{Al}^{\text{VI}}$  (3 ppm) were not detected in the  $^{27}\text{Al}$  SS NMR spectrum (Figure 22).<sup>208</sup>

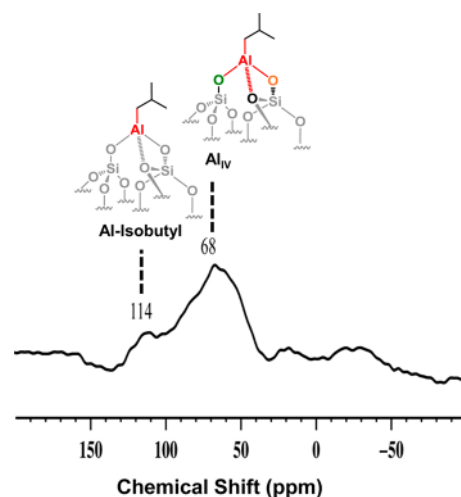


**Figure 22.**  $^{27}\text{Al}$  SS NMR spectrum of tetracoordinated Al–H after thermal treatment. Reproduced with permission from ref 208. Copyright 2016 American Chemical Society.

Gauvin, Taoufik, Scott et al.<sup>209,211</sup> showed that characterization and structural analysis of SOMC catalysts (methyl-trioxorhenium (MTO) on  $\gamma\text{-Al}_2\text{O}_3$ ) is possible by  $^{27}\text{Al}$  solid state NMR. Figure 23 shows the 2D  $^1\text{H}$ – $^{27}\text{Al}$  D-HMQC MAS NMR spectrum of MTO/ $\text{Cl-Al}_2\text{O}_3$ . All three aluminum sites were detected (Figure 23a): (i) tetracoordinated  $\text{Al}^{\text{IV}}$  ( $\text{Al}_\text{T}$ ), (ii) pentacoordinated  $\text{Al}^{\text{V}}$  ( $\text{Al}_\text{P}$ ), and (iii) hexacoordinated  $\text{Al}^{\text{VI}}$  ( $\text{Al}_\text{H}$ ). Deeper investigations of the spectrum revealed two distinct, main patterns: (i) the area with dashed lines highlights the regions of  $\text{Cl-Al}_2\text{O}_3$ , which are mainly unaffected by grafting and (ii) the area surrounded by the solid line includes the  $^1\text{H}$  chemical shift of  $\text{Re-CH}_3$ , which correlates with all types of aluminum atoms. The low chemical shift region correlates with  $\text{Al}_\text{T}/\text{Al}_\text{H}$ , whereas the high shift region correlates with  $\text{Al}_\text{P}/\text{Al}_\text{H}$ . These pairwise correlations suggest strong interactions between rhenium and a bridging oxygen

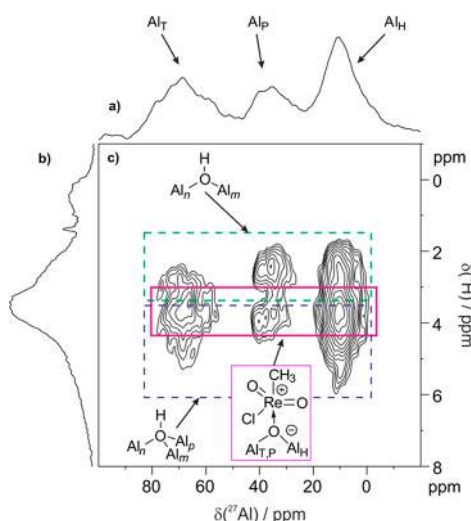


**Figure 23.** SS NMR of methyltrioxorhenium MTO/Cl–Al<sub>2</sub>O<sub>3</sub> (a) <sup>27</sup>Al projection, (b) <sup>1</sup>H MAS, and (c) <sup>1</sup>H–<sup>27</sup>Al D-HMQC MAS NMR (18.8 T, spinning speed 20 kHz, recycle delay 2 s, recoupling time 500 μs). Reproduced with permission from ref 211. Copyright 2016 American Chemical Society.

(Al<sub>n</sub>OAl<sub>m</sub>, *n* = T or P of the surface) as it is suggested in Figure 23c.

**2.3.3.2. <sup>17</sup>O MAS NMR Spectroscopy.** <sup>17</sup>O SS NMR spectroscopy of metal oxides is an interesting tool for the insightful characterization of supported species. Further, hydrogen bonding and dynamics on surfaces of catalytically important materials can be measured. The challenge of <sup>17</sup>O MAS NMR spectroscopy is that <sup>17</sup>O has an extremely low natural abundance (0.037%) and quadrupolar nature (*I* = 5/2), resulting in line broadening that cannot be resolved by magic angle spinning (MAS).<sup>212</sup> To obtain reasonable SS NMR spectra, silica surfaces were either treated with <sup>17</sup>O enriched water<sup>213,214</sup> or <sup>17</sup>O<sub>2</sub> gas.<sup>213,215</sup> Figure 24 shows that key

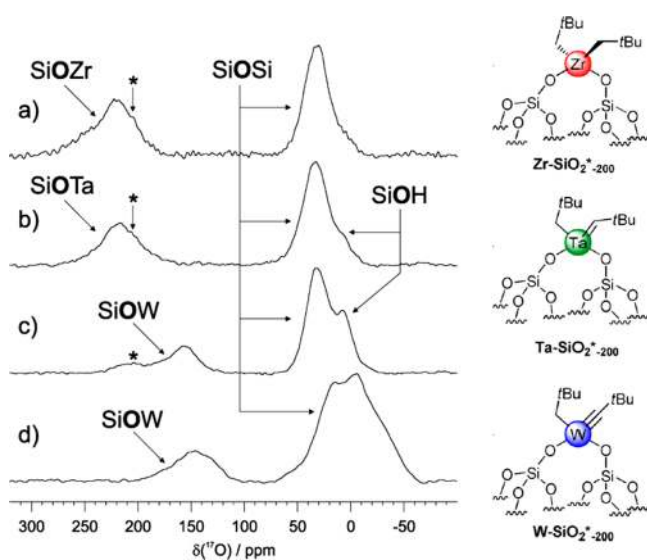


**Figure 24.** <sup>17</sup>O MAS NMR spectra (18.8 T, 19 kHz for (a–c) and 21 kHz for (d)) of (a) Zr–SiO<sub>2–200</sub>, (b) Ta–SiO<sub>2–200</sub>, (c) W–SiO<sub>2–200</sub>, and (d) W–SiO<sub>2–200</sub>. Asterisks indicate position of spinning side bands. Reproduced with permission from ref 213. Copyright 2012 American Chemical Society.

information on SOMC complexes can be extracted for various oxygen environments such as silanols (around 0–10 ppm), siloxanes (20–50 ppm), and metal-bound siloxides (150–250 ppm).

Further developments in SS NMR spectroscopy related to anisotropic nuclei showed that natural abundance <sup>17</sup>O SS NMR of mesoporous SBA15 is possible using DNP enhanced SS NMR without using <sup>17</sup>O labeled samples.<sup>216,217</sup>

### 3. COMPUTATIONAL TOOLS

The use of quantum chemistry methods is considered nowadays as powerful tools to understand the atomic scale properties of surfaces and their role on adsorption and reactivity processes. Our goal is not to provide a detailed description of the various possible computational methods, this can be found in different textbooks,<sup>218–220</sup> and it is described in details in a recent review.<sup>221</sup> Here, we try to summarize the theoretical approaches mostly used in the field and to show some relevant examples where combining theoretical DFT calculations with advanced characterization techniques allowed to provide deep insights into understanding the fundamental properties of SACs, SAACs, and SOMC-based complexes including stability, electronic features, and reaction mechanisms.

#### 3.1. Models

Theoretical simulations of solid materials are in general performed starting from the information on the crystalline phases provided by the experimental characterization techniques, such as the atomic positions in the unit cell of the considered material and the symmetry elements controlled by the space group.

Support catalyst structures are in general modeled by periodic slab models containing several atomic layers. The surfaces are constructed from the optimized bulk cell dimensions and obtained by cleaving the original bulk through a matrix transformation along a given Miller (*hkl*) crystallographic plane to mimic the obtained experimental surface.<sup>222,223</sup> Differently from the bulk, only translation vectors parallel to the surface enforce the periodic boundary conditions because periodicity is lost in the noncrystallographic direction perpendicular to the slab plane. Technical reasons related to the use of plane waves-based methods enforce the adoption of a tridimensional unit cell for slabs as well. This requires that large vacuum heights have to be set in the direction perpendicular to the surfaces to prevent nonphysical electronic or fictitious interactions between the periodically repeated slabs along this direction. This is different from periodic quantum mechanical calculations carried out using a linear combination of atomic orbitals (the so-called LCAO method) by employing Gaussian or Slater type basis sets, in which the definition of the true bidimensional slab is completely rigorous, where the electrostatic potential above and below the slab decays exponentially with the distance from the slab.<sup>222,223</sup> In all cases, the adequacy of the adopted slab must be checked by considering convergence of geometry, energy, and electronic properties as a function of the slab thickness and, for plane wave methods, vacuum thicknesses separating the repeating slabs. Slabs containing various possible termination types are required to be tested in order to determine the most favorable surface termination. As a typical example, we show in Figure 25 that the same (010) crystallographic direction of crystalline silica ( $\alpha$ -quartz) can

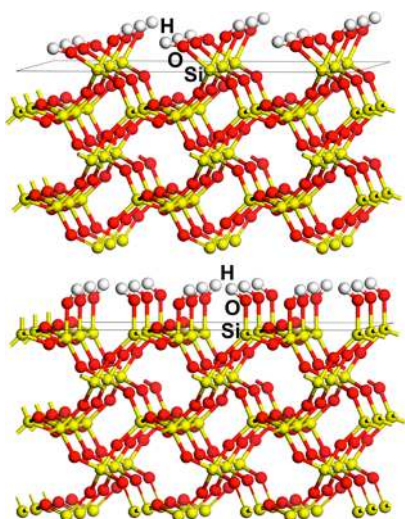


**Figure 25.** Two possible terminations of the same (010) crystallographic exposed facet of hydroxylated crystalline silica ( $\alpha$ -quartz) with geminal (top) or vicinal (bottom) Si–OH groups. Adapted with permission from ref 226. Copyright 2013 American Chemical Society.

have two different terminations with geminal or vicinal Si–OH groups depending on how the cut height has taken place along the direction perpendicular to the slab. Therefore, further calculations are needed to find out the best arrangement of the surface Si–OH in order to maximize the H-bond interaction and, consequently, to reduce the surface formation energy. On the basis of this, the crystallographic plane together with the termination type chosen should be well clarified to more reasonably define the material under real conditions. For oxides, extra care should be exerted in order to avoid either charged slabs or slabs with a large dipole moment across the slab itself since they are electronically unstable.<sup>224,225</sup> During geometry optimization, the bottom layers located far away from the surface can be maintained frozen, while the top layers together with a few subsurface layers should in principle be fully relaxed. Dipole corrections along the surface directions are required to be included to avoid such possible errors induced by the periodic boundary conditions.

Once the support has been defined, a different approach is followed based on the catalytic system under investigation. For instance, for SAC calculations, a single metal atom is adsorbed on the surface layer of the slab, while for SAAC calculations, a single metal atom from the surface layer of the slab is replaced by another metal atom. In both cases, a large surface layer area is required to mimic the metal content obtained experimentally, or to prevent interaction between metal sites in neighboring simulation cells. Moreover, several locations of the single metal atom on top of the slab surface must be explored in order to find the energetically most favorable geometry. Dispersion corrections are in general included to better describe the metal–support interaction.

Moving to SOMC, the active site is modeled by linking to the surface layer of the slab the metal atom together with the ligands occupying its first coordination sphere. However, in this area, the majority of studies refer to amorphous silica supports and, consequently, no structural detail of the slab surface and of the possible grafting points can be accessed by experimental techniques, forcing to adopt only possible models, often corresponding to ideal situations. One approach is to achieve the degree of disorder typical of amorphous

materials by performing molecular dynamics simulations at high temperature followed by a quenching step until the physicochemical desired properties are obtained.<sup>227,228</sup> However, this method is highly time-consuming and the use of quantum mechanical techniques become often unaffordable. In this state, leaving out the exact definition of the bulk structure and focusing only on the groups present on the surface represent a possible solution. To this extent, there is an alternative approach to the periodic slabs, the so-called cluster approach<sup>229</sup> widely reported in the literature for mechanistic studies on several SOMC-catalyzed reactions. This model consists of designing the structure of the active site by limiting the number of units of the support involved. In this way, the cluster behaves like a “normal molecule” and the standard quantum mechanical methods used in homogeneous catalysis can be used (see [Methods](#) section). This approach presents several advantages, apart from the requirement of minor computational resources. The possibility to use very accurate methods (i.e., accelerate CCSD(T) methods) as standard reference allows to finely tune the calculation method in order to reach chemical accuracy.<sup>230</sup> Solvent molecules can be included in the simulation by continuum methods<sup>231</sup> to take into account the effect of the solvent on properties like adsorption and substrate coordination to the metal and/or to the support. Finally, and most importantly, the evaluation of reaction barriers and pathways is much more accessible by using the algorithms and programs developed for modeling homogeneous catalysis.

As expected, the size of the cluster can vary by adding more or less neighbor atoms around the metal center. Moreover, different approaches can be used to design the shape of the cluster. For example, in the case of SiO<sub>2</sub> based supports, two approaches have been reported in the literature. The former consists of the “tree like” model, built by designing an increasing number of shells ( $-\text{OSi}(\text{OH})_3$  unit) around the active site; the latter is the “cage like”<sup>232</sup> model in which a cage of SiO<sub>2</sub> units having a silsesquioxane type geometry is built starting from the atom of the support directly bonded to the metal center (see [Figure 26](#)). Nowadays, the cage approach is the most accredited because of the natural rigidity of the silsesquioxane cage relative to the larger flexibility of the tree that requires a high number of geometry constraints in order to

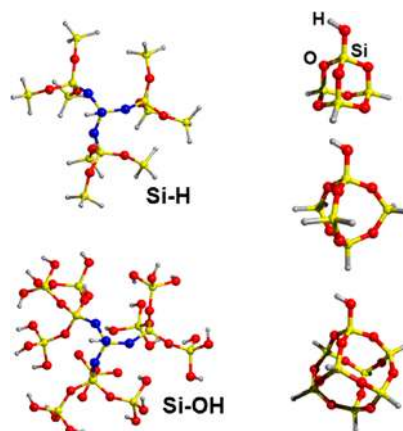


**Figure 26.** (left) Tree-like models terminated by Si–H and Si–OH groups. The SiO<sub>3</sub>OH moiety representing the surface SiOH group is depicted in blue. (right) Cage-like cluster models. Reproduced with permission from ref 226. Copyright 2013 American Chemical Society.



avoid distortions. In all cases, the clusters are terminated by Si–H or Si–OH groups to retain tetrahedral Si atoms.<sup>233</sup>

As expected, the cluster approach also has several limitations. For instance, it can be used only when the activity of the catalytic site depends on localized features of the site rather than on long-range interactions. A delicate aspect to consider when approaching this method is also the accuracy in describing the electronic states of the surface, which may depend on the system being studied. Silica and zeolites supported SOMC catalysts behave well for this aspect because they show a large band gap that allows a reasonably good description of surface electronic response by cluster model. Moreover, care should be taken in choosing the size of the cluster in order to confer some sort of elasticity to the system, particularly important when surface reconstruction is expected after interaction of the support with the substrate (for example, with metal oxides). Finally, the ideal geometry of the cluster could be scarcely representative of the geometries occurring in the real amorphous catalyst.

By applying the methodologies discussed above for simulating support catalyst structures, various models based on both periodic slab and finite cluster approaches have been proposed in the literature over the past years to properly describe the surface topology and reactivity of  $\gamma$ -Al<sub>2</sub>O<sub>3</sub>,<sup>211,234–237</sup> which is often used as support in catalysis thanks to its stability and Lewis acidity. Using slab models including periodic boundary approach, the structures and energetics of (111) and (110) surfaces of  $\gamma$ -Al<sub>2</sub>O<sub>3</sub> and the CO oxidation by single-atom catalysts M<sub>1</sub>/ $\gamma$ -Al<sub>2</sub>O<sub>3</sub> (M = Pd, Fe, Co, and Ni) were recently investigated.<sup>235,236</sup> A few years earlier, Rh<sub>1</sub>/ $\gamma$ -Al<sub>2</sub>O<sub>3</sub> as single-atom catalyst for O<sub>2</sub> activation and CO oxidation was examined from the theoretical standpoint.<sup>234</sup> The intrinsic variety and complexity of the alumina surface (i.e., presence of physisorbed water molecules, chemisorbed H and OH species, etc.) makes modeling challenging. To this extent, the cluster approach remains widely used since it allows a realistic model of the defects and/or of specific sites with a different number of adsorbed water molecules and aluminum/hydroxyl group ratio. Common models discussed in literature consisted of neutral and stoichiometric (Al<sub>2</sub>O<sub>3</sub>)<sub>*n*</sub> type clusters, where *n* = 8, 11, 14, and 18 obtained from the cut of  $\gamma$ -Al<sub>2</sub>O<sub>3</sub> infinite surface.<sup>237</sup>

To overcome these limits and to try to merge the advantages of both periodic and cluster approach, an expanded cluster approach based on combined quantum mechanics/molecular mechanics methods has been developed. This method consists of using bigger clusters defined by two parts, the active part of the catalytic site described with a high level of theory (quantum mechanics methods) and the rest of the system simulated with a lower level of theory (classical force fields methods).<sup>238</sup>

### 3.2. Methods

The structures considered for SAC or SAAC are fully optimized mainly in the framework of the spin-polarized periodic density functional theory (DFT) within the plane wave (PW) approach and the generalized gradient approximation (GGA) for the exchange–correlation functional in the Perdew–Burke–Ernzerhof (PBE)<sup>239</sup> formulation implemented in solid-state programs. The frozen-core all-electron projector-augmented wave (PAW) scheme<sup>240</sup> is used to describe the core electrons and the electronic wave functions are expanded in plane wave basis with the sufficient kinetic cutoff energy.

The Monkhorst–Pack scheme of *k*-points mesh is applied to carry out the numerical integrations in the reciprocal space and sample the Brillouin zone.<sup>241</sup> The ground-state atomic geometries are obtained by minimizing the Hellmann–Feynmann forces on the atoms and the electronic self-consistency tolerance at each ionic step.

The binding energy of the single metal atom to the support for SAC and the cohesive energy of the single metal atom in the corresponding metal host for SAAC are computed to evaluate the binding strength between the deposited metal or the doped metal and the support. The electronic properties of the most favorable SAC and SAAC structures are examined by density of states and Bader charge calculations. These analyses provide rational insights into the orbital's nature involved in the formation of the new chemical bonding between the deposited or the doped metal and the support, giving a hint about any possible charge transfers, by identifying the atoms involved in this process and the amount of transferred charge. Transition states along reaction pathways are usually approached using the climbing-image nudged elastic band (CI-NEB) method.<sup>242–244</sup> The initial and final state geometries for each step of all models are tested, and the ones with lowest energies are selected as the reactants and products in the minimum energy path. Localization of transition states can be further improved by refining geometries from CI-NEB calculations using specific transition state searching algorithms, such as the dimer method.<sup>245</sup> The transition states (TS) are characterized by vibrational frequency analysis with a single mode of imaginary frequency. Usually, all calculations are performed at the generalized gradient approximation (GGA) level of DFT, including dispersion correction terms.

In case of the cluster models for SOMC, geometries are fully optimized at the DFT level using either a GGA functional or a slightly more expensive hybrid GGA functional. The functional and basis set used can vary depending on the system studied, with the general approach of combining relativistic effective core potentials for second and third row metals and explicit basis set for main group atoms. Transition states can be approached with one of the many techniques used in homogeneous catalysis, and the nature of all stationary points is confirmed by the calculation of analytical second derivatives. In principle, intrinsic reaction coordinate calculations (IRC) should be performed to verify that the localized transition state connects properly with the considered reactants and products. Better quality energetics can be achieved via single point energy calculations on the optimized geometries by using larger basis sets, more expensive functionals, highly accurate wave function methods, including accelerated CCSD(T) ones, and by including solvent effects using a continuum solvation model.

## 4. CLASSIFICATION BY TYPES OF REACTION AND/OR ACTIVATION

### 4.1. Hydrogenation

Hydrogenation is a ubiquitous reaction, mainly used in chemical industry for conversion of unsaturated hydrocarbons to saturated ones. The first hydrogenation catalyst was discovered by Paul Sabatier, who observed that, at an elevated temperature, CO<sub>2</sub> reacts with hydrogen in the presence of nickel catalyst to produce methane and water (Sabatier reaction).<sup>246</sup> For this discovery, he was awarded the Nobel Prize in 1912. In this section, we will discuss the hydrogenation

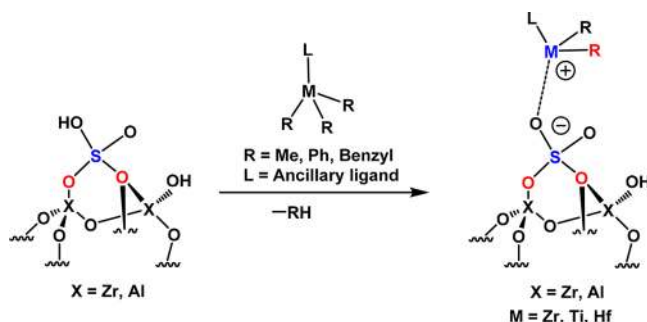
of various organic double/triple bonds and aromatic compounds using SOMCat, SAC, and SAAC.

**4.1.1.1. Via SOMC.** 4.1.1.1. *Hydrogenation of Olefins.* For hydrogenation reactions via SOMCat, mainly supported Zr, Cr, and Co SOMC complexes have been used. In the 1980s, a well-defined silica supported zirconium bis-hydride ( $(\equiv\text{Si}-\text{O})_2\text{ZrH}_2$ ) catalyst was used for the reduction of 1-butene to butane. The zirconium complex ( $(\equiv\text{Si}-\text{O})_2\text{ZrH}_2$ ) was prepared by reaction of  $\text{Zr}(\text{Np})_4$  (Np: neopentyl) with  $\text{SiO}_{2-200}$  (Aerosil silica dehydroxylated at 200 °C under high vacuum ( $10^{-5}$  bar) for 12 h). After the end of the reaction, a bipodal zirconium species,  $(\equiv\text{Si}-\text{O})_2\text{ZNp}_2$ , was formed. Under treatment with hydrogen, a bipodal zirconium bis-hydride ( $(\equiv\text{Si}-\text{O})_2\text{ZrH}_2$ ) was produced. In a typical catalytic run, a slurry of  $(\equiv\text{Si}-\text{O})_2\text{ZrH}_2$  was prepared in toluene and a 20-fold excess of 1-butene was added in the presence of  $\text{H}_2$  (1 atm) at 25 °C in 30 h. At the end of the reaction, *n*-butane was observed (Scheme 4). Similarly, *cis*- and *trans*-2-butene

of ethylene and hydrogen ( $4 \text{ mL min}^{-1}$ ,  $400^\circ\text{C}$ ) passed through a bed of aluminum hydride catalyst, ethane was formed with the remarkable and unexpected TOF of  $6.9 \text{ h}^{-1}$  in absence of transition metals. In a control reaction carried out using pristine  $\text{Al}_2\text{O}_3$  as catalyst no ethane formation was observed. The authors claimed that the observed reactivity could be attributed to the peculiar highly strained structure of the supported aluminum hydride species.

**4.1.1.2. Hydrogenation of Aromatics.** Delferro, Marks et al. grafted various zirconium organometallic complexes on sulfated  $\text{ZrO}_2$  (ZrS), Sulfated  $\text{Al}_2\text{O}_3$  (ALS), and  $\text{ZrO}_2\text{--WO}_3$  (ZrW) (Scheme 6).<sup>107</sup>

**Scheme 6. Synthesis of Supported Organometallic Compounds by SOMC for Aromatics Hydrogenation**



These catalysts were tested for the reduction of benzene to cyclohexane, a useful reaction for removal of carcinogenic benzene from crude oil. Benzene and toluene hydrogenation reactions were investigated mostly by using  $\text{Cp}^*\text{ZrR}_3$  ( $\text{Cp}^* = [\eta^5\text{-C}_5(\text{CH}_3)_5]$ ,  $\text{R} = \text{alkyl, aryl}$ ) supported on the above-mentioned sulfated oxides. It was observed that the catalytic activity toward benzene was much higher than toluene. Importantly, hydrogenation performance decreased with decline in surface acidity. The highest TOF ( $1200 \text{ h}^{-1}$ ) was obtained with  $\text{Cp}^*\text{ZrMe}_3$  on ZrS support. Indeed, the surface acidity of the supports follows the order: ZrS ( $-16.1$ ), ALS ( $-14.6$ ), and ZrW ( $-14.6$ ). Additionally, the reactivity and the selectivity for benzene hydrogenation decreased by increasing the distance between the surface and the organometallic complexes.<sup>107</sup> To understand the selectivity of the catalyst toward benzene hydrogenation, a mixture of benzene and toluene ( $1 \text{ mL}$  each  $\text{v/v}$ ) was used as reactant. Despite low activity in toluene dehydrogenation, the catalyst prepared from  $\text{Cp}^*\text{ZrMe}_3$  and ZrS was strongly inhibited by the presence of toluene. In contrast, catalysts prepared from  $\text{Cp}^*\text{ZrPh}_3$  and  $\text{Cp}^*\text{ZrBz}_3$  (Bz: benzyl) on the same support were unaffected. Following kinetic studies, it was found that presence of more sterically demanding hydrocarbonyl moieties at the Zr center

would lead to increase of the metal–surface distance, yielding catalysts less prone to inhibition.

$\text{Cp}^*\text{ZrBz}_3$  on ZnS was also investigated in equimolar mixture of benzene with other alkylarenes (ethylbenzene, mesitylene, pyridine, thiophene). For mesitylene/benzene and ethylbenzene/benzene mixtures, the selectivities for benzene hydrogenation were 99% and 86%, respectively, whereas for the other two substrates, no conversion was observed.<sup>107</sup>

**4.1.2. Via SAAC.** The characteristics of single atom alloy catalysts (SAACs) are (i) low concentration of the active metal on the surface of the host metal and (ii) the higher thermodynamic stability of the active metal on the surface of the host metal so that dimers and trimers of the active metal cannot be formed.

Single atom alloys of Pd on Cu(111) were prepared by Sykes et al.<sup>250–253</sup> In the Pd/Cu(111) alloy, where the Pd concentration is extremely low, Pd is the active metal and Cu(111) is the host metal (presumably inactive). With this kind of alloy, the reduction of acetylene and styrene to ethane and ethylbenzene were studied.<sup>250</sup> The best results were obtained with 0.01 monolayer (ML) of Pd on Cu(111).<sup>250</sup> In the case of styrene, 13% of conversion was obtained with 95% of selectivity to ethylbenzene. In the case of acetylene, 3% conversion was recorded with 95% selectivity to ethane. The reaction was proposed to proceed with decomposition of  $\text{H}_2$  on active metal followed by spillover to nearby Cu surface where the unsaturated reactants were adsorbed and reduction took place (Figure 27).<sup>250</sup>

Following this work, Flytzani-Stephanopoulos et al.<sup>254</sup> prepared similar Pd–Cu alloy on  $\text{Al}_2\text{O}_3$ . Also in this case, the Pd concentration was extremely small. Pd was deposited on Cu by galvanic replacement. This SAAC was tested for selective reduction of phenyl acetylene to styrene with 94% selectivity. This reaction selectivity exceeded the one of Pd/ $\text{Al}_2\text{O}_3$  or Cu/ $\text{Al}_2\text{O}_3$  catalyst (Figure 28).<sup>254</sup>

A range of Pd coverages (0.01–5 ML) “alloyed” onto Cu(111) were prepared.<sup>254</sup> High resolution STM imaging and TPD spectroscopy showed hydrogen spillovers from the Pd to Cu (111) surface at a range of Pd concentration ( $0.01 > 0.5 \text{ ML}$ ). This spillover hydrogen activated the Cu surface for the selective reduction of phenyl acetylene to styrene. The best result was obtained with  $\text{Pd}_{0.18}\text{Cu}_{15}/\text{Al}_2\text{O}_3$  where 94% selectivity to styrene was observed at a conversion of 90%. Comparing this result with a similar loading of Pd ( $\text{Pd}_{0.18}/\text{Al}_2\text{O}_3$ ), only 62% of selectivity was observed. Mayer et al.<sup>255</sup> prepared a Pd–Ag alloy and used it for reduction of acrolein to allyl alcohol. Three different concentrations of Pd–Ag alloy (0.01% Pd + 8% Ag, 0.03% Pd + 8% Ag, and 0.05% Pd + 8% Ag) catalyst were prepared.<sup>255</sup> The best activity and selectivity for the conversion of acrolein to allyl alcohol was observed with 0.01% Pd + 8% Ag (made by coimpregnation, Figure 29)

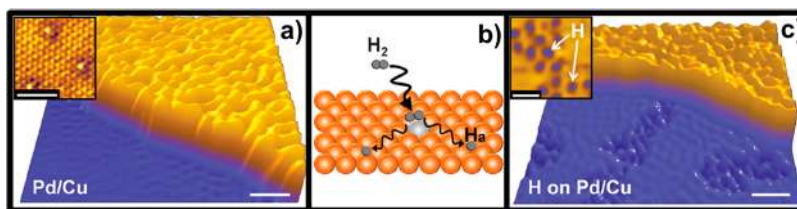


**Figure 27.** Representation of Pd/Cu and mechanism of hydrogenation of styrene. Reproduced with permission from ref 250. Copyright 2012 The American Association for the Advancement of Science.



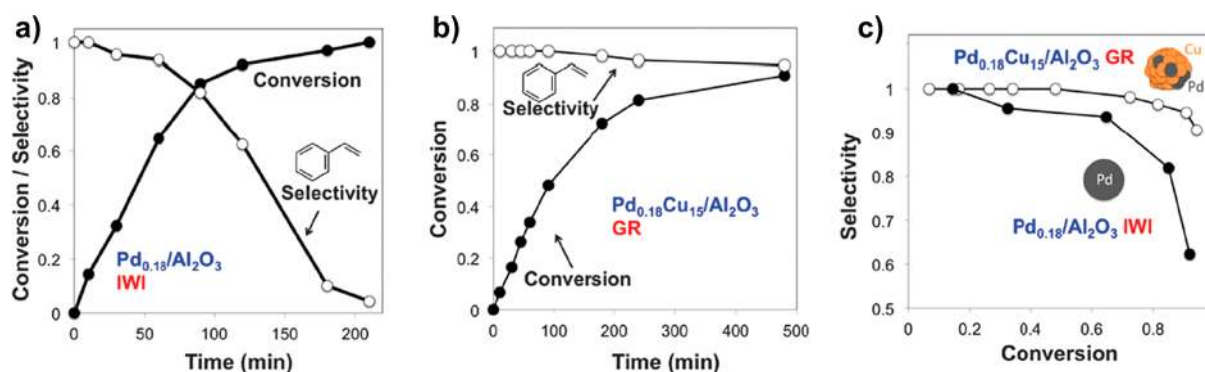


**Figure 28.** (a,b) Time resolved batch reactor data at 25 °C comparing  $\text{Pd}_{0.18}/\text{Al}_2\text{O}_3$  to  $\text{Pd}_{0.18}\text{Cu}_{15}/\text{Al}_2\text{O}_3$ . (c) Time-independent plot of selectivity as a function of conversion for  $\text{Pd}_{0.18}/\text{Al}_2\text{O}_3$  and  $\text{Pd}_{0.18}\text{Cu}_{15}/\text{Al}_2\text{O}_3$ . Reproduced with permission from ref 254. Copyright 2013 Royal Society of Chemistry.

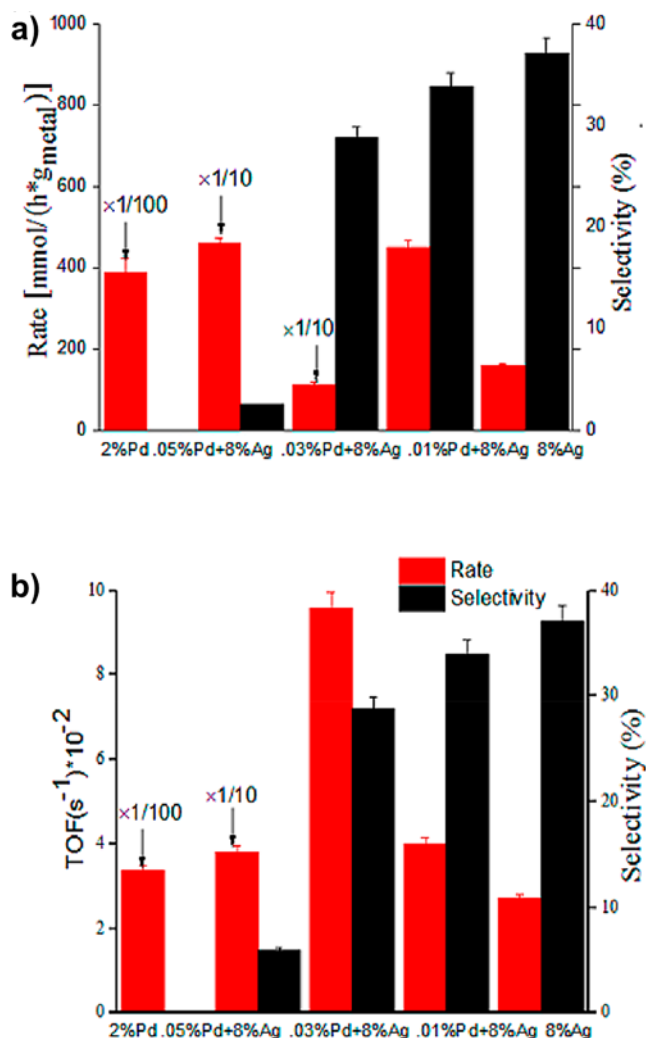


**Figure 29.** Activities (both (a) per metal atom basis and (b) TOF) and selectivities to allyl alcohol of Pd, Ag, and Pd–Ag catalysts synthesized via Co-IWI. All samples are supported on  $\text{SiO}_2$ . 2% Pd/ $\text{SiO}_2$  and 0.05% Pd + 8% Ag/ $\text{SiO}_2$  were tested at 100 °C and 5 atm pressure; the reaction temperature of 0.01% Pd + 8% Ag, 0.03% Pd + 8% Ag/ $\text{SiO}_2$ , and 8% Ag/ $\text{SiO}_2$  was 200 °C, and their reaction pressure was 5 atm. Reproduced with permission from ref 255. Copyright 2015 American Chemical Society.

as compared to monometallic silver catalyst of the same size. DFT calculations were carried out to understand the reactivity

of the acrolein. It was found that, while acrolein adsorbs weakly on the pure silver surface, the presence of the Pd atom enhances acrolein adsorption through  $\text{C}=\text{C}$  rather than  $\text{C}=\text{O}$ .<sup>255</sup> It was also suggested that the presence of isolated Pd atom increases the activity by providing an active center for the  $\text{H}_2$  dissociation. Hence, the selectivity increases due to favorable changes in the configuration of adsorbed acrolein.<sup>255</sup>

Recently, Pd/Au(111) single atom alloys were synthesized and used for selective hydrogenation of hexyne to hexene.<sup>256</sup> Single Pd atoms on Au surface enhanced the hydrogenation ability of Au by a factor of 10 without decreasing the selectivity. The catalytic activity of the Pd/Au(111) single atom alloy catalyst was compared with a 10% Pd/C catalyst. At a 100% conversion of 1-hexyne, Pd/Au(111) alloy gave about 85% selectivity toward 1-hexene (94% 1-hexene and 4% 2-hexene), whereas Pd/C performed with only 10% selectivity for 1-hexene and 90% for *n*-hexane. Pd/Au SAA/ $\text{Al}_2\text{O}_3$  was highly selective for the activation of 1-hexyne compared to Au/ $\text{SiO}_2$ , although they possess similar energy barrier (46.7 and 44.7 kJ/mol). The authors reported that the high selectivity toward 1-hexene is due to the weak adsorption of the alkene over Pd/Au SAA/ $\text{SiO}_2$ . Metallic Au is well-known to bind hydrocarbons feebly,<sup>256</sup> which enhances the selectivity toward 1-hexene and avoids complete reduction of 1-hexyne to *n*-hexane. In the case of Pd/C, the desorption barrier of the olefin is higher than the hydrogenation barrier which leads to a complete reduction of the hexyne to hexane.<sup>256</sup>

Following the work of Zhang on platinum,<sup>63,91</sup> Yang et al.<sup>92</sup> improved the loading of Pt single metal using poly phosphomolybdic acid support (PMA). This was achieved by anchoring Pt on 4-fold hollow sites of PMA. According to the authors, these PMA-anchored Pt single atoms are very efficient for hydrogenation of nitrobenzene and cyclohexanone because they efficiently split hydrogen due to their slightly positive charge.<sup>92</sup> Activated charcoal was chosen as support for Pt anchored PMA and, after a reduction step, Pt<sub>1</sub> SAC formed on PMA-modified activated charcoal (Pt-PMA/AC). Whereas, all oxygen containing ligands were removed during reduction, according to EXAFS data, the coordination number of Pt–O–Pt or Pt–O could be three or four. DFT calculations were carried out to understand the exact bonding order finding that the Pt atoms were in a 4-fold hollow site of PMA.<sup>92</sup> Similarly, Pt/AC was prepared by reaction of  $\text{Pt}(\text{acac})_2$  with activated charcoal followed by reduction over  $\text{H}_2$ . These catalysts were tested for reduction of nitrobenzene, cyclohexanone, styrene, and phenyl acetylene. Note that Pt-PMA/AC was superior to

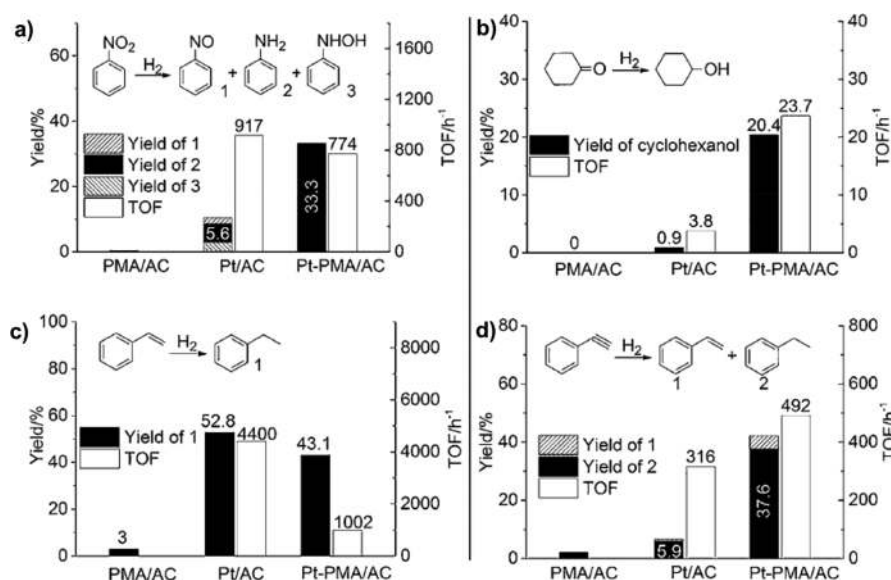


**Figure 30.** Catalytic performance of poly phosphomolybdic acid support on modified activated charcoal (PMA/AC), Pt/AC, and Pt-PMA/AC in hydrogenation reactions of (a) nitrobenzene (53.6 mL), Pt, nitrobenzene = 1:2000 (mol mol<sup>-1</sup>); (b) cyclohexanone, Pt, cyclohexanone = 1:100 (mol mol<sup>-1</sup>); (c) styrene, Pt, styrene = 1:2000 (mol mol<sup>-1</sup>); (d) phenyl acetylene, Pt, phenylacetylene = 1:1000 (mol mol<sup>-1</sup>). Reproduced with permission from ref 92. Copyright 2016 John Wiley and Sons.

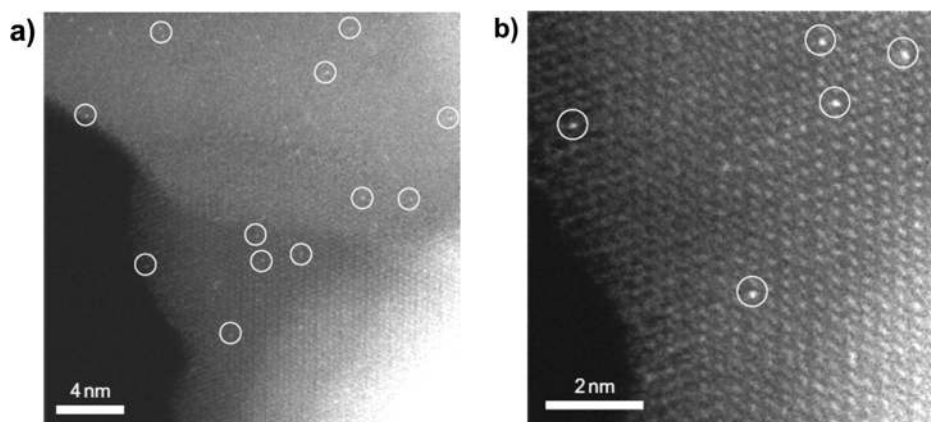


**Figure 31.** HAADF-STEM images of samples of Pt-SAC on FeO<sub>x</sub>. (a,b) In sample a, Pt single atoms (white circles) are seen to be uniformly dispersed on the FeO<sub>x</sub> support (a) and occupy exactly the positions of the Fe atoms (b). Reproduced with permission from ref 63. Copyright 2011 Springer Nature.

other catalysts in terms of yield and TOF for reduction of nitrobenzene to aniline, and cyclohexanone to cyclohexanol. It was also observed that Pt-PMA/AC reduces phenyl acetylene to ethylbenzene in a much more efficient way and with high TOF when compared to other catalysts, whereas it was less active for reduction of styrene. The difference in activity could be attributed to their absorption capability onto the material (Figure 30).<sup>92</sup>

**4.1.3. Via SAC.** With the unearthing of SACs, a plethora of catalysts have been developed for various applications. Herein, we will be discussing SACs for the reduction of olefins/alkynes and carbonyls. Zhang et al. fabricated a single Pt atom catalyst on iron oxide (FeO<sub>x</sub>) nanocrystallites. By high-resolution high-angle annular dark-field scanning transmission electron microscopy (HAADF-STEM), it was proved that Pt atoms were well dispersed and isolated on the surface of FeO<sub>x</sub> nano crystals (Figure 31).<sup>63</sup> Pt-SACs were very efficient for CO oxidation and two times more active than the well-known Au/

Fe<sub>2</sub>O<sub>3</sub> CO oxidation catalysts.<sup>63</sup> This SAC became a hot asset in the field of heterogeneous catalysis.

Noble metal catalysts (like those based on Pd, Pt, Ru, etc.) are well-known hydrogenation catalyst. However, during hydrogenation reactions of multifunctional compounds, it is very challenging to obtain the target product while avoiding unnecessary over reduction steps. Lu et al.<sup>257</sup> showed that single Pd atoms supported on graphene (Pd<sub>1</sub>/graphene) reduce 1,3-butadienes (95% conversion) to butenes with 100% selectivity.<sup>257</sup> The selectivity for 1-butene is about 71% (Figure 32). These results were compared with the results obtained from commercially available Pd/C and Pd-NPs on graphene (Pd-NPs/graphene), the selectivity to butene decreased dramatically at 70% conversion in the case of Pd/C, whereas Pd-NPs/graphene displayed 100% selectivity to butenes at 90% conversion (Figure 32). However, when Pd-NPs/graphene were annealed at 500 °C, the selectivity to butenes decreased to a level similar to Pd/C (Figure 32). It is believed that such decrease of selectivities was due to the loss

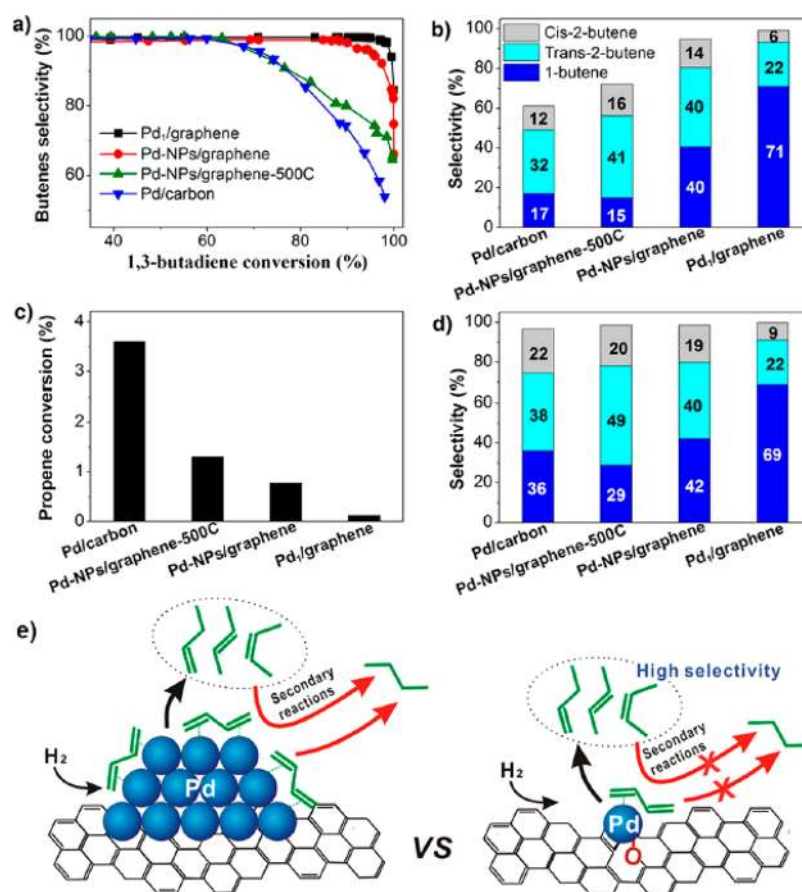


**Figure 32.** Catalytic performances of Pd<sub>1</sub>/graphene, Pd-NPs/graphene, Pd-NPs/graphene-500 °C, and Pd/carbon samples in selective hydrogenation of 1,3-butadiene. (a) Butenes selectivity as a function of conversion by changing the reaction temperatures; (b) the distribution of butenes at 95% conversion. Propene conversion (c) and the distribution of butenes (d) at 98% 1,3-butadiene conversion in hydrogenation of 1,3-butadiene in the presence of propene. (e) Schematic illustration of improvement of butenes selectivity on single atom Pd<sub>1</sub>/graphene catalyst. Note: the figure legend in (b) also applies to (d). Reproduced with permission from ref 257. Copyright 2015 American Chemical Society.

of Pd single atoms, present in Pd-NPs/graphene, during the annealing process.<sup>257</sup>

To better understand the efficiency of the Pd<sub>1</sub>/graphene catalyst in terms of butene selectivity, a feed containing a mixture of propene and butadiene was used where 70% of the feed was propene.<sup>257</sup> The single atom (Pd<sub>1</sub>/graphene) catalyst converted 98% of butadiene to butenes with 100% selectivity by suppressing propene conversion to 0.1%. The selectivity for 1-butene was 69% (Figure 32). This excellent performance can be explained by the mode of absorption of reactants to Pd. In the case of Pd single atom, it is believed that the binding mode with butadiene is mono- $\pi$ -absorption mode which is different from Pd nanoparticles where bi- $\pi$ -absorption mode occurs, favoring the total reduction of the reactants (Figure 32).<sup>257</sup> Similarly, Lopez and Perez-Ramirez et al.<sup>258</sup> trapped Pd single atoms in the cavity of the mesoporous polymeric graphitic carbon nitride ([Pd]mpg-C<sub>3</sub>N<sub>4</sub>) and used it for hydrogenation of acetylene. This well-defined [Pd]mpg-C<sub>3</sub>N<sub>4</sub> catalyst was tested for reduction of 1-hexyne to 1-hexene and its activity compared with the well-known Lindlar catalyst at 343 K and 5 bar of H<sub>2</sub>. It was observed that the activity of [Pd]mpg-C<sub>3</sub>N<sub>4</sub> is  $1.41 \times 10^3 \text{ mol}_{\text{product}} \text{ mol}_{\text{Pd}}^{-1} \text{ h}^{-1}$  with high selectivity (90%) toward 1-hexene, whereas the Lindlar catalyst shows a similar selectivity (90%) but with a much lower activity ( $0.34 \times 10^3 \text{ mol}_{\text{product}} \text{ mol}_{\text{Pd}}^{-1} \text{ h}^{-1}$ ) in spite of high Pd (5%) content.<sup>258</sup>

To conclude this section, we observed that SOMCat can carry out hydrogenation of the olefinic bonds and aromatic rings efficiently and behave like homogeneous catalyst where almost all elementary steps are well-known and enable drawing a mechanistic path. In the case of SAC and SAAC, the catalysts exhibited excellent activities and selectivities as compared to nanoparticles or bulk atoms. However, not much is known about the elementary steps as it is difficult to isolate or characterize the intermediates during the course of the reaction.

## 4.2. Hydrogenolysis, Alkane Metathesis via C–H and C–C Bond Activation

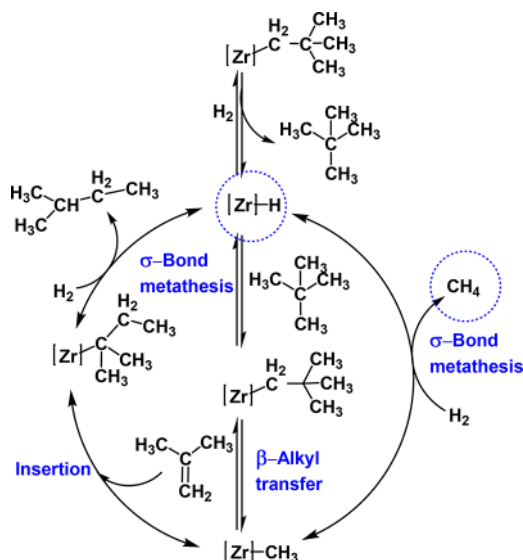
### 4.2.1. Via SOMC. 4.2.1.1. Hydrogenolysis of Alkanes.

Alkanes are the most abundant organic compounds in nature. Activation of C–H and C–C bond of hydrocarbons is one of the most difficult reactions because alkanes display very low reactivity toward most organometallic complexes. They are, however, very important in the fields of energy, fine chemicals, and petrochemical industries, thus attracting high interest from the scientific community. Generally, transition metal hydrides and metal alkyls with d<sup>0</sup> configuration are used for low temperature activation of alkanes. The first C–H bond activation reaction using SOMC-based strategy was reported in 1991<sup>259,260</sup> when silica supported ZrNp<sub>4</sub> ( $\equiv\text{Si}-\text{O}-\text{ZrNp}_3$ ) was reacted with hydrogen to produce a mixture of a *mono*-hydride ( $\equiv\text{Si}-\text{O}-$ )<sub>3</sub>ZrH and *bis*-hydride ( $\equiv\text{Si}-\text{O}-$ )<sub>2</sub>ZrH<sub>2</sub>.



In presence of  $\text{H}_2$  at  $100\text{ }^\circ\text{C}$  [ $(\equiv\text{Si}-\text{O}-)\text{ZrNp}_3$ ] did not yield neopentane, but instead, a mixture of methane and ethane. It was also observed that at lower temperature ( $50\text{ }^\circ\text{C}$ ) and at 50% conversion, methane and isobutane were mostly formed. With time, isobutane transformed into methane and propane; propane transformed into methane and ethane. To rationalize this reaction, a catalytic path was drawn involving all observed intermediates: (i) C–H activation of the neopentane (by  $\sigma$ -bond metathesis) followed by (ii)  $\beta$ -methyl transfer resulting in isobutene (Scheme 7). The initial C–H activation step was further proved by the evolution of  $\text{H}_2$  after adding 1 mol of cyclooctane to  $[\text{Zr}]-\text{H}$  at room temperature.<sup>259</sup>

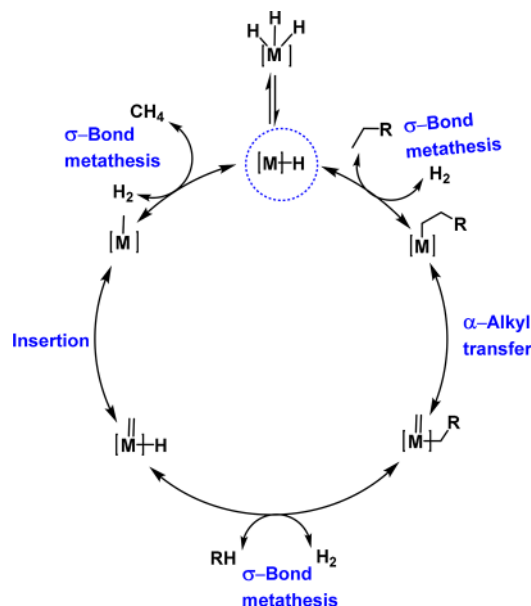
**Scheme 7.** First Evidence of C–H and C–C Bond Cleavage with  $(\equiv\text{Si}-\text{O}-)\text{ZrNp}_3$ ;  $[\text{Zr}]: (\equiv\text{Si}-\text{O}-)_3\text{ZrH}^a$



<sup>a</sup>Reproduced with permission from ref 259. Copyright 1991 John Wiley & Sons.

In the next step, isobutane was obtained by reduction of isobutene: (iii) Isobutene reacts with  $[\text{Zr}]-\text{CH}_3$  by anti-Markovnikov addition, leading to  $[\text{Zr}]-\text{(2-methyl butyl)}$ . (iv) By hydrogenolysis of the  $[\text{Zr}]-\text{alkyl}$  bond, isobutane is formed. The cycle (i–iv) continues until total conversion into methane and ethane. The hydrogenolysis reaction was extended to group 5 and group 6 metals. Hydrides of silica–alumina supported group 4 (Ti, Zr, Hf), 5 (Ta), and 6 (W) metals were prepared from their parent SOMC complex.<sup>261</sup> Whereas silica and silica–alumina<sup>261</sup> supported group 4 hydrides are known not to cleave ethane,  $[\text{Ta}]-\text{H}$  and  $[\text{W}]-\text{H}$  were able to convert ethane to methane.<sup>261</sup> In a continuous flow reactor at  $180\text{ }^\circ\text{C}$ ,  $[\text{Ta}]-\text{H}$  converted 27% of ethane to methane, whereas  $[\text{W}]-\text{H}$  showed 22% conversion under identical conditions.<sup>261</sup> These results suggest the occurrence of a different mechanism than with group IV catalysts (Scheme 8): (i) C–H bond activation of alkanes (by  $\sigma$ -bond metathesis) with metal hydride and release of hydrogen, (ii) carbene deinsertion ( $\alpha$ -alkyl transfer), which results in the formation of metal alkyl–alkylidene species, (iii) hydrogenolysis of the metal alkyl–methylidene leading to a metal methylidene hydride, (iv) insertion of the hydride into metal methylidene resulting in a metal methyl fragment, and (v) hydrogenation of the metal alkyl fragment, resulting in the original metal hydride catalyst with liberation of methane.<sup>261</sup>

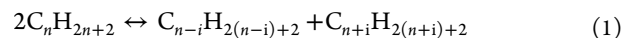
**Scheme 8.** Elementary Steps Are Shown for the Hydrogenolysis of Alkanes with Silica Supported Group 5 and 6 Metals<sup>a</sup>



<sup>a</sup>Reproduced with permission from ref 261. Copyright 2012 Royal Society of Chemistry.

Therefore, the basic difference between group 4 and group 5, 6 hydrides is that group 4 metal-hydride catalysts prefer  $\beta$ -alkyl transfer, whereas both group 5 and 6 hydrides favor an  $\alpha$ -alkyl transfer, resulting in the formation of methane as main product.<sup>261</sup>

**4.2.1.2. Alkane Metathesis.** Alkane metathesis is a catalytic reaction where two molecules of a given alkane convert into the lower and higher alkane (eq 1).<sup>262</sup>

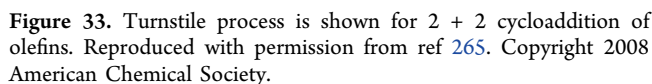


where  $i = 1, 2, \dots, n-1$ ; with  $i = 1, 2$  favored for  $n < 4$ .

Conversion of propane into higher and lower alkanes at  $400\text{ }^\circ\text{C}$  and in the presence of two catalysts  $\text{Pt}/\text{Al}_2\text{O}_3$  and  $\text{WO}_3/\text{SiO}_2$  was first observed in 1973.<sup>263</sup> This process was named “alkane redistribution”. Almost 25 years later, Basset et al. observed that a well-defined silica supported  $[\text{Ta}]-\text{H}$  catalyst was able to convert propane to, mainly, butane and ethane with lower amounts of methane and pentane (at  $150\text{ }^\circ\text{C}$  and 1 atm of  $\text{H}_2$ ). This new reaction was called “alkane metathesis” by analogy with the well-known olefin and alkyne metathesis reactions.<sup>262</sup> A potential application of alkane metathesis could be transformation of methane to transportation fuel for which no practical process is currently available, at least by direct route; methane could be converted to ethane through nonoxidative coupling (see section 5), followed by conversion of ethane to transportation fuel using alkane metathesis reaction.<sup>264</sup> This is not unrealistic because it was discovered that butane itself can be transformed to liquid hydrocarbons via alkane metathesis catalysts.<sup>261</sup> The mechanism of alkane metathesis was elucidated by identification of the primary products at very low contact time. DFT studies were able to clarify the whole mechanistic picture highlighting key differences with respect to olefin metathesis.

For example, the expected direct pathway consisting of  $[2 + 2]$ -cyclo-addition and cyclo-reversion is energy demanding for

stages of the reaction has been investigated computationally. During the activation step transforming the [Ta]–H species into [Ta](alkyl)(alkylidene), H<sub>2</sub> was released, and hydrogenolysis took place. In contrast, the absence of H<sub>2</sub> production during the catalytic cycle pushed the reaction toward metathesis.<sup>266</sup>



Group 4 metal hydrides are not active for alkane metathesis. Alkane metathesis reaction was observed with group 5 metal hydrides and group 6 metal alkyls and metal hydrides. Surprisingly, silica supported  $[W]-H$  generated from  $[(\equiv Si-O)W(\equiv C^tBu)Np_2]$  was almost inactive for alkane metathesis.<sup>267</sup> It was proposed that during the course of the reaction,  $[W]$  leached from the support deactivating the catalyst. To overcome this difficulty, a support with acidic properties, silica–alumina (SAL), was chosen.<sup>268</sup> Silica–alumina has strong Lewis and Brønsted acidity though it is not a perfectly crystalline solid.<sup>269</sup>  $W(\equiv C^tBu)Np_3$  was grafted on SAL dehydroxylated at 500 °C under vacuum.<sup>270</sup> Precatalyst  $[(\equiv Si-O)_{SAL}W(\equiv C^tBu)Np_2]$  was prepared by chemisorption of  $W(\equiv C^tBu)Np_3$ , and after hydrogenation (at 1 atm and 150 °C),  $[W]_{SAL(500)}-H$  was formed (Scheme 9).<sup>270</sup> The latter catalyst (TON = 121) was found to be more active

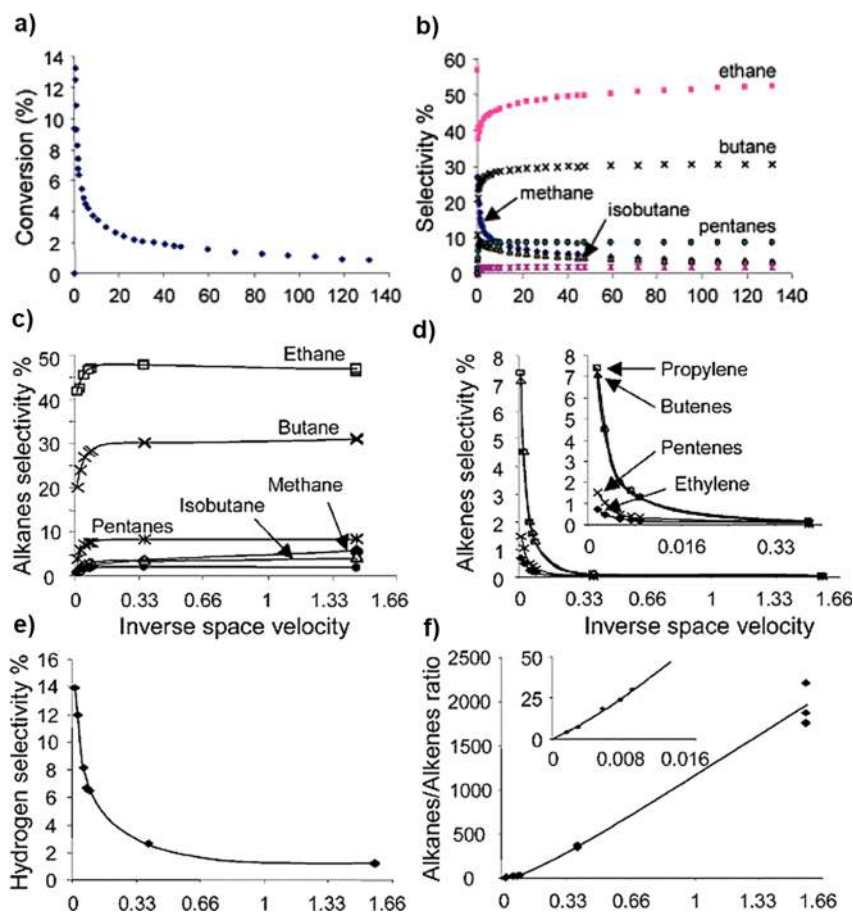
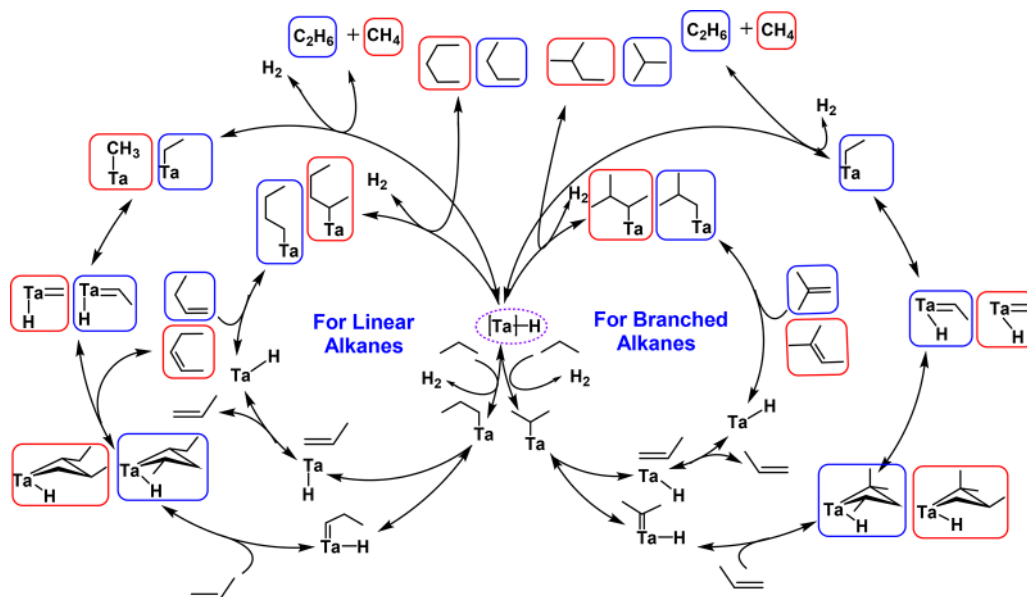


**Figure 34.** (a) Conversion and (b) selectivities obtained during propane metathesis catalyzed by  $[(\equiv\text{Si}-\text{O}-)_2\text{Ta}-\text{H}]$ , (5.33 wt % Ta) in a continuous flow reactor (150 °C, 1 atm, 1 mL/min, VHSV 38 h<sup>-1</sup>). Selectivity vs inverse space velocity expressed in  $[(\text{min})(\text{volume of catalyst})/(\text{volume of propane})]$  for (c) alkanes, (d) alkenes, and (e) H<sub>2</sub>. (f) Alkanes/alkenes ratio vs inverse space velocity. Reproduced with permission from ref 272. Copyright 2005 American Chemical Society.

**Scheme 10.** Mechanistic Pathway Derived from Kinetics and DFT Calculations for the Formation of Linear and Branched Alkane<sup>272</sup>



in alkane metathesis than silica supported  $[\text{Ta}]-\text{H}$  (TON = 60) and silica-alumina supported  $[\text{Ta}]_{\text{SAL}}-\text{H}$  (TON = 60).<sup>268,271</sup>

Propane metathesis was also carried out in a continuous flow reactor using silica supported  $[\text{Ta}]-\text{H}$  as catalyst. Maximum conversion was reached after 100 h (Figure 34) with the



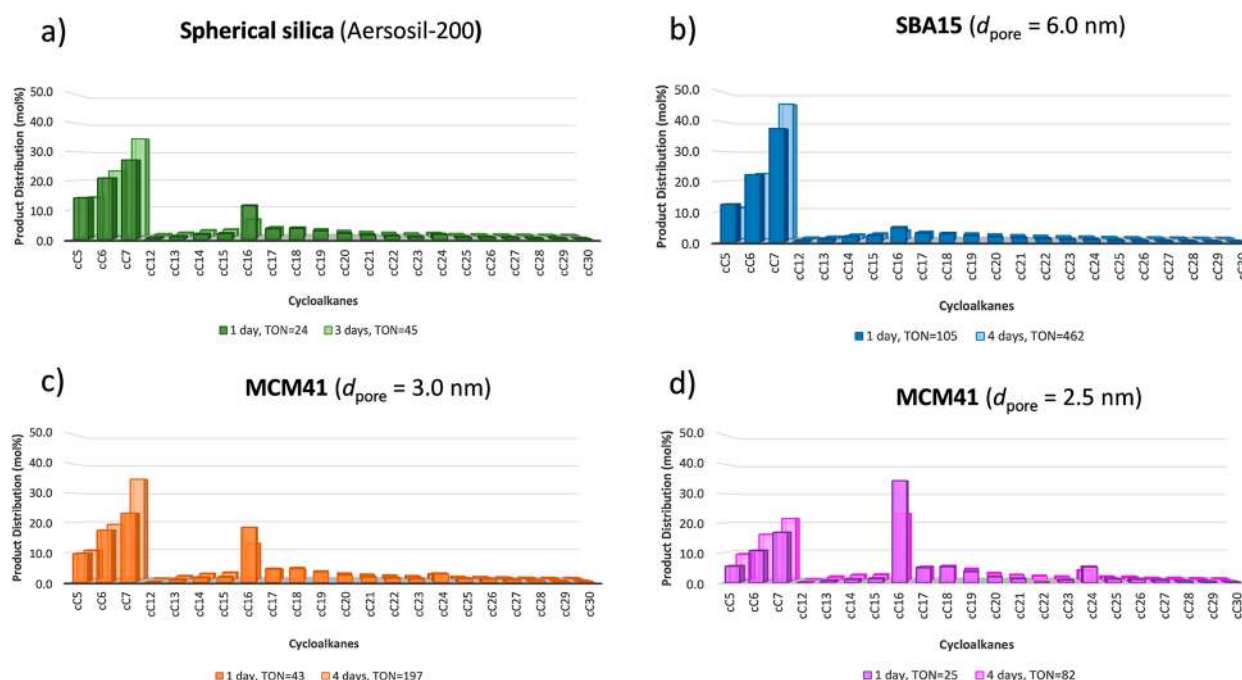
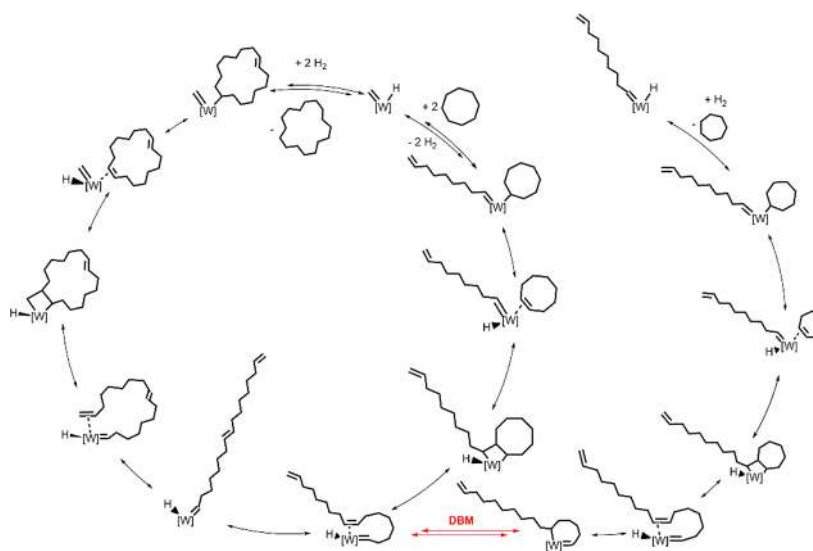


**Figure 35.** (a–d) Comparing product distributions of cyclooctane metathesis using silica supported ( $(\equiv\text{SiO}-)(\text{WMe}_5)$ ) precursor on various supports. Reproduced with permission from ref 277. Copyright 2017 American Chemical Society.

#### Scheme 11. Proposed Cyclooctane Metathesis Mechanism Using $(\equiv\text{Si}-\text{O}-)(\text{WMe}_5)$



following product selectivities: 56% ethane, 30% butane, 4% isobutane, 7% pentane, 1% iso pentane, and 2% hexanes (Figure 34).<sup>272</sup> At short time on stream, the selectivity toward methane was higher. This is reasonable, because at high conversions (as in the initial phase of the reaction), more hydrogen is produced, leading to hydrogenolysis of [Ta]-alkyls (Figure 34).<sup>272</sup>

To prepare new and more active catalysts for alkane metathesis, it was important to obtain further mechanistic understanding and to identify primary products such as olefin and hydrogen as identified in previous studies.<sup>272</sup> This suggests that dehydrogenation of paraffin to olefin and hydrogen is followed by olefin metathesis and the newly formed olefins are hydrogenated to new paraffins. All these steps were assumed to occur on a single tantalum atom having multifunctionalities:

dehydrogenation/hydrogenation and olefin metathesis. On the basis of the above results, a mechanism was proposed (Scheme 10).<sup>272</sup>

From the reaction mechanism, it was understood that group 5 and group 6 metal hydride and metal methyl (metal carbene hydride) catalysts can be very active for alkane metathesis reaction. A first attempt to prepare more active catalysts was the synthesis of a complex with a metal methyl coordination sphere  $[(\equiv\text{Si}-\text{O}-)\text{W}(\text{CH}_3)_5]$ .<sup>196</sup> This silica supported precatalyst was synthesized by reacting  $\text{W}(\text{CH}_3)_6$  and  $\text{SiO}_{2-700}$  (silica dehydroxylated at 700 °C).  $\text{W}(\text{CH}_3)_6$  is explosive at room temperature,<sup>273</sup> but once supported on silica, it is stable at room temperature. This precatalyst was tested for propane metathesis reaction reaching a TON of 126.<sup>196</sup> Later, a carbene hydride of [W]-methyl was prepared by the reaction

of  $[(\equiv\text{Si}-\text{O}-)\text{W}(\text{CH}_3)_5]$  with hydrogen from  $-78^\circ\text{C}$  to room temperature.<sup>35</sup> The structure of the carbene hydride species  $[(\equiv\text{Si}-\text{O}-)\text{W}(=\text{CH}_2)\text{H}_3]$  was confirmed by DFT studies and was very efficient in propane metathesis with a TON of 261.<sup>35</sup> In the next step, a tandem catalyst was prepared on the same support having a dehydrogenation catalyst (based on group 4 metals such as Zr, Ti) and an olefin metathesis catalyst (based on group 6 metal as W).<sup>197,274</sup> For the first time, a well-defined bimetallic catalyst was synthesized and tested for propane metathesis reaction. The bimetallic catalyst  $[(\equiv\text{Si}-\text{O}-)\text{W}(\text{CH}_3)_5]/[(\equiv\text{Si}-\text{O}-)\text{Ti}(\text{Np})_3]$  was very efficient in propane metathesis with a TON of 10000, which was the highest TON obtained to date for any well-defined surface organometallic catalyst.<sup>197,274</sup>

#### 4.2.1.3. Cycloalkane Metathesis and Confinement Effect.

Tungsten pentamethyl supported on spherical silica nanoparticles  $(\equiv\text{SiO}-)(\text{WMe}_5)$  was also the first precatalyst for the heterogeneous metathesis of cyclic alkanes. At moderate temperatures ( $>80^\circ\text{C}$ ), this system promoted ring expansion (mostly cyclohexadecane  $\text{C}_{16}$ ) and ring contraction (mostly cycloheptane  $\text{C}_7$ ) of cyclooctane (Figure 35). Cyclic alkanes span from  $\text{C}_5$ – $\text{C}_{30}$  without the formation of olefins or polymeric products.<sup>275,276</sup>

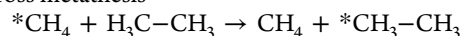
The reason for observing such a broad distribution of ring contraction and ring expansion products is double bond migration (DBM, Scheme 11) likely occurring during reaction. The  $[\text{W}]\text{-H}$  might insert into the double bond followed by  $\beta\text{-H}$  elimination, which allows the formation of cyclic alkanes other than  $\text{C}_8$ ,  $\text{C}_{16}$ ,  $\text{C}_{24}$ , or  $\text{C}_{32}$ . The product selectivity of cyclooctane metathesis changes when using a confinement strategy by immobilizing  $\text{WMe}_6$  inside the cavities of mesoporous materials (MCM41 or SBA15) with various pore sizes with different diameters ( $d_{\text{pore}} = 60, 30, \text{ and } 25 \text{ \AA}$ ).<sup>277</sup> The combination of TEM and DNP SENS results confirmed that most of the active sites (90%) were located and homogeneously distributed inside the mesopores of the support.<sup>186,277</sup> Experiments in cyclooctane metathesis at  $100^\circ\text{C}$  showed that confinement effects observed in smaller pores (30 and 25  $\text{\AA}$ ) improve selectivity toward the dimeric product (cyclohexadecane). In contrast, in larger pores (60  $\text{\AA}$ ), a broad product distribution is dominated by ring contracted cycloalkanes.

This means that the bigger the pores, the smaller the size of the products. Calculations by density functional theory (DFT) revealed the origin of this counterintuitive result: the key intermediates for the transition state leading to  $\text{C}_7$  occupy more space than those leading to  $\text{C}_{16}$ , hence the formation of ring contraction products is less favorable in a confined environment.<sup>277</sup>

**4.2.1.4. Alkane Cross-Metathesis. Cross Metathesis of Methane and Propane (or Ethane).** Cross metathesis of methane and ethane was carried out using SOMC-prepared  $[\text{Ta}]\text{-H}$  catalyst (eq 2).<sup>278</sup> A degenerate process was expected. Isotopically labeled methane  $^{13}\text{CH}_4$ , and unlabeled ethane were used for this reaction (batch reactor,  $T = 165^\circ\text{C}$ ).

Cross metathesis of methane and ethane/propane:

cross metathesis



cross metathesis  $\text{C}_3\text{H}_8 \rightarrow 2\text{C}_2\text{H}_6$

hydrogenolysis  $\text{H}_2 + \text{C}_3\text{H}_8 \rightarrow \text{CH}_4 + \text{C}_2\text{H}_6$

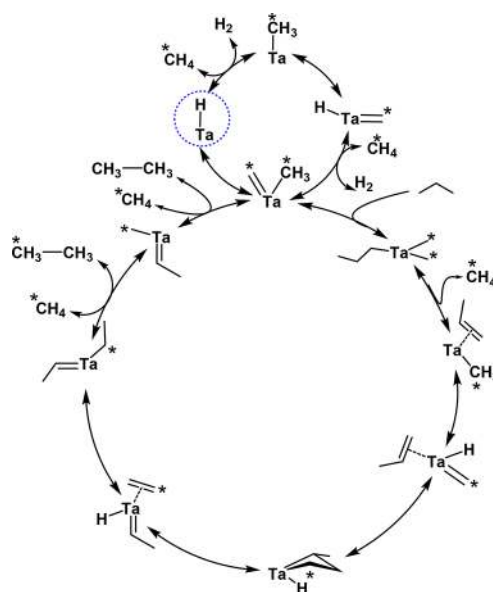
self-metathesis  $\text{C}_3\text{H}_8 \rightarrow 1/2\text{C}_2\text{H}_6 + 1/2\text{C}_4\text{H}_{10}$  (2)

Products were analyzed by GC-MS, finding a mixture of  $^{13}\text{C}$  enriched methane and ethane in 50:1 ratio. Along with mono-, di-, and unlabeled ethane, a considerable amount of unlabeled methane was detected. The formation of unlabeled methane is understandable as it comes from hydrogenolysis of ethane:  $\text{H}_2$  is produced during the  $\text{C-H}$  activation step. Mono- and dilabeled ethane were formed by the stepwise incorporation of enriched methane into ethane moieties. To understand the reaction mechanism (and to obtain productive metathesis), methane and propane were reacted in a continuous flow reactor.<sup>278</sup> Together with cross metathesis products, also unwanted hydrogenolysis products and self-metathesis products were observed. Complete cross metathesis of equimolar propane and methane (1 mol each) should provide exclusively ethane. In contrast, hydrogenolysis gave one mole of ethane; as self-metathesis gave 0.5 mol ethane and 0.5 mol butane (eq 2).

To avoid or minimize unwanted side products, cross metathesis of methane and propane was performed with a high methane to propane ratio (1250) on  $[\text{Ta}]\text{-H}$  in a continuous flow reactor at  $250^\circ\text{C}$ . More than 85% of dilabeled ethane was formed confirming the successful cross metathesis between methane and propane. Formation of dilabeled ethane was due to successive, degenerate reaction of monolabeled ethane with labeled methane at high contact time, leading to dilabeled ethane as the main isotopomer (Scheme 12).<sup>278</sup>

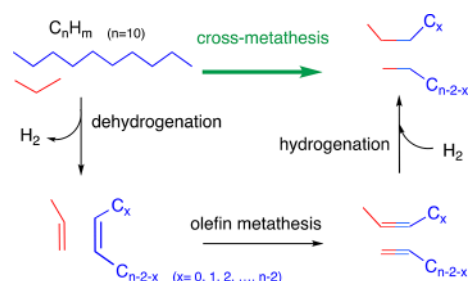
**Cross Metathesis between *n*-Decane and Propane.** Alkane cross-metathesis between *n*-decane and propane occurs under mild conditions using  $[(\equiv\text{Si}-\text{O}-)\text{W}(\text{Me})_5]$  treated with hydrogen at  $150^\circ\text{C}$ .<sup>279</sup> Under such conditions, the precursor is transformed into the active form of the catalyst:  $[(\equiv\text{Si}-\text{O}-)\text{W}(\text{H})_3(=\text{CH}_2)]$ . Experiments with isotopic labeled

**Scheme 12. Plausible Mechanism for Cross Metathesis of Methane and Propane**<sup>278</sup>



alkanes ( $^{13}\text{C}$  1-propane +  $n$ -decane or  $n$ -propane +  $\text{C}_{10}\text{D}_{22}$ ) proved the occurrence of cross metathesis products. A plausible reaction mechanism is shown in Scheme 13.

**Scheme 13. Cross Metathesis of Propane and  $n$ -Decane<sup>a</sup>**



<sup>a</sup>Reproduced with permission from ref 279. Copyright 2019 American Chemical Society.

The  $\text{C}_3/\text{C}_{10}$  ratio was found to be the most important parameter governing selectivity of cross metathesis and was varied to optimize the yield of cross-metathesis products (Figure 36).

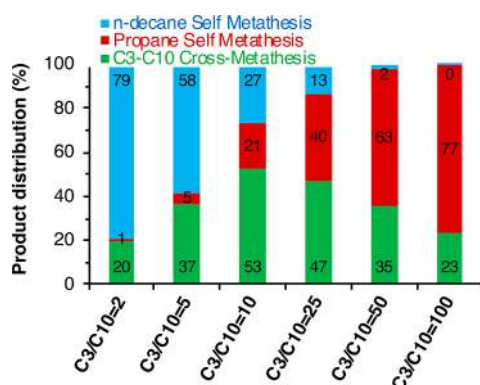


**Figure 36.** Influence of the  $\text{C}_3/\text{C}_{10}$  molar ratio on the percentage of cross-metathesis products. Results from fully deuterated  $n$ -decane ( $\text{C}_{10}\text{D}_{22}$ ) and propane in the range of  $\text{C}_3/\text{C}_{10} = 2$ –100 with the precursor  $((\equiv\text{SiO}-)\text{W}(-\text{CH}_3)_2(\text{H}_3))$  at  $T = 150^\circ\text{C}$  (green, cross-metathesis products; blue,  $n$ -decane self-metathesis products; red, propane self-metathesis products). Reproduced with permission from ref 279. Copyright 2019 American Chemical Society.

When alkane metathesis was carried out with a mixture of labeled propane and  $n$ -decane, three catalytic cycles were observed to occur (Scheme 14): self-metathesis of propane (red cycle), self-metathesis of  $n$ -decane (blue cycle), and cross-metathesis between propane and  $n$ -decane (green cycle). For the latter, several possible cross-metathesis steps between the alkylidene species from one alkane with the olefin intermediates from the other alkane (Scheme 14, in dashed green circles) may occur during the olefin metathesis step. Fragments of both starting materials were incorporated into the cross-metathesis products, with one, two, or three methylene groups from the initial propane. This is in agreement with the experimental observation using labeled alkanes.

The proposed mechanism involves C–H activation by  $\sigma$ -bond metathesis followed by  $\beta$ -H elimination forming the metal hydride and the olefin.

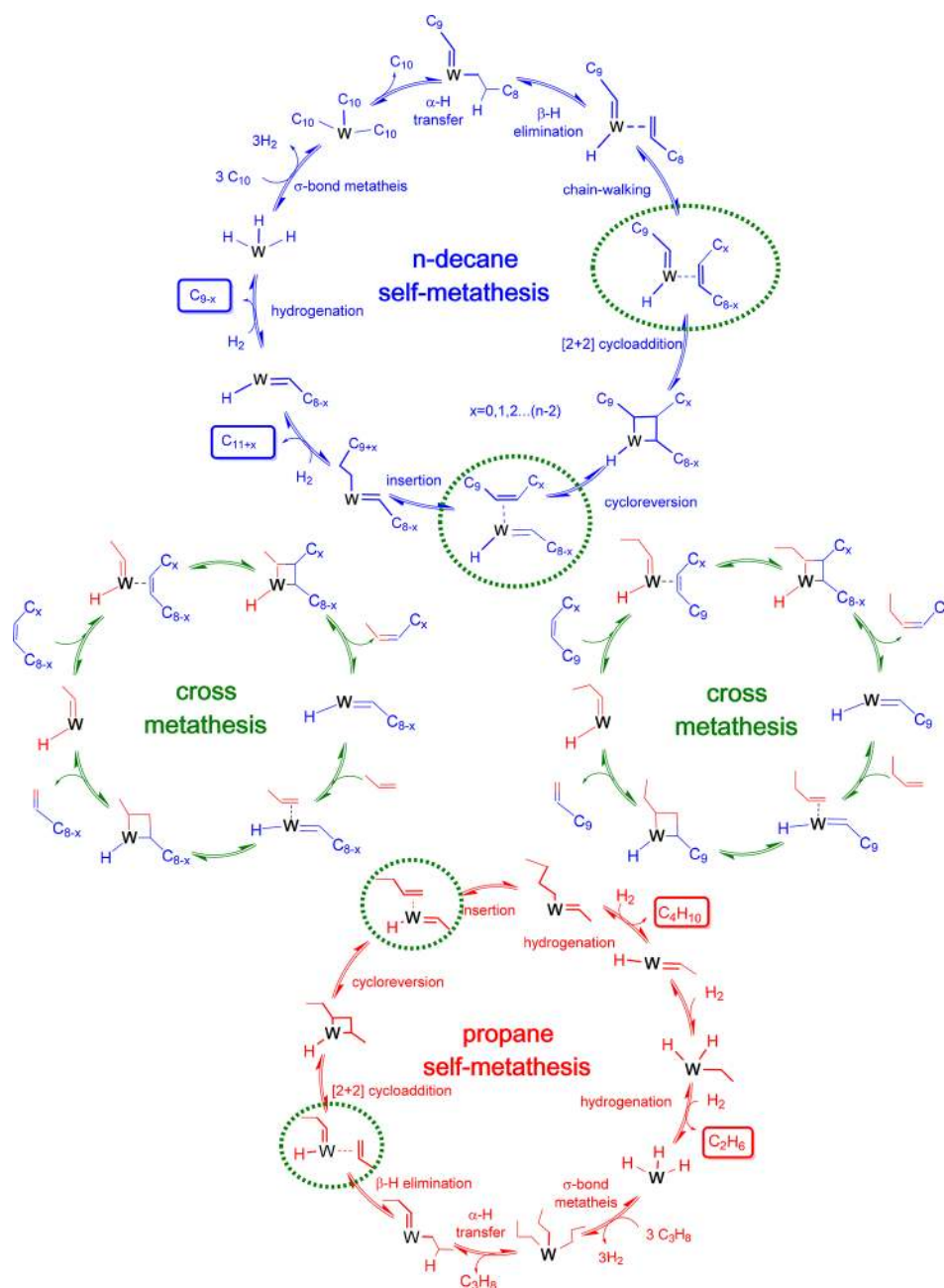
In the second step of olefin metathesis, the generated olefins may react with the hydridocarbene species (formed by  $\alpha$ -H transfer from the metal–alkyl species obtained from each single component) to form the less sterically constrained metallacycle. This metallacyclobutane undergoes metathetical cleavage giving new olefins and hydridocarbene species. In the olefin metathesis step, the cross metathesis reaction competes with self-metathesis of each component. Success of the cross metathesis reaction depends on availability of the various possible metallocarbenes; it can be tuned by the molar ratio between these two fragments. The availability of the carbene derived from propane activation is more limited because  $n$ -decane metathesis is  $\sim 8$  times faster than propane metathesis. Therefore, to maximize the percentage of the cross metathesis products, it is necessary to have a ratio of propane to  $n$ -decane of at least 8, close to the optimum  $\text{C}_3/\text{C}_{10} = 10$  observed experimentally.

**Cross Metathesis between Toluene and Ethane.** The cross metathesis reaction was extended to alkyl chains of aromatic compounds such as toluene. Cross metathesis of toluene and ethane was carried out in batch reactor in the presence of  $[\text{Ta}]\text{-H}$  as precatalyst. Ethane and toluene (ratio = 3.7/97.6) were reacted with  $[\text{Ta}]\text{-H}$  catalyst at  $250^\circ\text{C}$  and 1 atm to produce ethylbenzene and xylene along with methane, propane, and butane.<sup>280</sup> A possible reaction mechanism is shown in Scheme 15.  $[\text{Ta}]\text{-H}$  reacts with the alkyl group forming molecular hydrogen. This activation step involves competition between the two reagents, e.g., ethane and toluene, as well as between the two types of C–H bonds in the toluene molecule, e.g., at the methyl group or on the aromatic ring (Scheme 15).

This leads to a mixture of tantalum–ethyl  $[(\equiv\text{Si}-\text{O})_2\text{Ta}(\text{C}_2\text{H}_5)]$ , –benzyl  $[(\equiv\text{Si}-\text{O})_2\text{Ta}(\text{CH}_2\text{C}_6\text{H}_5)]$ , or methyl phenyl  $[(\equiv\text{Si}-\text{O})_2\text{Ta}(\text{C}_6\text{H}_4\text{CH}_3)]$  complexes which have been effectively identified by  $^{13}\text{C}$  CP MAS NMR. In a second step, these complexes mainly undergo reaction with a molecule of ethane to liberate propane, ethylbenzene, or xylenes, respectively (note that xylene means  $\text{sp}^2$  (aromatic) C–H bonds activation by the  $[\text{Ta}]\text{-H}$ ) and form a tantalum–methyl intermediate; during this step, the kinetic of the reaction with ethane of the three intermediates will govern the final selectivity of the different products. The last step common to all cycles is the displacement of the methyl group from tantalum by either an ethane or a toluene molecule to regenerate the key intermediates: the tantalum–ethyl, –benzyl, or –methylphenyl complexes.<sup>280</sup> The reaction is slightly catalytic forming 1.7 mol of ethylbenzene for each mole of  $[\text{Ta}]\text{-H}$  catalyst. During reaction, deactivation of the catalyst was envisioned, resulting in very low TON. To improve the catalytic performance, 10%  $\text{H}_2$  was introduced in the reaction mixture during the reaction. As expected, at steady state, TOF for ethane increased from  $0.049\text{ h}^{-1}$  (absence of hydrogen) to  $0.13\text{ h}^{-1}$  (presence of hydrogen) and for toluene, it increased from  $0.013\text{ h}^{-1}$  (absence of hydrogen) to  $0.07\text{ h}^{-1}$  (presence of hydrogen).<sup>280</sup> Alongside ethylbenzene, relevant amounts of methyl-cyclohexane, benzene, and cyclohexane were also observed. These products may result either from hydrogenation of the reactant or from the hydrogenolysis process. The first step (C–H activation) is fully dependent upon the ratio of reactants. As ethane pressure increases, it favors the formation of  $[(\equiv\text{Si}-\text{O})_2\text{Ta}(\text{CH}_2\text{CH}_3)]$ , favoring self-metathesis of ethane. Similarly, when the pressure of toluene increases, the formation of the reaction intermediates  $[(\equiv\text{Si}-\text{O})_2\text{Ta}(\text{CH}_2\text{C}_6\text{H}_5)]$  and  $[(\equiv\text{Si}-\text{O})_2\text{Ta}(\text{C}_6\text{H}_4\text{CH}_3)]$



Scheme 14. Cross-Metathesis Mechanism between *n*-Decane and Propane As Well As Competing Self-Metathesis of *n*-Decane and Propane<sup>a</sup>



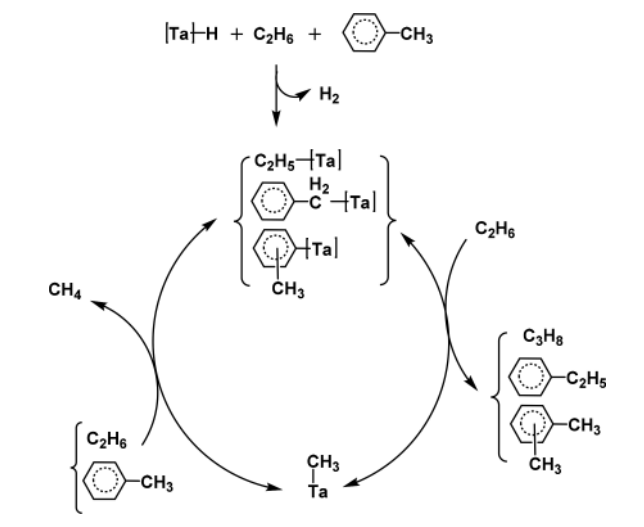
<sup>a</sup>Reproduced with permission from ref 279. Copyright 2019 American Chemical Society.

was preferred, leading to higher amount of ethylbenzene in the product (Scheme 15).<sup>280</sup>

**4.2.2. Via SAAC.** 4.2.2.1. *Hydrogenolysis.* No equivalent reaction to alkane metathesis exists in SAC or SAAC because at this moment there is lack of well-defined metal hydride species of early transition metals. The only example of hydrogenolysis reaction via single atom alloy catalysts (SAAC) was reported by Zhang et al. using Pt–Cu/SiO<sub>2</sub> for hydrogenolysis of methyl glycolate (MG) to ethanol.<sup>281</sup> In the latter study, several loadings of Pt single atoms alloyed with Cu were prepared and tested for hydrogenolysis of MG. The single atom alloys of Pt–Cu/SiO<sub>2</sub> were prepared stepwise; in the first step, silica-supported Cu was prepared via urea assisted gelation (UAG) method using a literature procedure.<sup>282</sup>

Subsequently, Pt was introduced by incipient wetness impregnation method (IWI) using Pt(NH<sub>3</sub>)<sub>4</sub>(OH)<sub>2</sub> as a precursor. The loading of Pt varied between 0.06–0.3 wt %, whereas the Cu loading remained constant (11.7%). XPS data revealed that both Cu/SiO<sub>2</sub> and 0.1Pt–Cu/SiO<sub>2</sub> (Pt–Cu/SiO<sub>2</sub> with 0.1 wt % Pt) contained a mixture of Cu<sup>0</sup> and Cu<sup>+</sup> surface species. These catalysts were tested for hydrogenolysis of MG, where it was observed that 0.1Pt–Cu/SiO<sub>2</sub> catalyst performed better than other Pt-based catalysts. In the hydrogenolysis reaction of MG, only 50% selectivity to ethanol at 100% MG conversion was obtained with Cu/SiO<sub>2</sub> at 553 K (Figure 37). MG conversion reached 100% above 473 K, whereas the highest selectivity for ethanol (69%) was observed at 523 K. Above this temperature, side products such as

**Scheme 15. Formation of Cross Metathesis Products Starting from Toluene and Ethane (Coming from  $sp^3$  (Aliphatic) and  $sp^2$  (Aromatic) C–H Bonds Activation)<sup>280</sup>**



propanol, 2-propanol, and butanol were observed. Compared to Cu/SiO<sub>2</sub> catalyst, 0.1Pt–Cu/SiO<sub>2</sub> SAA catalyst exhibited higher ethanol selectivity (77%) at 503 K with 100% conversion (Figure 37).<sup>281</sup>

The other SAAC (0.3Pt–Cu/SiO<sub>2</sub> and 0.06Pt–Cu/SiO<sub>2</sub>) produced mostly ethylene glycol, 2-propanol, propanol, and butanol (Scheme 16 and Figure 37).<sup>281</sup>

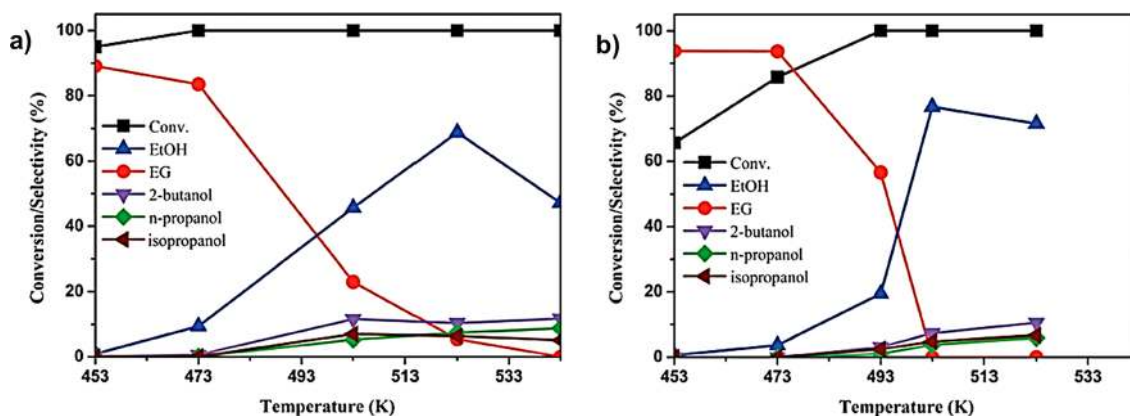
Characterization of Pt SAA reveals that the dispersion of Cu was highest at the Pt content of 0.1 wt % and improved the Cu<sup>+</sup>/Cu<sup>0</sup> ratio; on the other hand, the single atoms of Pt promoted the activation of H<sub>2</sub> while minimizing the C–C cleavage reaction, hence improving the ethanol selectivity.<sup>281</sup>

**4.2.3. Via SAC.** To the best of our knowledge, there are no examples of such reactions with single atom catalysts. This is a drastic and meaningful difference between SAC and SOMCat. In SOMCat, the presence of metal hydride is necessary to activate the C–H bond of the paraffin. It is likely that if conditions are met to transform the so-called single atom into a single atom hydride, then alkane metathesis might be observed by SAC.

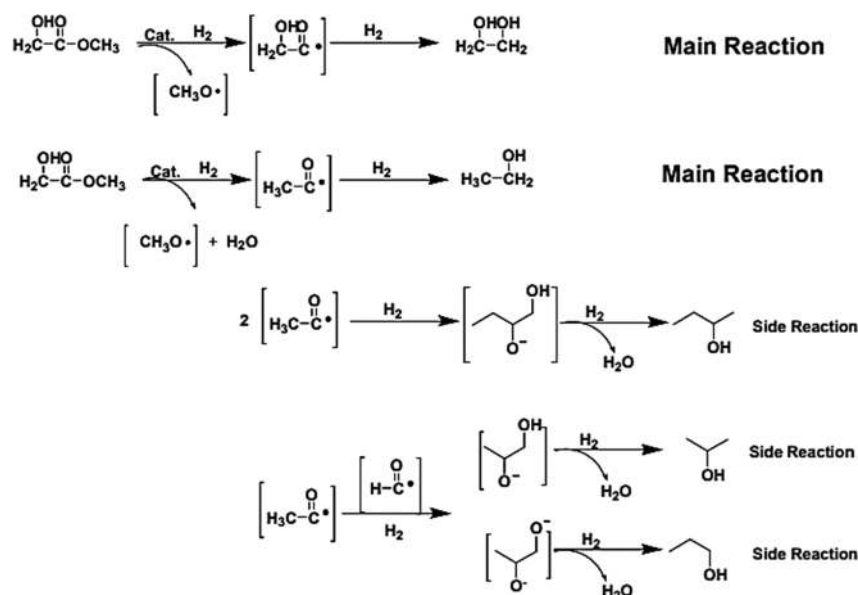
### 4.3. Light Alkanes Dehydrogenation

**4.3.1. Via SOMC.** **4.3.1.1. Propane Dehydrogenation (PDH).** Ga<sub>2</sub>O<sub>3</sub> is a well-established catalyst for the dehydrogenation of alkanes.<sup>283,284</sup> However, the nature of the active site is not well-understood,<sup>285–287</sup> and the catalyst suffers from deactivation by coking<sup>288,289</sup> and, possibly, by reduction of gallium. Therefore, the synthesis of well-defined gallium centers on silica, in place of using bulk oxides, might lead to more active and reproducible single metal sites and provide mechanistic information. Coperet et al. reported the grafting of Ga(OSi(OtBu)<sub>3</sub>)<sub>3</sub>·(THF) (1) on silica (Scheme 17), leading to single-site gallium complex 2.<sup>105</sup> Interestingly, in place of the expected monopodal complex,<sup>290</sup> the authors proposed formation of a tripodal species based on elemental analysis, <sup>13</sup>C MAS SSNMR, and EXAFS. As observed in other cases, for instance, when dealing with supported vanadium oxo complexes,<sup>34,291</sup> formation of 2 might take place via an initial monopodal complex followed by its restructuring by reaction with neighboring strained siloxane bridges, leading to multiple bonds with the surface and to regeneration of silanols as experimentally proven by the authors.<sup>105</sup> After calcination, complex 3 [(≡Si–O–)<sub>3</sub>Ga(XOSi≡)], where X is H from a silanol or Si from a siloxane bridge) was obtained by removal of the alcohol molecule that was, likely, partially replaced by coordination with a siloxane bridge or a silanol as suggested by EXAFS (number of oxygen neighbors: 3.6). The absence of Ga–Ga contributions in the EXAFS analysis confirmed the formation of isolated gallium sites. The catalytic performance toward PDH was tested at 550 °C. Under such condition, the selectivity for propylene after 30 min was 94.3% with a TOF of 20.4 mol C<sub>3</sub>H<sub>6</sub>/(mol Ga·h) and conversion of 9.3%. After 20 h on stream, the selectivity remained nearly constant (93%) with a TOF of 14.2 h<sup>–1</sup> and 6.5% conversion.

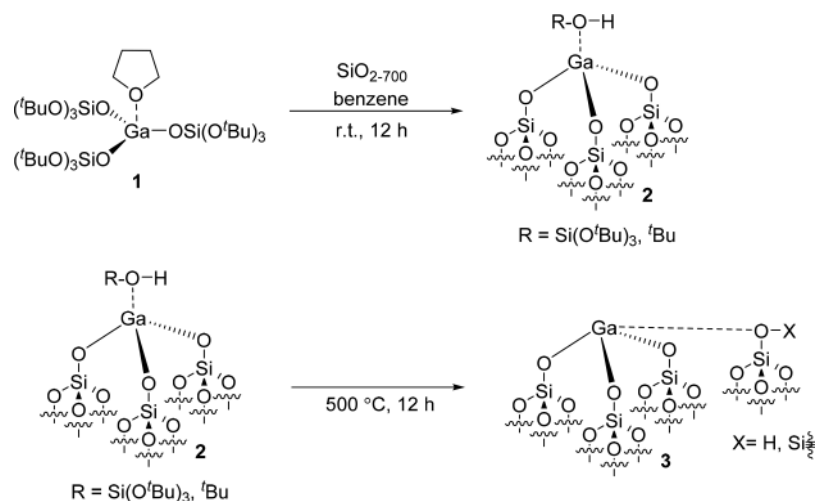
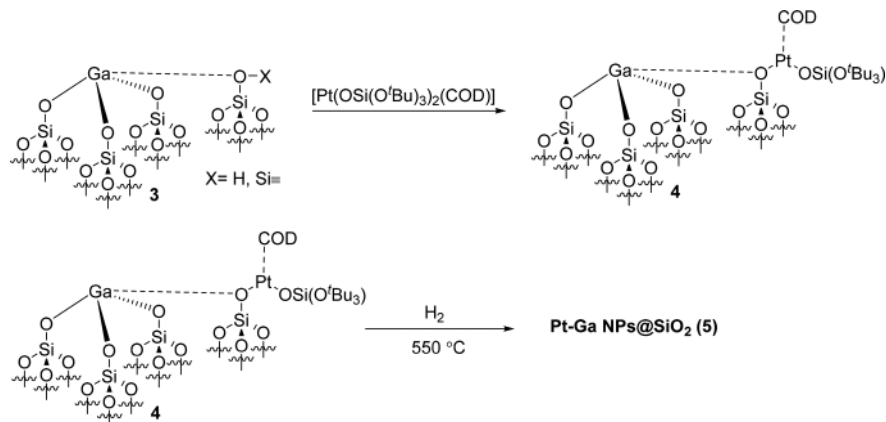
The authors noted that 3 is an order of magnitude more active than bulk Ga<sub>2</sub>O<sub>3</sub> oxide<sup>292</sup> and about five times more active than isolated gallium sites prepared by Miller and Hock.<sup>287</sup> Additionally, deactivation was an order of magnitude slower than for bulk Ga<sub>2</sub>O<sub>3</sub> oxide.<sup>292</sup> Given that only limited amounts of coke were observed on the catalyst, partial reduction of the metal to afford Ga<sup>1+</sup> sites, as observed by a shift of 3.6 eV in the XANES spectrum of spent 3, could explain the drop in catalytic activity. However, Miller and Hock have shown that a shift of up to 6 eV in XANES spectrum of gallium is not necessarily related to a change in



**Figure 37.** Catalytic performances of Cu/SiO<sub>2</sub> (a) and 0.1Pt–Cu/SiO<sub>2</sub> (b) at different temperatures. Reaction conditions: W8 h space velocity (WHSV) = 2.0 h<sup>–1</sup>, H<sub>2</sub>/MG = 120 and P(H<sub>2</sub>) = 3 MPa. Reproduced with permission from ref 281. Copyright 2018 Royal Society of Chemistry.

Scheme 16. Proposed Reaction Pathway for MG Hydrogenolysis<sup>a</sup>

<sup>a</sup>Reproduced with permission from ref 281. Copyright 2018 Royal Society of Chemistry.

Scheme 17. Grafting of Ga(OSi(O<sup>t</sup>Bu)<sub>3</sub>)<sub>3</sub>·(THF) (1) on SiO<sub>2-700</sub> to Afford 2 and Thermolysis to 3Scheme 18. Grafting of Pt(−OSi(O<sup>t</sup>Bu)<sub>3</sub>)<sub>2</sub>(COD) on 3 to Afford 4 and Reduction of 4 in H<sub>2</sub> Flow, Leading to 5

oxidation state and that the presence of gallium alkyls should be taken into account.<sup>287</sup> Overall, this work shows that isolated

gallium sites on silica prepared by SOMC are intrinsically more active and selective than gallium in bulk oxides because of

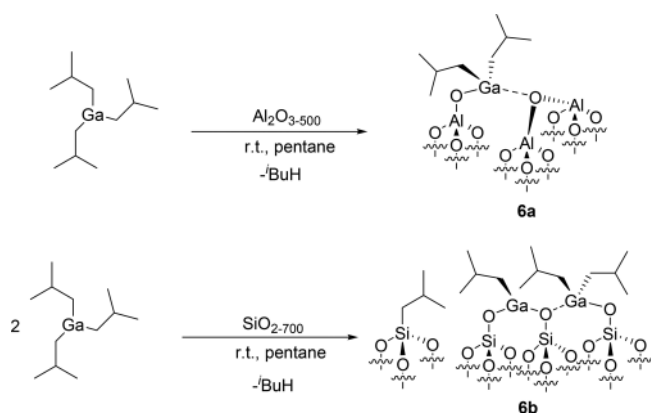


better dispersion of the metal and of reduced tendency to undergo deactivation. Given the well-established activity of Pt–Ga catalysts in PDH,<sup>293,294</sup> in continuation of previous work, Coperet et al. designed a new Pt–Ga catalyst<sup>295</sup> based on the combination of SOMC and thermolytic molecular precursor approaches.<sup>296</sup> To this aim, a metal–organic platinum precursor Pt(–OSi(O<sup>t</sup>Bu)<sub>3</sub>)<sub>2</sub>(COD) (COD = cyclooctadiene) was grafted on material 3 to afford 4 (Scheme 18). Material 4 contained Ga<sup>3+</sup> and Pt<sup>2+</sup> sites in nearly equimolar ratio. Treatment of 4 at 500 °C under flow of H<sub>2</sub> led to 5.

The nanoparticles of 5 were studied by XPS and EXAFS spectroscopy. Whereas a fraction of the gallium centers was still found in the initial Ga<sup>3+</sup> state, reduced gallium atoms (Ga<sup>δ+</sup>) were identified. Additionally, no Ga–Ga contribution was identified in the nanoparticles. Platinum was found as Pt<sup>0</sup>. Overall, the authors suggested the formation of Ga<sup>δ+</sup>Pt<sup>0</sup> nanoparticles with the gallium atoms dispersed mostly on the nanoparticle's surface. When 5 was tested for the dehydrogenation of propane at 550 °C in a dynamic reactor, the authors initially observed about 32% propane conversion with excellent selectivity for propylene (>99%). The catalyst performance with respect to propylene selectivity was lower for higher contact time. After 20 h under optimal conditions, the catalyst maintained the high selectivity observed, but the conversion dropped to about 17%. Nevertheless, the authors noted that the productivity after 20 h was still higher than the initial activity of other Ga–Pt systems that also had much lower lifetime (less than 2 h).<sup>294,297</sup> Also, under identical conditions, 5 performed better than the individual catalytic components (Pt<sup>0</sup>@SiO<sub>2</sub>) and (Ga<sup>3+</sup>@SiO<sub>2</sub>). The authors proposed that deactivation took place by carbon deposition on the catalyst. The catalyst could be regenerated by exposure to atmospheric conditions which dealloyed the Ga<sup>δ+</sup>Pt<sup>0</sup> nanoparticles. A new reduction in H<sub>2</sub> atmosphere reformed the catalyst with a performance equal to 75% of the pristine NPs.

In a different but comparable SOMC-based approach, Szeto et al. grafted Ga(<sup>t</sup>Bu)<sub>3</sub> on dehydroxylated alumina (Al<sub>2</sub>O<sub>3–500</sub>) and silica (SiO<sub>2–700</sub>).<sup>113</sup> For the grafting on Al<sub>2</sub>O<sub>3–500</sub>, spectroscopic characterization supported the structure [(GaBu)<sub>2</sub>(–OAl)] L (6a) derived from monopodal grafting pathway (L: neutral oxygen ligand from the alumina surface, Scheme 19). Despite the fact that grafting on SiO<sub>2–700</sub> generally takes place in a monopodal fashion with the formation of isolated compounds,<sup>290,298</sup> the reaction of

**Scheme 19.** Grafting of Ga(<sup>t</sup>Bu)<sub>3</sub> on Dehydroxylated Alumina and Silica Supports to Afford 6a and 6b, Respectively

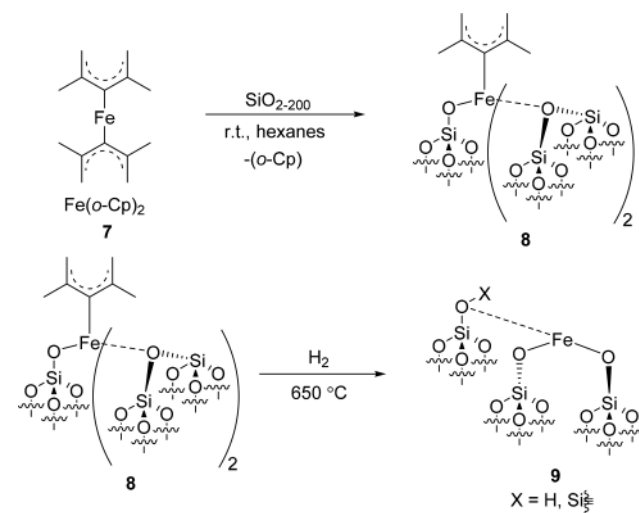


Ga(<sup>t</sup>Bu)<sub>3</sub> with SiO<sub>2–700</sub> led to formation of bimetallic Ga complexes (6b) as supported by careful EXAFS analysis (Scheme 19). Additionally, the authors showed that part of the isobutyl groups would transfer to the support by reaction with a strained siloxane bridge resulting in an increase of podality, as observed in other cases.<sup>34,291</sup> When the catalysts were tested for PDH at 550 °C, 6a displayed the best activity with 24% propane conversion and selectivity over 90%. After 1500 min on stream, the conversion declined to 8%. The catalyst supported on silica showed lower initial conversion (8%) and similarly declining performance in terms of yields and selectivity (which dropped to 2.5% and 72.3%, respectively, after 1500 min). These results appear at variance with those previously obtained by Coperet et al. using 3 that could, in principle, be attributed to the different nuclearity of the surface complexes. However, when Szeto et al. prepared 3, they obtained similar catalytic profile as per 6b.

Overall, the results obtained by Szeto et al. show that alumina is a more efficient support for propane dehydrogenation, possibly because the reaction mechanism is believed to involve C–H activation by the Ga–O bond that should be more favorable on Ga–O–Al sites. However, it is also possible that the Lewis acid sites of alumina play a role in the activation of the substrate or interact with the dispersed Ga centers. However, no specific mechanistic information was provided.

Miller and Hock prepared isolated Fe<sup>II</sup> complexes by grafting metallocene, bis(2,4-dimethylpentadienyl) iron (Fe(*o*-Cp)<sub>2</sub>, 7) on silica dehydroxylated at 200 °C.<sup>299</sup> The initial supported surface Fe species (8, Scheme 20) was found

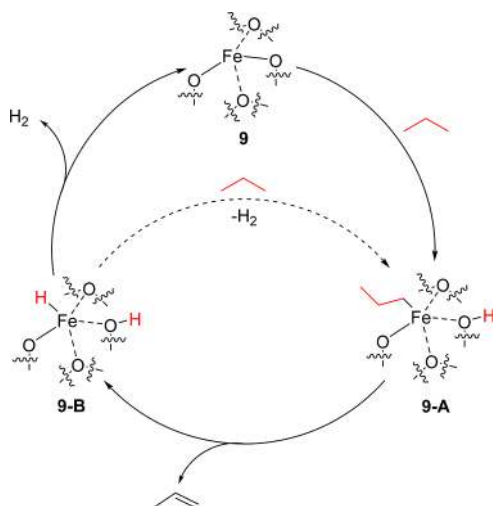
**Scheme 20.** Generation of Single-Site Fe<sup>2+</sup> Species on Silica Surface by Grafting of 7 Followed by Thermolysis in H<sub>2</sub>



to be in +2 oxidation state by XANES analysis and to bear a residual pentadienyl ligand because of exclusive monopodal grafting. However, EXAFS investigation highlighted the existence of additional coordination bonds with the surface. The +2 oxidation state was maintained after reduction with H<sub>2</sub> at 650 °C to generate 9 by the removal of the organic ligand and formation of a bipodal compound. When 9 was tested in ODH at low conversion (5%) at 650 °C, the overall propylene selectivity was about 70% with the catalytic performance remaining stable for 18 h (TOF 1.4 h<sup>–1</sup> after 18 h). The moderate selectivity was attributed to the unselective process of thermal cracking.

The catalytic performance of **9** was compared to that of supported iron NPs obtained by grafting  $\text{Fe}[\text{-N}(\text{SiMe}_3)_2]_2$  on silica followed by reduction in  $\text{H}_2$  (**10**). Whereas **10** was more active, by a factor of 40, than **9** in consuming propane, the selectivity to propylene was just 14%. Silica supported  $\text{Fe}^{\text{II}}$  oxide clusters on silica were virtually inactive in PDH. These control experiments suggest that the active species is represented by isolated  $\text{Fe}^{\text{II}}$  centers on silica. On the basis of the lack of evidence of a change of oxidation state of iron during catalysis, the authors proposed a heterolytic reaction mechanism where iron remains in the  $\text{Fe}^{2+}$  oxidation state (Scheme 21). Accordingly, heterolytic cleavage<sup>300</sup> of the Fe–

**Scheme 21.** Proposed Reaction Pathways for the Dehydrogenation of Propane Catalyzed by **9**



O–Si bond takes place by reaction with propane to form a  $\text{Fe}^{\text{II}}$ -alkyl species and a silanol (**9-A**, Scheme 21). From the latter intermediate, propylene is generated from the Fe-propyl fragment by  $\beta$ -hydride elimination, leading to a supported iron hydride (**9-B**). The catalyst is finally regenerated by formation of  $\text{H}_2$  from the Fe–H and SiO–H bonds. Alternatively (dashed line in Scheme 21), the iron hydride might react with a new molecule of propane to give **9-A** and hydrogen by  $\sigma$ -bond metathesis without returning to the initial species **9**. No DFT calculation was provided for this mechanism.

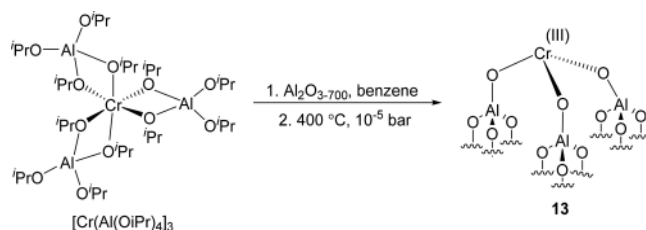
Conley et al. prepared isolated  $\text{Cr}^{3+}$  centers on silica ( $\equiv\text{SiO-}$ )<sub>3</sub>Cr (**12**) by reacting  $\text{Cr}(\text{-OSi}(\text{-O}^t\text{Bu})_3)_3 \cdot 2\text{THF}$  with  $\text{SiO}_{2-700}$  to afford (**11**), followed by thermolysis of the organic ligands at  $400^\circ\text{C}$  under vacuum (Scheme 22).<sup>29</sup> **12**, that was also employed in the same study to investigate the catalytic competency of isolated  $\text{Cr}^{3+}$  sites in ethylene polymerization, is reminiscent of the industrially applied  $\text{Cr}^{3+}/\text{Al}_2\text{O}_3$  dehydrogenation catalyst.<sup>292,301</sup> The catalytic activity of **12** at  $550^\circ\text{C}$  was found to steadily decrease from an initial TOF of  $10.3\text{ h}^{-1}$  at

$550^\circ\text{C}$  to a TOF of  $2.8\text{ h}^{-1}$  with a selectivity of 72%. This drop of catalytic performance is also found in the industrial catalyst that, indeed, requires continuous regeneration.<sup>292</sup>

For PDH promoted by **12**, the authors proposed a mechanism similar to that described in Scheme 21, with the C–H bond of propane being activated, by heterolytic splitting on the Cr–O bond with production of Cr-alkyl and  $\equiv\text{Si-OH}$  moieties. DFT calculations on the mechanism of propylene formation revealed a very high barrier of activation in the latter step. The barrier was as high as 57 kcal/mol for the activation of the methyl protons and only slightly lower (55.8 kcal/mol) for the methylene protons suggesting that both pathways could be very difficult if possible. However, in both cases, the  $\beta$ -hydride elimination barrier was also over 50 kcal/mol. Considering the observation that both chromium alkyl intermediates were located over 25 kcal/mol above the energy of the reagents, the transition state of  $\beta$ -hydride elimination by these pathways would be about 75–80 kcal/mol higher in energy than the starting point. However, other alternative calculated mechanisms did not lead to more reasonable barriers.

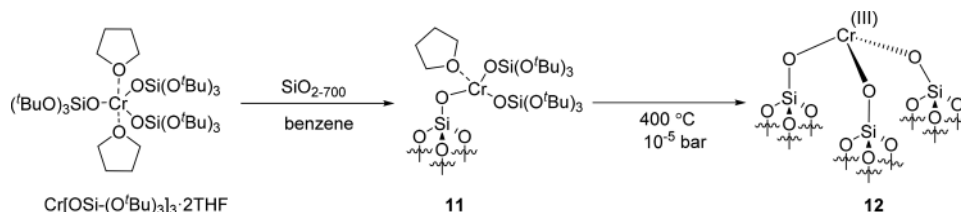
In the continuation of the previous work,<sup>248</sup> isolated  $\text{Cr}^{3+}$  sites were created on dehydroxylated alumina ( $\text{Al}_2\text{O}_{3-700}$ ) by grafting  $[\text{Cr}(\text{Al}(\text{O}^i\text{Pr})_4)_3]$  in place of previously employed  $\text{Cr}[\text{-OSi}(\text{-O}^t\text{Bu})_3]_3 \cdot 2\text{THF}$  to avoid the presence of silicon atoms on the alumina surface. The subsequent thermolysis of the organic ligands led to formation of **13** (Scheme 23).

**Scheme 23.** Preparation of Isolated  $\text{Cr}^{\text{(III)}}$  Sites on Alumina (**12**) by Grafting  $[\text{Cr}(\text{Al}(\text{O}^i\text{Pr})_4)_3]$  Followed by Thermolysis



The authors studied the activity of **13** in the dehydrogenation of propane at  $550^\circ\text{C}$  along with the traditional  $\text{CrO}_x/\text{Al}_2\text{O}_3$  catalyst, prepared by impregnation as in industry<sup>292</sup> and previously reported **12**.<sup>29</sup> Unsurprisingly, catalytic activity was found to be higher for **13** than for **12** because of the increased Lewis acidity of the  $\text{Cr}^{3+}$  center in **13**. The latter catalyst provided an initial TOF of 60 (mol  $\text{C}_3\text{H}_8$ ) (mol Cr)<sup>−1</sup> h<sup>−1</sup> that was about three times higher than for **12** but with a selectivity of just 66% (it was 72% for **12**).  $\text{CrO}_x/\text{Al}_2\text{O}_3$  displayed a TOF that was about the half as for **13** but with higher selectivity (88%). The lower selectivity found for **13** is consistent with the higher amount of exposed Brønsted acidic sites, known to promote cracking of alkanes,<sup>302</sup> found on this catalyst. For

**Scheme 22.** Preparation of Isolated  $\text{Cr}^{\text{(III)}}$  Sites on Silica (**12**) by a Combined SOMC- and Precursor Thermolysis Approach



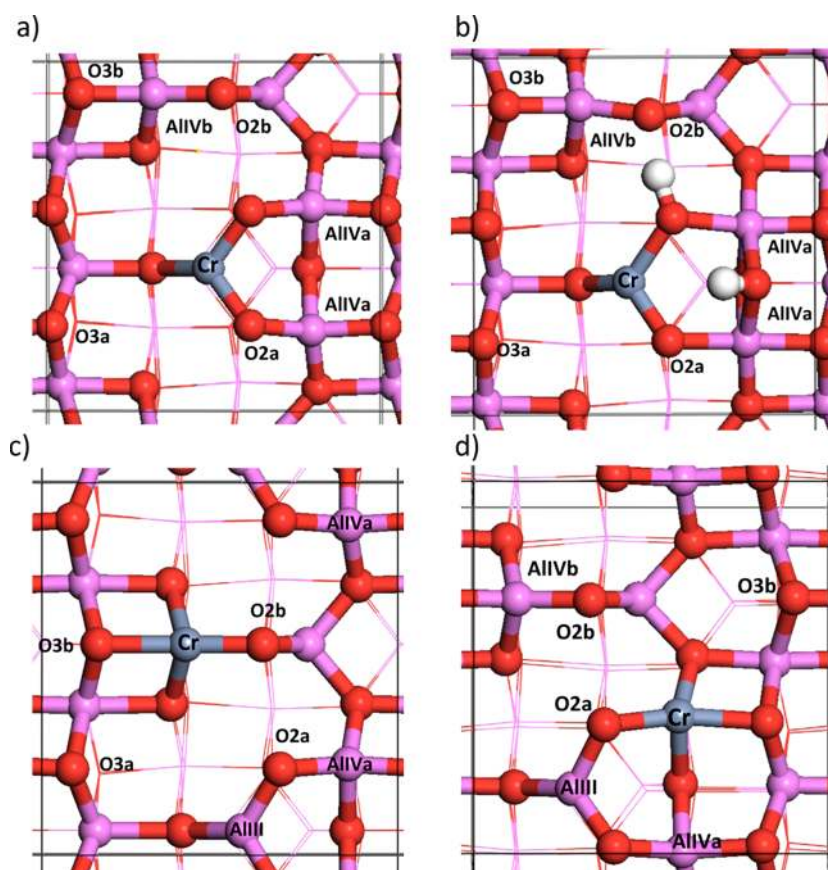
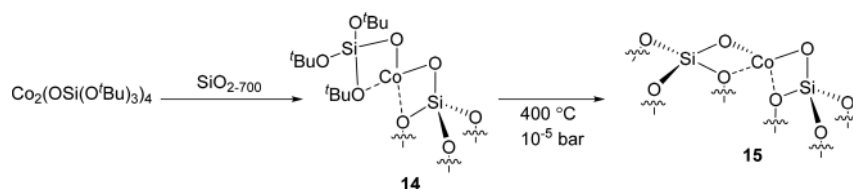


**Figure 38.** (top view) Model of  $\gamma$ - $\text{Al}_2\text{O}_3$  surface employed by Delley et al. in ref 248, “Single-site model of  $\text{Cr}^{(\text{III})}$  substituted at the  $\text{Al}_{\text{III}}$  site” on the (a) dehydroxylated s0 and (b) hydroxylated s1 ( $3.0 \text{ OH}/\text{nm}^2$ ) 110 surface of  $\gamma$ - $\text{Al}_2\text{O}_3$ . Single-site models of  $\text{Cr}^{(\text{III})}$  sites substituted at the (c)  $\text{Al}_{\text{IVb}}$  and (d)  $\text{Al}_{\text{IVa}}$  sites of the 110 surface of  $\gamma$ - $\text{Al}_2\text{O}_3$ . Cr, Al, H, and O atoms are depicted in blue, purple, white, and red, respectively. Reproduced with permission from ref 248. Copyright 2017 American Chemical Society.

**Scheme 24. Preparation of Isolated  $\text{Co}^{2+}$  Sites on Alumina (15) by Grafting Dimeric  $\text{Co}_2(-\text{OSi}(\text{OtBu})_3)_4$  Followed by Thermolysis**



better understanding of the reaction mechanism, the authors analyzed the heterolytic activation of propane on 13 by DFT approach.

To this aim, the authors employed models of  $\text{Cr}^{3+}$ -functionalized  $\gamma$ - $\text{Al}_2\text{O}_3$  considering different kinds of surfaces (s0, s1) and substitution sites (Figure 38). In particular, the most Lewis acidic sites, where Cr occupies the  $\text{Al}_{\text{III}}$  and the  $\text{Al}_{\text{IVb}}$  positions, were investigated. While several positions of the Cr atoms in the structure of alumina gave high reaction barriers comparable to those previously calculated for 12,<sup>29</sup> the  $\text{Cr}_{\text{IVb}}\text{-O2b}$  site (Figure 38) showed more affordable barriers; 46.1 kcal/mol was calculated for C–H activation by the Cr–O–Al bond and the following steps of  $\beta$ -hydride transfer (25 kcal/mol, located about 51 kcal/mol above the energy of the reagents) and H–H coupling (about 20 kcal/mol) were also less energy demanding than for 12, in agreement with the experimental results. This work shows that application of the SOMC methodology, by leading to a better dispersion of

chromium atoms on the surface, can lead to systems with higher catalytic activity than the traditional  $\text{CrO}_x/\text{Al}_2\text{O}_3$  system. However, the presence of large areas of unfunctionalized Brønsted acidic alumina surface had a detrimental impact on selectivity.

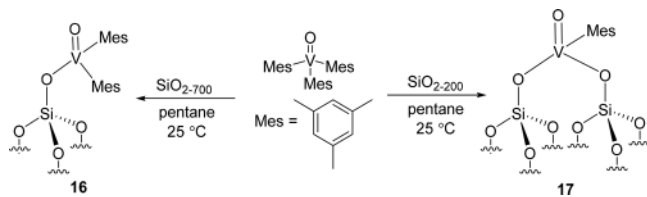
In 2015, Hu et al. reported the generation of isolated  $\text{Co}^{2+}$  sites on silica by electrostatic absorption of cobalt ions in water. The resulting material, when used for PDH at 550 °C, led to formation of propylene with 95% selectivity with no coke formation and improvement of performance after 20 h on stream.<sup>303</sup> Inspired by these results, Estes et al. prepared isolated cobalt sites on silica surface by the SOMC approach by grafting dimeric  $\text{Co}_2(-\text{OSi}(\text{OtBu})_3)_4$  on  $\text{SiO}_2\text{-700}$ .<sup>52</sup> The grafting reaction resulted in dimer dissociation and formation of isolated  $\text{Co}^{2+}$  complexes (14) whose ligands were removed by thermolysis under vacuum at 500 °C to afford 15 (Scheme 24).



The monomeric nature of the cobalt center was demonstrated via CO absorption experiments, UV–vis, and especially, EXAFS, that showed the absence of Co–Co contributions. The isolated  $\text{Co}^{2+}$  ions on silica were studied for the dehydrogenation of propane at 550 °C, obtaining slightly different results and trends than the above-mentioned work by Hu et al.<sup>303</sup> The initial conversion of propane was 10% (TOF for propylene 12.6  $\text{h}^{-1}$ ) and dropped to 5% (TOF for propylene 5  $\text{h}^{-1}$ ) within 10 h on stream. Methane and ethylene were formed as by-products as effect of propane cracking. No improvement of conversion was observed during the time on stream. Additionally, excess  $\text{H}_2$  evolved as an effect of coking. Interestingly, coking decreased after the initial 60–90 min and became negligible. Thus, selectivity rose from 8:1:2  $\text{C}_3\text{H}_6/\text{C}_2\text{H}_4/\text{coke}$  to 12.3:1  $\text{C}_3\text{H}_6/\text{C}_2\text{H}_4$  after 1.5 h. The selectivity eventually decreased reaching a stable ratio (8.3:1  $\text{C}_3\text{H}_6/\text{C}_2\text{H}_4$ ) after 10 h on stream. On the basis of a comparison with the work of Hu et al.,<sup>303</sup> the authors claimed an increase of catalytic activity of an order of magnitude for the SOMC-prepared catalyst, which is attributable to higher amounts of active sites. The drop of activity of the catalyst after 10 h on stream was attributed to the progressive formation of relatively large cobalt nanoparticles (up to 45 nm) as found on the spent catalyst. As in the previously discussed cases, the authors proposed C–H bond activation via heterolytic splitting by the Co–O bond with formation of a Co-alkyl and  $\equiv\text{Si}-\text{OH}$  as key mechanistic step for dehydrogenation; however, DFT calculations were not provided.

Supported vanadium oxide is an established catalyst for propane dehydrogenation (PDH)<sup>292,304–306</sup> and oxidative propane dehydrogenation (OPDH). Szeto et al. reported the first preparation of a vanadium oxo catalysts for PDH via SOMC by reacting  $[\text{V}(\text{=O})(\text{Mes})_3]$  (Mes, mesityl = 2,4,6-trimethylphenyl) with  $\text{SiO}_{2-700}$  and  $\text{SiO}_{2-200}$ , leading to complexes **16** and **17**, respectively (Scheme 25).<sup>49</sup> Elemental

**Scheme 25.** Preparation of Monopodal (**16**) and Bipodal (**17**) Vanadium Oxo Catalysts by Reaction of  $\text{SiO}_{2-700}$  and  $\text{SiO}_{2-200}$  with  $[\text{V}(\text{=O})(\text{Mes})_3]$

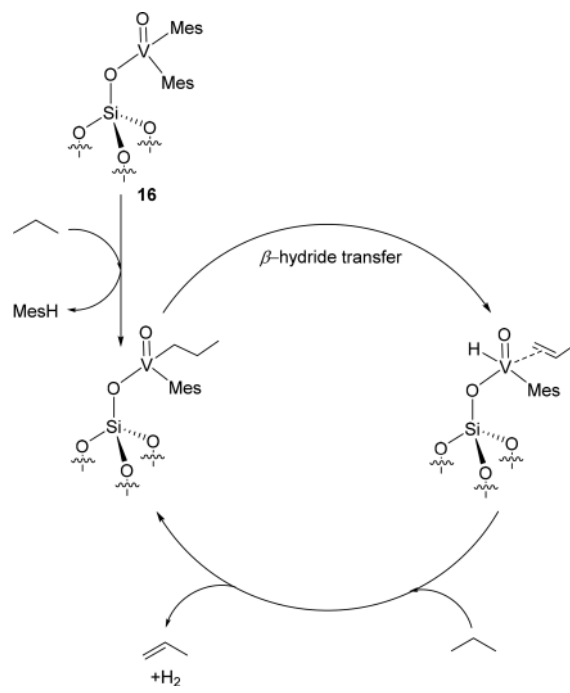


analysis and EXAFS spectroscopy showed that the compound grafted on  $\text{SiO}_{2-700}$  corresponded to an isolated, monopodal  $\text{V}=\text{O}$  complex with two mesityl ligands and a  $\sigma$ -bond with the surface. The complex grafted on  $\text{SiO}_{2-200}$  led, as expected, to a bipodal complex with the loss of an additional mesitylene ligand (Scheme 25).

Differently from the previously discussed examples, the authors did not attempt to remove the organic ligands by thermolysis prior to application in catalysis. Both complexes were tested for the dehydrogenation of propane at 500 °C. The bipodal species led to a slightly better performance than the monopodal; indeed, whereas both complexes initially provided 17% propane conversion, this declined to 12% after 1 week on stream for the bipodal catalyst and to 9% for the monopodal. This was attributed by the authors to the fact that the bipodal

species is less prone to form polymeric vanadia on the support surface compared to the monopodal. Also, the selectivity was slightly better for the bipodal catalyst (90% versus 83%), the byproducts being ethylene and methane. Compared to the above-discussed catalysts in this review, the ability of these vanadium oxo species to function after 1 week on stream is remarkable. In addition, the SOMC-based catalysts **16** and **17** were more active and selective than the  $\text{V}_2\text{O}_5/\text{SiO}_2$  system by Takahara et al. prepared by aqueous impregnation.<sup>307</sup> This effect was attributed to the presence of domains of inactive oligomeric vanadia in the latter catalyst. Concerning the mechanism of the process, the authors proposed a mechanism where mesitylene is released from the complex after reaction with propane (likely via  $\sigma$ -bond metathesis) and formation of V-propyl that could yield propylene via  $\beta$ -hydride transfer to vanadium (Scheme 26).<sup>308</sup> This mechanism postulates that the

**Scheme 26.** Possible Mechanism of PDH Catalyzed by **16**



mesityl groups are preserved at the V center at 500 °C. Alternatively, the authors proposed the involvement of the V–O and  $\text{V}=\text{O}$  moieties of the complex and of vanadium in the  $\text{V}^{+4}$  ( $\text{V}-\text{OH}$ ) and  $\text{V}^{+3}$  oxidation states.<sup>304,306,309</sup>

**4.3.1.2. Oxidative Dehydrogenation of Propane.** The most debated mechanistic aspects of propane oxidative dehydrogenation (PODH) by supported vanadium oxide are the role of the different surface functionalities ( $\text{V}=\text{O}$ ,  $\text{V}-\text{O}-\text{V}$ , and  $\text{V}-\text{O}$  support bonds) in the first activation of propane and their influence on selectivity,<sup>310–312</sup> the role of the support,<sup>313</sup> and the importance of vanadium isolation<sup>37,314,315</sup> with respect to systems where dimeric,<sup>311,316</sup> polymeric, or bidimensional<sup>317,318</sup> vanadia domains are present.<sup>319</sup> Barman et al. explored the grafting of dimeric complex **18** on  $\text{SiO}_{2-700}$  by SOMC with the aim of preparing well-defined and isolated silica-supported dimeric or monomeric vanadyl moieties and to investigate their activity and selectivity in ODHP.<sup>37</sup> With the evidence brought by elemental analysis and spectroscopic techniques including EXAFS, the authors were able to show that mostly monomeric complexes (**19**) were formed on the support, likely

Scheme 27. Synthesis of Isolated  $\text{VO}_4$  Moieties on Silica (20) by Grafting of Dimeric Complex 18 Followed by Oxidative Thermal Treatment

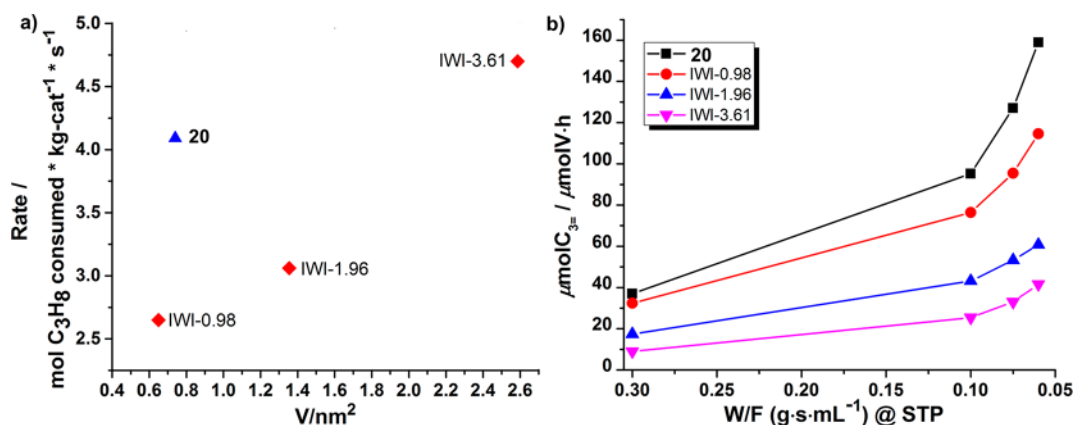
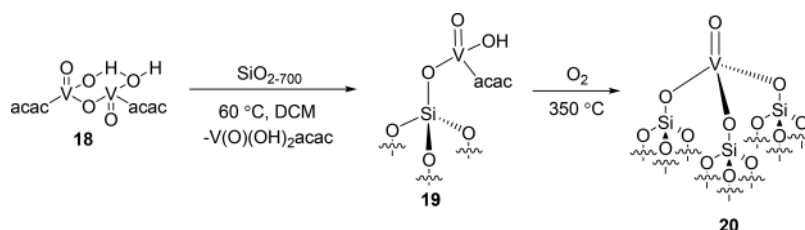
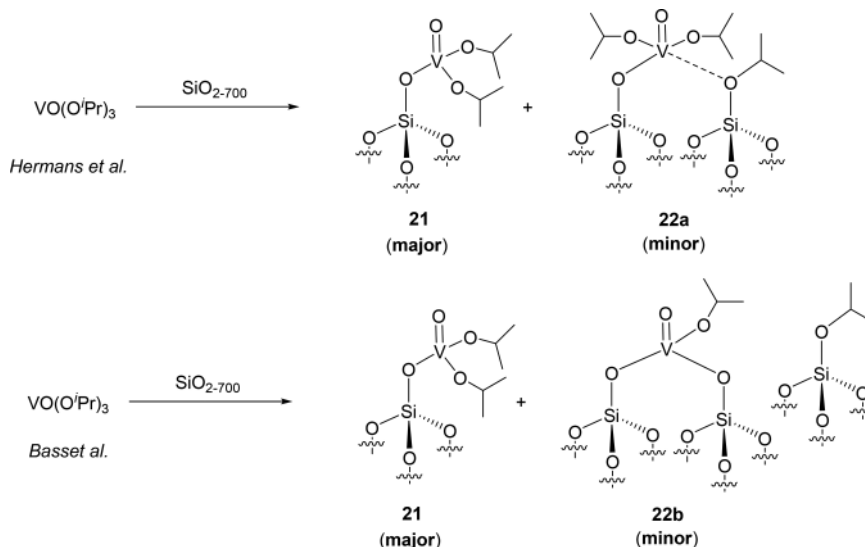


Figure 39. (a) Rate of propane consumption plotted as a function of the vanadium surface coverage (reaction conditions:  $t = 525^\circ\text{C}$ ;  $W/F = 0.3 \text{ g} \cdot \text{s} \cdot \text{mL}^{-1}$ ;  $W$ , weight of catalyst in grams;  $F$ , total flow in  $\text{mL} \cdot \text{s}^{-1}$ ). (b) Productivity of propylene as a function of contact time for 20 and for the IWI-catalysts (reaction conditions:  $t = 525^\circ\text{C}$ ;  $\text{C}_3\text{H}_8:\text{O}_2:\text{N}_2:\text{He} = 15:7.5:15:62.5$ ;  $F = 10\text{--}50 \text{ mL} \cdot \text{min}^{-1}$ ). Adapted with permission from ref 37. Copyright 2016 American Chemical Society.

Scheme 28. Grafting of  $\text{V}(=\text{O})(-\text{O}^i\text{Pr})_3$  on  $\text{SiO}_{2-700}$  According to Hermans et al. (Top)<sup>34</sup> and to Basset et al. (Bottom)<sup>291</sup>



by dissociation of the dimeric precursor (Scheme 27) as in the case of complex 14. The grafted complexes displayed  $\text{VO-H}$  and  $\text{acac}$  ( $\text{acac}$ : acetylacetonate) groups. These were transformed into isolated, tetrahedral  $\text{VO}_4$  complexes (20) upon thermal treatment with pure  $\text{O}_2$ . The vanadium loading in 20 was about 1 wt %.

The thus prepared catalyst was tested for the ODHP at  $525^\circ\text{C}$  and compared with catalysts prepared by the traditional incipient wetness impregnation (IWI) methodology (these are indicated below as IWI-X, where X is the weight percent of vanadium in the material). The latter are likely to display

mixtures of isolated  $\text{VO}_4$  sites and polymeric bidimensional vanadia domains.<sup>320–322</sup> Under the applied reaction conditions, 20 performed as the most active catalyst with a conversion of propane comparable to that of IWI-3.61% (containing nearly four times the weight of vanadium as for 20, Figure 39a) and a productivity of propylene that was considerably higher than the materials prepared by IWI, irrespective of their catalytic loading (Figure 39b). 20 provided 66% selectivity for propylene at 12% propane conversion that is comparable or higher than that displayed by the impregnation catalysts at similar propane conversion. Overall,

this study shows that SOMC can be applied for the preparation of isolated  $\text{V}=\text{O}$  functionalities that are more catalytically active than those existing in poorly defined impregnation catalysts. While several studies on catalysts prepared by impregnation methodology report a lack of correlation between catalytic activity and coverage,<sup>317</sup> it is expected that compounds prepared by impregnation contain fractions of nonisolated, polymeric vanadia domains even at low vanadium loading,<sup>320,321,323,324</sup> possibly leading to the observed difference in activity between the isolated  $\text{VO}_4$  moieties of **20** and the IWI catalysts.

In a different work, Herman's et al. grafted  $\text{V}(\text{=O})(-\text{O}^i\text{Pr})_3$  on the surface of  $\text{SiO}_{2-700}$  by the SOMC methodology and observed the formation of two different kinds of complexes, the expected monopodal  $[(\equiv\text{Si}-\text{O}-)\text{V}(\text{=O})(-\text{O}^i\text{Pr})_2]$  (**21**, Scheme 28) species as a major product and a minor species attributed by the authors to the reaction of  $\text{V}(\text{=O})(\text{O}^i\text{Pr})_3$  with a strained siloxane bridge of the surface, resulting in the transfer of isopropoxide to the support (**22a**, Scheme 28).<sup>34</sup> In a comparable study, Basset et al. also identified two complexes on the surface; however, they attributed the formation of the minor component to the reaction of **21** with a siloxane bridge resulting in a bipodal species (**22b**, Scheme 28).<sup>291</sup> Hermans et al. investigated the thermal restructuring of **21** at 600 °C observing the simultaneous release of propylene and the formation of  $\text{V}-\text{OH}$  moieties based on the appearance of a signal at  $3656\text{ cm}^{-1}$  in the in situ IR spectrum of the sample. On the basis of these data, they proposed a mechanism for the thermal restructuring of  $[(\equiv\text{Si}-\text{O}-)\text{V}(\text{=O})(\text{O}^i\text{Pr})_2]$  in which the vanadyl moiety abstracts a proton from the adjacent methyl group via a six-membered transition state. Consequently, a  $\text{V}-\text{OH}$  moiety is formed and propylene is released.

The supported vanadium complex eventually evolved into isolated tetrahedral  $\text{VO}_4$  moieties analogous to **20** (Scheme 27) that were applied as catalysts for ODHP at 490 °C. Under such reaction conditions, the authors reported about 65% selectivity at 6% propylene conversion. Interestingly, there was no difference of activity between the isolated  $\text{VO}_4$  moieties and an impregnation catalyst prepared with comparable loading. The authors concluded that grafting and impregnation lead to similar catalysts and active sites which is at variance with what was observed by Barman et al. using isolated  $\text{VO}_4$  complexes (**20**) versus impregnation catalysts as discussed above.

**4.3.1.3. Other Dehydrogenations by SOMC.** Whereas the concept of single atom alloy catalysis has slowly emerged in recent years, a number of studies have been at the origin of this concept and have anticipated the idea of isolated active metal atoms at the surface of a nanoparticle of a more inert metal. Probably, the most striking results were obtained by means of surface organometallic chemistry on metals (SOMC/Metal).<sup>330</sup> According to this strategy, organometallic compounds react with supported metal nanoparticles more selectively than with the support itself, at least when the temperature is kept as low as possible and hydrogen is present. This concept has been exploited to enhance selectivity in the dehydrogenation of isobutane to isobutene.<sup>331</sup> In the initial development of the catalyst, the selective hydrogenolysis of  $\text{Sn}(n\text{-C}_4\text{H}_9)_4$  on silica-supported platinum nanoparticles at 50 °C was found to lead to  $\text{Pt}_s[\equiv\text{Sn}(n\text{-C}_4\text{H}_9)_3]$  ( $\text{Pt}_s$ : surface Pt atom). The amount of  $\text{Sn}(n\text{-C}_4\text{H}_9)_4$  which reacted with the platinum surface led to a  $\text{Sn}/\text{Pt}_s$  ratio  $<1$ , even when excess  $\text{Sn}(n\text{-C}_4\text{H}_9)_4$  compared to  $\text{Pt}_s$  was introduced.  $\text{Pt}_s[\equiv\text{Sn}(n\text{-C}_4\text{H}_9)_3]$

could be completely dealkylated by hydrogenolysis at 300 °C. At 550 °C, the tin atoms were incorporated in the surface of platinum nanoparticles.<sup>332</sup> Consequently, Pt atoms were progressively surrounded by catalytically inactive tin atoms until reaching the situation where they were completely isolated as single atoms of platinum. Indeed, the bimetallic material obtained adsorbed less hydrogen than the starting monometallic catalyst. On the basis of  $\text{H}_2$  and  $\text{O}_2$  chemisorption experiments, it was found that for  $\text{Sn}/\text{Pt}$  molar ratio of 0.31 ( $\text{Pt}/\text{Sn}_{0.31}$ ),  $\text{Sn}/\text{Pt}_s = 0.85$ . Accordingly, when catalysts prepared by using different  $\text{Sn}/\text{Pt}_s$  ratios were applied for the dehydrogenation of isobutane, the selectivity for isobutene increased drastically with the  $\text{Sn}/\text{Pt}$  ratio to reach 99% for  $\text{Pt}/\text{Sn}_{0.31}$  (Figure 40).<sup>331</sup> This effect can be explained

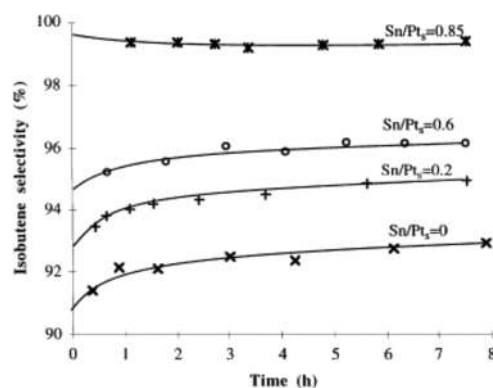


**Figure 40.** Effect of  $\text{Sn}/\text{Pt}_s$  ratio on the selectivity of isobutane dehydrogenation with  $\text{Pt}_s\text{Sn}_x$  catalysts supported on silica. Reproduced with permission from ref 331. Copyright 1998 Elsevier.

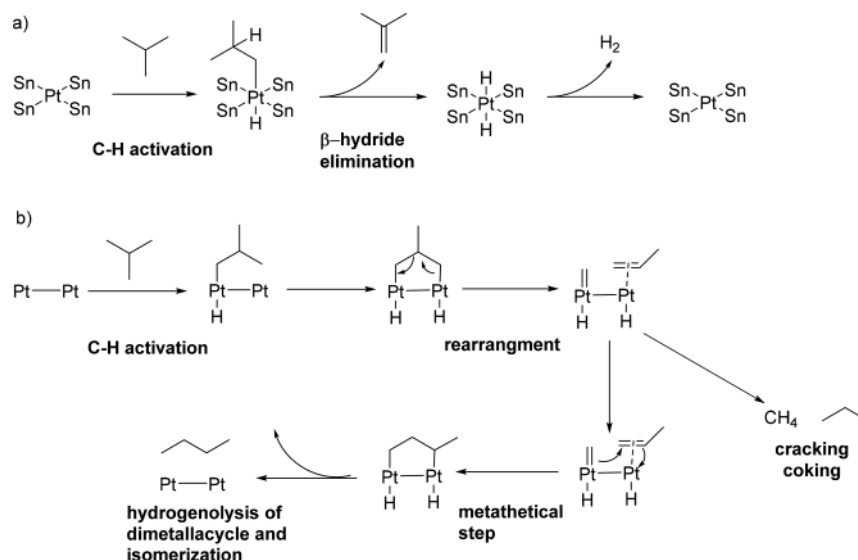
knowing that the formation of coke requires ensembles of platinum atoms, whereas dehydrogenation can occur on a single atom by formation of a Pt-isobutyl surface fragment ( $\text{C}-\text{H}$  activation) followed by a selective  $\beta\text{-H}$  elimination process with formation of isobutene.

Therefore, platinum site isolation can enhance selectivity and suppress coke formation (Scheme 29). This mechanism is purely derived from the mechanism of olefin homologations on various silica supported metals (Ru, Fe, Ni, Rh) and is an alternative to the classical insertion mechanism in Fischer-Tropsch synthesis where olefins are primary products.<sup>333,334</sup>

**4.3.2. Via SAC.** Inspired by the ability of  $\text{CeO}_2$  to trap ionic platinum by a “kind” of strong metal-support interactions, Xiong et al.<sup>325</sup> prepared atomically dispersed platinum on  $\text{CeO}_2$  using a previously developed concept.<sup>326</sup> Accordingly, platinum particles, formed on ceria by incipient wetness impregnation, were dispersed at the atomic level on the support by treatment at high temperature (800 °C) in flowing air. The thus prepared catalyst was tested for the dehydrogenation of propane at 680 °C. While complete conversion of propane was observed, no propylene was formed, showing that the material was not selective for alkane dehydrogenation. The exclusive formation of methane and  $\text{CO}_2$  suggests that the catalyst is active in  $\text{C}-\text{C}$  bond cleavage (cracking of propane). This result was justified by computational analysis showing that, although dehydrogenation of propane is facile, strong absorption of propylene on Pt via  $\sigma$ -bonds leads to side reactions with  $\text{C}-\text{C}$  bond cleavage. As Pt-Sn alloys are well-known dehydrogenation catalysts,<sup>327,328</sup> the authors added tin to the material to improve selectivity. The impregnation of tin



Scheme 29. (a) Mechanism of Selective Dehydrogenation of Isobutane on Isolated Platinum Atoms Surrounded by Tin Atoms; (b) Mechanism of Skeletal Isomerization and Coking by Non-Isolated Platinum Atoms<sup>331</sup>



and platinum in a 5:1 molar ratio, followed by the redispersion treatment under air at 800 °C, led to a less well-defined catalyst constituted by Pt–Sn subnanometric clusters containing more platinum than tin (Pt:Sn = 3:1) and regions of atomically dispersed metal atoms with large predominance of tin (as SnO<sub>2</sub>). When the latter catalyst was tested for propane dehydrogenation at 680 °C, it performed well, affording about 45% conversion and 78% selectivity in the initial 2 h of reaction. Whereas the activity subsequently dropped to 40%, the selectivity toward propylene increased to 85%. The catalytic results, along with TEM, XPS, and EDS investigation are consistent with the migration of platinum and tin from the atomically dispersed form to yield small (1.1 nm) metallic Pt–Sn clusters (PtSn<sub>3</sub>) that were less active in converting propane but much more selective. This was confirmed by DFT calculations showing that propylene is less strongly absorbed on the PtSn<sub>3</sub> clusters but the dehydrogenation barrier increases. The catalytic performance was stable for 6 h as the authors prevented formation of coke by adding water vapor to the stream. After treatment with O<sub>2</sub> at high temperature, the regenerated catalyst was shown to perform as the pristine material (including the trend of higher conversion and lower selectivity in the initial 2 h) for two more cycles, suggesting restoration of the initial state by oxidation of PtSn<sub>3</sub> nanoparticles after 2 h on stream (Figure 41) as observed by STEM investigation. The authors gave this process the audacious term of “self-assembly”.

Compared to the commercial catalyst on Al<sub>2</sub>O<sub>3</sub> support that is not regenerated under oxidizing conditions and led to the formation of much larger clusters (8 nm) during catalysis, the use of ceria as support allowed the atomic redispersion of Pt upon treatment with O<sub>2</sub>, the use of water to avoid coke deposition and inhibited the formation of large clusters under applied reaction conditions because of the ability of ceria to trap Pt atoms.<sup>326</sup>

On the basis of the lack of selectivity of ionic platinum atoms toward propane dehydrogenation as shown in the former example, Sun et al. investigated the activity of isolated metallic platinum atoms “dispersed” in copper nanoparticles.<sup>329</sup> The authors showed by DFT calculations that when

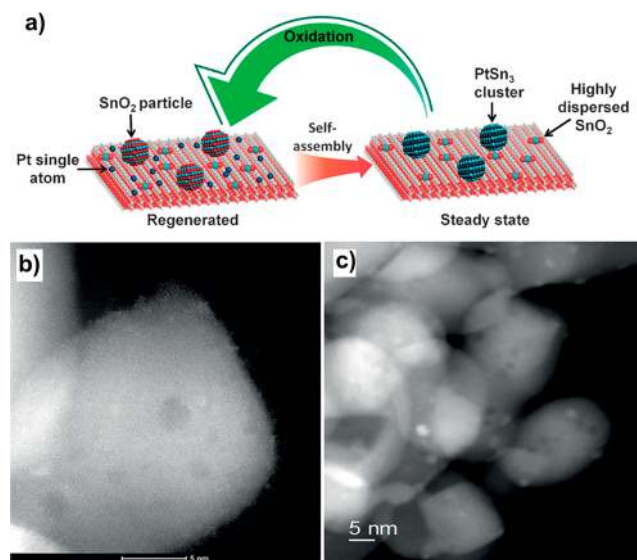


Figure 41. (a) Representation of the process of assembly of the PtSn<sub>3</sub> nanoparticles during PDH at 680 °C and of the regeneration of the catalyst to the initial state by treatment with O<sub>2</sub> at 580 °C. (b) STEM image of the catalyst after regeneration. (c) STEM image of spent catalyst after PDH. Adapted with permission from ref 325. Copyright 2017 John Wiley and Sons.

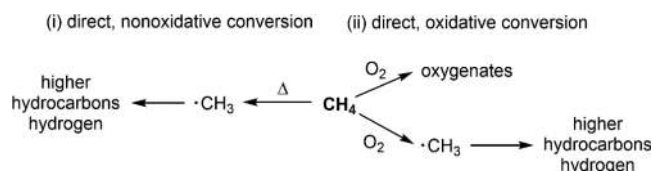
the platinum atoms are embedded in inert copper, the barrier for propane dehydrogenation remains reasonable (increase of 0.4 eV compared to pure platinum), whereas the deep dehydrogenation of propylene becomes strongly endothermic with higher barrier (>2 eV) compared to the accessible barrier (<1 eV) calculated for Pt(111). This observation suggested the possibility of achieving higher selectivity and reasonable activity by preparing single Pt atoms dispersed in copper. Therefore, the authors proposed that such catalyst could break the scalar relationship according to which increased selectivity to propylene is always paralleled by lower intrinsic activity for propane dehydrogenation. The authors verified their computational results by preparing Pt single atoms–copper nanoparticles by coimpregnation of platinum and copper salts on γ-

alumina followed by calcination and reduction with  $\text{H}_2$ . Superficial Pt–Cu alloys were formed with the platinum atoms exposed on the surface of the copper NPs. The monatomic nature of Pt was demonstrated by CO adsorption experiments; the single Pt atoms showing a characteristic IR at band  $2018\text{ cm}^{-1}$  due to linear CO adsorption on single Pt atoms for Pt/Cu ratios equal to or lower than 0.1:6.7. This was confirmed by AC-HAADF-STEM, EXAFS, and preliminary propane dehydrogenation experiments, showing that the performance of the catalyst improved up to a Pt/Cu ratio of 0.1:6.7 and remained constant for higher dilution of platinum. In particular, the catalyst with Pt/Cu ratio of 0.1:10 displayed 90% selectivity for propylene at 13.1% conversion and only a marginal loss of activity after 120 h on stream. In comparison, the poorly dispersed 0.1 Pt/ $\text{Al}_2\text{O}_3$  displayed 70% propylene selectivity at 5.8% propane conversion and a much higher rate of deactivation.

#### 4.4. Methane Activation

Methane can be converted into higher valuable and easier transportable products as olefins, aromatics, and methanol through oxidative and nonoxidative strategies. The indirect conversion of methane into hydrocarbons, alcohols, light olefins, or gasoline<sup>335</sup> can be accomplished by commercial processes, e.g., syngas combined with Fischer–Tropsch.<sup>336,337</sup> Alternatively, methane can be converted through direct routes without involving the intermediate syngas production step, which is more economical and environmentally friendly. Scheme 30 summarizes strategies to directly convert methane.

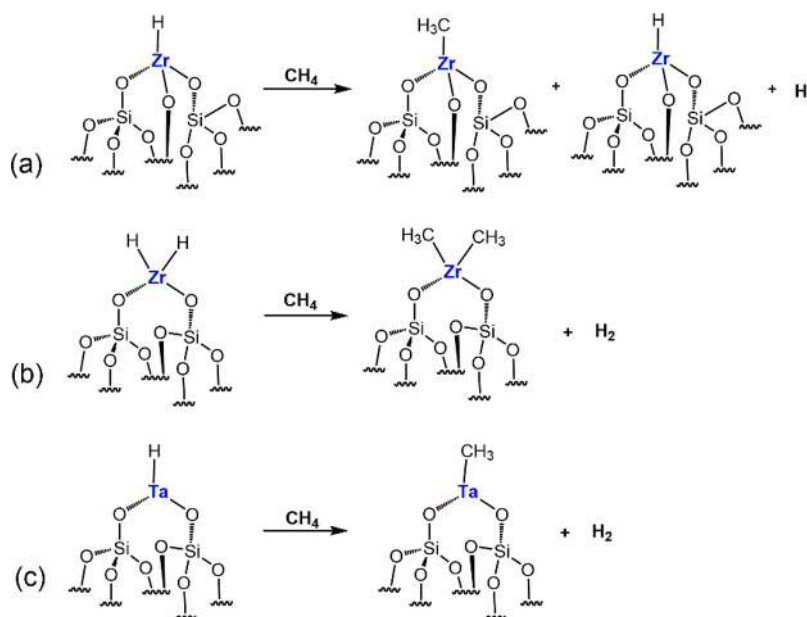
**Scheme 30. Pathways for Direct Methane Conversions**



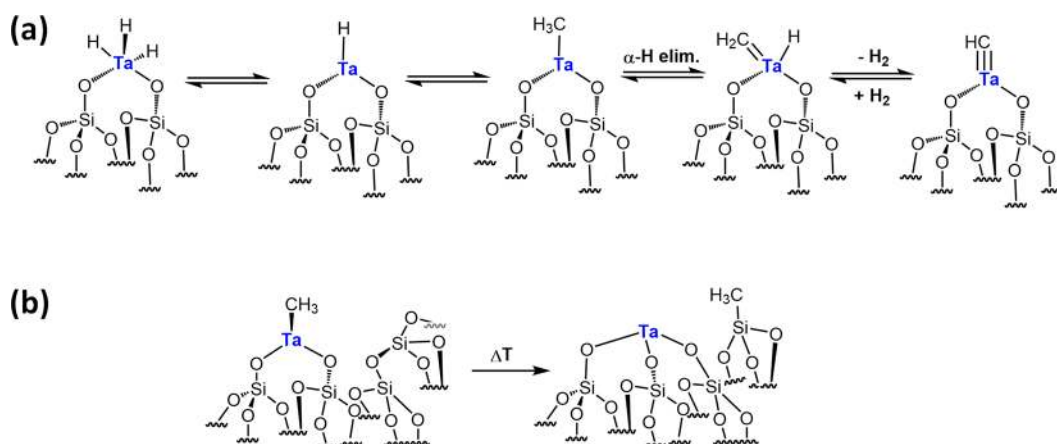
(i) In the direct, oxidative route,<sup>338,339</sup> ethane, ethylene, or oxygenates can be produced.<sup>340</sup> In comparison to direct, nonoxidative coupling of methane, the production of hydrocarbons is thermodynamically favorable;<sup>341</sup> however, products are readily oxidized to form CO and  $\text{CO}_2$  and  $\text{H}_2\text{O}$ . Oxidative coupling of methane cannot yield more than 30% ethylene,<sup>342</sup> and the selectivity decreases dramatically at high conversion of methane. (ii) In the direct, nonoxidative routes,<sup>335,343–345</sup> light alkanes and alkenes, aromatics, coke, and the respective amount of hydrogen can be produced. The thermodynamics toward light hydrocarbons, olefins, and aromatics are less favorable compared to the oxidative route, but neither CO nor  $\text{CO}_2$  are produced. Another recent interesting route is to transform natural gas to hydrogen and carbon.<sup>346</sup> Yet, only a small fraction of methane is consumed by chemical industries, while the vast majority is burned for the production of energy.<sup>347</sup> The reason for the low conversion of methane for producing alternative feedstock is related to the high chemical and thermal inertness of the C–H bond (434 kJ/mol), the low electron affinity, and low polarizability.<sup>348</sup> Developing highly efficient catalysts capable of directly converting methane into transportable liquid chemicals presents an alternative to petroleum as chemical feedstock. Usually, methane conversion requires high temperatures (600–1100 °C)<sup>349–351</sup> which are not favorable for industrial applications. Scientists have been working on reducing the reaction temperature, and successful results were obtained by SOMC.<sup>344,345</sup> However, promoting the conversion of methane under mild conditions remains a challenge because of thermodynamic constraints.<sup>335</sup> Another challenge is the deactivation of catalysts due to coke formation (under nonoxidative conditions)<sup>352</sup> and/or  $\text{CO}_2$  generation (under oxidative conditions).

As in the previous parts of this review, we will consider separately the SAC-, SAAC-, and the SOMC methodology, trying to compare these two methods in terms of achievements and understanding with examples of methane conversion under nonoxidative (into alkanes, olefins, and aromatics) and oxidative conditions (into alkanes, oxygenates). While the

**Scheme 31. Stoichiometric Activation of Methane by Silica Supported Early Transition Metal Hydrides**<sup>357–359</sup>



Scheme 32. (a) Initiation Reaction in the Low Temperature Activation of Methane with a Silica Supported [Ta]-Hydride and (b) Deactivation Mechanism by Methyl Transfer<sup>344</sup>



catalytic performance of SACs is attributed to the atomic dispersion of metal atoms with low coordination number, quantum confinement, and/or strong metal–support (mostly metal oxides) interactions,<sup>15,353</sup> the performance of SOMCat is attributed to the presence of a well-defined metal hydrides with  $d^0$  configuration, which makes the catalytic pathway predictable by elementary steps of molecular chemistry.<sup>26</sup>

**4.4.1. Via SOMC.** **4.4.1.1. Concepts and Methods.** The power of SOMC is to design catalysts for certain reactions and to predict the reaction pathway by synthesis and characterization of intermediates. Typically, early transition metal complexes are used because the metal is in its highest oxidation state; it therefore has a  $d^0$  electron configuration and is consequently highly electrophilic.<sup>260</sup> The first example of intramolecular methane activation was observed in 1983 in molecular chemistry exchanging a methyl with a  $^{13}\text{C}$  labeled methane in a lutetium complex.<sup>354</sup> In 1991, it was discovered that zirconium hydride grafted onto the surface of silica  $[(\equiv\text{SiO})_3\text{ZrH}]$  acquires such high electrophilic properties enabling  $\sigma$ -bond metathesis between the  $[\text{Zr}]$ -hydride and the C–H bond of methane (Scheme 31).<sup>260,355</sup> Even better results were obtained with silica supported  $[\text{Zr}]$ -dihydride  $[(\equiv\text{SiO})_2\text{ZrH}_2]$ , which reacts quickly and completely with methane to yield  $[(\equiv\text{SiO})_2\text{ZrMe}_2]$  (Scheme 31).<sup>356,357</sup> The reaction of  $[(\equiv\text{SiO})_{(4-x)}\text{Zr}(\text{H})_x]$  ( $x = 1$  or  $2$ ) with methane was followed by solid state NMR ( $^1\text{H}$  MAS NMR), which showed a partial disappearance of the resonance of  $[(\equiv\text{SiO})_3\text{ZrH}]$  [ $\delta$  (ZrH) = 10 ppm], whereas that of  $[(\equiv\text{SiO})_2\text{ZrH}_2]$  [ $\delta$  (ZrH<sub>2</sub>) = 12 ppm] completely disappeared.<sup>357</sup> No other changes were observed as compared to the NMR spectra of starting material. The different reactivity of the methane incorporation by both zirconium hydrides was corroborated by in situ IR.

It was obvious to move on, to test silica supported  $[\text{Ta}]$ -H  $[(\equiv\text{SiO})_2\text{TaH}]$ <sup>358</sup> (and hydrogenated  $(\equiv\text{SiO})_2\text{Ta}(\text{H})_3$ )<sup>271</sup> for methane activation (Scheme 31).<sup>359</sup> This SOMC-catalyst is known to catalyze the total hydrogenolysis of light alkanes, including the hydrogenolysis of ethane<sup>261</sup> into methane. This is in contrast to the silica-supported zirconium hydrides which do not cleave ethane.<sup>359</sup> To convert methane into ethane (or higher hydrocarbons), the reversibility of ethane hydrogenolysis reaction with  $[\text{Ta}]$ -H was considered.<sup>359</sup>

**4.4.1.2. Nonoxidative Conversion of Methane (to Alkanes, Olefins, and Aromatics).** The high activity of SOMC-based

catalysts is explained by the high electron deficiency of silica supported (linked to two surface oxygen atoms)  $[\text{Ta}]$ -H and  $[\text{Ta}]$ -H<sub>3</sub> (8 and 10 electron systems, respectively), which are prone to undergo  $\sigma$ -bond metathesis.<sup>271,358</sup> The evidence for defining such a mechanism is favored by the well-defined and controllable character of such species obtained by SOMC.

For methane conversion to alkanes and olefins, two systems have been described. Both catalysts were described to be active in the hydrogenolysis of ethane to methane. The first example of nonoxidative coupling of methane to ethane and hydrogen via SOMC-based complexes was discovered in 2008,<sup>344</sup> using silica supported single-site  $[\text{Ta}]$ -H catalyst. Methane is converted over  $[\text{Ta}]$ -H in a continuous flow reactor (250–450 °C, 50 bar of  $\text{CH}_4$  pressure) to hydrogen and ethane (selectivity  $\geq 98\%$ ) with traces of other hydrocarbons (propane and ethylene) (TON = 40, 147 h, 475 °C, 50 bar). This silica-supported tantalum hydride,  $[(\equiv\text{SiO})_2\text{TaH}]$ , proves to be the first single-site catalyst for the direct nonoxidative coupling transformation of methane into ethane and hydrogen at moderate temperatures ( $T < 300$  °C), with a high selectivity ( $>98\%$ ). The reaction likely involves the  $[(\equiv\text{SiO})_2\text{TaH}(\text{CH}_2)]$  species as a key intermediate. All the products formed during the initiation (Scheme 32) have been identified by NMR and various spectroscopies. It is obtained by  $\sigma$ -bond metathesis between the C–H bond of methane and the Ta–H bond, followed by the  $\alpha$ -H elimination leading to  $[(\equiv\text{SiO})_2\text{TaH}(\text{CH}_2)]$ . A second molecule of methane reacts with the Ta–H bond to give  $[(\equiv\text{SiO})_2\text{Ta}(\text{Me})(\text{CH}_2)]$ . Then the methyl ligand can migrate onto the tantalum–methylidene, affording the tantalum–ethyl. Ethane is then liberated by reaction with hydrogen produced in the previous steps.

In 2010, it was found that  $[\text{W}]$ -H supported on silica–alumina or alumina coupled with a membrane could achieve better yield than  $[\text{Ta}]$ .<sup>345,360</sup> Because the coupling of methane to ethane and hydrogen is limited by thermodynamics at low temperature, it was necessary to shift the equilibrium by using a membrane reactor able to displace the hydrogen. A significant increase of the yield could thus be achieved.<sup>345</sup> Only ethane, traces of propane and hydrogen were observed, but no olefins.  $[\text{W}]$ -H catalysts are significantly more stable (up to 10 days with a constant conversion maintaining the high selectivities for ethane) than their  $[\text{Ta}]$ -H counterparts.



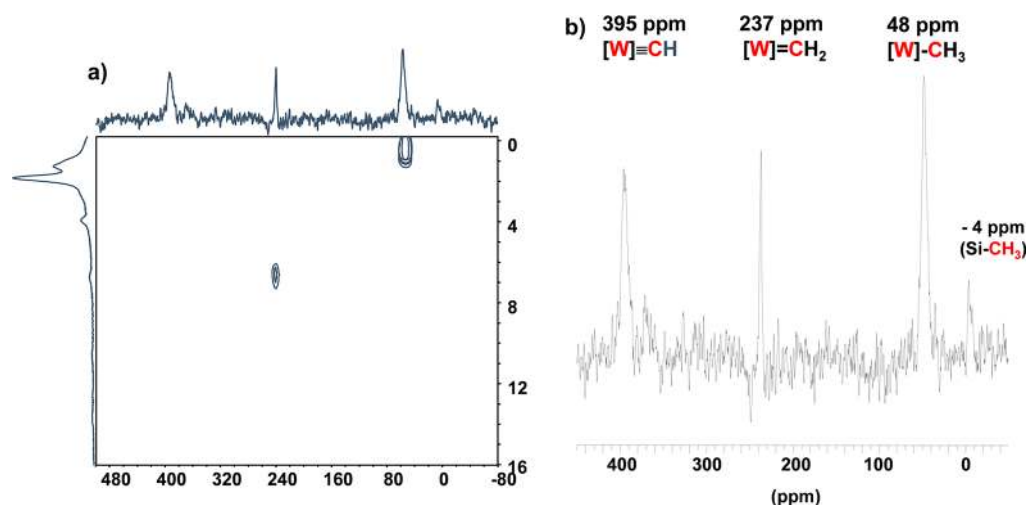
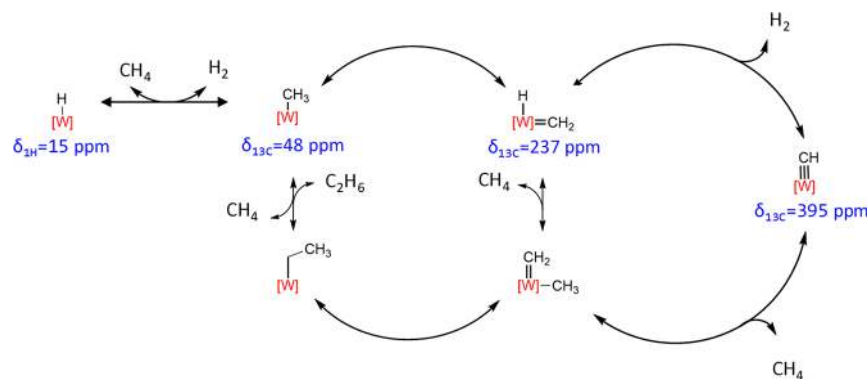


**Figure 42.** (a) HETCOR and (b)  $^{13}\text{C}$  CP-MAS and SS NMR spectra of  $[\text{W}]\text{-H}$  supported silica–alumina obtained after  $^{13}\text{CH}_4$  activation at  $150\text{ }^\circ\text{C}$  for 24 h. Reproduced with permission from ref 345. Copyright 2010 Royal Society of Chemistry.

**Scheme 33. Detailed Mechanism of Coupling of Methane to Ethane, Ethylene, and Hydrogen Using Single Site  $[\text{W}]\text{-H}$  Catalysts Including SS NMR Signals<sup>345</sup>**



To understand the reaction mechanism, reaction intermediates of  $[\text{Ta}]\text{-H}$  and  $[\text{W}]\text{-H}$  were characterized by spectroscopic methods (IR, SS NMR) after  $^{13}\text{CH}_4$  activation ( $150\text{ }^\circ\text{C}$  for 24 h). For both metals, IR studies show a strong decrease of the  $\nu(\text{M}-\text{H})$  bands after contacting the  $[\text{M}]\text{-H}$  with  $\text{CH}_4$ .  $^{13}\text{C}$  CP MAS NMR spectra showed four distinct resonances corresponding to  $\text{Si}-\text{CH}_3$ ,  $[\text{M}]-\text{CH}_3$ ,  $[\text{M}]=\text{CH}_2$ , and  $[\text{M}]\equiv\text{CH}$  for both systems (Figure 42).

Solid-state characterizations by  $^{13}\text{C}$  SS NMR suggest that  $[\text{Ta}]\text{-H}$  and  $[\text{W}]\text{-H}$  follow a similar reaction mechanism which includes  $[\text{M}]\text{-hydride}$ ,  $[\text{M}]-\text{CH}_3$ ,  $[\text{M}]=\text{CH}_2$ , and  $[\text{M}]\equiv\text{CH}$ . The proposed mechanism is shown in Scheme 33. The first activation step is  $\sigma$ -bond metathesis of methane with  $[\text{M}]\text{-H}$  forming  $[\text{M}]-\text{CH}_3$  and  $\text{H}_2$ .  $[\text{M}](=\text{CH}_2)(\text{H})$  is then generated by  $\alpha$ -H transfer.  $[\text{M}]\equiv\text{CH}$  is formed by further  $\alpha$ -H abstraction followed by evolution of  $\text{H}_2$ . Another methane molecule reacts with the carbyne to form  $[\text{M}](=\text{CH}_2)(\text{CH}_3)$ . Alternatively,  $[\text{M}](=\text{CH}_2)(\text{CH}_3)$  can be also formed by methane activation with  $[\text{M}](=\text{CH}_2)\text{H}$ . Insertion of the methylidene into the  $[\text{M}]\text{-methyl}$  bond leads to the formation of  $[\text{M}](\text{-CH}_2\text{-CH}_3)$ . Eventually, ethane is then released by  $\sigma$ -bond metathesis with another molecule of methane. For  $[\text{Ta}]\text{-H}$ ,  $\beta$ -H elimination also occurs (viii), followed by the release of ethylene and  $[\text{Ta}]\text{-H}$  (ix).

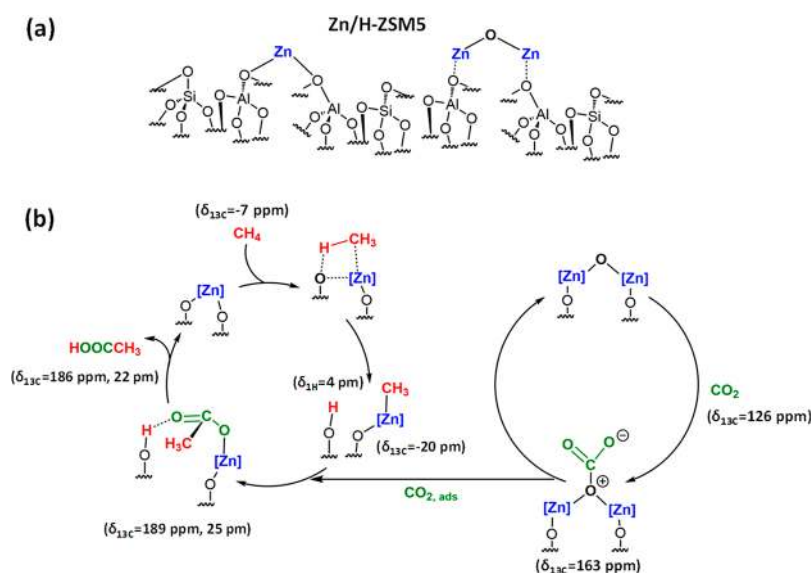
The aging of the catalyst is observed by the appearance of a  $\text{Si}-\text{Me}$  which is observed at  $-10\text{ ppm}$ . The catalyst is

deactivated by a reaction of one methyl of  $[\text{M}]-\text{CH}_3$  to the adjacent silicon by opening a  $\text{Si}-\text{O}-\text{Si}$  bond. Hence, the catalyst is unable to form the active site, a methylidene and a hydride  $[\text{M}](=\text{CH}_2)(\text{H})$ .<sup>345</sup>

**4.4.1.3. Oxidative Conversion of Methane (to Oxygenates).** Surface organometallic systems active for the conversion of methane into oxygenates<sup>361</sup> were inspired by the homogeneous Periana system  $\text{Pd}/\text{H}_2\text{SO}_4$ ,<sup>362,363</sup> which is the most efficient system to date for the direct conversion of methane to oxygenates under mild conditions. However, the environmental concerns and the utilization of precious metals set drawbacks for its potential use. Considering the role of the acidic part of the catalytic Periana system, the potential of solid acids in the methane to acetic acid transformation was evaluated.

In 2013, SOMC-based catalysts were prepared by chemisorption of four different dehydrated Keggin-type heteropolyacids ( $\text{H}_4\text{SiW}_{12}\text{O}_{40}$ ,  $\text{H}_3\text{PW}_{12}\text{O}_{40}$ ,  $\text{H}_4\text{SiMo}_{12}\text{O}_{40}$ ,  $\text{H}_3\text{PMo}_{12}\text{O}_{40}$ ) on partially dehydroxylated silica  $\text{SiO}_{2-500}$ .<sup>364</sup> The prepared system reacts with methane to produce a stoichiometric amount of acetic acid at room temperature and atmospheric pressure. Heteropolyacids can be easily modified by the inclusion of metals (for instance, in the addenda or as counter cations) with a significant effect on their reactivity. For example, zinc incorporated materials have been shown to be active for the transformation of light alkanes.<sup>364–368</sup> Zn

Scheme 34. (a) Proposed Structure for Zn/H-ZSM5 and (b) Proposed for the Co-conversion of CH<sub>4</sub> and CO<sub>2</sub> over Zn/H-ZSM5 to Acetic Acid Including SS NMR Signals<sup>369</sup>

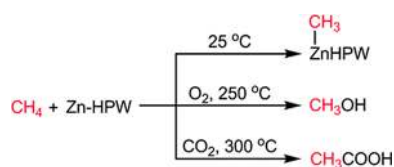


accelerates the heterolytic dissociation of the CH-bond of CH<sub>4</sub> by reacting with Zn<sup>2+</sup>O<sup>2-</sup>.<sup>369</sup> Zinc-modified zeolites (ZSM5, BEA) activate methane under mild conditions at a temperature range of 523–773 K.<sup>370–378</sup> For methane conversion with CO<sub>2</sub> on a bifunctional zeolite or zinc-modified HZSM-5 zeolite at the relatively low temperature range of 523–773 K, the formation of acetic acid was observed by SS NMR.<sup>22,369,377</sup> The coconversion mechanism of CH<sub>4</sub> and CO<sub>2</sub> on Zn/H-ZSM5 includes three key steps (Scheme 34): (i) the simultaneous formation of zinc methyl species and Brønsted proton via methane activation, (ii) the insertion of CO<sub>2</sub> into the Zn–C bond of surface zinc methyl species to produce surface acetate species (–Zn–OOCCH<sub>3</sub>) as a key intermediate, and (iii) the final formation of acetic acid via the proton abstraction from Brønsted acid sites to surface acetate species.

In 2014, a Zn-exchanged heteropolyacid<sup>361</sup> was synthesized via ion exchange from the parent phosphotungstic acid (HPW) in water. The product was characterized by tools of SOMC as FTIR and SSNMR and tools of heterogeneous catalysis, as TGA-DSC, isopropylamine-TPD, XRD-diffraction, and elemental analysis. Three different experiments were performed with Zn-HPW-SiO<sub>2</sub>: (i) CH<sub>4</sub> (25 °C), with (ii) CH<sub>4</sub> and O<sub>2</sub> (250 °C), and with (iii) CH<sub>4</sub> and CO<sub>2</sub> (300 °C), proving a high activity and selectivity as proved by SS NMR.<sup>361</sup>

At room temperature, Zn-HPW-SiO<sub>2</sub> activates CH<sub>4</sub> which is confirmed by the appearance of a <sup>13</sup>C CP MAS NMR signal at –23 ppm, showing that [Zn]–CH<sub>3</sub> was formed (Scheme 35).

Scheme 35. Illustration of Methane of Conversion on Zn-Modified Heteropolyacid<sup>a</sup>



<sup>a</sup>Reproduced with permission from ref 361. Copyright 2014 Royal Society of Chemistry.

In the presence of O<sub>2</sub> and at 250 °C, Zn-HPW-SiO<sub>2</sub> converts CH<sub>4</sub> into CH<sub>3</sub>OH. The <sup>13</sup>C CP MAS NMR spectrum shows a signal at 49 ppm, which represents the condensation of gas phase methanol on the silica surface. This demonstrates that methane is oxidized to methanol. In the presence of CO<sub>2</sub> and at 300 °C, n-HPW-SiO<sub>2</sub> converts CH<sub>4</sub> into acetic acid (CH<sub>3</sub>COOH) in the presence of CO<sub>2</sub> at 300 °C. A signal at 20 ppm (–CH<sub>3</sub>) and 180 ppm (–COOH) was observed by <sup>13</sup>C CP MAS NMR, which confirms the formation of acetic acid. These results confirm that Zn-HPW/SiO<sub>2</sub> can activate methane for stoichiometric conversion to methanol (with O<sub>2</sub>) and acetic acid (with CO<sub>2</sub>). Remarkably, the activation of methane is achieved already at room temperature as evidenced by the first-time detection of Zn–CH<sub>3</sub> on a Zn modified heteropolyacid.

**4.4.2. Via SAC.** **4.4.2.1. Concepts and Methods.** It has been reported that C–H bond activation can proceed over an isolated transition-metal center, yielding M–CH<sub>3</sub> species.<sup>379</sup> For example, platinum has been widely used to activate the C–H bond in hydrocarbons<sup>293,380,381</sup> as well as for methane,<sup>382</sup> absorbing CH<sub>4</sub> on Pt(111) at mostly C<sub>3v</sub> symmetry.<sup>383</sup> However, due to the high tendency of Pt to bind CH<sub>x</sub> intermediates, coke can be formed easily, typically at high temperatures (>800 °C).<sup>384,385</sup> By tuning the electronic structure of Pt, e.g., by incorporating, doping and/or alloying surfaces as Al<sub>2</sub>O<sub>3</sub>,<sup>386</sup> TiO<sub>2</sub>,<sup>387</sup> CeO<sub>2</sub>,<sup>388</sup> and Cu,<sup>389</sup> a catalyst with a superior catalytic performance and a reduced coke formation can be observed. Besides Pt, also other late transition metal SACs (e.g., Pd,<sup>390</sup> Rh<sup>391–393</sup>) are known to have a high activity and selectivity for methane activation. Fung et al. proposed theoretical investigations for screening the efficiency of SACs for methane activation showing that the methane absorption energy (*E*<sub>Ads</sub>) is an expressive descriptor. Experiments showed that besides Pt (supported on TiO<sub>2</sub>), successful results were also found for SACs including Rh, Ir, Os, Re, and Ru which are prone to activate methane at low temperatures (Figure 43).<sup>387</sup>

Most noble transition metals have a low earth abundance, high price, and a tendency for easy catalytic poisoning.<sup>394–396</sup> Therefore, cheaper alternatives such as Cr-, Mn-, Fe-, Co-, and

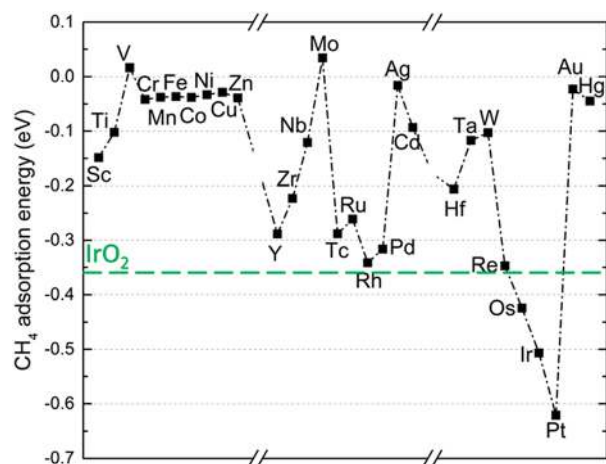


**Figure 43.** Adsorption energies of methane on the M1 (single-atom) site on rutile TiO<sub>2</sub>(110) with M being 3d, 4d, and 5d transition metals, in comparison with that on rutile IrO<sub>2</sub> (110) (green line). The Ti data represents the undoped rutile TiO<sub>2</sub>(110). Reproduced with permission from ref 387. Copyright 2018 Royal Society of Chemistry.

Cu were evaluated by DFT calculations with regard to their energy methane-activation barriers. Results suggest that the C–H bond of methane can be easily activated for Fe or Co compared to Cr, Mn, and Cu (Figure 44).<sup>397</sup>

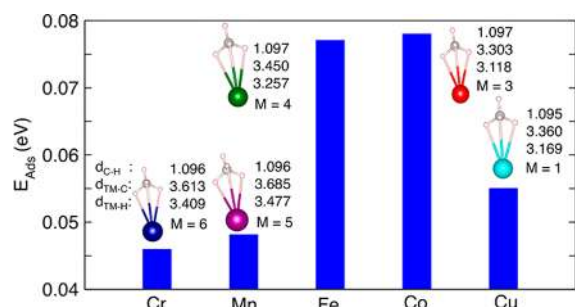


**Figure 44.** Binding strengths ( $E_{\text{Ads}}$ ) of methane and their corresponding optimized structures of TM–methane complexes showing the various bond lengths dC–H, dTM–C, and dTM–H in Å units. M ( $\mu\text{B}$ ) denotes the total spin magnetic moments for each of the geometries. Reproduced with permission from ref 397. Copyright 2018 John Wiley and Sons.

Among the metals, Fe, Cu, and Co showed favorable results with regard to methane activation. This is partially related to the strong binding energies for single atoms of Fe ( $E_{\text{ads}} = 0.077$  eV) and Co ( $E_{\text{ads}} = 0.078$  eV) because strong binding may lead to an easy bond cleavage of methane.<sup>397</sup> Those metals are extensively used for SACS, in combination with classical supports such as silica,<sup>350</sup> graphene, zeolites,<sup>398</sup> and more recently with MOFs.<sup>399</sup>

In summary, mainly transition metals such as Pt,<sup>386,388,389</sup> Pd,<sup>400</sup> Rh,<sup>391–393</sup> Fe,<sup>350,401</sup> Co,<sup>402</sup> and Ni<sup>403</sup> supported on oxides (e.g., TiO<sub>2</sub>, CeO<sub>2</sub>, IrO<sub>2</sub>, ZrO<sub>2</sub>),<sup>387,388,391,400,403</sup> silica,<sup>350,389,404</sup> or carbonaceous materials (as graphene, graphene nanotubes (GN))<sup>397,402</sup> were found to be active for methane C–H activation. For the particular case of methane to methanol conversion, a DFT-study proposes that  $\alpha$ -Al<sub>2</sub>O<sub>3</sub>, ZnO, and Ge<sub>2</sub>O<sub>3</sub> have favorable properties because of (i) low reactivity for CH<sub>4</sub> activation, (ii) low reactivity toward oxidizing agents, and (iii) strong methanol adsorption.<sup>405</sup>

**4.4.2.2. Nonoxidative Conversion of Methane (to Alkanes, Olefins, and Aromatics).** CH-activation of methane under nonoxidative conditions have unfavorable thermodynamics toward C–C coupling and require high activation energies.<sup>406</sup> For the nonoxidative coupling of methane to light hydrocarbons and aromatics, two systems have been described to be highly efficient in SAC: Fe@SiO<sub>2</sub><sup>350</sup> and Pt@CeO<sub>2</sub><sup>388</sup> operating at temperatures between 900 and 1100 °C. The single site iron-catalyst Fe@SiO<sub>2</sub><sup>350,407</sup> (Fe = 0.5 wt %) is “embedded” (lattice-confined) on nonacidic silica as the support (Figure 45), which improves the performance of highly dispersed Fe cations on ZSM5.<sup>408–411</sup> When isolating Pt atoms on the surfaces of Cu (as alloy) Cu,<sup>389</sup> CeO<sub>2</sub>,<sup>388</sup> or Al<sub>2</sub>O<sub>3</sub>,<sup>386</sup> it was shown that the activity of the system is still related to platinum having more sophisticated electronic properties. For example, the activation mechanism for PtAl<sub>2</sub>O<sub>3</sub><sup>386</sup> clusters shows that platinum rather than the oxygen of Al<sub>2</sub>O<sub>3</sub><sup>–</sup> activates CH<sub>4</sub> in the initial step of reaction and that the alumina-oxygen is only relevant at a later stage of the reaction.<sup>386</sup> DFT calculations have predicted that Pt, with a low coordination number, can prevent the successive dehydrogenation of methane by stabilizing the [Pt]–CH<sub>3</sub> intermediate.<sup>412–414</sup> Pt/Cu-alloys showed to have intermediate barriers for C–H activation in between the ones of pure Pt(111) and Cu(111). The energy barrier toward coke

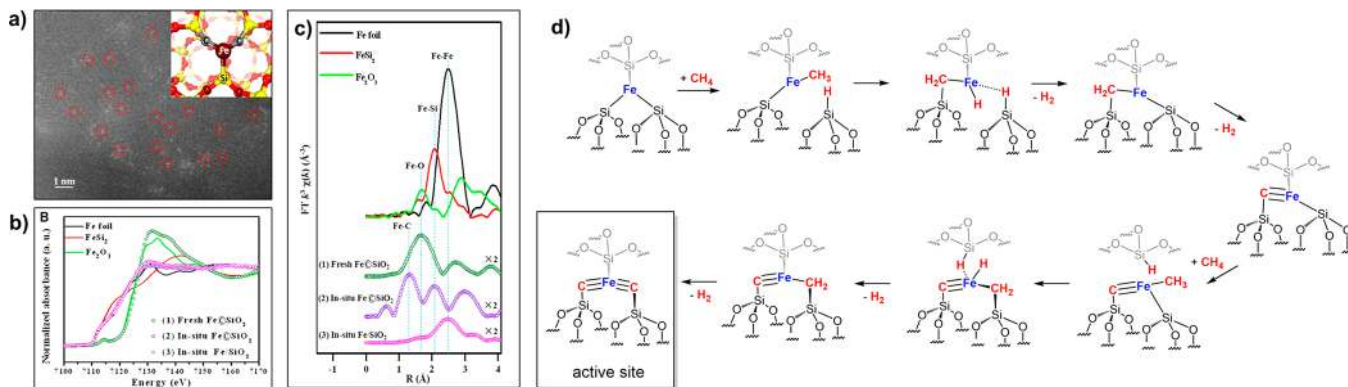


**Figure 45.** (a) STEM-HAADF image of the catalyst after reaction with the inset showing the computational model of the single iron atom bonded to two C atoms and one Si atom within the silica matrix, (b) in situ XANES upon activation, (c) Fourier transformed (FT) weighted ( $k$ )-function of the EXAFS spectra, and (d) proposed mechanism for activation of Fe-species. Reproduced with permission from ref 350. Copyright 2014 The American Association for the Advancement of Science.



formation is higher than the one for Pt(III), suggesting that Pt/Cu is coke resistant.<sup>389</sup> Similarly, Pt@CeO<sub>2</sub> shows a high dispersion of Pt (0.5 wt %) on CeO<sub>2</sub> and the metal–support interaction leads to a very active catalyst toward C–H bond activation of methane, without coke formation.<sup>388</sup> This shows that the electronic properties of Pt can be indeed tuned toward less coke formation and hence higher selectivity of product.

Fe@SiO<sub>2</sub> and Pt@CeO<sub>2</sub> are synthesized by high temperature of calcination (at a temperature higher than 1000 °C). Fe@SiO<sub>2</sub> was prepared by fusion of Fe<sub>2</sub>SiO<sub>4</sub> and SiO<sub>2</sub> at 1500 °C, and Pt@CeO<sub>2</sub> was prepared by calcination of Pt-impregnated porous ceria nanoparticles at 1000 °C. Typical characterization methods were used to elucidate the structure of both SACs. In fresh Fe@SiO<sub>2</sub>, highly dispersed iron oxide was detected on the silica matrix by TEM and EXAFS (Figure 45). The iron oxide species in the fresh 0.5% Fe@SiO<sub>2</sub> material interacts extensively with the support after making contact with CH<sub>4</sub> at 900 °C. Single iron atoms become embedded in the silica matrix through bonding to Si and C atoms as proved by EXAFS (Figure 45). Thus, these otherwise extremely reactive, coordinatively unsaturated iron atoms are stabilized and persist under the very harsh reaction conditions, even for 60 h of reaction time.

The EXAFS spectrum of 0.5% Pt@CeO<sub>2</sub> (Figure 46) exhibits only one pronounced peak associated with the first-

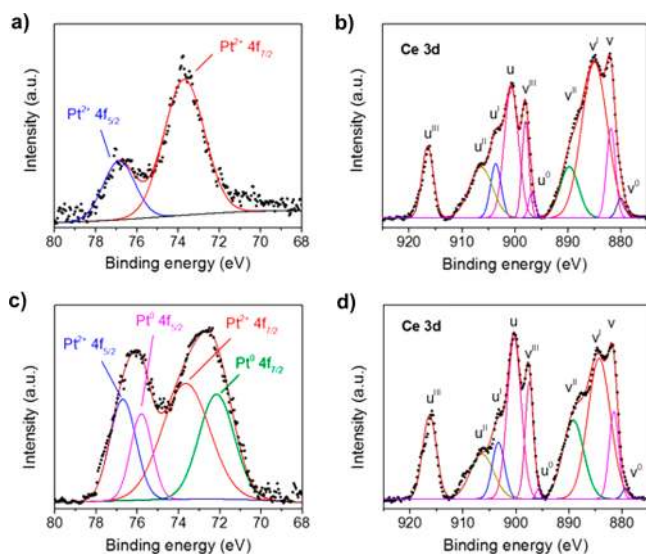


**Figure 46.** XPS spectra collected of (a,b) 0.5% Pt@CeO<sub>2</sub> and (c,d) PtNPs/CeO<sub>2</sub> catalysts at the (a,c) Pt 4f and (b,d) Ce 3d edges. Reproduced with permission from ref <sup>388</sup>. Copyright 2018 American Chemical Society.

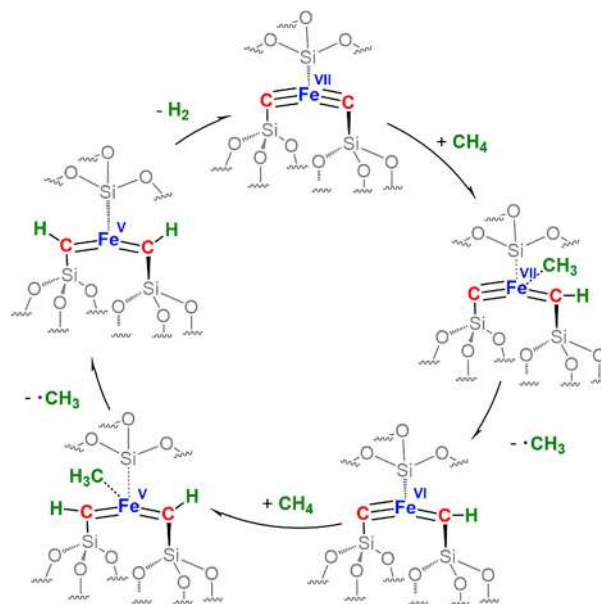
shell Pt–O bond (with Pt–O coordination number of 5 at ~2.03 Å). The absence of Pt–Pt and higher-shell Pt–O–Pt scatterings demonstrate atomic dispersion of Pt in the catalyst with Pt in the oxidation state of Pt<sup>2+</sup>.

Isolated iron sites confined in a silica matrix<sup>350</sup> and isolated platinum sites<sup>388</sup> confined in nanoceria enable nonoxidative, direct conversion of methane. In both cases, catalysis was performed at high working temperatures (>900 °C). Fe@SiO<sub>2</sub> showed an 8% conversion of methane at 950 °C with 48% selectivity to C<sub>2</sub>-hydrocarbons and at 1090 °C (WHSV = 21400 mL/g<sub>cat</sub>·h) a maximum conversion of 48% forming 99% of hydrocarbons with a 48% selectivity for ethylene and 20–30% for each, benzene and naphthalene. The catalyst was

stable for 60 h. Pt@CeO<sub>2</sub> (WHSV = 6000 mL/g<sub>cat</sub>·h) converts 14.4% of methane at 975 °C with a 74.6% selectivity toward C<sub>2</sub> products (ethane, ethylene, and acetylene). The selectivity toward C<sub>2</sub>-hydrocarbons gradually decreases with increasing temperatures from 98.4% (at 900 °C) to 66.7% (at 1000 °C). Starting at ≥950 °C, aromatic products appear. The selectivities toward aromatics increased with increasing temperature, achieving 26.6% for benzene and 2.1% for naphthalene, while maintaining a high selectivity for ethylene showing the formation of light hydrocarbons for Pt@CeO<sub>2</sub>.

Bao et al. postulated a free radical mechanism at 1100 °C in gas phase starting from the active site of Fe@SiO<sub>2</sub> (Scheme 36). The oxidation state of iron is supposed to increase to

**Scheme 36.** Proposed Radical Mechanism for Activation of Methane with Fe@SiO<sub>2</sub><sup>350</sup>



+VII. C–H activation on the iron sites generates CH<sub>3</sub>· radicals, which desorb from the surface of the catalyst and subsequently undergo a series of gas-phase processes to form ethylene, benzene, and naphthalene as the only products. A similar, radical mechanism was proposed by Labinger in the oxidative coupling of methane.<sup>342</sup>

**4.4.2.3. Oxidative Conversion of Methane (to Alkanes, Olefins, and Oxygenates).** For the oxidative conversion of methane to oxygenates, there are two challenges: (i) The first one is the high activation barrier for C–H bond activation of methane, and (ii) the second one is the easiness of total oxidation to CO or CO<sub>2</sub>. Herein, we discuss some distinctive examples of SACs for oxidative conversion of methane.

Rhodium turned out to be another interesting transition metal for the oxidative conversion of methane conversion by SAC on various supports: (i) Rh/ZrO<sub>2</sub>,<sup>391</sup> (ii) Rh/ZSM-5,<sup>392,393</sup> and Rh/TiO<sub>2</sub>.<sup>393</sup> The highest methanol production was observed for Rh-ZrO<sub>2</sub>,<sup>391</sup> when methane was reacted in the presence of H<sub>2</sub>O<sub>2</sub>. Rh/ZSM5 and Rh/TiO<sub>2</sub><sup>393</sup> convert methane to acetic acid in the presence of CH<sub>4</sub> and CO.<sup>393</sup>

Different concentrations of Rh/ZrO<sub>2</sub><sup>391</sup> were synthesized by wet impregnation of RhCl<sub>3</sub> onto zirconia. The single site character of the 0.3 wt % sample was confirmed by EXAFS and TEM. The Rh oxidation state of 0.3 wt % Rh/ZrO<sub>2</sub> catalysts was measured by XPS (Figure 47) finding a binding energy of

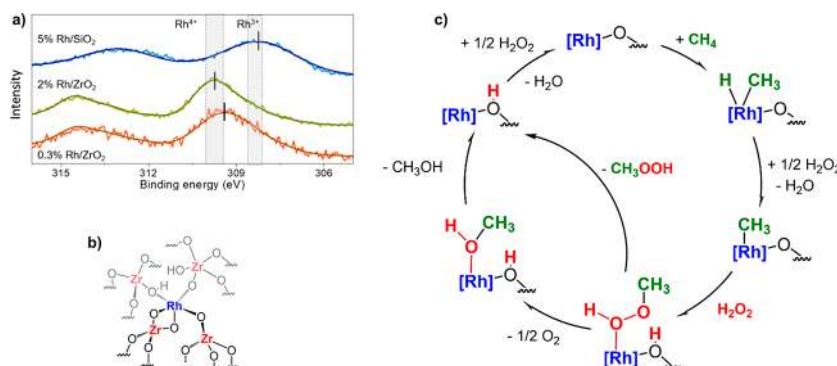


**Figure 47.** (a) EXAFS of Rh/ZrO<sub>2</sub> at different concentrations. Reproduce with permission from ref 391. Copyright 2017 American Chemical Society. (b) Proposed structure of 0.3% Rh/ZrO<sub>2</sub> having oxidation state +3.7. (c) Mechanism of oxidative conversion of methane to methanol and formic acid.

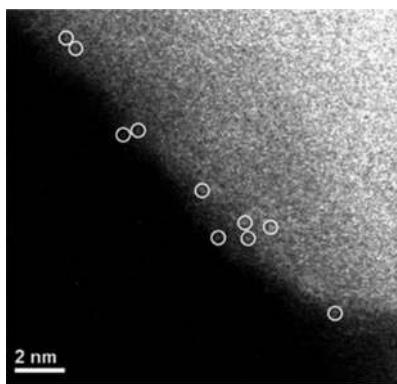
the XPS Rh 3d 5/2 peak of 309.4 eV. This value<sup>415–417</sup> suggests 0.3 wt % Rh/ZrO<sub>2</sub> having an average oxidation state of 3.7. The proposed structure is shown in Figure 47.

Rh/ZrO<sub>2</sub> activates CH<sub>4</sub> on the [Rh]-site which is dissociatively adsorbed as –CH<sub>3</sub> and –H. The adsorbed [Rh]–CH<sub>3</sub> easily reacts with an adsorbed H<sub>2</sub>O<sub>2</sub> to form MeOOH. Deoxygenation of MeOOH into MeOH is then energetically favored, which is in accordance with time-resolved reaction results (Figure 47).

At low temperatures, direct methane oxidation was observed to produce ethane in the presence of a small amount of O<sub>2</sub> at 260 °C and atmospheric pressure. DFT calculations also showed that dissociative adsorption of two CH<sub>4</sub> molecules and subsequent formation of ethane are energetically plausible on the single-atomic Rh site. CH<sub>4</sub> reacts with rhodium by CH activation to form H–[Rh]–CH<sub>3</sub>. Subsequent migration of the methyl group to a nearby O atom permits dissociative adsorption of another CH<sub>4</sub> molecule. The adsorption of second CH<sub>4</sub> is slightly endothermic but coupling of two –CH<sub>3</sub> into C<sub>2</sub>H<sub>6</sub> is exothermic, allowing a favorable formation of ethane on Rh<sub>1</sub>/ZrO<sub>2</sub>.<sup>391</sup>

Rh/ZSM5 (HAADF-TEM in Figure 48) and Rh/TiO<sub>2</sub> are able to convert methane to acetic acid (22 000 μmol g<sub>cat</sub><sup>–1</sup> at *t* = 3 h) in the presence of CH<sub>4</sub> and CO at 150 °C and a pressure of 30 bar.<sup>393</sup>

Two catalysts have been prepared by incipient wetness impregnation of H-ZSM5 forming Rh/ZSM5.<sup>392,393</sup> It is proposed that isolated Rh<sup>+</sup> (after treatment with H<sub>2</sub>)<sup>393</sup> or

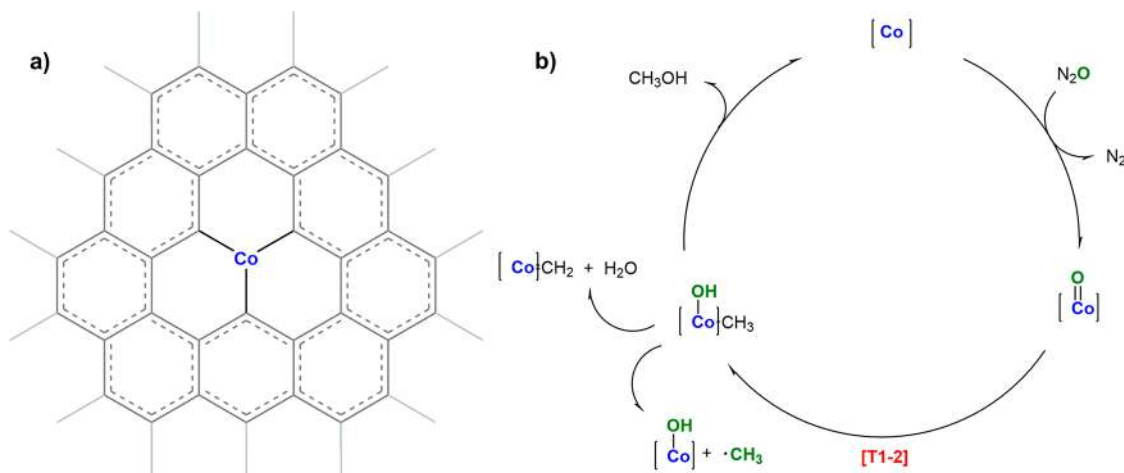
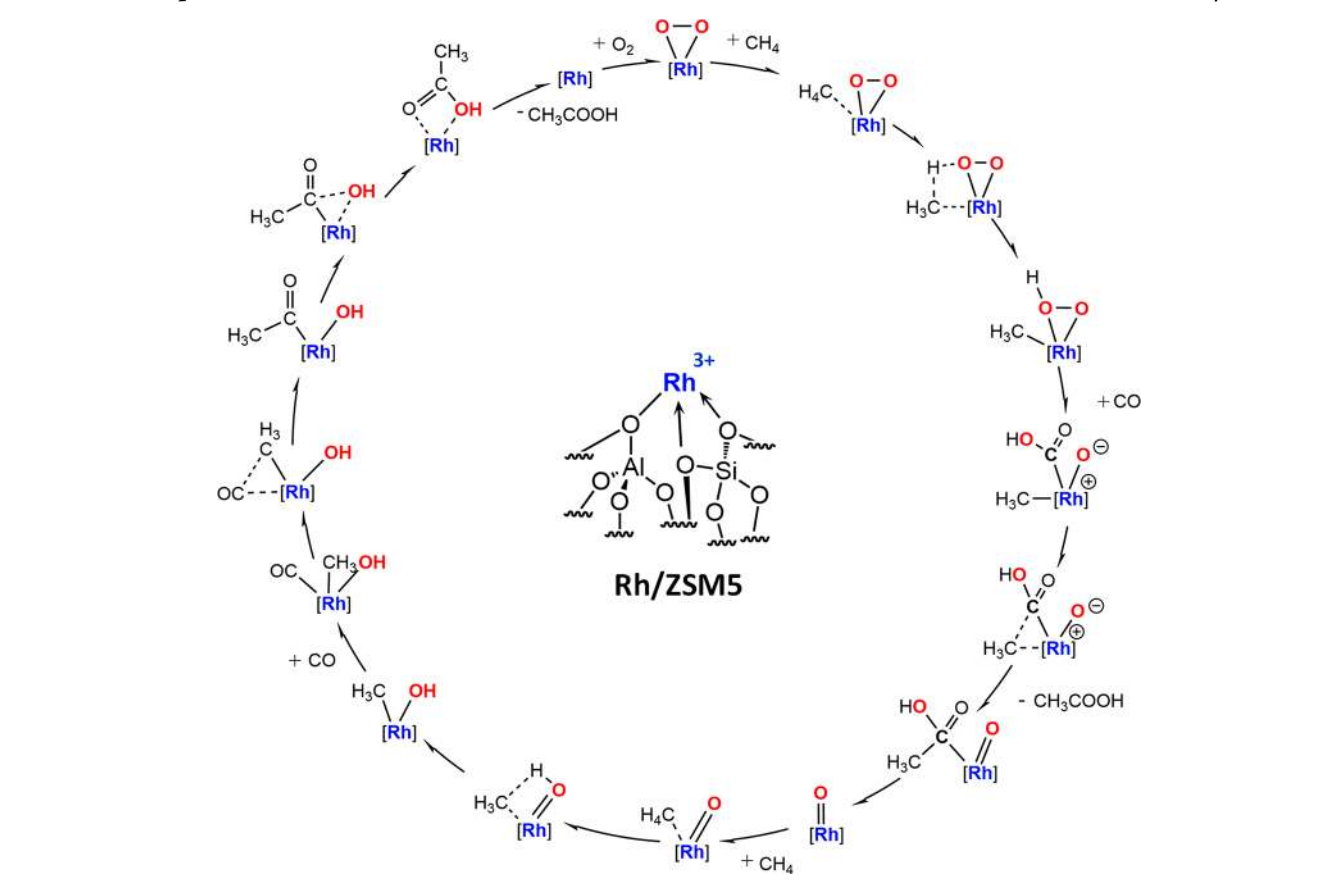


**Figure 48.** Aberration-corrected HAADF/STEM image of as-synthesized Rh-ZSM-5. Reproduced with permission from ref 393. Copyright 2017 Springer Nature.

Rh<sup>3+</sup><sup>392</sup> cations facilitates the activation of methane in the presence of O<sub>2</sub>.<sup>392,393</sup> In both cases, it is expected that the Rh cations replace the Brønsted sites and thus bind to the Al atoms. Figure 48 proposes a structure of Rh/ZSM5 where the Rh atom binds to three oxygen atoms of the ZSM5 framework.<sup>392</sup> A detailed mechanism has been proposed by Tang et al.<sup>392</sup> (Scheme 37). This mechanism involves the occurrence of a Rh<sup>(V)</sup> species, an oxidation state of rhodium which is more and more involved in catalysis.<sup>418</sup> Rh/ZSM5 is activated with oxygen forming Rh–O<sub>2</sub>. The C–H bond of methane and the oxygen of Rh(η<sup>2</sup>-O<sub>2</sub>) forms a methyl and hydroxyl adsorbed on the [Rh] atom. Then, a CO molecule can insert into the Rh–O–H bond forming Rh–COOH. The –COOH residue couples with the adsorbed methyl group to form a weakly adsorbed acetic acid, which is subsequently desorbed, yielding the first CH<sub>3</sub>COOH molecule. The remaining [Rh]=O oxo group activates the C–H bond of the second CH<sub>4</sub> molecule to form a methyl and a hydroxyl group adsorbed on the Rh atom. The second CO molecule binds to the unsaturated [Rh] site and subsequently inserts into the methyl–Rh bond forming an acetyl group. The hydroxyl group couples with the carbon atom of C=O of the acetyl group and the second acetic acid is formed. Desorption of the second acetic acid molecule recovers the Rh site, which then bonds with a molecular O<sub>2</sub>, forming [Rh]–O<sub>2</sub> ready for next catalytic cycle.

The EXAFS spectra show Rh–Rh bonding (coordination number = 0.6 ± 0.2), indicating the formation of some Rh clusters during the methane conversion reaction. However, no homogeneous reaction occurred because of leaching. CH<sub>3</sub>OH was detected by <sup>13</sup>C NMR, confirming that the methyl group carbon is derived solely from methane.<sup>393</sup>

Other interesting materials for the direct, oxidative activation of methane are graphene-supported 3d-single TM atoms such as Cr, Mn, Fe, Co, and Cu.<sup>397</sup> A correlation between catalytic activity and magnetic properties of the graphene supported systems through hydrocarbon activation was found. The best properties were found for Co and Fe. Co/graphene is a high performance catalyst for methane activation.<sup>402</sup> CoO<sup>419</sup> is reported to bear a high reaction selectivity but very low reaction efficiency for the conversion of methane to methanol (Figure 49).<sup>420,421</sup> The reaction mechanism was proved by first principle calculations: A two-step reaction mechanism for direct methane oxidation to methanol over a single atom [Co]-embedded graphene (Gr) catalyst, with N<sub>2</sub>O as the O-donor molecule. C–H activation is

Scheme 37. Proposed Structure of Rh/ZSM5 and Reaction Mechanism for Formation of Acetic Acid from CH<sub>4</sub><sup>392</sup>Figure 49. (a) Proposed structure of Co/GN and (b) mechanism for the oxidation of methane with N<sub>2</sub>O to form methanol.<sup>402</sup>

the rate-limiting step. The high reaction activity and selectivity under mild conditions were predicted for this catalyst.

The energy barrier of the transition state TS1–2 is 16.4 kcal/mol (in Figure 49),<sup>402</sup> close to those of Cu-ZSM-5 (18.45 kcal/mol),<sup>422</sup> Cu-MOR (17.5, 21.4 kcal/mol),<sup>423,424</sup> AuPd nanoparticles,<sup>425</sup> Co-ZSM-5 (15.0 kcal/mol),<sup>426</sup> Fe-ZSM-5 zeolites (15.0–39.9 kcal/mol),<sup>427</sup> and FeO/Gr<sup>428</sup> catalysts.

Single site iron catalysts on graphene and boron nitride<sup>429</sup> are also active for methane to methanol conversion (Figure 50). In 2015,<sup>429</sup> Fe on graphene and boron nitride were proposed to be potential catalysts for methane to methanol conversion. DFT calculations suggest that atomic iron (or

Pd)<sup>405</sup> embedded in the BN sheet would be an excellent center for the C–H activation of methane, better than the atomic iron embedded graphene. For the partial oxidation of methane by the iron–oxo species, the iron embedded graphene was found to be better than the BN sheet, mainly due to the very high energy demand for the transformation of the surface methoxy species to a methanol product.

In 2018, the single site iron catalyst FeN<sub>4</sub>/GN<sup>401</sup> was prepared by embedding iron sites on graphene nanosheets FeN<sub>4</sub>/GN (Fe = 2.7 wt %). This catalyst converts methane into methanol at room temperature (TOF = 0.47/hm 10 h).



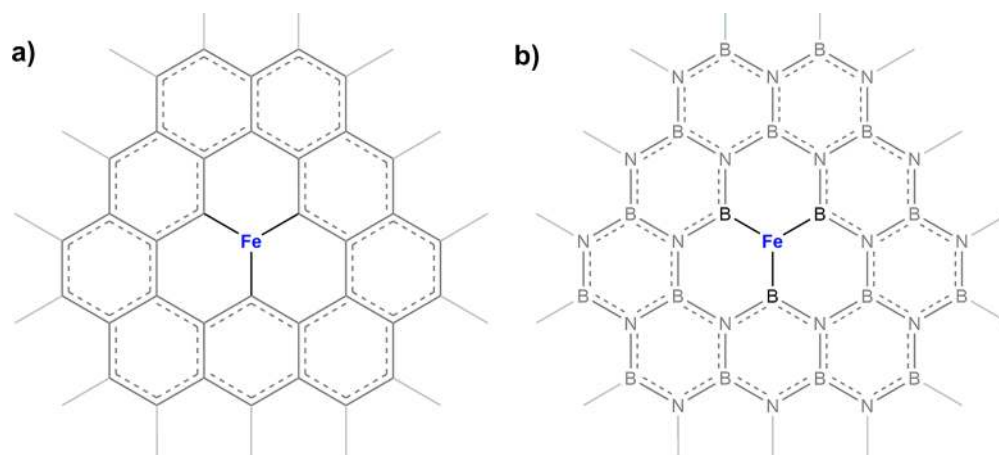


Figure 50. Proposed structures for Fe/GN (a) and Fe/BN (b).<sup>429</sup>

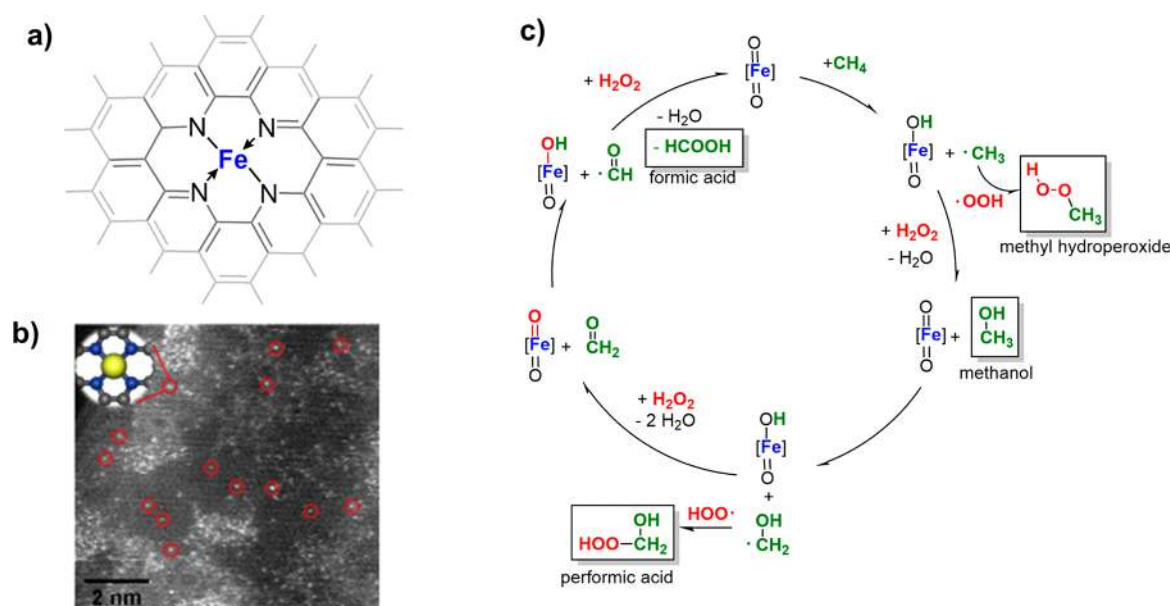


Figure 51. (a) Proposed structure of FeN<sub>4</sub>/GN and (b) HAADF-STEM image of FeN<sub>4</sub>/GN (red circles show some single iron atoms in the matrix of graphene nanosheets). Reproduced with permission from ref 401. Copyright 2018 Elsevier. (c) Proposed mechanism of ethane conversion on FeN<sub>4</sub>/GN.

The single site character of Fe/GN was characterized by AFM and HAADF-STEM (Figure 51).

Cui et al.<sup>401</sup> suggested that the conversion proceeds via an O–FeN<sub>4</sub>–O, which is formed by a reaction of H<sub>2</sub>O<sub>2</sub>. O–FeN<sub>4</sub>–O and H<sub>2</sub>O can activate CH<sub>4</sub> to form the methyl radical with a low reaction energy barrier (0.79 eV, 18 kcal/mol). The methyl radical is then converted into 94% oxygenated products (Figure 51).<sup>401</sup> It was possible to detect CH<sub>3</sub>OH and CH<sub>3</sub>OOH (more initially) by <sup>13</sup>C NMR and <sup>13</sup>C DEPT-135. Toward the end of the reaction, CH<sub>3</sub>OH converts into HOCH<sub>2</sub>OOH and HCOOH and 6% of CO<sub>2</sub>. Other catalysts (MnN<sub>4</sub>/GN, CoN<sub>4</sub>/GN, NiN<sub>4</sub>/GN, CuN<sub>4</sub>/GN and molecular catalyst FePc) have been tested, but best performance is obtained with FeN<sub>4</sub>/GN. H<sub>2</sub>O<sub>2</sub> reacts with FeN<sub>4</sub>/GN to form oxidized O–FeN<sub>4</sub>–O and H<sub>2</sub>O, which is able to activate CH<sub>4</sub> to form the methyl radical with a low reaction energy barrier (18 kcal/mol). The methyl radical is then converted into oxygenated products.

Another example of a Fe single atom catalyst used for methane oxidation<sup>399</sup> is the isolated Fe unit incorporated into

an Al-based MOF (MIL53). MOFs have a high degree of synthetic control, therefore an ideal support for SAC. In this example, Fe was incorporated into the MOF by the electrochemical route to avoid extra-framework species. A catalyst with a loading of 5.4 wt % of iron was synthesized, which was found to be active for methane oxidation. The structure was identified by EXAFS, XRD, and CO<sub>2</sub> adsorption measurements proposing a monomeric and dimeric Fe species in the MOF. The antiferromagnetically coupled dimers have a Fe–O–Fe bond and showed the highest effect on catalysis.

Iron,<sup>430,431</sup> copper,<sup>424,432–437</sup> and other metal-oxo clusters<sup>438,439</sup> have also been used on various zeolite topologies for the stoichiometric activation of methane to methanol. Cu or Fe sites are activated into oxo species by O<sub>2</sub> or N<sub>2</sub>O, and then the active sites react with CH<sub>4</sub> producing methoxy groups. For example, Pappas et al.<sup>398</sup> studied the activation of Cu/SSZ13 under oxygen-containing atmosphere at high temperatures. A maximum conversion reaching 0.172 mol methanol/mol Cu (107 μmol/g) was found at 450 °C after 120 min with 187 mbar partial pressure of O<sub>2</sub>. The mechanism of the methane

activation studied by XAS and EXAFS and Raman, confirming a single site structure of  $\text{Cu}^{2+}$  is shown in Figure 52.

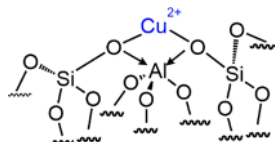


Figure 52. Proposed structure of Cu/SSZ13 with Si/Al ratio of 15 and Cu/Al ratio of 0.5.<sup>398</sup>

**4.4.3. Via SAAC.** As discussed in the previous section, platinum has a high tendency to bind methane and  $\text{CH}_x$  intermediates during the conversion of methane<sup>384,385</sup> which leads to a strong coke formation. When diluting the concentration of Pt to a single atom, the activity can be throttled enabling the desired conversion from methane to higher hydrocarbons. Marcinkowski et. al recently found a Pt/Cu single atom alloy catalyst to be coke resistant for CH activation.<sup>389</sup> The principle was to make an alloy of Pt/Cu by spreading out Pt(III) on the surfaces of Cu(III).<sup>389</sup> The single atom character was demonstrated by intermediates of CH-activated  $\text{CH}_4$  on Pt/Cu (Figure 53). Pt/Cu has an intermediate barrier height in between the ones of pure Pt(111) and Cu(111). The energy barriers (TS4 in Figure 53) toward coke is higher, hence, Pt/Cu has a resistance for coke formation. Similar results were observed with Pt@ $\text{CeO}_2$ .

## 4.5. Emerging Reactions in SOMCat and SAC Chemistry

**4.5.1. Imine Metathesis.** Imine metathesis reaction has been known since 1922 by Ingold and Piggott.<sup>440</sup> However, the study on C–N bond forming reaction is less advanced as compared to C–C bond forming reaction. Recently, well-defined surface organometallic fragments (M-carbene/hydride) are widely used for improved alkane metathesis reaction, olefin metathesis reaction, oxidative coupling of methane, etc., which are mainly C–C bond forming reaction.<sup>196,197,274,441</sup> Keeping in mind the importance of imido complexes in organic synthesis and catalysis,<sup>442</sup>  $[\text{M}] = \text{NR}$  fragments have been investigated for improved imine metathesis reaction. The first well-defined silica supported imine metathesis catalyst was  $[(\equiv\text{Si}-\text{O})\text{Zr}(\equiv\text{NEt})\text{NEt}_2]$ .<sup>51</sup> This catalyst was prepared by reaction of  $\text{SiO}_{2-700}$  with  $\text{Zr}(\text{NEt}_2)_4$  in pentane following a thermal treatment at 200 °C under vacuum (Scheme 38).<sup>51</sup>

It was understood that the initial surface complex  $[(\equiv\text{Si}-\text{O})\text{Zr}(\text{NEt}_2)_3]$  at 200 °C is transformed into a three membered metalla-cycle intermediate (metallaaziridine) by  $\beta$ -hydride abstraction followed by removal of  $\text{NHET}_2$ . This three membered metalla-cycle is further transformed into  $[(\equiv\text{Si}-\text{O})\text{Zr}^{(\text{IV})}(\equiv\text{NEt})(\text{NEt}_2)]$  **25** by releasing an olefin (Scheme 38).<sup>51</sup> To observe the transformation of the imido to another imido during imine metathesis, **25** was reacted with phenyl benzyl imine in toluene at 80 °C. After work up and purification steps, a new surface complex  $[(\equiv\text{Si}-\text{O})\text{Zr}(\equiv\text{Ph})(\text{NEt}_2)]$  **26** was isolated and fully characterized by solid state NMR, IR, and elemental analysis (Scheme 39).

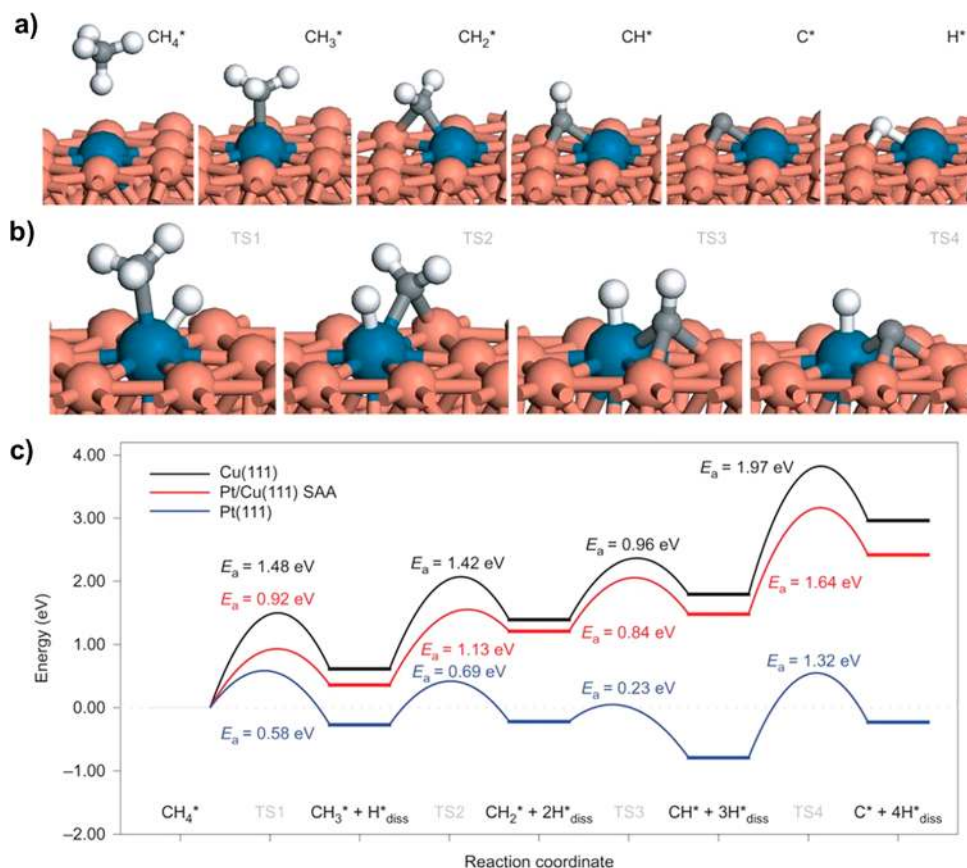
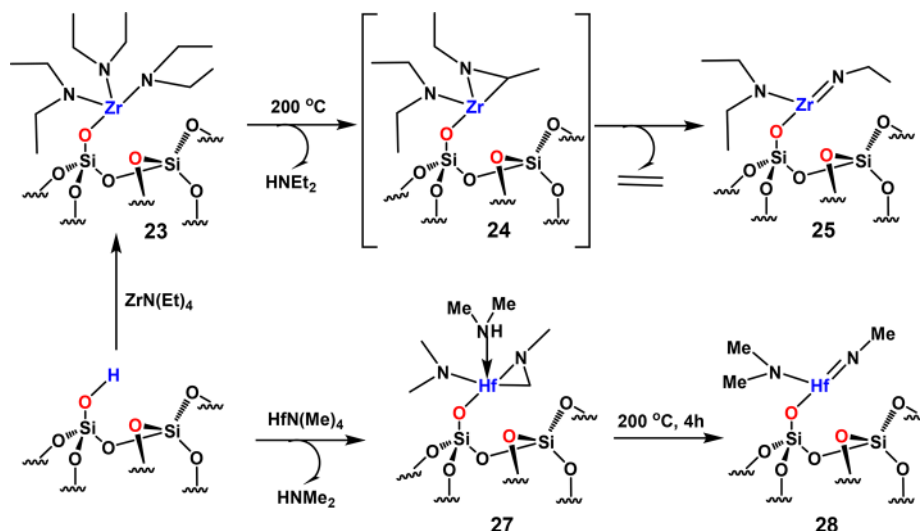
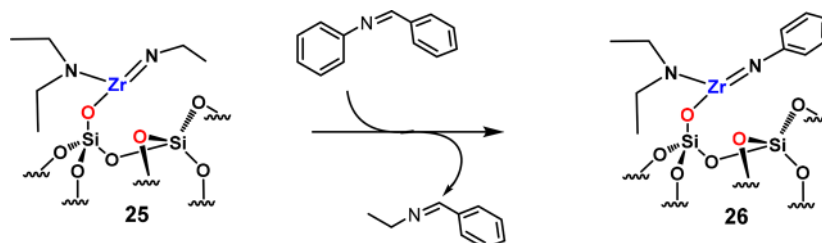
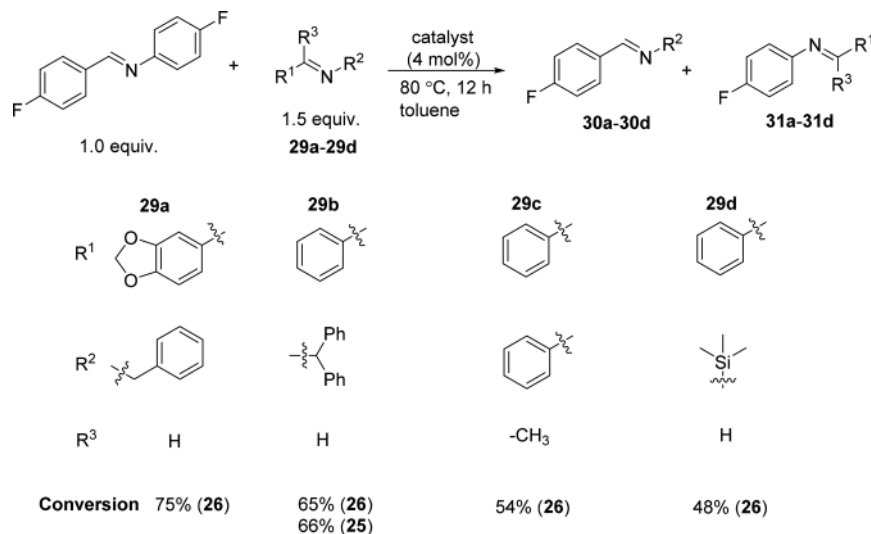


Figure 53. Comparison of reaction pathways between pure and SAA surfaces. Reproduced with permission from ref 389. Copyright 2018 Springer Nature.

Scheme 38. Synthesis of Metal Imido Fragments from Homoleptic Zr<sup>51</sup> and Hf<sup>100</sup> Amido ComplexesScheme 39. Isolation of a New Surface Complex 26 Was Observed during Stoichiometric Imine Metathesis Reaction<sup>51</sup>

Scheme 40. Model Imine Metathesis Reaction Studied with Catalysts 25 and 26



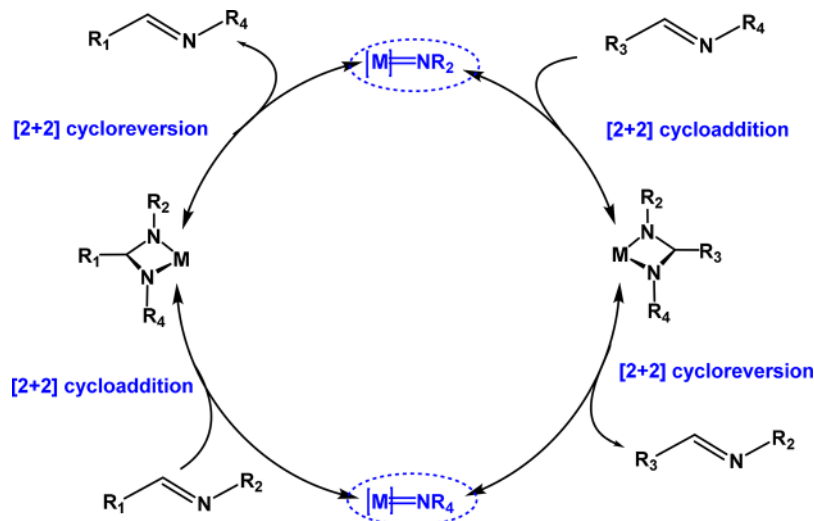
The isolation of the surface complex **26** confirms that imine metathesis reaction undergoes a 4-centered metallacycle intermediate before affording the final product.

Surface complexes **25** and **26** were tested for imine metathesis between (4-fluorobenzylidene)-(4-fluorophenyl) and various imines (**29a–29d**, Scheme 40) with conversions ranging between 48% and 76% and moderate TON values between 12 and 19 depending on the imine.<sup>51</sup> When studied for the same reaction (reaction of (4-fluorobenzylidene)-(4-fluorophenyl) with **29b**), **25** and **26** displayed nearly identical catalytic performance (Scheme 40). Following this initial

study, the application of Hf-based complexes was studied.<sup>100</sup> Hf surface complex  $[(\equiv\text{Si}-\text{O}-)\text{Hf}(=\text{NMe})(-\text{NMe}_2)]$  **28** was prepared in a similar fashion as the analogous Zr complex. In this case, the metalla-aziridine intermediate **27** was isolated and fully characterized by solid state NMR, DNP SENS, and EXAFS. It was observed that NHMe, which is supposed to be released during the formation of metalla-aziridine intermediate, coordinates with the metal complex.<sup>100</sup> The structure of the intermediate Hf aziridine complex was characterized as  $[(\equiv\text{Si}-\text{O}-)\text{Hf}(\eta^2, \pi\text{MeNCH}_2)(\eta^1-\text{NMe}_2)(\eta^1-\text{HNMe}_2)]$  (Scheme 38).<sup>100</sup> Upon heating this complex at 200 °C for 4 h, it is



Scheme 41. Imine Metathesis Mechanism Carried out by Metal Imide Fragment



further transformed to  $[(\equiv\text{Si}-\text{O}-)\text{Hf}(\equiv\text{NMe})(\eta^1\text{-NMe}_2)]$  **28**. This catalyst was used for imine metathesis reaction for a wide range of imines. In the imine metathesis of *N*-(4-phenylbenzylidene)benzylamine and *N*-benzylidene-*tert*-butylamine, equilibrium was reached after 1 h with a conversion of 50%, whereas control blank reaction showed only 11% conversion. On the basis of the metathesis product, a mechanism was proposed; the initial stage of the imine metathesis is coordination of the reactant (via the imine fragment) with the electropositive metal followed by formation of metallacycle intermediate [2 + 2 cycloaddition]. After cycloreversion, a new imine fragment is released with the formation of a new  $[\text{M}]=\text{NR}_4$  fragment.<sup>100</sup> The second imine comes in contact with the new surface fragment and again generates a metallacycle and after cycloreversion, a new imine results with the formation of starting  $[\text{M}]=\text{NR}_2$  (Scheme 41).

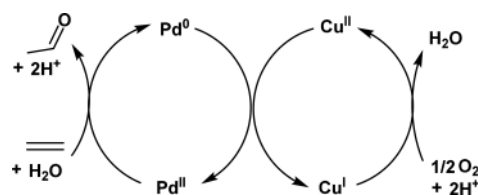
This reaction is not only restricted to group 4 metal imides; also, group 6 molybdenum imides were also tried successfully for this reaction. Silica supported molybdenum imido catalysts were proved to be equally efficient as those of group 4 metal imido by carrying out imine metathesis by reaching equilibrium within 6–24 h.<sup>443</sup>

**4.5.2. Metathetic Oxidation of Olefins.** Aldehydes are building blocks for many fine chemicals. Specifically, acetaldehyde is used as a starting material for chemicals like vinyl acetate, penta-erythritol, crotonaldehyde, resins, etc., and the primary source for the production of acetaldehyde is the Wacker process.<sup>444</sup> In this process, ethylene is oxidized in the presence of a dual catalytic system ( $\text{PdCl}_2/\text{CuCl}_2$ ). In this process,  $\text{Pd}^{2+}$  oxidizes ethylene to acetaldehyde and is simultaneously reduced from  $\text{Pd}^{(\text{II})}$  to  $\text{Pd}^{(0)}$ . Cu acts as a cocatalyst and oxidizes again  $\text{Pd}(0)$  to  $\text{Pd}(\text{II})$ , and the process goes on (Scheme 42).<sup>444</sup>

Although this process is reliable and widely used for the production of acetaldehyde, the main disadvantage is the formation of HCl during the reaction which corrodes the reactor.

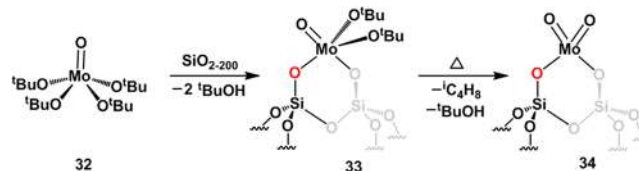
Recently, to mimic the industrial molybdenum oxide catalyst ( $\text{MoO}_3$ ), a well-defined bis-oxo molybdenum surface catalyst was synthesized using SOMC strategy and used for conversion of olefins to aldehyde in the presence of molecular oxygen, this reaction is named “metathetic oxidation” because the concept

Scheme 42. Wacker Oxidation Process



used to discover this reaction was reminiscent of the olefin metathesis reaction.<sup>31</sup> The **predictive design idea** was to use a  $[\text{Mo}]=\text{O}$  in the same way as  $[\text{M}]=\text{CHR}$  is used in olefin metathesis. The reaction was found to occur quite selectively with  $[\text{Mo}](=\text{O})_2$ . This is the reason why the term metathetic oxidation was used. This is the first example where in a single step, olefins (internal and terminal) are converted under oxygen to aldehydes metathetically in the presence of molecular oxygen.<sup>31</sup>

Silica supported molybdenum complex was prepared by reaction of oxo-molybdenum tetrabutoxide  $[(\text{Mo}=\text{O})(\text{O}^t\text{Bu})_4]$  **32** with  $\text{SiO}_{2-200}$  in pentane (Scheme 43). The

Scheme 43. Schematic Illustration of the Preparation of Single-Site  $[(\equiv\text{Si}-\text{O})_2\text{-Mo}(=\text{O})]$  Catalyst

resulting intermediate  $[(\equiv\text{Si}-\text{O})_2\text{-Mo}(=\text{O})(\text{O}^t\text{Bu})_2]$  (**33**) was further heated, resulting in  $[(\equiv\text{Si}-\text{O})_2\text{-Mo}(=\text{O})]$  (**34**) with the evolution of butanol and isobutene (Scheme 43). These complexes are fully characterized by SS NMR, IR, elemental analysis, and by EXAFS.<sup>31</sup>

After full characterization of the supported bis oxo molybdenum complex **34**, it was used for oxidation of olefins in a continuous flow reactor at a temperature range of 400–450 °C. When propylene (7.5% v/v) was contacted with  $\text{O}_2$  (10% v/v) at 400 °C, 5–6% propylene conversion was observed and the selectivities varied between **33** and **35** for

Table 2. Catalytic Results Obtained with 34 Using Propylene and Molecular Oxygen as Reagents

| temp (°C) | feed (%) C <sub>3</sub> =, O <sub>2</sub> , N <sub>2</sub> , He | conv C <sub>3</sub> = (%) | selectivity (%) |       |                     |          |
|-----------|---|---------------------------|-----------------|-------|---------------------|----------|
|           |   |                           | CO <sub>2</sub> | CO    | CH <sub>3</sub> CHO | acrolein |
| 400       | 7.5, 10, 12.5, 70   | 5–6                       | 30–32           | 9–10  | 33–35               | 9–11     |
| 450       | 7.5, 10, 12.5, 70   | 12–14                     | 31–34           | 11–14 | 25–29               | 9–12     |
| 450       | 7.5, 5, 12.5, 75  | 9–9.5                     | 23–24           | 9–10  | 30–31               | 13–14    |
| 450       | 7.5, 2.5, 12.5, 77.5  | 5–6                       | 21–23           | 10–11 | 28–29               | 10–11    |

acetaldehyde, 40–45% for CO and CO<sub>2</sub>, and about 10% for acrolein. Conversion nearly doubled at 450 °C under otherwise identical conditions without strongly affecting acetaldehyde selectivity. When the ratio of propylene to O<sub>2</sub> was varied from 7.5:10 to 7.5:5 and 7.5:2.5 at 450 °C, conversion progressively dropped but the selectivity for acetaldehyde remained around 30% (Table 2).

The formed amounts of CO and CO<sub>2</sub> came from thermal decomposition of formic acid, which is formed during over oxidation of propylene. Particularly, CO comes from the oxidation of formaldehyde which is formed due to 2 + 2 cycloaddition of molecular oxygen and  $\alpha$ -olefins. The limited amount of acrolein formed might be due to C–H bond activation of methyl group of propylene, followed by oxygen insertion and  $\beta$ -H elimination.

This reaction was extended to *cis*-2-butene. As expected, *cis*-2-butene exhibited a higher selectivity toward the formation of acetaldehyde (~71%) at lower conversion (~5%) at 350 °C (Figure 54).<sup>31</sup>

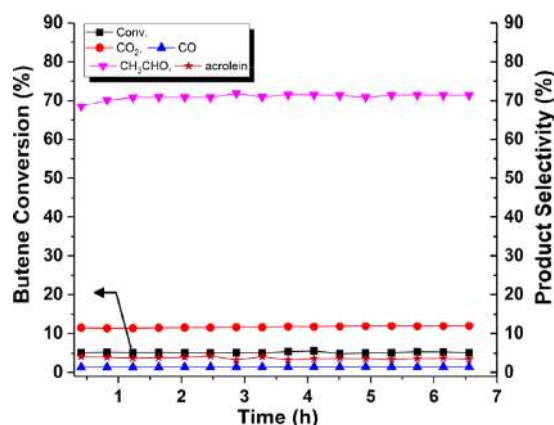
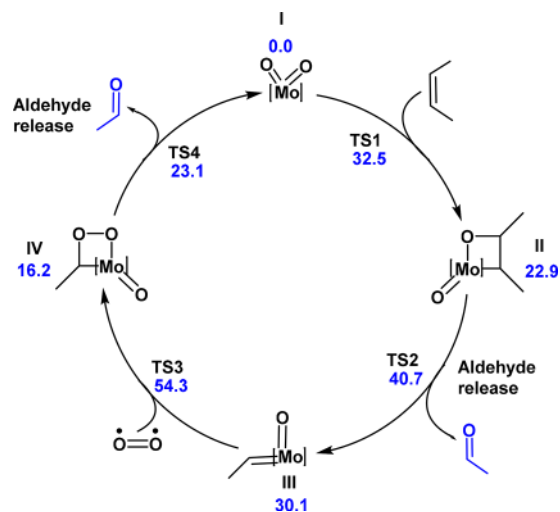


Figure 54. Conversion and selectivity as a function of time-on-stream for the *cis*-2-butene oxidation over [(≡Si–O)<sub>2</sub>–Mo(=O)] (34) at 350 °C. Reproduced with permission from ref 31. Copyright 2018 American Chemical Society.

By increasing the temperature, the selectivity to acetaldehyde decreases with simultaneous formation of CO and CO<sub>2</sub>. Starting from these experimental results, the complete reaction cycle has been investigated by DFT calculations (Scheme 44).

The reaction involves four steps: (i) 2 + 2 addition of the olefin to the molybdenum bis-oxo species, leading to a metallacyclobutane intermediate, (ii) cycloreversion of the metallacyclobutane and release of one acetaldehyde with generation of metal-oxo carbene, (iii) the 2 + 2 cycloaddition of O<sub>2</sub> to the metalcarbene, and (iv) opening of the metallo-peroxo intermediate and releasing of the second molecule of acetaldehyde with regeneration of the starting Mo bis oxo catalyst. The catalytic cycle involves species in different spin state with the flipping from triplet to singlet state occurring

Scheme 44. Reaction Pathway for the Formation of Acetaldehyde through Metathetic Oxidation of *cis*-2-Butene by [(≡Si–O)<sub>2</sub>–Mo(=O)] (34)<sup>a</sup>



<sup>a</sup>Free energies are in kcal/mol. Reproduced with permission from ref 31. Copyright 2018 American Chemical Society.

during the rate determining addition of the O<sub>2</sub> molecule (TS3 in Scheme 44). Overall, the reaction is strongly exothermic (–84 kcal/mol) and the quite high kinetic barriers are still consistent with the experimental conditions.<sup>31</sup>

**4.5.3. Catalytic Hydrogenation of N<sub>2</sub> into NH<sub>3</sub>.** Ammonia synthesis is among the most globally important processes in the chemical industry owing to the use of NH<sub>3</sub> as the source of most fertilizers. There is a strong correlation between the increase of human population from 1900 to nowadays and the demand for worldwide ammonia production.<sup>445</sup> According to data provided by Apodaca, 2013 worldwide production of NH<sub>3</sub>, with China, India, the Russian Federation, the United States, and the European Union as the top of producers, reached 0.14 Gt. It is estimated that 3% of the global CO<sub>2</sub> emissions into the atmosphere are due to industrial, large-scale NH<sub>3</sub> synthesis,<sup>446</sup> which contributes to the release of approximately 1 billion tons of waste CO<sub>2</sub> per year.<sup>447</sup> Overall, it is clear that ammonia production has positive effects on the world nutrition and negative effects on the environment. Although Nobel laureate Fritz Haber<sup>448</sup> reported the use of osmium (also uranium) as the first industrial catalyst for NH<sub>3</sub> synthesis from air-source dinitrogen (N<sub>2</sub>), the scarcity of these rare metals meant that the only alternative until the mid-1980s of the last century was based on iron oxides materials.<sup>449</sup> These provided stable activities during reaction and practically unlimited access due to the low-cost and abundance of Fe ores. However, the very harsh operating conditions, with temperatures around 350–525 °C and pressures varying between 10–30 MPa (100–300 atm) of Fe-based Haber–Bosch catalytic NH<sub>3</sub> synthesis,<sup>450</sup> ask for the

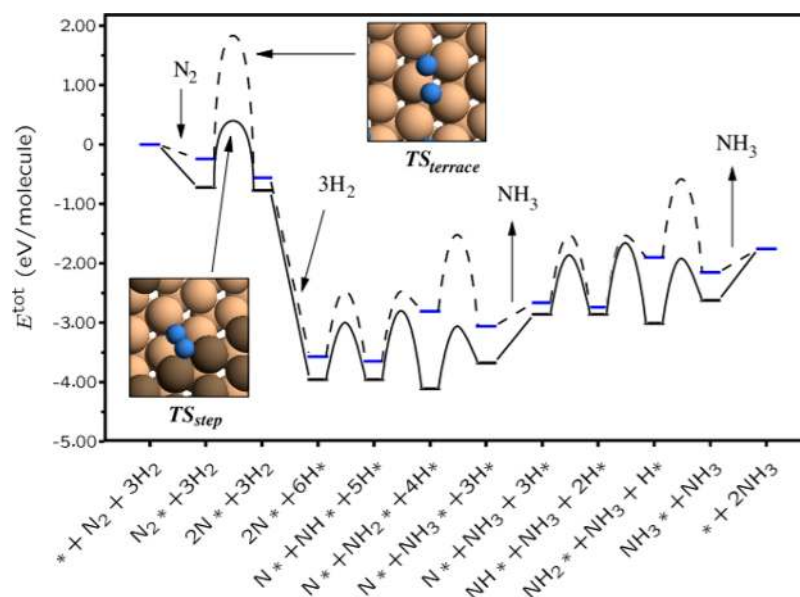
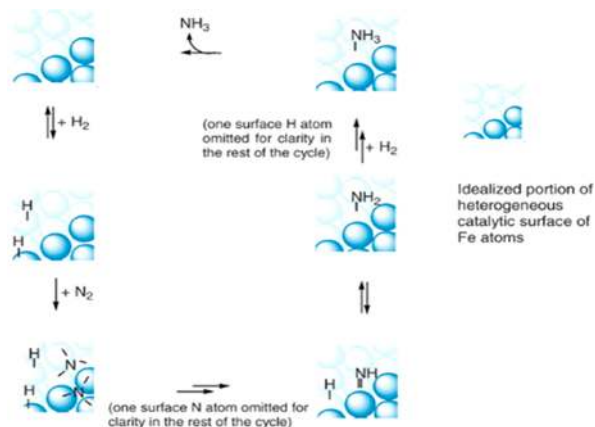


**Figure 55.** Showing the dissociative mechanism of  $N_2$  to ammonia on B5 sites. Reproduced with permission from ref 454. Copyright 2006 Elsevier.

searching of new alternatives. To date, ruthenium<sup>451</sup> was considered as the only possible realistic replacement. Although biologically active nitrogenases enzymes contain most of the time only a single metal atom, e.g., Mo, V, or Fe, it was commonly believed that for heterogeneous catalysts, several atoms (up to 7 to 8 metal atoms) or **B5 sites** were necessary for dinitrogen dissociation<sup>452,453</sup> and a concomitant activation and reduction of dinitrogen. The idea of this approach was a dissociative mechanism in which  $N_2$  is dissociated into two chemisorbed N atoms prior to their hydrogenation (Figure 55 and Scheme 45).

Recent results, both via SOMCat and SAC methodologies, have destroyed the common belief of the need of an ensemble of atoms to dissociate  $N_2$ . The DFT methods were proposing a nondissociative mechanism. There were two successive discoveries in SOMCat which showed that the dissociation of nitrogen is not necessary to produce  $NH_3$ .

**Scheme 45.** Modeling Study Showing All the Steps of Dinitrogen Dissociation on a Flat Fe Surface (Dotted Line) and on Stepped Fe (B5 Sites) (Full Line) According to Avenier et al.<sup>a</sup>



<sup>a</sup>Reproduced with permission from ref 455. Copyright 2007 The American Association for the Advancement of Science.

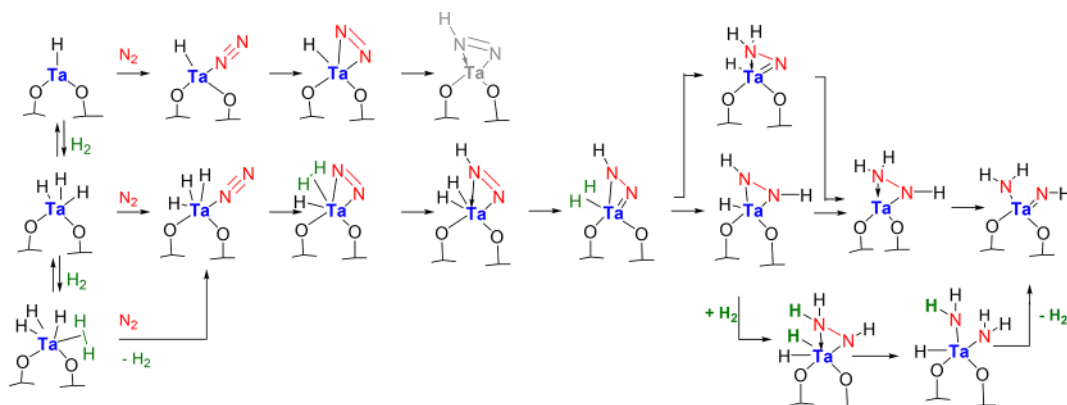
**4.5.3.1. Via SOMC.** First it was found that  $N_2$  dissociation and partial hydrogenation to amido ligands could occur on an isolated surface tantalum atoms supported on silica  $[(\equiv Si-O-)TaH_x(SiO_{2-700})_x = 1,3]$ ,<sup>455</sup> an unexpected result in the heterogeneous catalysis community. This work later inspired Li and Li<sup>453</sup> and Eisenstein et al.<sup>456</sup> in the elucidation of the mechanism of  $N_2$  dissociation and partial hydrogenation on a single Ta atom through a DFT approach. They hypothesized that the formation of the  $[(\equiv Si-O-)Ta(H)(-NH_2)_2]$  species by hydrogenation of  $[(\equiv Si-O-)Ta(H)(\eta^2-N_2)]$  followed an associative mechanism (Scheme 46), releasing about 90 kcal mol<sup>-1</sup>.

Although this work helped in the understanding of the chemistry of  $N_2$  activation and hydrogenation by well-defined single-site Ta-hydrides on silica, catalytic  $NH_3$  synthesis could not be observed with Ta due to the high stability of the silica supported  $[(Si-O)_2Ta(-NH_2)(=NH)]$  (Scheme 46).

**4.5.3.2. Via SAC.** Recently, an important theoretical paper appeared in which Hiromasa Tanaka et al.<sup>457</sup> have studied, by DFT, the grafting of an  $Fe_3$  cluster on the  $\theta-Al_2O_3(010)$ . They claim that it is a SAC or single cluster catalysis (SCC) strategy, although this is not purely single atom but a cluster of three Fe atoms linked together in a triangular geometry. They have studied the whole catalytic mechanism for conversion of  $N_2$  to  $NH_3$  on  $Fe_3/\theta-Al_2O_3(010)$  and found that an “associative mechanism”, in which the adsorbed  $N_2$  is first hydrogenated to  $-N=NH$  dominates the “dissociative mechanism”. This associative mechanism is attributed to the large spin polarization, low oxidation state of iron, and multistep redox capability of  $Fe_3$  cluster. The “associative mechanism” liberates the turnover frequency (TOF) for ammonia production from the limitation due to the Brønsted–Evans–Polanyi (BEP) relationship,<sup>458</sup> and the calculated TOF on  $Fe_3/\theta-Al_2O_3(010)$  is comparable to that of the so-called “Ru B5” site.<sup>459–461</sup>

Previous theoretical studies discussed the possibility of ammonia synthesis at low temperature and low pressure, but the TOF was limited due to the Brønsted–Evans–Polanyi (BEP) relationship.<sup>458,462</sup> The BEP relationship regulates the dissociation barrier of  $N_2$  and the desorption energies of  $NH_3$  scale linearly with the adsorption energy of N atom.<sup>458,463,464</sup>



Scheme 46. Associative Mechanism of N<sub>2</sub> Dissociation/Stoichiometric Reduction on a Single Ta Atom Obtained by SOMC<sup>a</sup>

<sup>a</sup>In this mechanism, the activation/reduction of N<sub>2</sub> is leading to a dead-end because [(Si-O-)<sub>2</sub>Ta(-NH<sub>2</sub>)(=NH)] is too stable as observed experimentally.

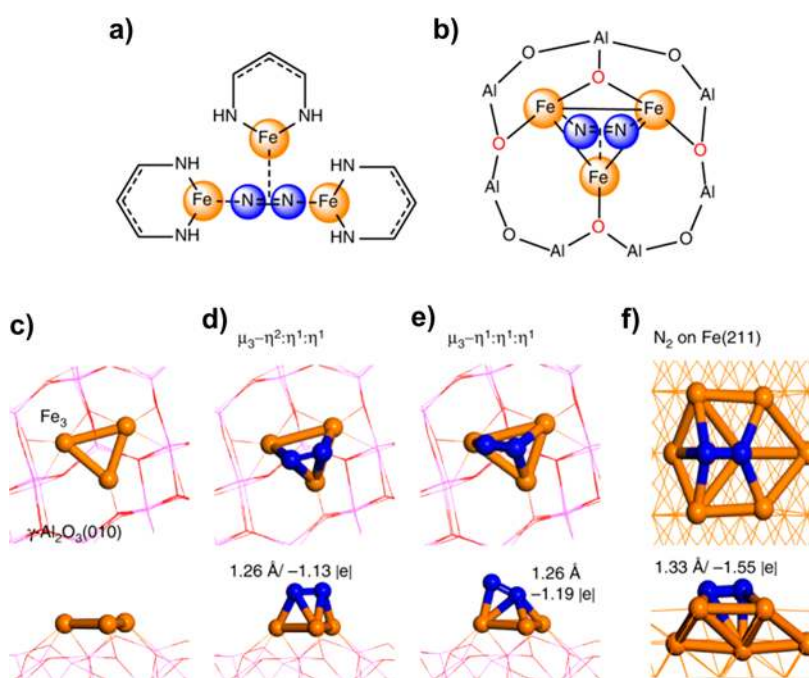


**Figure 56.** (a) Schematic representation of N<sub>2</sub> coordinated with three Fe(I)-ion homogeneous complexes in the side-on/end-on/end-on ( $\mu_3\text{-}\eta^2\text{:}\eta^1\eta^1$ ) configuration; (b) schematic representation of N<sub>2</sub> coordinated with heterogeneous Fe<sub>3</sub>/θ-Al<sub>2</sub>O<sub>3</sub>(010) in the same configuration; (c) optimized Fe<sub>3</sub> cluster on θ-Al<sub>2</sub>O<sub>3</sub>(010); (d,e) optimized configurations of N<sub>2</sub> adsorption on Fe<sub>3</sub>/θ-Al<sub>2</sub>O<sub>3</sub>(010); (f) N<sub>2</sub> adsorption configuration on the C7 site of Fe(211) surface. Reproduced with permission from ref 473. Copyright 2018 Springer Nature.

Stronger adsorption of N atom implies lower N<sub>2</sub> dissociation barrier but higher NH<sub>x</sub> desorption energies, such as on Re, Mo, and Fe metal surfaces, while weaker adsorption of N atom indicates higher N<sub>2</sub> dissociation barrier and lower NH<sub>x</sub> desorption energies, such as on Pd, Co, and Ni metal surfaces. Thus, a good metal catalyst for ammonia synthesis must have a moderate atomic N adsorption energy, around where the top of volcano plot is located.<sup>462,464</sup>

The remarkable recent development of surface single-atom catalyst (SAC) and single-cluster catalyst (SCC) demonstrates the possibility to build homogeneous catalytic active centers on heterogeneous solid surfaces.<sup>15,63,465–467</sup>

Several authors were inspired by nitrogenase, in which for some examples, bis Mo complexes<sup>457</sup> and iron complexes are responsible for N<sub>2</sub> activation and ammonia synthesis.<sup>468–470</sup> A series of multinuclear iron complexes were tried by DFT to

mimic the nitrogenase. It was found by modeling that the formally Fe(I) and Fe(0) complexes can weaken or even break N<sub>2</sub> triple bond at low temperature.<sup>471,472</sup> They proposed an active center of Fe<sub>3</sub> cluster anchored on the θ-Al<sub>2</sub>O<sub>3</sub>(010) surface. They also predicted that the direct dissociation of N<sub>2</sub> on this center is difficult (dissociative mechanism), but N<sub>2</sub> is easily hydrogenated to form the \*NNH species (associative mechanism), which has a much lower N–N bond dissociation barrier than that of \*N<sub>2</sub> (Figures S6, S7).

**4.5.4. Selective Catalytic Reduction of NO<sub>x</sub> by Ammonia (NH<sub>3</sub>–SCR).** The regulation on exhaust gases coming from cars is a challenge for automotive industry and for human health. One way to get rid of NO with regard to this issue is the reaction with NH<sub>3</sub>, which is described in the following equation:

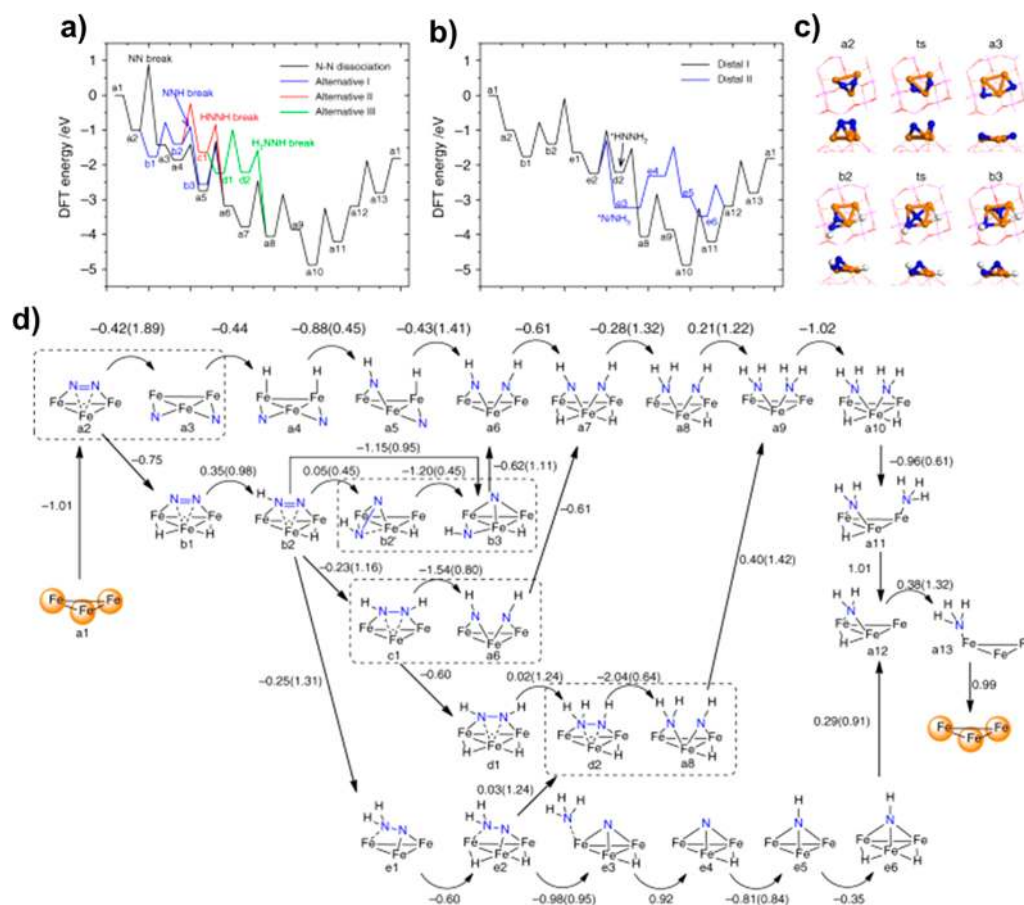
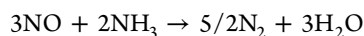


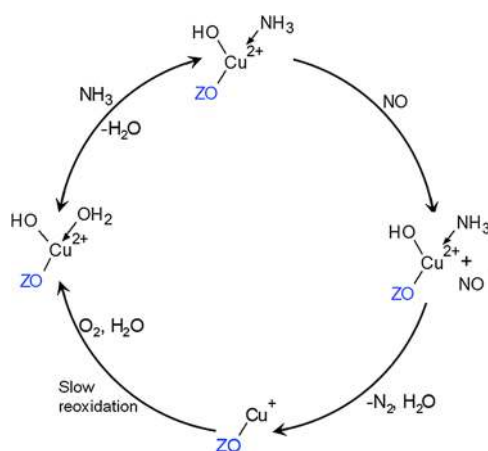
**Figure 57.** Energy diagrams for ammonia synthesis: (a) dissociative mechanism, and three pathways of associative mechanism with N–N bond dissociation at  $^*\text{NNH}$ ,  $^*\text{HNNH}$ , and  $^*\text{HNNH}_2$  intermediates by the alternating hydrogenation route. (b) Two pathways of associative mechanism by the distal hydrogenation route. (c) Initial, transition, and final states of  $^*\text{N}_2$  and  $^*\text{NNH}$  dissociation step. (d) Schematic depiction of the six reaction pathways for conversion of  $\text{N}_2$  to  $\text{NH}_3$  catalyzed by  $\text{Fe}_3/\theta\text{-Al}_2\text{O}_3(010)$ . Reaction energies are shown for every step and barriers are enclosed in brackets. The dissociation steps of  $^*\text{N}_2$ ,  $^*\text{NNH}$ ,  $^*\text{HNNH}$ , and  $^*\text{HNNH}_2$  intermediates are enclosed within dashed lines. Reproduced with permission from ref 473. Copyright 2018 Springer Nature.



Spectacular results have been obtained from chabazite-based catalysts Cu-SSZ-13 and Cu-SAPO-34. Interestingly, these catalysts based on Cu/zeolites are very likely to be single atoms of Cu present in the cavities of the zeolite (6 or 8 membered rings).<sup>474</sup> Many state of the art techniques have been used to characterize those materials particularly in *operando* high energy resolution fluorescence detected XAS (HERFD-XAS) and valence-to-core X-ray emission spectroscopy (V2C XES)<sup>143</sup> (see the Tools section). Most of the results tend to favor a mechanism occurring on  $\text{Cu}^{2+}$  linked to the Z–O–framework and surrounded by coordinated molecular water (Scheme 47).

It is probably the gaseous NO (a reducing agent as it gives  $\text{NO}^+$  and a reduced  $\text{Cu}^+$ ), which will react with coordinated ammonia or one of its derivatives (amide or imido) to give  $\text{N}_2$  and  $\text{H}_2\text{O}$ . Obviously, the real elementary steps of this process are still unknown at the moment, but at least this is the beginning of an understanding at a molecular level of this important reaction for environment. It is a rare example where single atom catalysts lead to a reasonable mechanism of a reaction, but one should mention here that each time a good definition of the catalyst is achieved by adequate techniques, the mechanism is pretty well understood.

**Scheme 47.** Mechanism of SCR on  $\text{Cu}^{2+}$ /Zeolite Proposed by Gunter et al.<sup>143</sup>



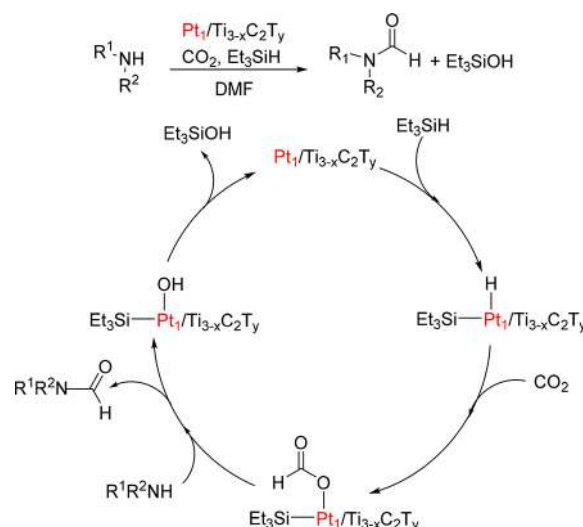
**4.5.5.  $\text{CO}_2$  Conversion for the Synthesis of Organic Compounds.** Conversion of  $\text{CO}_2$  to useful chemicals by catalytic methods is regarded as key strategy for recycling part of anthropogenic emissions by transformation into fuels and commodity chemicals.<sup>475–477</sup>  $\text{CO}_2$  conversion can be carried out with reduction of the central carbon atom, such as in the

synthesis of CO,<sup>478</sup> methane,<sup>479</sup> methanol,<sup>480,481</sup> and amines,<sup>482</sup> or it can be nonreductive. The latter kind of process is generally less energy-intensive<sup>483</sup> and can be carried out even under ambient conditions using very simple catalysts.<sup>484,485</sup> Moreover, it does not require sources of H<sub>2</sub> and leads to useful chemicals such as carbonates,<sup>486–488</sup> oxazolidinones,<sup>489</sup> and acrylates.<sup>490,491</sup> Use of CO<sub>2</sub> as substrate is known for both SOMCat and SAC although only partially explored for a limited set of reactions. In this context, one remarkable application of SOMC is for the preparation of catalysts for the reforming of CO<sub>2</sub> with methane<sup>492,493</sup> and for CO<sub>2</sub> reduction to methanol.<sup>494,495</sup> However, in these cases, catalysis is carried out by tiny, narrowly dispersed nanoparticles formed upon reduction of SOMC-prepared complexes and not by well-defined surface complexes or single atoms; metal atoms of the support are also involved in CO<sub>2</sub> activation.<sup>494</sup> In the case of SAC, CO<sub>2</sub> reduction to small molecules such as CO,<sup>496,497</sup> formate,<sup>498</sup> and methane<sup>499</sup> has become an active field of research in recent years. However, limited attention has been dedicated to the synthesis of more elaborated organic compounds. In this section, we provide a short overview of emerging processes where CO<sub>2</sub> is converted to organic products such as formamides and cyclic carbonates.

**4.5.5.1. Via SOMC.** In the case of SOMC, two main types of reactions have been investigated on single-site supported complexes: the insertion of CO<sub>2</sub> into well-defined silica-supported zirconium hydrides to produce formates<sup>170,500,501</sup> and the use of surface coordination fragments of niobium<sup>50</sup> and zirconium<sup>502</sup> chlorides as isolated or bimetallic catalysts for the synthesis of industrially relevant cyclic carbonates.<sup>475,503</sup> These heterogeneous inorganic Lewis acids can carry out the cycloaddition of CO<sub>2</sub> to epoxides under mild conditions ( $T = 60\text{ }^{\circ}\text{C}$ ,  $P_{\text{CO}_2} = 1\text{--}10\text{ bar}$ ). In the case of SOMC-prepared zirconium complexes, actual industrial flue gas could be used as impure source of CO<sub>2</sub>.<sup>502</sup> These studies were carefully reviewed in previous work and will not be discussed here in detail except for comparison with SAC-based catalysts.

**4.5.5.2. Via SAC.** Chen et al. used titanium surface deficit-defects of Ti<sub>3–x</sub>C<sub>2</sub>T<sub>y</sub> nanosheets (metal carbide with titanium vacancies; T: O, OH, F) to support and stabilize platinum atoms by formation of strong bonds with neighboring carbon atoms.<sup>504</sup> When [PtCl<sub>6</sub>]<sup>2–</sup> anions were adsorbed on Ti<sub>3–x</sub>C<sub>2</sub>T<sub>y</sub> nanosheets, presenting titanium vacancies due to treatment with HCl/LiF, reduction of platinum was observed without H<sub>2</sub> treatment to yield Pt<sub>1</sub>/Ti<sub>3–x</sub>C<sub>2</sub>T<sub>y</sub>. Indeed, XPS investigation showed that the platinum atoms were reduced to an average oxidation number between 0 and +2. This was accompanied by oxidation of titanium atoms at the defect sites. EXAFS analysis demonstrated that platinum atoms were placed at positions previously occupied by titanium atoms before HCl/LiF treatment and surrounded by three carbon atoms each. No Pt–Pt contribution was identified, thus excluding formation of nanoparticles. Pt<sub>1</sub>/Ti<sub>3–x</sub>C<sub>2</sub>T<sub>y</sub> was used as catalyst for the N-formylation of amines using CO<sub>2</sub> as source of carbonyl and triethylsilane (Et<sub>3</sub>SiH) as stoichiometric reductant (Scheme 48). Pt<sub>1</sub>/Ti<sub>3–x</sub>C<sub>2</sub>T<sub>y</sub> was able to formylate several aromatic and aliphatic secondary amines in very high yields and selectivity. It also showed good reusability with a progressive but moderate loss of performance within five catalytic cycles. Importantly, platinum nanoparticles supported on carbon or on Ti<sub>3–x</sub>C<sub>2</sub>T<sub>y</sub> afforded much lower yields of formylated products than Pt<sub>1</sub>/

**Scheme 48.** Formylation of Amines with CO<sub>2</sub> Using Pt<sub>1</sub>/Ti<sub>3–x</sub>C<sub>2</sub>T<sub>y</sub> as Catalyst and Et<sub>3</sub>SiH as Reducing Agent<sup>a504</sup>



<sup>a</sup>The proposed and calculated mechanistic routes are also shown.

Ti<sub>3–x</sub>C<sub>2</sub>T<sub>y</sub> when tested under identical conditions using aniline as substrate.

Mechanistic studies (Scheme 48) revealed a formylation pathway where the Si–H bond of the silane is activated by platinum followed by CO<sub>2</sub> insertion in the Pt–H bond. Attack of the amine on the latter intermediate leads to formamide product, whereas reductive elimination of silanol restores the catalyst.

The largest reaction barrier (1.24 eV) using Pt<sub>1</sub>/Ti<sub>3–x</sub>C<sub>2</sub>T<sub>y</sub> was calculated for the step of silanol reductive elimination. Remarkably, when the same mechanistic barrier was calculated for platinum nanoparticles, the step of amine attack on the Pt–OCO<sub>2</sub>H moiety was found to have a barrier of 2.57 eV; much higher than 1.04 eV determined for Pt<sub>1</sub>/Ti<sub>3–x</sub>C<sub>2</sub>T<sub>y</sub>. This difference was attributed to higher steric hindrance and different coordination environment of platinum in the nanoparticles. There are no reports of an equivalent formylation reaction in SOMCat, but it is likely that it could be afforded by supporting low-valent platinum complexes on a metal oxide surface to leave a sufficient number of open coordination sites for binding Et<sub>3</sub>SiH.

The synthesis of organic carbonates from CO<sub>2</sub> and epoxides has become a very active field of investigation in the past decade<sup>505–507</sup> as it allows fixation of CO<sub>2</sub> under mild<sup>508</sup> or ambient<sup>484,485,509</sup> conditions and affords useful compounds that serve as chemical intermediates for synthesis of plastics<sup>503,510,511</sup> and solvents.<sup>512,513</sup> Among several classes of heterogeneous catalysts,<sup>488</sup> systems involving single-atoms acting as Lewis acids for epoxide activation are well-established, including metal centers in MOFs,<sup>514–516</sup> in immobilized molecular complexes on silica<sup>517</sup> or as components of porous organic polymers.<sup>518,519</sup> These materials have been carefully reviewed.<sup>488,519</sup> In this section, we will describe two materials where single atoms are not part of preformed metal–organic complexes or MOFs.

Wang et al. targeted the preparation of highly active heterogeneous catalysts for the synthesis of cyclic carbonates from CO<sub>2</sub> by preparation of single atoms of zinc embedded in nitrogen-doped graphene (NG).<sup>520</sup> The catalytic material was prepared by mixing electrochemically exfoliated graphene with



melamine as a source of nitrogen atoms and zinc oleate as a source of metal. Following pyrolysis, atomically dispersed zinc atoms were found to be embedded in the nitrogen-doped carbon material (the final material was denoted as NG-aZnN). The morphology of the material was constituted by hollow graphitic shells dispersed on NG. The coordination environment of zinc was investigated by XPS and EXAFS. The latter technique revealed the zinc center as tetracoordinated. Moreover, a first coordination shell scattering peak at 1.56 Å was attributed to potential Zn–N bonding and was corroborated by the observation of overlapping EDS distributions for N and Zn. On the basis of these data, the authors attributed  $[\text{ZnN}_4]$  coordination to the zinc atom of NG-aZnN.

NG-aZnN was investigated as a catalyst for the cycloaddition of  $\text{CO}_2$  to epoxides using propylene oxide as a model substrate in the presence of quaternary ammonium bromide salts as a homogeneous nucleophilic catalytic component. When used in combination with relatively expensive tetraheptylammonium bromide, NG-aZnN led to the formation of propylene carbonate (PC) in quantitative yield at 120 °C, 10 bar  $\text{CO}_2$ . It is worthy of note that these reaction conditions are harsher than reported for state-of-the-art catalysts presenting SAC embedded in salen<sup>521</sup> or porphyrin complexes.<sup>522</sup> The use of NG-aZnN could be successfully extended to other terminal epoxides, but more challenging internal epoxides led to only moderate yields. When harsher reaction conditions were applied (160 °C, 10 bar  $\text{CO}_2$ ), 98% PC was obtained in just 1 h, leading to very high TON and TOF values (TON = 8666, TOF = 2889  $\text{h}^{-1}$ ). However, the authors did not discuss the possible occurrence of  $\text{Zn}^{2+}$  (a powerful homogeneous catalyst in this kind of reaction) leaching to the reaction solution. The reaction mechanism for the NG-aZnN-catalyzed cycloaddition was proposed to follow the classical steps<sup>484,524</sup> of nucleophilic ring-opening of the Zn-coordinated epoxide by the bromide anion,  $\text{CO}_2$  insertion in the alkoxide and five-membered ring closure as depicted in Scheme 49.

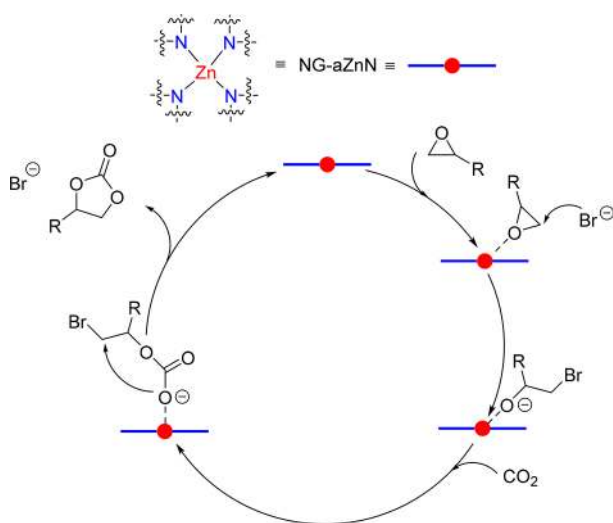
A different approach to the production of single zinc atoms in  $[\text{ZnN}_4]$  coordination environment but with a much higher

metal loading (11.3% versus 1.62% of the previous example) was reported by Jiang et al.<sup>525</sup> The authors produced hollow N-doped nanoparticles bearing isolated zinc atoms (HPC) by pyrolysis of ZIF-8 MOF grown around functionalized polystyrene nanospheres. The polystyrene core was removed by treatment in DMF (dimethylformamide). Pyrolysis of the thus-prepared ZIF-8 led to carbon nanoparticles rich of nitrogen and zinc (Figure 58). Despite the high zinc loading, the isolation of the Zn atoms was confirmed by HAADF-STEM investigation, whereas the absence of ZnO could be excluded by XRD and XPS analyses. XANES and EXAFS spectroscopies revealed zinc oxidation number between 0 and +2 and  $[\text{ZnN}_4]$ -type coordination which is similar to parent MOF ZIF-8, respectively. The presence of such coordination environment allows high loading of atomically dispersed metal. Additionally, it was observed that HPC had the ability to harvest light in a broad range of frequencies (230–800 nm) due to its hollow structure which allowed multiple reflections within the internal cavity.

HPC was applied as catalyst for the cycloaddition of  $\text{CO}_2$  to several epoxides in the presence of TBAB as a source of nucleophilic anions for epoxide ring opening (Scheme 49). The reaction was carried out under atmospheric  $\text{CO}_2$  pressure and using full-spectrum irradiation as source of heat. The carbonate product of epibromohydrin as model substrate was obtained in nearly quantitative yield (94%) under such conditions with HPC pyrolyzed at 800 °C (HPC-800) as the best material. However, the yield dropped to just 51% when the irradiation range was restricted to visible light. Control experiments were carried out to confirm the importance of the hollow structure, the recyclability of HPC-800, and the heterogeneous character of the reaction (filtration test). This study demonstrates that it is possible to obtain single atom catalysts with high metal loading and the possibility of using light irradiation for  $\text{CO}_2$  conversion by SAC.

Overall, there has been limited investigation on the use of SAC and SOMCat for the synthesis of  $\text{CO}_2$ -derived organic products; nevertheless, both SAC (synthesis of formamides, cyclic carbonates) and SOMC-prepared catalysts (synthesis of cyclic carbonates) have been reported with promising results. For the synthesis of organic compounds that involves reduction of  $\text{CO}_2$ , such as formamides, and that requires the use of noble metals and the addition of reducing agents, SAC appears to be favored over SOMCat for its ability to employ supports able to stabilize single noble metal atoms in low-valent oxidation state under reductive conditions. Both methodologies are suitable for the synthesis of cyclic carbonates by cycloaddition of  $\text{CO}_2$  to epoxides because the latter reaction requires only a Lewis acidic metal center (Scheme 49) and allows high flexibility in the coordination environment of the metal. When comparing SOMCat and SAC for the synthesis of carbonates, it should be noted that the former methodology allows  $\text{CO}_2$  conversion under very mild conditions (60 °C, 1 bar) without the need of full-spectrum irradiation and can use flue gas  $\text{CO}_2$  as feedstock.<sup>502</sup> Another potential advantage of SOMCat over SAC, for the specific case of  $\text{CO}_2$ –epoxide cycloaddition, is the possibility to coimmobilize the nucleophilic ammonium salt cocatalyst with the metal on silica using aminosilane derivatives.<sup>505</sup> This kind of functionalization is unlikely to be applicable for the examples of SAC reviewed above in partially homogeneous systems. Importantly, single-site isolation is not necessarily the best option in the synthesis of carbonates as, in several cases,

**Scheme 49.** Proposed Mechanistic Cycle for the Cycloaddition of  $\text{CO}_2$  to Epoxides Catalyzed by NG-aZnN/TBAB<sup>520</sup>



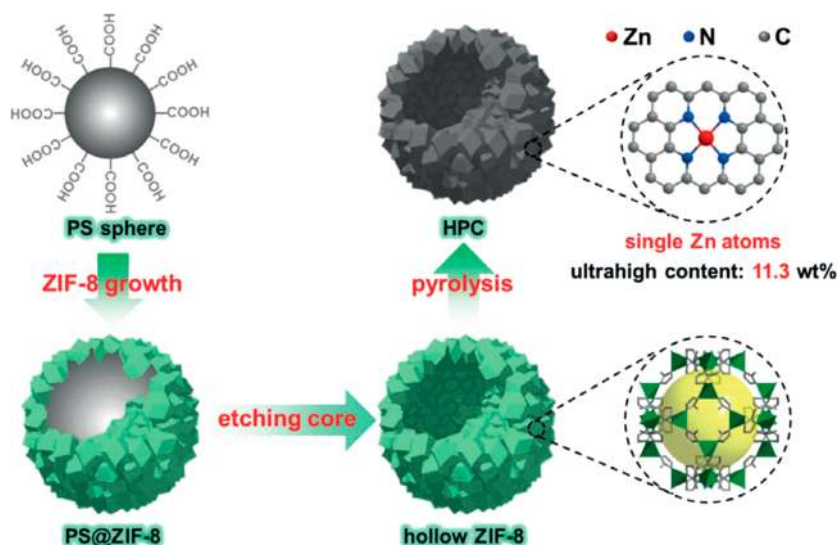


**Figure 58.** Preparation of HPC nanoparticles starting from hollow ZIF-8 MOF grown around functionalized polystyrene nanospheres. Reproduced with permission from ref 525. Copyright 2019 John Wiley and Sons.

bimetallic systems were found to function better than the corresponding monatomic complexes.<sup>50,526</sup> Given the promising results reported in this brief overview, it is expected that both techniques might soon find applications in several emerging organic transformations involving CO<sub>2</sub>.<sup>476,499,527</sup>

## 5. CONCLUSIONS AND PERSPECTIVES

In this review, we have emphasized the analogies and differences between SAC, SAAC, and SOMCat in several classical processes involving C–H, C–C, O<sub>2</sub>, N<sub>2</sub>, and CO<sub>2</sub> activation and in several emerging reactions. The fact that a single atom possesses catalytic activity was a kind of revolution in classical heterogeneous catalysis but not when considering homogeneous catalysis or biocatalysis. Single atom catalysts evolved recently through synthesis of smaller and smaller nanoparticles until reaching the size of a single atom, but the concept of catalysis by isolated single atoms was suggested earlier in heterogeneous catalysis by metal nanoparticles. It was observed that an isolated atom surrounded by inert metal atoms could achieve very selective reactions. This area was defined as single atom alloy catalysis (SAAC). Earlier than SAC or SAAC, a previously developed discipline, SOMCat, had already shown that single atoms, with a well-defined coordination sphere, could be involved in a variety of catalytic reactions. More importantly, SOMCat progressively evolved into a predictive approach by introducing the concept of surface organometallic fragment SOMF and surface coordination fragment SCF. By simply analyzing the possible mechanism of any reaction from molecular chemistry concepts, and by accessing the catalytic cycle using the suitable surface organometallic fragment or surface coordination fragments, it was possible to discover new reactions or improve existing ones.

A selection of the most powerful characterization methods applied for both for SAC and SOMCat were presented: transmission electron microscopy, X-ray spectroscopies (XANES, EXAFS, XES), and NMR. Transmission electron microscopy aims primarily at demonstrating that an atomic dispersion has been achieved through the sample. Combining X-ray fluorescence or electron energy loss spectroscopies in the microscope helps to identify the nature of the single atoms,

especially when several types are present. X-ray spectroscopies allow determining of the oxidation states of metal, coordination geometry, and the nature of ligands bounded to metal center (especially with XES), including those located at the metal–support interface. This is important in the context of single-atom catalysis because support atoms are actually ligands and influence reactivity and catalytic performance. On the other hand, the characterization of the ligand is better revealed using NMR spectroscopy. NMR spectroscopy gives an edge over other spectroscopic techniques when it comes to determination of structure of a metal complex attached with ligand fragments. Not only it is used for the structure elucidation of the molecular complex, but with advanced NMR technique it is now very convenient to trap and determine the reaction intermediate in a catalytic cycle. Specifically, for SOMC complexes, it is the most desirable tools for structure determination. As additional tool to provide rational insights into the fundamental properties of the discussed systems, a modeling perspective based on DFT has also been presented. The different approaches commonly used to study theoretically the physicochemical features and the reactivity of the metallic species on the support were discussed.

The catalysis section of this review has been classified based on the different kinds of reactions:

### 5.1. Hydrogenation

SOMCat, SAAC, and SAC can carry out hydrogenation of alkynes, alkenes, dienes, and aromatics. SOMC-prepared Zr hydrides can be used in 2-butenes hydrogenation without any problem and the mechanism is well understood. Note that bis-hydrides are more active than monohydrides. Another surprising reaction was published by Coperet, who discovered the hydrogenation of propene on Co on silica. The originality of this mechanism comes from the heterolytic splitting of hydrogen on a Co–O bond. This surprising result is, however, consistent with previous studies by Cvetanovic and Baranski, in which the heterolytic splitting of hydrogen was discovered on magnesia and zinc oxide.<sup>528</sup> Interestingly, by SOMCat, cationic Ti, Zr, and Hf supported on sulfated-alumina's can hydrogenate aromatics. Overall, this is a surprising reaction because

the catalysis community would not expect that it could occur on a single atom.

With SAAC many hydrogenation reactions were observed on single Pd/Cu, Pd/Ag, and Pd/Au atoms. Selectivity could be observed on phenyl acetylene to styrene on Pd/Ag. The single atoms of Pd/Ag could hydrogenate acrolein to allylic alcohols. The reduction of nitrobenzene to aniline with various possible selectivities was observed with Pd/Au.

Regarding SAC, interesting results were observed on single Pd atoms on graphene, where butadiene can be hydrogenated to various isomers of butenes. Interestingly, single Pd atoms avoid secondary hydrogenation reactions to butane because a single atom cannot coordinate the butadiene molecule by its two double bonds. In contrast, Pd nanoparticles can coordinate butadiene by both double bonds, resulting in butane formation.

Hydrogenation reactions can occur with various degrees of selectivity on any kind of single atom (SAC SAAC or SOMCat) without showing any strong difference of selectivity or activity between these domains. Perhaps, one could say that heterolytic splitting of hydrogen and hydrogenation of aromatics could be considered as a particular advantage of SOMCat. The hydrogenation of butadiene is a positive case for SAC.

## 5.2. Hydrogenolysis

Hydrogenolysis of paraffins was probably the first reaction discovered with SOMCat taking place at low temperature. It was carried out with well-defined zirconium hydrides on silica, a very electron deficient compound (formally eight electron species, without considering  $p\pi-d\pi$  back-bonding). The mechanism was very straightforward considering the well-known elementary steps of  $\sigma$ -bond metathesis and  $\beta$ -alkyl transfer of organometallic chemistry already observed with early transition metals or lanthanides. However, when moving from group 4 to groups 5 and 6, the  $\beta$ -alkyl transfer did not occur anymore. Instead,  $\alpha$ -alkyl transfer took place leading to a carbene-hydride.

The next step after hydrogenolysis was the “metathesis of alkanes” using Ta/silica for which the mechanism was elucidated by identification of the primary products of reaction (olefin and hydrogen). Afterward, the metathesis reaction was extended to W and then to bimetallic systems such as Ti/W, for which knowledge of the mechanism suggested stepwise preparation of Ti centers for dehydrogenation of paraffins to olefins and of W complexes for olefins metathesis. Spectacular TON values were thus obtained. These discoveries clearly reflect the concept of SOMCat becoming a predictive science for heterogeneous catalysis with single atom materials. Mechanistic understanding of both hydrogenolysis and metathesis of alkanes was at the origin of several new reactions such as cross-metathesis of light and heavy alkanes, cleavage of alkanes by methane, nonoxidative coupling of alkanes, metathesis of cyclo-alkanes, and transformation of methane or higher alkanes to liquid fuels. Such reactions do not find equivalent in catalysis by SAC and SAAC; with SAAC, there is just one example of hydrogenolysis of methyl glycolate (MG) to ethanol with Pt/Cu. The mechanism seems to occur via a free radical mechanism. With SAC, and to our knowledge, there is no metathesis of alkanes because most of the examples in SAC are dealing with late transition metals. It is very likely that when with SAC, one will be able to move from late

transition metals to early transition metals, alkane metathesis will be observed.

## 5.3. Dehydrogenation

SOMCat dehydrogenation of paraffins to olefins was reported with Ga associated with Pt/silica, Ga/silica,  $\text{Fe}^{2+}$ /silica,  $\text{Cr}^{3+}$ /alumina,  $\text{Co}^{2+}$ /alumina, and  $\text{V}^{5+}$ /silica. Not all the results are in agreement, especially in the Ga case, and the reaction mechanism is not yet totally clear. Computational approaches have revealed very high energy barriers for the proposed C–H activation by the metal–support bond. Interestingly, for this reaction, the ligands of SOMC-prepared catalysts were generally removed by thermolysis to generate single atoms covalently bound to the support. Therefore, the comparison between SOMCat and SAC corresponds to a comparison between non-noble and noble single atoms. The latter species are highly active for the conversion of hydrocarbons but generally lack of selectivity and lead to cracking by C–C activation. It is evident that single noble atoms need to be embedded in a matrix of inactive atoms to achieve selectivity toward dehydrogenation.

## 5.4. Methane Activation

The development of heterogeneous catalysts that are active for methane activation and conversion was discussed. Research is going toward well-defined systems where single atoms act as active centers. In this review, some examples of SAC, SAAC, and SOMCat were highlighted to illustrate similarities and differences. The reported examples demonstrate that the three fields are converging toward species with well-defined, single-site character to exclude inactive sites which affect activity and selectivity. We showed that there are numerous examples of SACs active for methane activation with extraordinary outcomes. These results could be further improved by eliminating impurities and species with nonsingle atom character.

## 5.5. Metathetic Oxidation

This new reaction is possible because well-defined molybdenum bis-oxo can be easily grafted on silica via two  $\sigma$ -bonded oxygen atoms. A very original mechanism that splits an internal olefin in the middle with creation of two aldehydes was reported. The reaction can be very selective. In this case, the active surface organometallic fragment is an oxo ligand  $[\text{M}]=\text{O}$ . This reaction is currently not available for SAC because of the absence of well-defined metal-oxo moieties.

## 5.6. Imine Metathesis

Similar to the previous case, two imines can be metathesized by cleavage of the  $\text{C}=\text{N}$  bond in the middle and redistribution of the imine fragments like in olefin metathesis. Interestingly, the surface organometallic fragment here is an imido ligand  $[\text{M}]=\text{NR}$ .

## 5.7. Emission Control for SCR Catalysts for Automotive Diesel NO<sub>x</sub>

This very useful reaction for exhaust car systems is important for the removal of  $\text{NO}_x$  and particles from the exhaust gases. These toxic gases are one of the main causes of pollution in all cities worldwide. Interestingly one of the best catalysts known thus far is a single-site Cu/zeolite system. The mechanism is fairly well understood. Cu acts as SAC with no specific extra ligands except the zeolite framework.



### 5.8. CO<sub>2</sub> Conversion to Organic Compounds

Catalysts based on SAC and SOMC have recently appeared for the highly sought-after preparation of organic compounds from CO<sub>2</sub>. For the synthesis of cyclic organic carbonates from cycloaddition of CO<sub>2</sub> to epoxides, new active materials have been successfully prepared by both methodologies by supporting Lewis acidic metal complexes (SOMC) or single atoms (SAC). In both cases, only the Lewis acidic catalytic component was immobilized, and the nucleophilic component was used as soluble additive. For future development of truly heterogeneous systems for this reaction, the SOMC approach seems advantageous over SAC because nucleophilic moieties can be easily added on metal oxide support (for instance by functionalization with 3-aminopropyltriethoxysilane derivatives). Additionally, SOMC allows more flexibility on the kind of metal and on its chemical environment. For reactions that involve CO<sub>2</sub> reduction, the SOMC methodology can be applied to prepare tiny (about 1 nm) and homogeneously dispersed nanoparticles upon reduction of supported single-site noble metal complexes. On the other hand, SAC allows to investigate the activity of isolated noble metal atoms that are stabilized on specific supports; using the latter concept, SAC-prepared single platinum atoms were reported to produce formamides from CO<sub>2</sub> and amines. Overall, both techniques are still limited to a restricted selection of reactions for CO<sub>2</sub> conversion and the portfolio of processes investigated on both techniques is expected to increase in years to come.

On the basis of the concepts highlighted throughout this paper we present below conclusive remarks on the affinities and differences between SOMCat and SAC and perspectives on the way both communities might collaborate in the future.

### 5.9. Affinities

Heterogeneous catalysis on well-defined metal sites has a great advantage over homogeneous catalysis: SAC, SAAC, and SOMCat do not suffer from deactivation by bimolecular processes. In both methodologies, extremely electron deficient catalysts with eight valence electrons can be stabilized. This is almost impossible to achieve in solution unless using a strategy of ligands design that, so far, was not successful. Such electron deficient atoms are at the origin of low temperature C–H and C–C bond activation in SOMCat (by respectively  $\sigma$ -bond metathesis followed by  $\alpha$ - or  $\beta$ -alkyl transfer).

The elementary steps for forming or breaking bonds can be rationalized in homogeneous catalysis based on knowledge of modern organometallic chemistry and of reaction mechanisms in molecular chemistry. It is obvious that both SAC and SOMCat, where the catalytic process occurs on a single metal sites like in most homogeneous reactions, are disciplines for which rational design of heterogeneous catalysts will have to be derived from molecular catalysis. The two communities of molecular chemistry and heterogeneous catalysis should be more connected to open a huge domain of emerging research for the future.

The main drawback of SOMCat and perhaps SAC is the high sensitivity of these species to moisture and oxygen (especially with early transition metals). Besides, both kinds of catalysts may migrate on the surface following thermal treatments: either by penetrating into the bulk of the oxide support (for early transition metals) or by aggregation to small metal particles (for late transition metals). In both cases, the activity or selectivity of the single atom is lost. The choice of

the supports is of the greatest importance to tune or limit the mobility of single atoms or surface organometallic complexes.

This is perhaps the reason why industry has not yet steered into the direction of SOMCat and/or SAC: organometallic chemistry appears too sensitive to environmental conditions, temperature, and so on. It is only the polymerization community, which has been dealing with air sensitive catalysts. A big effort has to be made in this direction. Research should be focused on reducing the sensitivity of highly electron deficient atoms and complexes against moisture. Some results were obtained by protecting highly efficient SAC or SOMC-based catalysts by grafting them in cavities of zeolites or mesoporous materials. Future work should focus also on more hydrophobic support materials. Synthesis of catalysts should follow the rational catalysis-by-design approach, which, however, does not always fit within industry requirements of simplicity and low costs. Nevertheless, catalysis by SAC and SOMCat can provide crucial information on the importance of site isolation, oxidation number, and coordination environment of the actual catalytically active species. These factors are crucial to improve the design of industrial catalysts.

### 5.10. Differences

With respect to characterization, SAC-based systems suffer from the fact that they might not always be constituted by identical, single-site species. Tools such as EXAFS, XANES, IR, and XPS give an average value among all surface species. In catalysts obtained by SOMC, the identical nature of all sites renders the interpretation of their structure easier and more reliable than SAC. The combination of all modern characterization tools (X-ray spectroscopies, NMR, and TEM can highlight with high accuracy the coordination sphere of the surface organometallic fragments. In case of SAC, a more careful control of their synthesis, support, temperature of deposition, and/or activation is necessary to develop SAC as single-site species.

Chemically, a main difference between the methodologies is that SACs (and SAACs) are generally produced from late transition metals (as Pt, Cu, Fe) by techniques (e.g., by impregnation, electrochemical routes, atomic layer deposition, etc.) that can be applied on a variety of supports such as metal oxides, zeolites, graphene, etc. On the other hand, surface organometallic catalysts are always prepared using organometallic precursors or, in some cases, coordination compounds (mainly from early transition metals as Zr, W, or Mo) on a well-defined surface (dehydroxylated silica, alumina, and recently also zeolites, MOF) to reach uniform distribution of active sites based on single atoms. The challenge of SOMCat is that early transition metals are very sensitive to oxygen, and the preparation and application of the catalysts is, in most cases, restricted to oxygen-free atmosphere. However, this approach allows for well-defined ligand systems and reactions, which can be followed by spectroscopic methodology such as SS NMR spectroscopy, IR spectroscopy, etc., to predict precise mechanisms and further improve the catalysts. Many SOMC-based catalysts have been developed even if their synthesis is, in most cases, more challenging than SAC. Results in the nonoxidative coupling of methane to ethane and hydrogen show that much lower activation temperatures compared to SACs are needed.<sup>344,345</sup> This is because of the well-defined character of surface organometallic catalysts.

The chemical difference between the active sites of SAC (and SAAC) and those of SOMC complexes reflects also in the

need for different computational models to simulate the catalysts. For instance, periodic slab models are employed for SAC (and SAAC) and mainly adsorption properties together with binding strength and electronic structure calculations are carried out limiting usually the amount of kinetic analysis performed. On the other hand, small cluster models are adopted for SOMCat and the computational studies often aim at clarifying the whole mechanistic picture.

### 5.11. Concluding Remarks and Future Development

As shown in this review, a clear advantage of SOMCat over SAC and SAAC is the presence of a well-defined coordination sphere on the metal center, designed on the basis of molecular chemistry mechanisms, that allows a predictive approach to catalysis. The generation of well-defined hydrides, metal alkyl, metal alkylidene, metal oxo, and bis-oxo moieties, among others, enables access to mechanistic information and to classes of reactions that are yet to be seen in catalysis by SAC and SAAC; in SAAC, in the presence of hydrogen, hydrides are very likely to be formed (Scheme 29), however, in SAC, nothing is really known about the ligands present on the atoms “adsorbed” on the support. Indeed, whereas isolated palladium atoms on copper surface or gold surface clearly activate hydrogen, the dissociated hydrogen atoms easily spill over to the support.<sup>250,529</sup> Nevertheless, very recent advances have shown that single atoms of early transition metals that are also widely exploited in SOMCat, such as Ta,<sup>46</sup> Mo,<sup>530,531</sup> and W,<sup>532,533</sup> can be prepared via different techniques on supports such as metal oxides (silicon wafer,<sup>46</sup> Ni(OH)<sub>2</sub><sup>532</sup>) and N-doped carbon,<sup>530,533</sup> where hydrogen spill over should not easily occur under mild conditions. One could expect that, using analogous SAC systems based on coordinatively unsaturated early transition metals, metal hydrides could be easily generated on supports that are normally inaccessible for SOMC (for instance carbon-based supports or several kinds of MOFs) and reactions such as alkane metathesis could certainly be observed, and perhaps spectacular results be obtained. It should also be possible to study processes such as low temperature hydrogenolysis of paraffins, but probably even more interesting is the low temperature hydrogenolysis of polyolefin. Similarly, metal-oxo and bis-oxo moieties could be generated on supported single atoms by controlled reaction with molecular oxygen. Indeed, it was shown that tantalum single atoms on silicate support could be oxidized by air after deposition and serve as epoxidation catalysts.<sup>46</sup> Such approach could be used for the metathetic oxidation of olefins and for oxidative dehydrogenations on single atoms of Mo and V, respectively. Overall, future developments could show that it is possible to “do chemistry” with SAC to develop new catalysts in place of direct application as-prepared. Careful functionalization of readily synthesized SAC on a variety of supports by introduction of catalytically active moieties discovered via SOMCat could represent a powerful approach toward improved catalysts with potential to merge beneficial aspects of both methodologies.

Regarding catalysis by SAAC, one should also consider the mechanisms from molecular chemistry. For instance, the mechanism of isobutane dehydrogenation or isomerization to isobutene or *n*-butane described in this review article are perfectly understood based on molecular mechanisms. Francois Gault and co-workers pioneered such an approach.<sup>534</sup> New developments are expected on the isolation of single atoms on nanoparticles composed of inactive metals. The

isolation of Pt atoms on a Pt/Sn nanoparticle, described in this review, could open new directions in this chemistry. This area should be developed further in the future.

### AUTHOR INFORMATION

#### Corresponding Author

\*Phone: 966 544 700 047. E-mail: [jeanmarie.basset@kaust.edu.sa](mailto:jeanmarie.basset@kaust.edu.sa).

#### ORCID

Valerio D'Elia: 0000-0002-5881-2496

Laura Falivene: 0000-0003-1509-6191

Moussab Harb: 0000-0001-5540-9792

Samy Ould Chikh: 0000-0002-3486-0944

Luigi Cavallo: 0000-0002-1398-338X

Jean-Marie Basset: 0000-0003-3166-8882

#### Notes

The authors declare no competing financial interest.

#### Biographies

Manoja Samantaray completed his Ph.D. from IIT Bombay India in 2009 in the field of synthesis and application of N-heterocyclic carbene in C–C and C–N bond forming reaction. After completing two years as a postdoctoral researcher at CPE, Lyon, France, in the field of ruthenium-based hybrid materials for RCM reaction, he moved to King Abdullah University of Science and Technology. Currently, he is working as a research scientist with Professor Jean-Marie Basset at the Catalysis Center in King Abdullah University of Science and Technology (KAUST). His primary research focus is on the design/synthesis of oxide-supported well-defined single site catalyst for alkane metathesis reaction. Besides alkane metathesis, he also worked on olefin, alkyne, and imine metathesis as well as olefin oxidation reaction.

Valerio D' Elia (from Avezzano, Italy) received his Master's in chemistry from the University of Perugia (2001). Following a period in the pharmaceutical industry (Dompe, L. Aquila), he received a Ph.D. (2009) in organic chemistry from the University of Regensburg (supervisor: O. Reiser). After postdoctoral research at LMU Munich (supervisor: H. Zipse), he moved to Kaust Catalysis Center in Saudi Arabia as a research scientist in the group of J.-M. Basset. Since 2015, he is a faculty member at the Vidyasirimedhi Institute of Science and Technology (VISTEC) in Thailand. His research interests are catalysis, CO<sub>2</sub> conversion, and cyclic carbonates.

Eva Pump's research focuses on the design, development, and mechanistic understanding of homogeneous and well-defined heterogeneous catalysts. Since 2015, she works with Prof. Jean-Marie Basset on heterogeneous catalysts prepared by the “surface organometallic chemistry” (SOMC) approach for applications related to sustainable energy production.

Laura Falivene is currently research scientist at King Abdullah University of Science and Technology (Saudi Arabia) within the Catalysis Center. She received her Ph.D. (2014) in computational chemistry at University of Salerno (Italy) under the supervision of Prof. Luigi Cavallo. Her research program is focused on providing a computational support to the screening and design of new catalyst architectures by developing molecular descriptors and performing detailed mechanistic studies in strict collaboration with experimental groups.

Moussab Harb is currently a research scientist in computational solid-state physical chemistry at the KAUST Catalysis Center (KCC), Saudi Arabia. He obtained his Ph.D. in 2008 from the Light-Matter

Institute (ILM) at the Claude Bernard University (UCBL), France. His research interests focus on heterogeneous catalysis and photocatalytic water splitting.

Samy Ould-Chikh obtained his Ph.D. degree in chemistry in 2008 from the Ecole Normale Supérieure in Lyon under the mentorship of Prof. M. Hemati. After pursuing research interests in the photocatalysis field as a postdoctoral fellow at IRCeLyon (Lyon, France), he moved to King Abdullah University of Science and Technology (Thuwal, Saudi Arabia) as a postdoctoral fellow. He was appointed research scientist in 2010 to handle the in operando characterization of catalysts using multiple imaging and spectroscopic techniques.

Luigi Cavallo earned his Ph.D. in 1991 at the University of Naples (Italy) and completed his education on DFT working with Prof. Tom Ziegler at the University of Calgary, where he contributed to the development of combined quantum mechanics/molecular mechanics techniques. He joined the University of Naples in 1994 as assistant professor, and he moved to the University of Salerno (Italy) in 2002 as associate professor. He joined the Catalysis Center at KAUST (Saudi Arabia), where he serves as Professor of Chemistry. His research interests focus on understanding (and possibly solving) problems in catalysis using the armory of tools known as computational chemistry.

Jean-Marie Basset received his Ph.D. in 1969 from the University of Lyon, France. After a postdoctoral position in Toronto, he moved to the Institute of Catalysis in Lyon (vice-director). He served as a scientific director of L'École Supérieure de Chimie Physique Electronique de Lyon (CPE Lyon). In 1987, he founded the Laboratory of Surface Organometallic Chemistry. He was President of the European Network on Catalysis. He founded the Kaust Catalysis Center in Saudi Arabia, dedicated to catalysis by design and has been the director for nine years. He is now distinguished professor at KAUST. He has over 600 publications and 55 patents. He is member of the French Academy of Science, founding member of the French Academy of Technologies, Member of the European Academy of Sciences, Member of the European Academy of Sciences and Arts, and member of the National Academy of Inventors (US).

## ACKNOWLEDGMENTS

We thank King Abdullah University of Science and Technology Division of Physical Science and Engineering for generous financial support. V.D.E. thanks the Thailand Research Fund (grant no. RSA6080059) for generous support.

## ABBREVIATIONS USED

|        |                                  |
|--------|----------------------------------|
| SOMC   | surface organometallic chemistry |
| SOMCat | surface organometallic catalysis |
| SOMF   | surface organometallic fragment  |
| SCF    | surface coordination fragment    |
| SAC    | single atom catalysis            |
| SAAC   | single atom alloy catalysis      |
| DFT    | density functional theory        |

## REFERENCES

- (1) Liu, L.; Corma, A. Metal Catalysts for Heterogeneous Catalysis: From Single Atoms to Nanoclusters and Nanoparticles. *Chem. Rev.* **2018**, *118*, 4981–5079.
- (2) Wang, A. Q.; Li, J.; Zhang, T. Heterogeneous Single-Atom Catalysis. *Nat. Rev. Chem.* **2018**, *2*, 65–81.
- (3) Zhu, C. Z.; Fu, S. F.; Shi, Q. R.; Du, D.; Lin, Y. H. Single-Atom Electrocatalysts. *Angew. Chem., Int. Ed.* **2017**, *56*, 13944–13960.

- (4) Zhang, H. B.; Liu, G. G.; Shi, L.; Ye, J. H. Single-Atom Catalysts: Emerging Multifunctional Materials in Heterogeneous Catalysis. *Adv. Energy Mater.* **2018**, *8*, 1701343.

- (5) Liu, J. Y. Catalysis by Supported Single Metal Atoms. *ACS Catal.* **2017**, *7*, 34–59.

- (6) Boudart, M. *Proceedings of the Sixth International Congress on Catalysis*; Bond, G. C., Ed.; The Chemical Society, London, 1976; p 1.

- (7) Sinfelt, J. H.; Yates, D. J. C.; Carter, J. L. Catalytic Hydrogenolysis and Dehydrogenation over Copper-Nickel Alloys. *J. Catal.* **1972**, *24*, 283.

- (8) Poncet, V.; Sachtler, W. M. Reactions Between Cyclopentane and Deuterium on Nickel and Nickel-Copper Alloys. *J. Catal.* **1972**, *24*, 250.

- (9) Burch, R. Importance of Electronic Ligand Effects in Metal Alloy Catalysts. *Acc. Chem. Res.* **1982**, *15*, 24–31.

- (10) Balandin, A. A. The Theory of Heterogeneous Catalytic Reactions. The Multiplet Hypothesis. Model of Dehydrogenation Catalysis. *Z. Phys. Chem., Abt. B* **1929**, *2*, 289–316.

- (11) Soma, Y.; Sachtler, W. M. H. Infrared-Spectra of Co Adsorbed on PdAg and NiCu Alloys. *Jpn. J. Appl. Phys.* **1974**, *13*, 241–244.

- (12) Dalmon, J. A.; Primet, M.; Martin, G. A.; Imelik, B. Magnetic and Infrared Study of Co Chemisorption on Silica Supported Nickel-Copper Alloys. *Surf. Sci.* **1975**, *50*, 95–108.

- (13) Frennet, A.; Lienard, G.; Crucq, A.; Degols, L. Effect of Multiple Sites and Competition in Adsorption on Kinetics of Reactions Catalyzed by Metals. *J. Catal.* **1978**, *53*, 150–163.

- (14) Rondelli, M.; Zwaschka, G.; Krause, M.; Rotzer, M. D.; Hedhili, M. N.; Hogerl, M. P.; D'Elia, V.; Schweinberger, F. F.; Basset, J. M.; Heiz, U. Exploring the Potential of Different-Sized Supported Subnanometer Pt Clusters as Catalysts for Wet Chemical Applications. *ACS Catal.* **2017**, *7*, 4152–4162.

- (15) Yang, X. F.; Wang, A. Q.; Qiao, B. T.; Li, J.; Liu, J. Y.; Zhang, T. Single-Atom Catalysts: A New Frontier in Heterogeneous Catalysis. *Acc. Chem. Res.* **2013**, *46*, 1740–1748.

- (16) Schwarz, H. Menage-a-trois: Single-Atom Catalysis, Mass Spectrometry, and Computational Chemistry. *Catal. Sci. Technol.* **2017**, *7*, 4302–4314.

- (17) Chen, Z. P.; Vorobyeva, E.; Mitchell, S.; Fako, E.; Lopez, N.; Collins, S. M.; Leary, R. K.; Midgley, P. A.; Hauert, R.; Perez-Ramirez, J. Single-Atom Heterogeneous Catalysts Based on Distinct Carbon Nitride Scaffolds. *Natl. Sci. Rev.* **2018**, *5*, 642–652.

- (18) Zhang, L. L.; Ren, Y. J.; Liu, W. G.; Wang, A. Q.; Zhang, T. Single-Atom Catalyst: A Rising Star for Green Synthesis of Fine Chemicals. *Natl. Sci. Rev.* **2018**, *5*, 653–672.

- (19) Cui, X. J.; Li, W.; Ryabchuk, P.; Junge, K.; Beller, M. Bridging Homogeneous and Heterogeneous Catalysis by Heterogeneous Single-Metal-Site Catalysts. *Nat. Catal.* **2018**, *1*, 385–397.

- (20) Basset, J.-M.; Baudouin, A.; Bayard, F.; Candy, J.; Copéret, C.; De Mallmann, A.; Godard, G.; Kuntz, E.; Lefebvre, F.; Lucas, C.; Norsic, S.; Pelzer, K.; Quadrelli, A.; Santini, C.; Soulivong, D.; Stoffelbach, F.; Taoufik, M.; Thieuleux, C.; Thivolle-Cazat, J.; Veyre, L. In *Modern Surface Organometallic Chemistry*; Basset, J.-M., Psaro, R., Roberto, D., Ugo, R., Eds.; Wiley-VCH Verlag GmbH & Co KGaA, Weinheim, 2009; Chapter 3, pp 75–136.

- (21) Anwender, R. SOMC@PMS. Surface Organometallic Chemistry at Periodic Mesoporous Silica. *Chem. Mater.* **2001**, *13*, 4419–4438.

- (22) Copéret, C. C-H Bond Activation and Organometallic Intermediates on Isolated Metal Centers on Oxide Surfaces. *Chem. Rev.* **2010**, *110*, 656–680.

- (23) Coperet, C.; Comas-Vives, A.; Conley, M. P.; Estes, D. P.; Fedorov, A.; Mougél, V.; Nagae, H.; Nunez-Zarur, F.; Zhizhko, P. A. Surface Organometallic and Coordination Chemistry Toward Single-Site Heterogeneous Catalysts: Strategies, Methods, Structures, and Activities. *Chem. Rev.* **2016**, *116*, 323–421.

- (24) Coperet, C.; Estes, D. P.; Larmier, K.; Searles, K. Isolated Surface Hydrides: Formation, Structure, and Reactivity. *Chem. Rev.* **2016**, *116*, 8463–8505.



- (25) Basset, J. M.; Coperet, C.; Soulivong, D.; Taoufik, M.; Cazat, J. T. Metathesis of Alkanes and Related Reactions. *Acc. Chem. Res.* **2010**, *43*, 323–334.
- (26) Samantaray, M. K.; Pump, E.; Bendjeriou-Sedjerari, A.; D'Elia, V.; Pelletier, J. D. A.; Guidotti, M.; Psaro, R.; Basset, J. M. Surface Organometallic Chemistry in Heterogeneous Catalysis. *Chem. Soc. Rev.* **2018**, *47*, 8403–8437.
- (27) Pelletier, J. D. A.; Basset, J. M. Catalysis by Design: Well-Defined Single-Site Heterogeneous Catalysts. *Acc. Chem. Res.* **2016**, *49*, 664–677.
- (28) Ruddy, D. A.; Ohler, N. L.; Bell, A. T.; Tilley, T. D. Thermolytic Molecular Precursor Route to Site-Isolated Vanadia-Silica Materials and Their Catalytic Performance in Methane Selective Oxidation. *J. Catal.* **2006**, *238*, 277–285.
- (29) Conley, M. P.; Delley, M. F.; Nunez-Zarur, F.; Comas-Vives, A.; Coperet, C. Heterolytic Activation of C-H Bonds on Cr(III)-O Surface Sites Is a Key Step in Catalytic Polymerization of Ethylene and Dehydrogenation of Propane. *Inorg. Chem.* **2015**, *54*, 5065–5078.
- (30) Dufaud, V. R.; Basset, J. M. Catalytic Hydrogenolysis at Low Temperature and Pressure of Polyethylene and Polypropylene to Diesels or Lower Alkanes by a Zirconium Hydride Supported on Silica-Alumina: A Step toward Polyolefin Degradation by the Microscopic Reverse of Ziegler-Natta Polymerization. *Angew. Chem., Int. Ed.* **1998**, *37*, 806–810.
- (31) Le Quemener, F.; Barman, S.; Merle, N.; Aljuhani, M. A.; Samantaray, M. K.; Saih, Y.; Szeto, K. C.; De Mallmann, A.; Minenkov, Y.; Huang, K. W.; Cavallo, L.; Taoufik, M.; Basset, J. M. Metathetic Oxidation of 2-Butenes to Acetaldehyde by Molecular Oxygen Using the Single-Site Olefin Metathesis Catalyst (SiO)<sub>2</sub>Mo(=O)(2). *ACS Catal.* **2018**, *8*, 7549–7555.
- (32) Basset, J. M.; Pelletier, J. D. A. Predictive Approach of Heterogeneous Catalysis. *Natl. Sci. Rev.* **2018**, *5*, 633–635.
- (33) Green, M. L. H. A New Approach to the Formal Classification of Covalent Compounds of the Elements. *J. Organomet. Chem.* **1995**, *500*, 127–148.
- (34) Love, A. M.; Carrero, C. A.; Chieragato, A.; Grant, J. T.; Conrad, S.; Verel, R.; Hermans, I. Elucidation of Anchoring and Restructuring Steps During Synthesis of Silica-Supported Vanadium Oxide Catalysts. *Chem. Mater.* **2016**, *28*, 5495–5504.
- (35) Maity, N.; Barman, S.; Callens, E.; Samantaray, M. K.; Abou-Hamad, E.; Minenkov, Y.; D'Elia, V.; Hoffman, A. S.; Widdifield, C. M.; Cavallo, L.; et al. Controlling the Hydrogenolysis of Silica-Supported Tungsten Pentamethyl Leads to a Class of Highly Electron Deficient Partially Alkylated Metal Hydrides. *Chem. Sci.* **2016**, *7*, 1558–1568.
- (36) Bouhoute, Y.; Garron, A.; Grekov, D.; Merle, N.; Szeto, K. C.; De Mallmann, A.; Del Rosal, I.; Maron, L.; Girard, G.; Gauvin, R. M.; Delevoye, L.; Taoufik, M. Well-Defined Supported Mononuclear Tungsten Oxo Species as Olefin Metathesis Pre-Catalysts. *ACS Catal.* **2014**, *4*, 4232–4241.
- (37) Barman, S.; Maity, N.; Bhatte, K.; Ould-Chikh, S.; Dachwald, O.; Haessner, C.; Saih, Y.; Abou-Hamad, E.; Llorens, I.; Hazemann, J. L.; et al. Single-Site VO<sub>x</sub> Moieties Generated on Silica by Surface Organometallic Chemistry: A Way to Enhance the Catalytic Activity in the Oxidative Dehydrogenation of Propane. *ACS Catal.* **2016**, *6*, 5908–5921.
- (38) Jones, C. W.; McKittrick, M. W.; Nguyen, J. V.; Yu, K. Design of Silica-Tethered Metal Complexes for Polymerization Catalysis. *Top. Catal.* **2005**, *34*, 67–76.
- (39) Zhou, S. D.; Li, J. L.; Schlagen, M.; Schwarz, H. Bond Activation by Metal-Carbene Complexes in the Gas Phase. *Acc. Chem. Res.* **2016**, *49*, 494–502.
- (40) Diefenbach, M.; Bronstrup, M.; Aschi, M.; Schroder, D.; Schwarz, H. HCN Synthesis from Methane and Ammonia: Mechanisms of Pt<sup>+</sup> Mediated C-N Coupling. *J. Am. Chem. Soc.* **1999**, *121*, 10614–10625.
- (41) Schrock, R. R. Catalytic Reduction of Dinitrogen to Ammonia at a Single Molybdenum Center. *Acc. Chem. Res.* **2005**, *38*, 955–962.
- (42) Burgess, B. K.; Lowe, D. J. Mechanism of Molybdenum Nitrogenase. *Chem. Rev.* **1996**, *96*, 2983–3011.
- (43) Peng, Y.; Lu, B.; Chen, S. Carbon-Supported Single Atom Catalysts for Electrochemical Energy Conversion and Storage. *Adv. Mater.* **2018**, *30*, 1801995.
- (44) Cheng, Y.; Zhao, S.; Johannessen, B.; Veder, J.-P.; Saunders, M.; Rowles, M. R.; Cheng, M.; Liu, C.; Chisholm, M. F.; De Marco, R.; Cheng, H.-M.; Yang, S.-Z.; Jiang, S. P. Atomically Dispersed Transition Metals on Carbon Nanotubes with Ultrahigh Loading for Selective Electrochemical Carbon Dioxide Reduction. *Adv. Mater.* **2018**, *30*, 1706287.
- (45) Shi, Q.; Fu, S.; Zhu, C.; Song, J.; Du, D.; Lin, Y. Metal–Organic Frameworks-Based Catalysts for Electrochemical Oxygen Evolution. *Mater. Horiz.* **2019**, *6*, 684–702.
- (46) Zwaschka, G.; Rondelli, M.; Krause, M.; Rötzer, M. D.; Hedhili, M. N.; Heiz, U.; Basset, J. M.; Schweinberger, F. F.; D'Elia, V. Supported Sub-Nanometer Ta Oxide Clusters as Model Catalysts for the Selective Epoxidation of Cyclooctene. *New J. Chem.* **2018**, *42*, 3035–3041.
- (47) Lefebvre, F. D.; Candy, J. P.; Santini, C. C.; Basset, J. M. Surface Organometallic Chemistry on Metals. Application to Chemicals and Fine Chemicals. *Top. Catal.* **1997**, *4*, 211–216.
- (48) Koenraad, P. M.; Flatté, M. E. Single Dopants in Semiconductors. *Nat. Mater.* **2011**, *10*, 91–100.
- (49) Szeto, K. C.; Loges, B.; Merle, N.; Popoff, N.; Quadrelli, E. A.; Jia, H. P.; Berrier, E.; De Mallmann, A.; Delevoye, L.; Gauvin, R. M.; Taoufik, M. Vanadium Oxo Organometallic Species Supported on Silica for the Selective Non-oxidative Dehydrogenation of Propane. *Organometallics* **2013**, *32*, 6452–6460.
- (50) D'Elia, V.; Dong, H. L.; Rossini, A. J.; Widdifield, C. M.; Vummaleti, S. V. C.; Minenkov, Y.; Poater, A.; Abou-Hamad, E.; Pelletier, J. D. A.; Cavallo, L.; et al. Cooperative Effect of Monopodal Silica-Supported Niobium Complex Pairs Enhancing Catalytic Cyclic Carbonate Production. *J. Am. Chem. Soc.* **2015**, *137*, 7728–7739.
- (51) Hamzaoui, B.; Pelletier, J. D. A.; Abou-Hamad, E.; Basset, J. M. Well-Defined Silica-Supported Zirconium-imido Complexes Mediated Heterogeneous Imine Metathesis. *Chem. Commun.* **2016**, *52*, 4617–4620.
- (52) Estes, D. P.; Siddiqi, G.; Allouche, F.; Kovtunov, K. V.; Safonova, O. V.; Trigub, A. L.; Koptug, I. V.; Coperet, C. C-H Activation on Co<sub>2</sub>O Sites: Isolated Surface Sites versus Molecular Analogs. *J. Am. Chem. Soc.* **2016**, *138*, 14987–14997.
- (53) Gajan, D.; Guillois, K.; Delichère, P.; Basset, J.-M.; Candy, J.-P.; Caps, V.; Coperet, C.; Lesage, A.; Emsley, L. Gold Nanoparticles Supported on Passivated Silica: Access to an Efficient Aerobic Epoxidation Catalyst and the Intrinsic Oxidation Activity of Gold. *J. Am. Chem. Soc.* **2009**, *131*, 14667–14669.
- (54) Erni, R.; Rossell, M. D.; Kisielowski, C.; Dahmen, U. Atomic-Resolution Imaging with a Sub-50-pm Electron Probe. *Phys. Rev. Lett.* **2009**, *102*, 096101.
- (55) Haider, M.; Uhlemann, S.; Schwan, E.; Rose, H.; Kabius, B.; Urban, K. Electron Microscopy Image Enhanced. *Nature* **1998**, *392*, 768–769.
- (56) Crewe, A. V.; Wall, J.; Langmore, J. Visibility of Single Atoms. *Science* **1970**, *168*, 1338–1340.
- (57) Lu, J.; Aydin, C.; Browning, N. D.; Gates, B. C. Imaging Isolated Gold Atom Catalytic Sites in Zeolite NaY. *Angew. Chem., Int. Ed.* **2012**, *51*, 5842–5846.
- (58) Zhu, H. B.; Rosenfeld, D. C.; Anjum, D. H.; Sangaru, S. S.; Saih, Y.; Ould-Chikh, S.; Basset, J. M. Ni-Ta-O Mixed Oxide Catalysts for the Low Temperature Oxidative Dehydrogenation of Ethane to Ethylene. *J. Catal.* **2015**, *329*, 291–306.
- (59) Fei, H. L.; Dong, J. C.; Arellano-Jimenez, M. J.; Ye, G. L.; Kim, N. D.; Samuel, E. L. G.; Peng, Z. W.; Zhu, Z.; Qin, F.; Bao, J. M.; Yacaman, M. J.; Ajayan, P. M.; Chen, D.; Tour, J. M. Atomic Cobalt on Nitrogen-Doped Graphene for Hydrogen Generation. *Nat. Commun.* **2015**, *6*, 8668.
- (60) Yin, P. Q.; Yao, T.; Wu, Y.; Zheng, L. R.; Lin, Y.; Liu, W.; Ju, H. X.; Zhu, J. F.; Hong, X.; Deng, Z. X.; et al. Single Cobalt Atoms with

Precise N-Coordination as Superior Oxygen Reduction Reaction Catalysts. *Angew. Chem., Int. Ed.* **2016**, *55*, 10800–10805.

(61) Liu, W. G.; Zhang, L. L.; Yan, W. S.; Liu, X. Y.; Yang, X. F.; Miao, S.; Wang, W. T.; Wang, A. Q.; Zhang, T. Single-Atom Dispersed Co-N-C Catalyst: Structure Identification and Performance for Hydrogenative Coupling of Nitroarenes. *Chem. Sci.* **2016**, *7*, 5758–5764.

(62) Zhang, S. R.; Shan, J. J.; Zhu, Y.; Frenkel, A. I.; Patlolla, A.; Huang, W. X.; Yoon, S. J.; Wang, L.; Yoshida, H.; Takeda, S.; et al. WGS Catalysis and In Situ Studies of  $\text{CoO}_{1-x}$ ,  $\text{PtCo}_n/\text{Co}_3\text{O}_4$ , and  $\text{Pt}_m\text{Co}_n/\text{CoO}_{1-x}$  Nanorod Catalysts. *J. Am. Chem. Soc.* **2013**, *135*, 8283–8293.

(63) Qiao, B. T.; Wang, A. Q.; Yang, X. F.; Allard, L. F.; Jiang, Z.; Cui, Y. T.; Liu, J. Y.; Li, J.; Zhang, T. Single-Atom Catalysis of CO Oxidation Using  $\text{Pt}_1/\text{FeO}_x$ . *Nat. Chem.* **2011**, *3*, 634–641.

(64) Isaacson, M. S.; Langmore, J.; Parker, N. W.; Kopf, D.; Utlaut, M. Study of Adsorption and Diffusion of Heavy-Atoms on Light-Element Substrates by Means of Atomic Resolution Stem. *Ultramicroscopy* **1976**, *1*, 359–376.

(65) Colliex, C.; Gloter, A.; March, K.; Mory, C.; Stephan, O.; Suenaga, K.; Tence, M. Capturing the Signature of Single Atoms with the Tiny Probe of a STEM. *Ultramicroscopy* **2012**, *123*, 80–89.

(66) Egerton, R. F. Mechanisms of Radiation Damage in Beam-Sensitive Specimens, for TEM Accelerating Voltages Between 10 and 300 kV. *Microsc. Res. Tech.* **2012**, *75*, 1550–1556.

(67) Zobelli, A.; Gloter, A.; Ewels, C. P.; Seifert, G.; Colliex, C. Electron Knock-on Cross Section of Carbon and Boron Nitride Nanotubes. *Phys. Rev. B: Condens. Matter Mater. Phys.* **2007**, *75*, 245402.

(68) Csencsits, R.; Gronsky, R. Damage of Zeolite-Y in the TEM and Its Effects on TEM Images. *Ultramicroscopy* **1987**, *23*, 421–431.

(69) Peng, L. M.; Dudarev, S. L.; Whelan, M. J. *High-Energy Electron Diffraction and Microscopy*; Oxford Science Publications: Oxford, UK, 2003.

(70) Ortalan, V.; Uzun, A.; Gates, B. C.; Browning, N. D. Towards Full-Structure Determination of Bimetallic Nanoparticles with an Aberration-Corrected Electron Microscope. *Nat. Nanotechnol.* **2010**, *5*, 843–847.

(71) Senga, R.; Suenaga, K. Single-Atom Detection of Light Elements: Imaging or Spectroscopy? *Ultramicroscopy* **2017**, *180*, 150–155.

(72) Tizei, L. H. G.; Nakanishi, R.; Kitaura, R.; Shinohara, H.; Suenaga, K. Core-Level Spectroscopy to Probe the Oxidation State of Single Europium Atoms. *Phys. Rev. Lett.* **2015**, *114*, 197602.

(73) Chung, H. T.; Cullen, D. A.; Higgins, D.; Sneed, B. T.; Holby, E. F.; More, K. L.; Zelenay, P. Direct Atomic-Level Insight into the Active Sites of a High-Performance PGM-free ORR Catalyst. *Science* **2017**, *357*, 479–483.

(74) Zhou, W.; Kapetanakis, M. D.; Prange, M. P.; Pantelides, S. T.; Pennycook, S. J.; Idrobo, J. C. Direct Determination of the Chemical Bonding of Individual Impurities in Graphene. *Phys. Rev. Lett.* **2012**, *109*, 206803.

(75) Nicholls, R. J.; Sader, K.; Warner, J. H.; Plant, S. R.; Porfyrakis, K.; Nellist, P. D.; Briggs, G. A. D.; Cockayne, D. J. H. Direct Imaging and Chemical Identification of the Encapsulated Metal Atoms in Bimetallic Endofullerene Peapods. *ACS Nano* **2010**, *4*, 3943–3948.

(76) Suenaga, K. Elemental Analysis down to the Single Atom with Electron Beams. *C. R. Phys.* **2014**, *15*, 151–157.

(77) Lin, Y. C.; Teng, P. Y.; Chiu, P. W.; Suenaga, K. Exploring the Single Atom Spin State by Electron Spectroscopy. *Phys. Rev. Lett.* **2015**, *115*, 206803.

(78) Muller, D. A.; Silcox, J. Delocalization in Inelastic-Scattering. *Ultramicroscopy* **1995**, *59*, 195–213.

(79) Suenaga, K.; Sato, Y.; Liu, Z.; Kataura, H.; Okazaki, T.; Kimoto, K.; Sawada, H.; Sasaki, T.; Omoto, K.; Tomita, T.; Kaneyama, T.; Kondo, Y. Visualizing and Identifying Single Atoms Using Electron Energy-Loss Spectroscopy with Low Accelerating Voltage. *Nat. Chem.* **2009**, *1*, 415–418.

(80) Senga, R.; Suenaga, K. Single-Atom Electron Energy Loss Spectroscopy of Light Elements. *Nat. Commun.* **2015**, *6*, 7943.

(81) Stroud, R. M.; Lovejoy, T. C.; Falke, M.; Bassim, N. D.; Corbin, G. J.; Dellby, N.; Hrnčirik, P.; Kaeppl, A.; Noack, M.; Hahn, W.; et al. Individual Heteroatom Identification with X-ray Spectroscopy. *Appl. Phys. Lett.* **2016**, *108*, 163101.

(82) Suenaga, K.; Okazaki, T.; Okunishi, E.; Matsumura, S. Detection of Photons Emitted from Single Erbium Atoms in Energy-Dispersive X-ray Spectroscopy. *Nat. Photonics* **2012**, *6*, 545–548.

(83) Tizei, L. H. G.; Iizumi, Y.; Okazaki, T.; Nakanishi, R.; Kitaura, R.; Shinohara, H.; Suenaga, K. Single Atom Spectroscopy: Decreased Scattering Delocalization at High Energy Losses, Effects of Atomic Movement and X-ray Fluorescence Yield. *Ultramicroscopy* **2016**, *160*, 239–246.

(84) Krause, M. O.; Nestor, C. W., Jr.; Sparks, C. J., Jr.; Ricci, E. *X-Ray Fluorescence Cross Sections for K and L X-Rays of the Elements*; U. S. Department of Energy, Oak Ridge National Laboratory, Springfield, VA, 1978.

(85) Stern, E. A. Theory of EXAFS. In *X-Ray Absorption: Principles, Applications, Techniques of EXAFS, SEXAFS and XANES*; Koningsberger, D. C., Prins, R., Eds.; John Wiley & Sons: New York, 1988.

(86) Malta, G.; Kondrat, S. A.; Freakley, S. J.; Davies, C. J.; Lu, L.; Dawson, S.; Thetford, A.; Gibson, E. K.; Morgan, D. J.; Jones, W.; et al. Identification of Single-Site Gold Catalysis in Acetylene Hydrochlorination. *Science* **2017**, *355*, 1399–1402.

(87) Peterson, E. J.; DeLaRiva, A. T.; Lin, S.; Johnson, R. S.; Guo, H.; Miller, J. T.; Kwak, J. H.; Peden, C. H. F.; Kiefer, B.; Allard, L. F.; Ribeiro, F. H.; Datye, A. K. Low-Temperature Carbon Monoxide Oxidation Catalysed by Regenerable Atomically Dispersed Palladium on Alumina. *Nat. Commun.* **2014**, *5*, 4885.

(88) Liu, P. X.; Zhao, Y.; Qin, R. X.; Mo, S. G.; Chen, G. X.; Gu, L.; Chevrier, D. M.; Zhang, P.; Guo, Q.; Zang, D. D.; et al. Photochemical Route for Synthesizing Atomically Dispersed Palladium Catalysts. *Science* **2016**, *352*, 797–801.

(89) Wang, L.; Zhang, W.; Wang, S.; Gao, Z.; Luo, Z.; Wang, X.; Zeng, R.; Li, A.; Li, H.; Wang, M.; Zheng, X.; Zhu, J.; Zhang, W.; Ma, C.; Si, R.; Zeng, J. Atomic-Level Insights in Optimizing Reaction Paths for Hydroformylation Reaction Over Rh/CoO Single-Atom Catalyst. *Nat. Commun.* **2016**, *7*, 14036.

(90) Wei, H.; Huang, K.; Wang, D.; Zhang, R.; Ge, B.; Ma, J.; Wen, B.; Zhang, S.; Li, Q.; Lei, M.; Zhang, C.; Irawan, J.; Liu, L.-M.; Wu, H. Iced Photochemical Reduction to Synthesize Atomically Dispersed Metals by Suppressing Nanocrystal Growth. *Nat. Commun.* **2017**, *8*, 1490.

(91) Wei, H. S.; Liu, X. Y.; Wang, A. Q.; Zhang, L. L.; Qiao, B. T.; Yang, X. F.; Huang, Y. Q.; Miao, S.; Liu, J. Y.; Zhang, T. FeOx-Supported Platinum Single-Atom and Pseudo-Single-Atom Catalysts for Chemoselective Hydrogenation of Functionalized Nitroarenes. *Nat. Commun.* **2014**, *5*, 5634.

(92) Zhang, B.; Asakura, H.; Zhang, J.; Zhang, J. G.; De, S.; Yan, N. Stabilizing a Platinum, Single-Atom Catalyst on Supported Phosphomolybdic Acid without Compromising Hydrogenation Activity. *Angew. Chem., Int. Ed.* **2016**, *55*, 8319–8323.

(93) Li, X. G.; Bi, W. T.; Zhang, L.; Tao, S.; Chu, W. S.; Zhang, Q.; Luo, Y.; Wu, C. Z.; Xie, Y. Single-Atom Pt as Co-Catalyst for Enhanced Photocatalytic  $\text{H}_2$  Evolution. *Adv. Mater.* **2016**, *28*, 2427–2431.

(94) Gallagher, J. R.; Li, T.; Zhao, H. Y.; Liu, J. J.; Lei, Y.; Zhang, X. Y.; Ren, Y.; Elam, J. W.; Meyer, R. J.; Winans, R. E.; Miller, J. T. In Situ Diffraction of Highly Dispersed Supported Platinum Nanoparticles. *Catal. Sci. Technol.* **2014**, *4*, 3053–3063.

(95) Stern, E. A. Theory of Extended X-Ray-Absorption Fine-Structure. *Phys. Rev. B* **1974**, *10*, 3027–3037.

(96) Lee, P. A.; Citrin, P. H.; Eisenberger, P.; Kincaid, B. M. Extended X-ray Absorption Fine-Structure - Its Strengths and Limitations as a Structural Tool. *Rev. Mod. Phys.* **1981**, *53*, 769–806.

- (97) Corker, J.; Lefebvre, F.; Lecuyer, C.; Dufaud, V.; Quignard, F.; Choplin, A.; Evans, J.; Basset, J. M. Catalytic Cleavage of the C-H and C-C Bonds of Alkanes by Surface Organometallic Chemistry: An EXAFS and IR Characterization of a Zr-H Catalyst. *Science* **1996**, *271*, 966–969.
- (98) Bouhoute, Y.; Grekov, D.; Szeto, K. C.; Merle, N.; De Mallmann, A.; Lefebvre, F.; Raffa, G.; Del Rosal, I.; Maron, L.; Gauvin, R. M.; et al. Accessing Realistic Models for the  $\text{WO}_3\text{-SiO}_2$  Industrial Catalyst through the Design of Organometallic Precursors. *ACS Catal.* **2016**, *6*, 1–18.
- (99) Chen, Y.; Ould-Chikh, S.; Abou-Hamad, E.; Callens, E.; Mohandas, J. C.; Khalid, S.; Basset, J. M. Facile and Efficient Synthesis of the Surface Tantalum Hydride ( $\text{≡SiO}$ )<sub>2</sub>TaH<sup>III</sup> and Tris-Siloxy Tantalum ( $\text{≡SiO}$ )<sub>3</sub>Ta<sup>III</sup> Starting from Novel Tantalum Surface Species ( $\text{≡SiO}$ )TaMe<sub>4</sub> and ( $\text{≡SiO}$ )<sub>2</sub>TaMe<sub>3</sub>. *Organometallics* **2014**, *33*, 1205–1211.
- (100) Aljuhani, M. A.; Barman, S.; Abou-Hamad, E.; Gurinov, A.; Ould-Chikh, S.; Guan, E.; Jedidi, A.; Cavallo, L.; Gates, B. C.; Pelletier, J. D. A.; et al. Imine Metathesis Catalyzed by a Silica-Supported Hafnium Imido Complex. *ACS Catal.* **2018**, *8*, 9440–9446.
- (101) Bouhoute, Y.; Del Rosal, I.; Szeto, K. C.; Merle, N.; Grekov, D.; De Mallmann, A.; Le Roux, E.; Delevoye, L.; Gauvin, R. M.; Maron, L.; et al. Modification of Silica-Supported Tungsten Neosilyl Oxo Precatalysts: Impact of Substituted Phenol on Activity and Stability in Olefin Metathesis. *Catal. Sci. Technol.* **2016**, *6*, 8532–8539.
- (102) Jezequel, M.; Dufaud, V.; Ruiz-Garcia, M. J.; Carrillo-Hermosilla, F.; Neugebauer, U.; Niccolai, G. P.; Lefebvre, F.; Bayard, F.; Corker, J.; Fiddy, S.; et al. Supported Metallocene Catalysts by Surface Organometallic Chemistry. Synthesis, Characterization, and Reactivity in Ethylene Polymerization of Oxide-Supported Mono- and Biscyclopentadienyl Zirconium Alkyl Complexes: Establishment of Structure/Reactivity Relationships. *J. Am. Chem. Soc.* **2001**, *123*, 3520–3540.
- (103) Werghi, B.; Bendjeriou-Sedjerari, A.; Jedidi, A.; Morlanes, N.; Abou-Hamad, E.; Bhatte, K.; Guan, E.; Ma, T.; Aguilar-Tapia, A.; Ould-Chikh, S.; et al. Tungsten Catalyst Incorporating a Well-Defined Tetracoordinated Aluminum Surface Ligand for Selective Metathesis of Propane,  $[(\text{≡Si-O-Si≡})(\text{≡Si-O-})_2\text{Al-O-W(≡CtBu)(H)}_2]$ . *ChemCatChem* **2019**, *11*, 614–620.
- (104) Zhu, H. B.; Ould-Chikh, S.; Dong, H. L.; Llorens, I.; Saih, Y.; Anjum, D. H.; Hazemann, J. L.; Basset, J. M.  $\text{VO}_x/\text{SiO}_2$  Catalyst Prepared by Grafting  $\text{VOCl}_3$  on Silica for Oxidative Dehydrogenation of Propane. *ChemCatChem* **2015**, *7*, 3332–3339.
- (105) Searles, K.; Siddiqui, G.; Safonova, O. V.; Coperet, C. Silica-Supported Isolated Gallium Sites as Highly Active, Selective and Stable Propane Dehydrogenation Catalysts. *Chem. Sci.* **2017**, *8*, 2661–2666.
- (106) Yamamoto, K.; Chan, K. W.; Mougél, V.; Nagae, H.; Tsurugi, H.; Safonova, O. V.; Mashima, K.; Coperet, C. Silica-Supported Isolated Molybdenum Di-oxo Species: Formation and Activation with Organosilicon Agent for Olefin Metathesis. *Chem. Commun.* **2018**, *54*, 3989–3992.
- (107) Gu, W. X.; Stalzer, M. M.; Nicholas, C. P.; Bhattacharyya, A.; Motta, A.; Gallagher, J. R.; Zhang, G. H.; Miller, J. T.; Kobayashi, T.; Pruski, M.; et al. Benzene Selectivity in Competitive Arene Hydrogenation: Effects of Single-Site Catalyst–Acidic Oxide Surface Binding Geometry. *J. Am. Chem. Soc.* **2015**, *137*, 6770–6780.
- (108) Williams, L. A.; Guo, N.; Motta, A.; Delferro, M.; Fragala, I. L.; Miller, J. T.; Marks, T. J. Surface Structural-Chemical Characterization of a Single-Site d(0) Heterogeneous Arene Hydrogenation Catalyst Having 100% Active Sites. *Proc. Natl. Acad. Sci. U. S. A.* **2013**, *110*, 413–418.
- (109) Deguns, E. W.; Taha, Z.; Meitzner, G. D.; Scott, S. L. An X-ray Absorption Study of Two  $\text{VOCl}_3$ -Modified Silicas: Evidence for Chloride-Silica Interactions. *J. Phys. Chem. B* **2005**, *109*, 5005–5011.
- (110) Munoz, M.; Argoul, P.; Farges, F. Continuous Cauchy Wavelet Transform Analyses of EXAFS Spectra: A Qualitative Approach. *Am. Mineral.* **2003**, *88*, 694–700.
- (111) Funke, H.; Scheinost, A. C.; Chukalina, M. Wavelet Analysis of Extended X-ray Absorption Fine Structure Data. *Phys. Rev. B: Condens. Matter Mater. Phys.* **2005**, *71*, 094110.
- (112) Savinelli, R. O.; Scott, S. L. Wavelet Transform EXAFS Analysis of Mono- and Dimolybdate Model Compounds and a Mo/HZSM-5 Dehydroaromatization Catalyst. *Phys. Chem. Chem. Phys.* **2010**, *12*, 5660–5667.
- (113) Szeto, K. C.; Jones, Z. R.; Merle, N.; Rios, C.; Gallo, A.; Le Quemener, F.; Delevoye, L.; Gauvin, R. M.; Scott, S. L.; Taoufik, M. A. Strong Support Effect in Selective Propane Dehydrogenation Catalyzed by  $\text{Ga(i-Bu)}_3$  Grafted onto gamma-Alumina and Silica. *ACS Catal.* **2018**, *8*, 7566–7577.
- (114) Fierro-Gonzalez, J. C.; Gates, B. C. Mononuclear Au-III and Au-I Complexes Bonded to Zeolite NaY: Catalysts for CO Oxidation at 298 K. *J. Phys. Chem. B* **2004**, *108*, 16999–17002.
- (115) Fierro-Gonzalez, J. C.; Kuba, S.; Hao, Y. L.; Gates, B. C. Oxide- and Zeolite-Supported Molecular Metal Complexes and Clusters: Physical Characterization and Determination of Structure, Bonding, and Metal Oxidation State. *J. Phys. Chem. B* **2006**, *110*, 13326–13351.
- (116) Serna, P.; Gates, B. C. Zeolite-Supported Rhodium Complexes and Clusters: Switching Catalytic Selectivity by Controlling Structures of Essentially Molecular Species. *J. Am. Chem. Soc.* **2011**, *133*, 4714–4717.
- (117) Fierro-Gonzalez, J. C.; Gates, B. C. Structural Changes of the Gold-Support Interface During CO Oxidation Catalyzed by Mononuclear Gold Complexes Bonded to Zeolite NaY: Evidence from Time-Resolved X-ray Absorption Spectroscopy. *Langmuir* **2005**, *21*, 5693–5695.
- (118) Ogino, I.; Gates, B. C. Transient Spectroscopic Characterization of the Genesis of a Ruthenium Complex Catalyst Supported on Zeolite Y. *J. Phys. Chem. C* **2009**, *113*, 20036–20043.
- (119) Yang, D.; Xu, P. H.; Browning, N. D.; Gates, B. C. Tracking Rh Atoms in Zeolite HY: First Steps of Metal Cluster Formation and Influence of Metal Nuclearity on Catalysis of Ethylene Hydrogenation and Ethylene Dimerization. *J. Phys. Chem. Lett.* **2016**, *7*, 2537–2543.
- (120) Yang, D.; Odoh, S. O.; Borycz, J.; Wang, T. C.; Farha, O. K.; Hupp, J. T.; Cramer, C. J.; Gagliardi, L.; Gates, B. C. Tuning Zr-6 Metal-Organic Framework (MOF) Nodes as Catalyst Supports: Site Densities and Electron-Donor Properties Influence Molecular Iridium Complexes as Ethylene Conversion Catalysts. *ACS Catal.* **2016**, *6*, 235–247.
- (121) Guan, E. J.; Gates, B. C. Stable Rhodium Pair Sites on MgO: Influence of Ligands and Rhodium Nuclearity on Catalysis of Ethylene Hydrogenation and H-D Exchange in the Reaction of  $\text{H}_2$  with  $\text{D}_2$ . *ACS Catal.* **2018**, *8*, 482–487.
- (122) Hoffman, A. S.; Debeve, L. M.; Zhang, S. J.; Perez-Aguilar, J. E.; Conley, E. T.; Justl, K. R.; Arslan, I.; Dixon, D. A.; Gates, B. C. Beating Heterogeneity of Single-Site Catalysts: MgO-Supported Iridium Complexes. *ACS Catal.* **2018**, *8*, 3489–3498.
- (123) Babucci, M.; Fang, C. Y.; Perez-Aguilar, J. E.; Hoffman, A. S.; Boubnov, A.; Guan, E. J.; Bare, S. R.; Gates, B. C.; Uzun, A. Controlling Catalytic Activity and Selectivity for Partial Hydrogenation by Tuning the Environment Around Active Sites in Iridium Complexes Bonded to Supports. *Chem. Sci.* **2019**, *10*, 2623–2632.
- (124) Masnadi, M. S.; El-Houjeiri, H. M.; Schunack, D.; Li, Y.; Englander, J. G.; Badahdah, A.; Monfort, J.-C.; Anderson, J. E.; Wallington, T. J.; Bergerson, J. A.; Gordon, D.; Koomey, J.; Przesmitzki, S.; Azevedo, I. L.; Bi, X. T.; Duffy, J. E.; Heath, G. A.; Keoleian, G. A.; McGlade, C.; Meehan, D. N.; Yeh, S.; You, F.; Wang, M.; Brandt, A. R. Global Carbon Intensity of Crude Oil Production. *Science* **2018**, *361*, 851–853.
- (125) Yang, D.; Gates, B. C. Catalysis by Metal Organic Frameworks: Perspective and Suggestions for Future Research. *ACS Catal.* **2019**, *9*, 1779–1798.



- (126) Bordiga, S.; Groppo, E.; Agostini, G.; van Bokhoven, J. A.; Lamberti, C. Reactivity of Surface Species in Heterogeneous Catalysts Probed by *In Situ* X-ray Absorption Techniques. *Chem. Rev.* **2013**, *113*, 1736–1850.
- (127) Westre, T. E.; Kennepohl, P.; DeWitt, J. G.; Hedman, B.; Hodgson, K. O.; Solomon, E. I. A Multiplet Analysis of Fe K-edge 1s- $\rightarrow$ 3d Pre-Edge Features of Iron Complexes. *J. Am. Chem. Soc.* **1997**, *119*, 6297–6314.
- (128) Yamamoto, T. Assignment of Pre-edge peaks in K-edge X-ray Absorption Spectra of 3d Transition Metal Compounds: Electric Dipole or Quadrupole? *X-Ray Spectrom.* **2008**, *37*, 572–584.
- (129) de Groot, F.; Vanko, G.; Glatzel, P. The 1s X-ray Absorption Pre-Edge Structures in Transition Metal Oxides. *J. Phys.: Condens. Matter* **2009**, *21*, 104207.
- (130) Atkins, A. J.; Bauer, M.; Jacob, C. R. The Chemical Sensitivity of X-ray Spectroscopy: High Energy Resolution XANES Versus X-ray Emission Spectroscopy of Substituted Ferrocenes. *Phys. Chem. Chem. Phys.* **2013**, *15*, 8095–8105.
- (131) Wilke, M.; Farges, F.; Petit, P. E.; Brown, G. E.; Martin, F. Oxidation State and Coordination of Fe in Minerals: an FeK-XANES Spectroscopic Study. *Am. Mineral.* **2001**, *86*, 714–730.
- (132) Battiston, A. A.; Bitter, J. H.; de Groot, F. M. F.; Overweg, A. R.; Stephan, O.; van Bokhoven, J. A.; Kooyman, P. J.; van der Spek, C.; Vanko, G.; Koningsberger, D. C. Evolution of Fe Species During the Synthesis of Over-Exchanged Fe/ZSM5 Obtained by Chemical Vapor deposition of FeCl<sub>3</sub>. *J. Catal.* **2003**, *213*, 251–271.
- (133) Rehr, J. J.; Albers, R. C. Theoretical Approaches to X-ray Absorption Fine Structure. *Rev. Mod. Phys.* **2000**, *72*, 621–654.
- (134) Joly, Y. X-ray Absorption Near-edge Structure Calculations Beyond the Muffin-Tin Approximation. *Phys. Rev. B: Condens. Matter Mater. Phys.* **2001**, *63*, 125120.
- (135) Hamalainen, K.; Siddons, D. P.; Hastings, J. B.; Berman, L. E. Elimination of the Inner-Shell Lifetime Broadening in X-ray-Absorption Spectroscopy. *Phys. Rev. Lett.* **1991**, *67*, 2850–2853.
- (136) Glatzel, P.; Sikora, M.; Smolentsev, G.; Fernandez-Garcia, M. Hard X-ray Photon-in Photon-out Spectroscopy. *Catal. Today* **2009**, *145*, 294–299.
- (137) Proux, O.; Lahera, E.; Del Net, W.; Kieffer, I.; Rovezzi, M.; Testemale, D.; Irar, M.; Thomas, S.; Aguilar-Tapia, A.; Bazarkina, E. F.; et al. High-Energy Resolution Fluorescence Detected X-ray Absorption Spectroscopy: A Powerful New Structural Tool in Environmental Biogeochemistry Sciences. *J. Environ. Qual.* **2017**, *46*, 1146–1157.
- (138) Hoffman, A. S.; Sokaras, D.; Zhang, S. J.; Debeve, L. M.; Fang, C. Y.; Gallo, A.; Kroll, T.; Dixon, D. A.; Bare, S. R.; Gates, B. C. High-Energy-Resolution X-ray Absorption Spectroscopy for Identification of Reactive Surface Species on Supported Single-Site Iridium Catalysts. *Chem. - Eur. J.* **2017**, *23*, 14760–14768.
- (139) Rehr, J. J.; Kas, J. J.; Vila, F. D.; Prange, M. P.; Jorissen, K. Parameter-Free Calculations of X-ray Spectra With FEFF9. *Phys. Chem. Chem. Phys.* **2010**, *12*, 5503–5513.
- (140) Bounov, A.; Carvalho, H. W. P.; Doronkin, D. E.; Gunter, T.; Gallo, E.; Atkins, A. J.; Jacob, C. R.; Grunwaldt, J. D. Selective Catalytic Reduction of NO Over Fe-ZSM-5: Mechanistic Insights by Operando HERFD-XANES and Valence-to-Core X-ray Emission Spectroscopy. *J. Am. Chem. Soc.* **2014**, *136*, 13006–13015.
- (141) Heijboer, W. M.; Glatzel, P.; Sawant, K. R.; Lobo, R. F.; Bergmann, U.; Barrea, R. A.; Koningsberger, D. C.; Weckhuysen, B. M.; de Groot, F. M. F. K Beta-Detected XANES of Framework-Substituted FeZSM-5 Zeolites. *J. Phys. Chem. B* **2004**, *108*, 10002–10011.
- (142) Giordanino, F.; Borfecchia, E.; Lomachenko, K. A.; Lazzarini, A.; Agostini, G.; Gallo, E.; Soldatov, A. V.; Beato, P.; Bordiga, S.; Lamberti, C. Interaction of NH<sub>3</sub> with Cu-SSZ-13 Catalyst: A Complementary FTIR, XANES, and XES Study. *J. Phys. Chem. Lett.* **2014**, *5*, 1552–1559.
- (143) Gunter, T.; Carvalho, H. W. P.; Doronkin, D. E.; Sheppard, T.; Glatzel, P.; Atkins, A. J.; Rudolph, J.; Jacob, C. R.; Casapu, M.; Grunwaldt, J. D. Structural Snapshots of the SCR Reaction Mechanism on Cu-SSZ-13. *Chem. Commun.* **2015**, *51*, 9227–9230.
- (144) Szlachetko, J.; Nachtegaal, M.; de Boni, E.; Willmann, M.; Safonova, O.; Sa, J.; Smolentsev, G.; Szlachetko, M.; van Bokhoven, J. A.; Dousse, J. C.; et al. A Von Hamos X-ray Spectrometer Based on a Segmented-Type Diffraction Crystal for Single-Shot X-ray Emission Spectroscopy and Time-Resolved Resonant Inelastic X-ray Scattering Studies. *Rev. Sci. Instrum.* **2012**, *83*, 103105.
- (145) Glatzel, P.; Bergmann, U. High Resolution 1s Core Hole X-ray Spectroscopy in 3d Transition Metal Complexes - Electronic and Structural Information. *Coord. Chem. Rev.* **2005**, *249*, 65–95.
- (146) Bergmann, U.; Horne, C. R.; Collins, T. J.; Workman, J. M.; Cramer, S. P. Chemical Dependence of Interatomic X-ray Transition Energies and Intensities - a Study of Mn K $\beta$ ' and K $\beta$ <sub>2,5</sub> Spectra. *Chem. Phys. Lett.* **1999**, *302*, 119–124.
- (147) Safonov, V. A.; Vykhodtseva, L. N.; Polukarov, Y. M.; Safonova, O. V.; Smolentsev, G.; Sikora, M.; Eeckhout, S. G.; Glatzel, P. Valence-to-Core X-ray Emission Spectroscopy Identification of Carbide Compounds in Nanocrystalline Cr Coatings Deposited from Cr(III) Electrolytes Containing Organic Substances. *J. Phys. Chem. B* **2006**, *110*, 23192–23196.
- (148) Eeckhout, S. G.; Safonova, O. V.; Smolentsev, G.; Biasioli, M.; Safonov, V. A.; Vykhodtseva, L. N.; Sikora, M.; Glatzel, P. Cr Local Environment by Valence-to-Core X-ray Emission Spectroscopy. *J. Anal. At. Spectrom.* **2009**, *24*, 215–223.
- (149) Lancaster, K. M.; Roemelt, M.; Ettenhuber, P.; Hu, Y. L.; Ribbe, M. W.; Neese, F.; Bergmann, U.; DeBeer, S. X-ray Emission Spectroscopy Evidences a Central Carbon in the Nitrogenase Iron-Molybdenum Cofactor. *Science* **2011**, *334*, 974–977.
- (150) Lezcano-Gonzalez, I.; Oord, R.; Rovezzi, M.; Glatzel, P.; Botchway, S. W.; Weckhuysen, B. M.; Beale, A. M. Molybdenum Speciation and its Impact on Catalytic Activity During Methane Dehydroaromatization in Zeolite ZSM-5 as Revealed by Operando X-ray Methods. *Angew. Chem., Int. Ed.* **2016**, *55*, 5215–5219.
- (151) Lomachenko, K. A.; Borfecchia, E.; Negri, C.; Berlier, G.; Lamberti, C.; Beato, P.; Falsig, H.; Bordiga, S. The Cu-CHA deNO(x) Catalyst in Action: Temperature-Dependent NH<sub>3</sub>-Assisted Selective Catalytic Reduction Monitored by Operando XAS and XES. *J. Am. Chem. Soc.* **2016**, *138*, 12025–12028.
- (152) Gallo, E.; Piovano, A.; Marini, C.; Mathon, O.; Pascarelli, S.; Glatzel, P.; Lamberti, C.; Berlier, G. Architecture of the Ti(IV) Sites in TiAlPO-5 Determined Using Ti K-Edge X-ray Absorption and X-ray Emission Spectroscopies. *J. Phys. Chem. C* **2014**, *118*, 11745–11751.
- (153) Groppo, E.; Gallo, E.; Seenivasan, K.; Lomachenko, K. A.; Sommazzi, A.; Bordiga, S.; Glatzel, P.; van Silfhout, R.; Kachatkou, A.; Bras, W.; et al. XAS and XES Techniques Shed Light on the Dark Side of Ziegler-Natta Catalysts: Active-Site Generation. *ChemCatChem* **2015**, *7*, 1432–1437.
- (154) DeBeer George, S.; Neese, F. Calibration of Scalar Relativistic Density Functional Theory for the Calculation of Sulfur K-Edge X-ray Absorption Spectra. *Inorg. Chem.* **2010**, *49*, 1849–1853.
- (155) Pollock, C. J.; DeBeer, S. Valence-to-Core X-ray Emission Spectroscopy: A Sensitive Probe of the Nature of a Bound Ligand. *J. Am. Chem. Soc.* **2011**, *133*, 5594–5601.
- (156) Pollock, C. J.; DeBeer, S. Insights into the Geometric and Electronic Structure of Transition Metal Centers from Valence-to-Core X-ray Emission Spectroscopy. *Acc. Chem. Res.* **2015**, *48*, 2967–2975.
- (157) Bauer, M. HERFD-XAS and Valence-to-Core-XES: New Tools to Push the Limits in Research with Hard X-rays? *Phys. Chem. Chem. Phys.* **2014**, *16*, 13827–13837.
- (158) Gallo, E.; Glatzel, P. Valence to Core X-ray Emission Spectroscopy. *Adv. Mater.* **2014**, *26*, 7730–7746.
- (159) Neese, F. The ORCA Program System. *Wires Comput. Mol. Sci.* **2012**, *2*, 73–78.
- (160) Blanc, F.; Coperet, C.; Lesage, A.; Emsley, L. High Resolution Solid-State NMR Spectroscopy in Surface Organometallic Chemistry:

Access to Molecular Understanding of Active Sites of Well-defined Heterogeneous Catalysts. *Chem. Soc. Rev.* **2008**, 37, 518–526.

(161) Pourpoint, F.; Lafon, O.; Gauvin, R.; Amoureux, J.-P.; Delevoye, L. Two-Dimensional Methods for Half-Integer Quadrupolar Nuclei. In *Modern Methods in Solid-State NMR: A Practitioner's Guide*; Hodgkinson, P., Ed.; Royal Society of Chemistry: Croydon, UK, 2018; Chapter 4, pp 97–133.

(162) Grekov, D.; Vancompernelle, T.; Taoufik, M.; Delevoye, L.; Gauvin, R. M. Solid-State NMR of Quadrupolar Nuclei for Investigations into Supported Organometallic Catalysts: Scope and Frontiers. *Chem. Soc. Rev.* **2018**, 47, 2572–2590.

(163) Copéret, C.; Liao, W.-C.; Gordon, C. P.; Ong, T.-C. Active Sites in Supported Single-Site Catalysts: An NMR Perspective. *J. Am. Chem. Soc.* **2017**, 139, 10588–10596.

(164) Yadav, N.; Seidi, F.; Del Gobbo, S.; D'Elia, V.; Crespy, D. Versatile Functionalization of Polymer Nanoparticles with Carbonate Groups via Hydroxyurethane Linkages. *Polym. Chem.* **2019**, 10, 3571–3584.

(165) Brus, J.; Czernek, J.; Urbanova, M.; Kobera, L.; Jegorov, A. An Efficient 2D  $^{11}\text{B}$ – $^{11}\text{B}$  Solid-State NMR Spectroscopy Strategy for Monitoring Covalent Self-Assembly of Boronic Acid-Derived Compounds: The Transformation and Unique Architecture of Bortezomib Molecules in the Solid State. *Phys. Chem. Chem. Phys.* **2017**, 19, 487–495.

(166) Tu, B.; Liu, X.; Wang, H.; Wang, W.; Zhai, P.; Fu, Z. Combining  $^{27}\text{Al}$  Solid-State NMR and First-Principles Simulations To Explore Crystal Structure in Disordered Aluminum Oxynitride. *Inorg. Chem.* **2016**, 55, 12930–12937.

(167) Mazoyer, E.; Trébosc, J.; Baudouin, A.; Boyron, O.; Pelletier, J.; Basset, J.-M.; Vitorino, M. J.; Nicholas, C. P.; Gauvin, R. M.; Taoufik, M.; Delevoye, L. Heteronuclear NMR Correlations To Probe the Local Structure of Catalytically Active Surface Aluminum Hydride Species on  $\gamma$ -Alumina. *Angew. Chem., Int. Ed.* **2010**, 49, 9854–9858.

(168) Li, Y.; Wu, X.-P.; Jiang, N.; Lin, M.; Shen, L.; Sun, H.; Wang, Y.; Wang, M.; Ke, X.; Yu, Z.; Gao, F.; Dong, L.; Guo, X.; Hou, W.; Ding, W.; Gong, X.-Q.; Grey, C. P.; Peng, L. Distinguishing Faceted Oxide Nanocrystals with  $^{17}\text{O}$  Solid-State NMR Spectroscopy. *Nat. Commun.* **2017**, 8, 581.

(169) Bryce, D. L. New Frontiers for Solid-State NMR Across the Periodic Table: a Snapshot of Modern Techniques and Instrumentation. *Dalton Trans* **2019**, 48, 8014–8020.

(170) Rataboul, F.; Baudouin, A.; Thieuleux, C.; Veyre, L.; Coperet, C.; Thivolle-Cazat, J.; Basset, J. M.; Lesage, A.; Emsley, L. Molecular Understanding of the Formation of Surface Zirconium Hydrides upon Thermal Treatment Under Hydrogen of  $[(\equiv\text{SiO})\text{Zr}(\text{CH}_2\text{tBu})_2]$  by Using Advanced Solid-State NMR Techniques. *J. Am. Chem. Soc.* **2004**, 126, 12541–12550.

(171) Avenier, P.; Lesage, A.; Taoufik, M.; Baudouin, A.; De Mallmann, A.; Fiddy, S.; Vautier, M.; Veyre, L.; Basset, J. M.; Emsley, L.; et al. Well-defined Surface Imido Amido Tantalum(V) Species from Ammonia and Silica-Supported Tantalum Hydrides. *J. Am. Chem. Soc.* **2007**, 129, 176–186.

(172) Blanc, F.; Coperet, C.; Thivolle-Cazat, J.; Basset, J. M.; Lesage, A.; Emsley, L.; Sinha, A.; Schrock, R. R. Surface Versus Molecular Siloxy Ligands in Well-Defined Olefin Metathesis Catalysts:  $[(\text{RO})_3\text{SiO}]\text{Mo}(\equiv\text{NAr})(\equiv\text{CH}^t\text{Bu})(\text{CH}_2^t\text{Bu})]$ . *Angew. Chem., Int. Ed.* **2006**, 45, 1216–1220.

(173) Chabanas, M.; Quadrelli, E. A.; Fenet, B.; Coperet, C.; Thivolle-Cazat, J.; Basset, J. M.; Lesage, A.; Emsley, L. Molecular insight into Surface Organometallic Chemistry Through the Combined Use of 2D HETCOR Solid-State NMR Spectroscopy and Silsesquioxane Analogues. *Angew. Chem., Int. Ed.* **2001**, 40, 4493–4496.

(174) Cole, H. B. R.; Torchia, D. A. An NMR-Study of the Backbone Dynamics of Staphylococcal Nuclease in the Crystalline State. *Chem. Phys.* **1991**, 158, 271–281.

(175) Rossini, A. J.; Zagdoun, A.; Lelli, M.; Lesage, A.; Coperet, C.; Emsley, L. Dynamic Nuclear Polarization Surface Enhanced NMR Spectroscopy. *Acc. Chem. Res.* **2013**, 46, 1942–1951.

(176) Kobayashi, T.; Perras, F. A.; Slowing, I. I.; Sadow, A. D.; Pruski, M. Dynamic Nuclear Polarization Solid-State NMR in Heterogeneous Catalysis Research. *ACS Catal.* **2015**, 5, 7055–7062.

(177) Lelli, M.; Gajan, D.; Lesage, A.; Caporini, M. A.; Vitzthum, V.; Mieville, P.; Heroguel, F.; Rascon, F.; Roussey, A.; Thieuleux, C.; et al. Fast Characterization of Functionalized Silica Materials by Silicon-29 Surface-Enhanced NMR Spectroscopy Using Dynamic Nuclear Polarization. *J. Am. Chem. Soc.* **2011**, 133, 2104–2107.

(178) Lesage, A.; Lelli, M.; Gajan, D.; Caporini, M. A.; Vitzthum, V.; Mieville, P.; Alauzun, J.; Roussey, A.; Thieuleux, C.; Mehdi, A.; Bodenhausen, G.; Coperet, C.; Emsley, L. Surface Enhanced NMR Spectroscopy by Dynamic Nuclear Polarization. *J. Am. Chem. Soc.* **2010**, 132, 15459–15461.

(179) Lafon, O.; Rosay, M.; Aussenac, F.; Lu, X.; Trébosc, J.; Cristini, O.; Kinowski, C.; Touati, N.; Vezin, H.; Amoureux, J.-P. Beyond the Silica Surface by Direct Silicon-29 Dynamic Nuclear Polarization. *Angew. Chem., Int. Ed.* **2011**, 50, 8367–8370.

(180) Vitzthum, V.; Mieville, P.; Carnevale, D.; Caporini, M. A.; Gajan, D.; Copéret, C.; Lelli, M.; Zagdoun, A.; Rossini, A. J.; Lesage, A.; Emsley, L.; Bodenhausen, G. Dynamic Nuclear Polarization of Quadrupolar Nuclei Using Cross Polarization from Protons: Surface-Enhanced Aluminium-27 NMR. *Chem. Commun.* **2012**, 48, 1988–1990.

(181) Lee, D.; Duong, N. T.; Lafon, O.; De Paëpe, G. Primostrato Solid-State NMR Enhanced by Dynamic Nuclear Polarization: Pentacoordinated  $\text{Al}^{3+}$  Ions Are Only Located at the Surface of Hydrated  $\gamma$ -Alumina. *J. Phys. Chem. C* **2014**, 118, 25065–25076.

(182) Lee, D.; Takahashi, H.; Thankamony, A. S. L.; Dacquin, J.-P.; Bardet, M.; Lafon, O.; De Paëpe, G. Enhanced Solid-State NMR Correlation Spectroscopy of Quadrupolar Nuclei Using Dynamic Nuclear Polarization. *J. Am. Chem. Soc.* **2012**, 134, 18491–18494.

(183) Gunther, W. R.; Michaelis, V. K.; Caporini, M. A.; Griffin, R. G.; Roman-Leshkov, Y. Dynamic Nuclear Polarization NMR Enables the Analysis of Sn-Beta Zeolite Prepared with Natural Abundance Sn-119 Precursors. *J. Am. Chem. Soc.* **2014**, 136, 6219–6222.

(184) Wolf, P.; Valla, M.; Rossini, A. J.; Comas-Vives, A.; Núñez-Zarur, F.; Malaman, B.; Lesage, A.; Emsley, L.; Copéret, C.; Hermans, I. NMR Signatures of the Active Sites in Sn- $\beta$  Zeolite. *Angew. Chem., Int. Ed.* **2014**, 53, 10179–10183.

(185) Lafon, O.; Thankamony, A. S. L.; Kobayashi, T.; Carnevale, D.; Vitzthum, V.; Slowing, I. I.; Kandel, K.; Vezin, H.; Amoureux, J. P.; Bodenhausen, G.; et al. Mesoporous Silica Nanoparticles Loaded with Surfactant: Low Temperature Magic Angle Spinning C-13 and Si-29 NMR Enhanced by Dynamic Nuclear Polarization. *J. Phys. Chem. C* **2013**, 117, 1375–1382.

(186) Pump, E.; Viger-Gravel, J.; Abou-Hamad, E.; Samantaray, M. K.; Hamzaoui, B.; Gurinov, A.; Anjum, D. H.; Gajan, D.; Lesage, A.; Bendjeriou-Sedjerari, A.; et al. Reactive Surface Organometallic Complexes Observed Using Dynamic Nuclear Polarization Surface Enhanced NMR Spectroscopy. *Chem. Sci.* **2017**, 8, 284–290.

(187) Liao, W. C.; Ong, T. C.; Gajan, D.; Bernada, F.; Sauvee, C.; Yulikov, M.; Pucino, M.; Schowner, R.; Schwarzwald, M.; Buchmeiser, M. R.; et al. Dendritic Polarizing Agents for DNP SENS. *Chem. Sci.* **2017**, 8, 416–422.

(188) Takahashi, H.; Hediger, S.; De Paëpe, G. Matrix-free Dynamic Nuclear Polarization Enables Solid-State NMR  $^{13}\text{C}$ – $^{13}\text{C}$  Correlation Spectroscopy of Proteins at Natural Isotopic Abundance. *Chem. Commun.* **2013**, 49, 9479–9481.

(189) Fernandez-de-Alba, C.; Takahashi, H.; Richard, A.; Chenavier, Y.; Dubois, L.; Maurel, V.; Lee, D.; Hediger, S.; De Paëpe, G. Matrix-Free DNP-Enhanced NMR Spectroscopy of Liposomes Using a Lipid-Anchored Biradical. *Chem. - Eur. J.* **2015**, 21, 4512–4517.

(190) Piveteau, L.; Ong, T. C.; Rossini, A. J.; Emsley, L.; Coperet, C.; Kovalenko, M. V. Structure of Colloidal Quantum Dots from Dynamic Nuclear Polarization Surface Enhanced NMR Spectroscopy. *J. Am. Chem. Soc.* **2015**, 137, 13964–13971.



- (191) Valentine, K. G.; Mathies, G.; Bedard, S.; Nucci, N. V.; Dodevski, I.; Stetz, M. A.; Can, T. V.; Griffin, R. G.; Wand, A. J. Reverse Micelles as a Platform for Dynamic Nuclear Polarization in Solution NMR of Proteins. *J. Am. Chem. Soc.* **2014**, *136*, 2800–2807.
- (192) Viger-Gravel, J.; Berruyer, P.; Gajan, D.; Basset, J. M.; Lesage, A.; Tordo, P.; Ouari, O.; Emsley, L. Frozen Acrylamide Gels as Dynamic Nuclear Polarization Matrices. *Angew. Chem., Int. Ed.* **2017**, *56*, 8726–8730.
- (193) Silverio, D. L.; van Kalker, H. A.; Ong, T. C.; Baudin, M.; Yulikov, M.; Veyre, L.; Berruyer, P.; Chaudhari, S.; Gajan, D.; Baudouin, D.; et al. Tailored Polarizing Hybrid Solids with Nitroxide Radicals Localized in Mesoporous Silica Walls. *Helv. Chim. Acta* **2017**, *100*, No. e1700101.
- (194) Pump, E.; Bendjeriou-Sedjerari, A.; Viger-Gravel, J.; Gajan, D.; Scotto, B.; Samantaray, M. K.; Abou-Hamad, E.; Gurinov, A.; Almaksoud, W.; Cao, Z.; et al. Predicting the DNP-SENS Efficiency in Reactive Heterogeneous Catalysts from Hydrophilicity. *Chem. Sci.* **2018**, *9*, 4866–4872.
- (195) Pfennig, V.; Seppelt, K. Crystal and Molecular Structures of Hexamethyltungsten and Hexamethylrhenium. *Science* **1996**, *271*, 626–628.
- (196) Samantaray, M. K.; Callens, E.; Abou-Hamad, E.; Rossini, A. J.; Widdifield, C. M.; Dey, R.; Emsley, L.; Basset, J. M. WMe<sub>6</sub> Tamed by Silica: Si-O-WMe<sub>3</sub> as an Efficient, Well-Defined Species for Alkane Metathesis, Leading to the Observation of a Supported W-Methyl/Methylidyne Species. *J. Am. Chem. Soc.* **2014**, *136*, 1054–1061.
- (197) Samantaray, M. K.; Dey, R.; Kavitate, S.; Abou-Hamad, E.; Bendjeriou-Sedjerari, A.; Hamieh, A.; Basset, J. M. Synergy Between Two Metal Catalysts: A Highly Active Silica-Supported Bimetallic W/Zr Catalyst for Metathesis of n-Decane. *J. Am. Chem. Soc.* **2016**, *138*, 8595–8602.
- (198) Gutmann, T.; Liu, J.; Rothmel, N.; Xu, Y.; Jaumann, E.; Werner, M.; Breitzke, H.; Sigurdsson, S. T.; Buntkowsky, G. Natural Abundance <sup>15</sup>N NMR by Dynamic Nuclear Polarization: Fast Analysis of Binding Sites of a Novel Amine-Carboxyl-Linked Immobilized Dirhodium Catalyst. *Chem. - Eur. J.* **2015**, *21*, 3798–3805.
- (199) Berruyer, P.; Lelli, M.; Conley, M. P.; Silverio, D. L.; Widdifield, C. M.; Siddiqi, G.; Gajan, D.; Lesage, A.; Copéret, C.; Emsley, L. Three-Dimensional Structure Determination of Surface Sites. *J. Am. Chem. Soc.* **2017**, *139*, 849–855.
- (200) Werghi, B.; Pump, E.; Tretiakov, M.; Abou-Hamad, E.; Gurinov, A.; Doggali, P.; Anjum, D. H.; Cavallo, L.; Bendjeriou-Sedjerari, A.; Basset, J.-M. Exploiting the Interactions Between the Ruthenium Hoveyda–Grubbs Catalyst and Al-Modified Mesoporous Silica: The Case of SBA15 vs. KCC-1. *Chem. Sci.* **2018**, *9*, 3531–3537.
- (201) Zaghdoun, A.; Casano, G.; Ouari, O.; Schwarzwälder, M.; Rossini, A. J.; Aussenac, F.; Yulikov, M.; Jeschke, G.; Copéret, C.; Lesage, A.; Tordo, P.; Emsley, L. Large Molecular Weight Nitroxide Biradicals Providing Efficient Dynamic Nuclear Polarization at Temperatures up to 200 K. *J. Am. Chem. Soc.* **2013**, *135*, 12790–12797.
- (202) Brodrecht, M.; Kumari, B.; Thankamony, A. S. S. L.; Breitzke, H.; Gutmann, T.; Buntkowsky, G. Structural Insights into Peptides Bound to the Surface of Silica Nanopores. *Chem. - Eur. J.* **2019**, *25*, 5214–5221.
- (203) Hamzaoui, B.; Bendjeriou-Sedjerari, A.; Pump, E.; Abou-Hamad, E.; Sougrat, R.; Gurinov, A.; Huang, K.-W.; Gajan, D.; Lesage, A.; Emsley, L.; Basset, J.-M. Atomic-Level Organization of Vicinal Acid–Base Pairs through the Chemisorption of Aniline and Derivatives onto Mesoporous SBA15. *Chem. Sci.* **2016**, *7*, 6099–6105.
- (204) Lilly Thankamony, A. S.; Lion, C.; Pourpoint, F.; Singh, B.; Perez Linde, A. J.; Carnevale, D.; Bodenhausen, G.; Vezin, H.; Lafon, O.; Polshettiwar, V. Insights into the Catalytic Activity of Nitridated Fibrous Silica (KCC-1) Nanocatalysts from <sup>15</sup>N and <sup>29</sup>Si NMR Spectroscopy Enhanced by Dynamic Nuclear Polarization. *Angew. Chem., Int. Ed.* **2015**, *54*, 2190–2193.
- (205) Bendjeriou-Sedjerari, A.; Pelletier, J. D. A.; Abou-Hamad, E.; Emsley, L.; Basset, J. M. A Well-defined Mesoporous Amine Silica Surface via a Selective Treatment of SBA-15 with Ammonia. *Chem. Commun.* **2012**, *48*, 3067–3069.
- (206) Shi, L.; Zou, Y.; He, H. Y. H-1 NMR Study of Hydroxy Groups in Mesoporous Molecular Sieve SBA-15. *Chem. Lett.* **2001**, *30*, 1164–1165.
- (207) Pelletier, J.; Espinas, J.; Vu, N.; Norsic, S.; Baudouin, A.; Delevoye, L.; Trébosc, J.; Le Roux, E.; Santini, C.; Basset, J.-M.; Gauvin, R. M.; Taoufik, M. A Well-Defined Silica-Supported Aluminium Alkyl through an Unprecedented, Consecutive Two-Step Protonolysis–Alkyl Transfer Mechanism. *Chem. Commun.* **2011**, *47*, 2979–2981.
- (208) Werghi, B.; Bendjeriou-Sedjerari, A.; Jedidi, A.; Abou-Hamad, E.; Cavallo, L.; Basset, J.-M. Single-Site Tetracoordinated Aluminum Hydride Supported on Mesoporous Silica. From Dream to Reality! *Organometallics* **2016**, *35*, 3288–3294.
- (209) Zhang, F.; Szeto, K. C.; Taoufik, M.; Delevoye, L.; Gauvin, R. M.; Scott, S. L. Enhanced Metathesis Activity and Stability of Methyltrioxorhenium on a Mostly Amorphous Alumina: Role of the Local Grafting Environment. *J. Am. Chem. Soc.* **2018**, *140*, 13854–13868.
- (210) Sauter, D. W.; Chiari, V.; Aykac, N.; Bouaouli, S.; Perrin, L.; Delevoye, L.; Gauvin, R. M.; Szeto, K. C.; Boisson, C.; Taoufik, M. Preparation of Monopodal and Bipodal Aluminum Surface Species by Selective Protonolysis of Highly Reactive [AlH<sub>3</sub>(NMe<sub>2</sub>Et)] on Silica. *Dalton Trans* **2017**, *46*, 11547–11551.
- (211) Gallo, A.; Fong, A.; Szeto, K. C.; Rieb, J.; Delevoye, L.; Gauvin, R. M.; Taoufik, M.; Peters, B.; Scott, S. L. Ligand Exchange-Mediated Activation and Stabilization of a Re-Based Olefin Metathesis Catalyst by Chlorinated Alumina. *J. Am. Chem. Soc.* **2016**, *138*, 12935–12947.
- (212) Michaelis, V. K.; Corzilius, B.; Smith, A. A.; Griffin, R. G. Dynamic Nuclear Polarization of <sup>17</sup>O: Direct Polarization. *J. Phys. Chem. B* **2013**, *117*, 14894–14906.
- (213) Merle, N.; Trébosc, J.; Baudouin, A.; Rosal, I. D.; Maron, L.; Szeto, K.; Genelot, M.; Mortreux, A.; Taoufik, M.; Delevoye, L.; Gauvin, R. M. <sup>17</sup>O NMR Gives Unprecedented Insights into the Structure of Supported Catalysts and Their Interaction with the Silica Carrier. *J. Am. Chem. Soc.* **2012**, *134*, 9263–9275.
- (214) Grekov, D.; Bouhoute, Y.; Szeto, K. C.; Merle, N.; De Mallmann, A.; Lefebvre, F.; Lucas, C.; Del Rosal, I.; Maron, L.; Gauvin, R. M.; Delevoye, L.; Taoufik, M. Silica-Supported Tungsten Neosilyl Oxo Precatalysts: Impact of the Podality on Activity and Stability in Olefin Metathesis. *Organometallics* **2016**, *35*, 2188–2196.
- (215) Merle, N.; Girard, G.; Popoff, N.; De Mallmann, A.; Bouhoute, Y.; Trébosc, J.; Berrier, E.; Paul, J.-F.; Nicholas, C. P.; Del Rosal, I.; Maron, L.; Gauvin, R. M.; Delevoye, L.; Taoufik, M. On the Track to Silica-Supported Tungsten Oxo Metathesis Catalysts: Input from <sup>17</sup>O Solid-State NMR. *Inorg. Chem.* **2013**, *52*, 10119–10130.
- (216) Perras, F. A.; Chaudhary, U.; Slowing, I. I.; Pruski, M. Probing Surface Hydrogen Bonding and Dynamics by Natural Abundance, Multidimensional, <sup>17</sup>O DNP-NMR Spectroscopy. *J. Phys. Chem. C* **2016**, *120*, 11535–11544.
- (217) Perras, F. A.; Kobayashi, T.; Pruski, M. Natural Abundance <sup>17</sup>O DNP Two-Dimensional and Surface-Enhanced NMR Spectroscopy. *J. Am. Chem. Soc.* **2015**, *137*, 8336–8339.
- (218) Cramer, C. J. *Essentials of Computational Chemistry: Theories and Models*, 2nd ed.; John Wiley and Sons: Chichester, England, 2004.
- (219) Jensen, F. *Introduction to Computational Chemistry*, 2nd ed.; John Wiley and Sons: Hoboken, NJ, 2007.
- (220) Szabo, A.; Ostlund, N. S. *Modern Quantum Chemistry: Introduction to Advanced Electronic Structure Theory*; Dover Publications, 1996.
- (221) Pyykko, P.; Stanton, J. F. Introduction to the Quantum Chemistry 2012 Issue. *Chem. Rev.* **2012**, *112*, 1–3.
- (222) Pisani, C. Ab-Initio Approaches to the Quantum-Mechanical Treatment of periodic Systems. In *Quantum-Mechanical Ab-initio Calculation of the Properties of Crystalline Materials*; Pisani, C., Ed.; Springer-Verlag: Berlin Heidelberg, 1996; Vol. 67, pp 47–75.



- (223) Dovesi, R.; Civalleri, B.; Orlando, R.; Roetti, C.; Saunders, V. R. Ab Initio Quantum Simulation in Solid State Chemistry. *Rev. Comp. Chem.* **2005**, *21*, 1–125.
- (224) Tasker, P. W. Stability of Ionic-Crystal Surfaces. *J. Phys. C: Solid State Phys.* **1979**, *12*, 4977–4984.
- (225) Meyer, B.; Marx, D. Density-Functional Study of the Structure and Stability of ZnO Surfaces. *Phys. Rev. B: Condens. Matter Mater. Phys.* **2003**, *67*, 039902.
- (226) Rimola, A.; Costa, D.; Sodupe, M.; Lambert, J. F.; Ugliengo, P. Silica Surface Features and Their Role in the Adsorption of Biomolecules: Computational Modeling and Experiments. *Chem. Rev.* **2013**, *113*, 4216–4313.
- (227) Ciacchi, L. C.; Payne, M. C. First-Principles Molecular-Dynamics Study of Native Oxide Growth on Si(001). *Phys. Rev. Lett.* **2005**, *95*, 196101.
- (228) Pedone, A. Properties Calculations of Silica-Based Glasses by Atomistic Simulations Techniques: A Review. *J. Phys. Chem. C* **2009**, *113*, 20773–20784.
- (229) Sauer, J. Molecular-Models in Ab Initio Studies of Solids and Surfaces - from Ionic-Crystals and Semiconductors to Catalysts. *Chem. Rev.* **1989**, *89*, 199–255.
- (230) Sherrill, C. D. Frontiers in Electronic Structure Theory. *J. Chem. Phys.* **2010**, *132*, 110902.
- (231) Tomasi, J.; Persico, M. Molecular-Interactions in Solution - an Overview of Methods Based on Continuous Distributions of the Solvent. *Chem. Rev.* **1994**, *94*, 2027–2094.
- (232) Meier, W. M.; Olson, D. H.; Baerlocher, C. Atlas of Zeolite Structure Types. *Zeolites* **1996**, *17*, 1–229.
- (233) Sauer, J.; Ugliengo, P.; Garrone, E.; Saunders, V. R. Theoretical-Study of Van-Der-Waals Complexes at Surface Sites in Comparison with the Experiment. *Chem. Rev.* **1994**, *94*, 2095–2160.
- (234) Ghosh, T. K.; Nair, N. N. Rh<sub>1</sub>/γ-Al<sub>2</sub>O<sub>3</sub> Single-Atom Catalysis of O<sub>2</sub> Activation and CO Oxidation: Mechanism, Effects of Hydration, Oxidation State, and Cluster Size. *ChemCatChem* **2013**, *5*, 1811–1821.
- (235) Yang, T.; Fukuda, R.; Hosokawa, S.; Tanaka, T.; Sakaki, S.; Ehara, M. A Theoretical Investigation on CO Oxidation by Single-Atom Catalysts M<sub>1</sub>/γ-Al<sub>2</sub>O<sub>3</sub> (M = Pd, Fe, Co, and Ni). *ChemCatChem* **2017**, *9*, 1222–1229.
- (236) Gu, J.; Wang, J.; Leszczynski, J. Structure and Energetics of (111) Surface of γ-Al<sub>2</sub>O<sub>3</sub>: Insights from DFT Including Periodic Boundary Approach. *ACS Omega* **2018**, *3*, 1881–1888.
- (237) Taoufik, M.; Szeto, K. C.; Merle, N.; Rosal, I. D.; Maron, L.; Trébosc, J.; Tricot, G.; Gauvin, R. M.; Delevoye, L. Heteronuclear NMR Spectroscopy as a Surface-Selective Technique: A Unique Look at the Hydroxyl Groups of γ-Alumina. *Chem. - Eur. J.* **2014**, *20*, 4038–4046.
- (238) Maseras, F.; Morokuma, K. Imommm - a New Integrated Ab-Initio Plus Molecular Mechanics Geometry Optimization Scheme of Equilibrium Structures and Transition-States. *J. Comput. Chem.* **1995**, *16*, 1170–1179.
- (239) Perdew, J. P.; Burke, K.; Ernzerhof, M. Generalized Gradient Approximation Made Simple. *Phys. Rev. Lett.* **1996**, *77*, 3865–3868.
- (240) Blochl, P. E. Projector Augmented-Wave Method. *Phys. Rev. B: Condens. Matter Mater. Phys.* **1994**, *50*, 17953–17979.
- (241) Monkhorst, H. J.; Pack, J. D. Special Points for Brillouin-Zone Integrations. *Phys. Rev. B* **1976**, *13*, 5188–5192.
- (242) Mills, G.; Jonsson, H.; Schenter, G. K. Reversible Work Transition-State Theory - Application to Dissociative Adsorption of Hydrogen. *Surf. Sci.* **1995**, *324*, 305–337.
- (243) Henkelman, G.; Jonsson, H. Improved Tangent Estimate in the Nudged Elastic Band Method for Finding Minimum Energy Paths and Saddle Points. *J. Chem. Phys.* **2000**, *113*, 9978–9985.
- (244) Henkelman, G.; Uberuaga, B. P.; Jonsson, H. A Climbing Image Nudged Elastic Band Method for Finding Saddle Points and Minimum Energy Paths. *J. Chem. Phys.* **2000**, *113*, 9901–9904.
- (245) Henkelman, G.; Jonsson, H. A Dimer Method for Finding Saddle Points on High Dimensional Potential Surfaces Using Only First Derivatives. *J. Chem. Phys.* **1999**, *111*, 7010–7022.
- (246) Naumov, V. A.; Krylov, O. V. Mechanism of the Sabatier Reaction on a Nickel-Catalyst. *Kinet. Catal.* **1979**, *20*, 1116–1119.
- (247) Schwartz, J.; Ward, M. D. Silica-Supported Zirconium Hydrides as Isomerization or Hydrogenation Catalysts for Long-Chain Olefins. *J. Mol. Catal.* **1980**, *8*, 465–469.
- (248) Delley, M. F.; Silaghi, M. C.; Nunez-Zarur, F.; Kovtunov, K. V.; Salnikov, O. G.; Estes, D. P.; Koptuyug, I. V.; Comas-Vives, A.; Coperet, C. X-H. Bond Activation on Cr(III)-O Sites (X = R, H): Key Steps in Dehydrogenation and Hydrogenation Processes. *Organometallics* **2017**, *36*, 234–244.
- (249) Anderson, A. B.; Nichols, J. A. Hydrogen on Zinc-Oxide - Theory of Its Heterolytic Adsorption. *J. Am. Chem. Soc.* **1986**, *108*, 4742–4746.
- (250) Kyriakou, G.; Boucher, M. B.; Jewell, A. D.; Lewis, E. A.; Lawton, T. J.; Baber, A. E.; Tierney, H. L.; Flytzani-Stephanopoulos, M.; Sykes, E. C. H. Isolated Metal Atom Geometries as a Strategy for Selective Heterogeneous Hydrogenations. *Science* **2012**, *335*, 1209–1212.
- (251) Tierney, H. L.; Baber, A. E.; Kitchin, J. R.; Sykes, E. C. H. Hydrogen Dissociation and Spillover on Individual Isolated Palladium Atoms. *Phys. Rev. Lett.* **2009**, *103*, 246102.
- (252) Tierney, H. L.; Baber, A. E.; Sykes, E. C. H. Atomic-Scale Imaging and Electronic Structure Determination of Catalytic Sites on Pd/Cu Near Surface Alloys. *J. Phys. Chem. C* **2009**, *113*, 7246–7250.
- (253) Bellisario, D. O.; Han, J. W.; Tierney, H. L.; Baber, A. E.; Sholl, D. S.; Sykes, E. C. H. Importance of Kinetics in Surface Alloying: A Comparison of the Diffusion Pathways of Pd and Ag Atoms on Cu(111). *J. Phys. Chem. C* **2009**, *113*, 12863–12869.
- (254) Boucher, M. B.; Zugic, B.; Cladaras, G.; Kammert, J.; Marcinkowski, M. D.; Lawton, T. J.; Sykes, E. C. H.; Flytzani-Stephanopoulos, M. Single-Atom Alloy Surface Analogs in Pd<sub>0.18</sub>Cu<sub>0.15</sub> Nanoparticles for Selective Hydrogenation Reactions. *Phys. Chem. Chem. Phys.* **2013**, *15*, 12187–12196.
- (255) Aich, P.; Wei, H. J.; Basan, B.; Kropf, A. J.; Schweitzer, N. M.; Marshall, C. L.; Miller, J. T.; Meyer, R. Single-Atom Alloy Pd-Ag Catalyst for Selective Hydrogenation of Acrolein. *J. Phys. Chem. C* **2015**, *119*, 18140–18148.
- (256) Liu, J. L.; Shan, J. J.; Lucci, F. R.; Cao, S. F.; Sykes, E. C. H.; Flytzani-Stephanopoulos, M. Palladium-Gold Single-Atom Alloy Catalysts for Liquid Phase Selective Hydrogenation of 1-Hexyne. *Catal. Sci. Technol.* **2017**, *7*, 4276–4284.
- (257) Yan, H.; Cheng, H.; Yi, H.; Lin, Y.; Yao, T.; Wang, C. L.; Li, J. J.; Wei, S. Q.; Lu, J. L. Single-Atom Pd<sub>1</sub>/Graphene Catalyst Achieved by Atomic Layer Deposition: Remarkable Performance in Selective Hydrogenation of 1,3-Butadiene. *J. Am. Chem. Soc.* **2015**, *137*, 10484–10487.
- (258) Vile, G.; Albani, D.; Nachtegaal, M.; Chen, Z. P.; Dontsova, D.; Antonietti, M.; Lopez, N.; Perez-Ramirez, J. A Stable Single-Site Palladium Catalyst for Hydrogenations. *Angew. Chem., Int. Ed.* **2015**, *54*, 11265–11269.
- (259) Lecuyer, C.; Quignard, F.; Choplin, A.; Olivier, D.; Basset, J. M. Surface Organometallic Chemistry on Oxides - Selective Catalytic Low-Temperature Hydrogenolysis of Alkanes by a Highly Electrophilic Zirconium Hydride Complex Supported on Silica. *Angew. Chem., Int. Ed. Engl.* **1991**, *30*, 1660–1661.
- (260) Quignard, F.; Choplin, A.; Basset, J. M. Alkane Activation by a Highly Electrophilic Zirconium Hydride Complex Supported on Silica. *J. Chem. Soc., Chem. Commun.* **1991**, 1589–1590.
- (261) Norsic, S.; Larabi, C.; Delgado, M.; Garron, A.; de Mallmann, A.; Santini, C.; Szeto, K. C.; Basset, J. M.; Taoufik, M. Low Temperature Hydrogenolysis of Waxes to Diesel Range Gasoline and Light Alkanes: Comparison of Catalytic Properties of Group 4, 5 and 6 Metal Hydrides Supported on Silica-Alumina. *Catal. Sci. Technol.* **2012**, *2*, 215–219.
- (262) Vidal, V.; Theolier, A.; Thivolle-Cazat, J.; Basset, J. M. Metathesis of Alkanes Catalyzed by Silica-Supported Transition Metal Hydrides. *Science* **1997**, *276*, 99–102.

- (263) Burnett, R. L.; Hughes, T. R. Mechanism and Poisoning of Molecular Redistribution Reaction of Alkanes with a Dual-Functional Catalyst System. *J. Catal.* **1973**, *31*, 55–64.
- (264) Basset, J. M.; Jean Thivolle-Cazat, M. T. Sudhakar Chakka Process for Converting Methane into Liquid Alkane Mixtures. European Patent EP2022772A1, Feb 11, 2009.
- (265) Schinzel, S.; Chermette, H.; Coperet, C.; Basset, J. M. Evaluation of the Carbene Hydride Mechanism in the Carbon-Carbon Bond Formation Process of Alkane Metathesis Through a DFT Study. *J. Am. Chem. Soc.* **2008**, *130*, 7984–7987.
- (266) Nunez-Zarur, F.; Solans-Monfort, X.; Restrepo, A. Mechanistic Insights into Alkane Metathesis Catalyzed by Silica-Supported Tantalum Hydrides: A DFT Study. *Inorg. Chem.* **2017**, *56*, 10458–10473.
- (267) Saint-Arroman, R. P.; Chabanas, M.; Baudouin, A.; Coperet, C.; Basset, J. H.; Lesage, A.; Emsley, L. Characterization of Surface Organometallic Complexes Using High Resolution 2D Solid-State NMR Spectroscopy. Application to the Full Characterization of a Silica Supported Metal Carbyne:  $\equiv\text{SiO-Mo}(\equiv\text{C-Bu}^t(\text{CH}_2\text{-Bu}^t)_2)$ . *J. Am. Chem. Soc.* **2001**, *123*, 3820–3821.
- (268) Le Roux, E.; Taoufik, M.; Coperet, C.; de Mallmann, A.; Thivolle-Cazat, J.; Basset, J. M.; Maunders, B. M.; Sunley, G. J. Development of Tungsten-Based Heterogeneous Alkane Metathesis Catalysts Through a Structure-Activity Relationship. *Angew. Chem., Int. Ed.* **2005**, *44*, 6755–6758.
- (269) Samantaray, M. K.; Dey, R.; Abou-Hamad, E.; Hamieh, A.; Basset, J. M. Effect of Support on Metathesis of n-Decane: Drastic Improvement in Alkane Metathesis with  $\text{WMe}_3$  Linked to Silica-Alumina. *Chem. - Eur. J.* **2015**, *21*, 6100–6106.
- (270) Le Roux, E.; Taoufik, M.; Baudouin, A.; Coperet, C.; Thivolle-Cazat, J.; Basset, J. M.; Maunders, B. M.; Sunley, G. J. Silica-Alumina-Supported, Tungsten-Based Heterogeneous Alkane Metathesis Catalyst: Is it Closer to a Silica- or an Alumina-Supported System? *Adv. Synth. Catal.* **2007**, *349*, 231–237.
- (271) Soignier, S.; Taoufik, M.; Le Roux, E.; Saggio, G.; Dablemont, C.; Baudouin, A.; Lefebvre, F.; de Mallmann, A.; Thivolle-Cazat, J.; Basset, J. M.; et al. Tantalum Hydrides Supported on MCM-41 Mesoporous Silica: Activation of Methane and Thermal Evolution of the Tantalum-Methyl Species. *Organometallics* **2006**, *25*, 1569–1577.
- (272) Basset, J. M.; Coperet, C.; Lefort, L.; Maunders, B. M.; Maury, O.; Le Roux, E.; Saggio, G.; Soignier, S.; Soulivong, D.; Sunley, G. J.; et al. Primary Products and Mechanistic Considerations in Alkane Metathesis. *J. Am. Chem. Soc.* **2005**, *127*, 8604–8605.
- (273) Shortland, A.; Wilkinson, G. Hexamethyltungsten. *J. Chem. Soc., Chem. Commun.* **1972**, 318a.
- (274) Samantaray, M. K.; Kavita, S.; Morlanes, N.; Abou-Hamad, E.; Hamieh, A.; Dey, R.; Basset, J. M. Unearthing a Well-Defined Highly Active Bimetallic W/Ti Precatalyst Anchored on a Single Silica Surface for Metathesis of Propane. *J. Am. Chem. Soc.* **2017**, *139*, 3522–3527.
- (275) Riache, N.; Callens, E.; Samantaray, M. K.; Kharbatia, N. M.; Atiqullah, M.; Basset, J. M. Cyclooctane Metathesis Catalyzed by Silica-Supported Tungsten Pentamethyl  $[(\equiv\text{SiO})\text{W}(\text{Me})_5]$ : Distribution of Macrocyclic Alkanes. *Chem. - Eur. J.* **2014**, *20*, 15089–15094.
- (276) Hamieh, A.; Chen, Y.; Abdel-Azeim, S.; Abou-hamad, E.; Goh, S.; Samantaray, M.; Dey, R.; Cavallo, L.; Basset, J. M. Well-Defined Surface Species  $[(\equiv\text{Si-O})\text{W}(=\text{O})\text{Me}_3]$  Prepared by Direct Methylation of  $[(\equiv\text{Si-O})\text{W}(=\text{O})\text{Cl}_3]$ , a Catalyst for Cycloalkane Metathesis and Transformation of Ethylene to Propylene. *ACS Catal.* **2015**, *5*, 2164–2171.
- (277) Pump, E.; Cao, Z.; Samantaray, M. K.; Bendjeriou-Sedjerari, A.; Cavallo, L.; Basset, J. M. Exploiting Confinement Effects to Tune Selectivity in Cyclooctane Metathesis. *ACS Catal.* **2017**, *7*, 6581–6586.
- (278) Soulivong, D.; Coperet, C.; Thivolle-Cazat, J.; Basset, J. M.; Maunders, B. M.; Pardy, R. B. A.; Sunley, G. J. Cross-Metathesis of Propane and Methane: A Catalytic Reaction of C-C Bond Cleavage of a Higher Alkane by Methane. *Angew. Chem., Int. Ed.* **2004**, *43*, 5366–5369.
- (279) Morlanes, N.; Kavita, S. G.; Rosenfeld, D. C.; Basset, J. M. Alkane Cross-Metathesis Reaction between Light and Heavy Linear Alkanes, on a Silica Supported Well-Defined Single-Site Catalyst. *ACS Catal.* **2019**, *9*, 1274–1282.
- (280) Taoufik, M.; Schwab, E.; Schultz, M.; Vanoppen, D.; Walter, M.; Thivolle-Cazat, J.; Basset, J. M. Cross-Metathesis Between Ethane and Toluene Catalyzed by  $[(\equiv\text{SiO})_2\text{TaH}]$ : The First Example of a Cross-Metathesis Reaction Between an Alkane and an Aromatic. *Chem. Commun.* **2004**, 1434–1435.
- (281) Yang, C. J.; Miao, Z. L.; Zhang, F.; Li, L.; Liu, Y. T.; Wang, A. Q.; Zhang, T. Hydrogenolysis of Methyl Glycolate to Ethanol Over a Pt-Cu/SiO<sub>2</sub> Single-Atom Alloy Catalyst: a Further Step From Cellulose to Ethanol. *Green Chem.* **2018**, *20*, 2142–2150.
- (282) Fontana, F.; Chen, C. C.; Aggarwal, V. K. Palladium-Catalyzed Insertion of CO<sub>2</sub> into Vinylaziridines: New Route to 5-Vinyl-oxazolidinones. *Org. Lett.* **2011**, *13*, 3454–3457.
- (283) Nakagawa, K.; Okamura, M.; Ikenaga, N.; Suzuki, T.; Nakagawa, K.; Okamura, M.; Suzuki, T.; Kobayashi, T.; Kobayashi, T. Dehydrogenation of Ethane Over Gallium Oxide in the Presence of Carbon Dioxide. *Chem. Commun.* **1998**, 1025–1026.
- (284) Nakagawa, K.; Kajita, C.; Okumura, K.; Ikenaga, N.; Nishitani-Gamo, M.; Ando, T.; Kobayashi, T.; Suzuki, T. Role of Carbon Dioxide in the Dehydrogenation of Ethane Over Gallium-Loaded Catalysts. *J. Catal.* **2001**, *203*, 87–93.
- (285) Mansoor, E.; Head-Gordon, M.; Bell, A. T. Computational Modeling of the Nature and Role of Ga Species for Light Alkane Dehydrogenation Catalyzed by Ga/H-MFI. *ACS Catal.* **2018**, *8*, 6146–6162.
- (286) Schreiber, M. W.; Plaisance, C. P.; Baumgartl, M.; Reuter, K.; Jentys, A.; Bermejo-Deval, R.; Lercher, J. A. Lewis-Bronsted Acid Pairs in Ga/H-ZSM-5 To Catalyze Dehydrogenation of Light Alkanes. *J. Am. Chem. Soc.* **2018**, *140*, 4849–4859.
- (287) Getsioian, A.; Das, U.; Camacho-Bunquin, J.; Zhang, G. H.; Gallagher, J. R.; Hu, B.; Cheah, S.; Schaidle, J. A.; Ruddy, D. A.; Hensley, J. E.; et al. Organometallic Model Complexes Elucidate the Active Gallium Species in Alkane Dehydrogenation Catalysts Based on Ligand Effects in Ga K-edge XANES. *Catal. Sci. Technol.* **2016**, *6*, 6339–6353.
- (288) Zheng, B.; Hua, W. M.; Yue, Y. H.; Gao, Z. Dehydrogenation of Propane to Propene Over Different Polymorphs of Gallium Oxide. *J. Catal.* **2005**, *232*, 143–151.
- (289) Shao, C. T.; Lang, W. Z.; Yan, X.; Guo, Y. J. Catalytic Performance of Gallium Oxide Based-Catalysts for the Propane Dehydrogenation Reaction: Effects of Support and Loading Amount. *RSC Adv.* **2017**, *7*, 4710–4723.
- (290) Qureshi, Z. S.; Hamieh, A.; Barman, S.; Maity, N.; Samantaray, M. K.; Ould-Chikh, S.; Abou-hamad, E.; Falivene, L.; D'Elia, V.; Rothenberger, A.; et al. SOMC-Designed Silica Supported Tungsten Oxo Imidazolin-2-iminato Methyl Precatalyst for Olefin Metathesis Reactions. *Inorg. Chem.* **2017**, *56*, 861–871.
- (291) Hogerl, M. P.; Goh, L. M. S.; Abou-Hamad, E.; Barman, S.; Dachwald, O.; Pasha, F. A.; Pelletier, J.; Kohler, K.; D'Elia, V.; Cavallo, L.; Basset, J.-M. SOMC Grafting of Vanadium Oxy-triisopropoxide ( $\text{VO}(\text{O}^i\text{Pr})_3$ ) on Dehydroxylated Silica; Analysis of Surface Complexes and Thermal Restructuring Mechanism. *RSC Adv.* **2018**, *8*, 20801–20808.
- (292) Sattler, J. J. H. B.; Ruiz-Martinez, J.; Santillan-Jimenez, E.; Weckhuysen, B. M. Catalytic Dehydrogenation of Light Alkanes on Metals and Metal Oxides. *Chem. Rev.* **2014**, *114*, 10613–10653.
- (293) Sattler, J. J. H. B.; Gonzalez-Jimenez, I. D.; Luo, L.; Stears, B. A.; Malek, A.; Barton, D. G.; Kilos, B. A.; Kaminsky, M. P.; Verhoeven, T. W. G. M.; Koers, E. J.; et al. Platinum-Promoted Ga/Al<sub>2</sub>O<sub>3</sub> as Highly Active, Selective, and Stable Catalyst for the Dehydrogenation of Propane. *Angew. Chem., Int. Ed.* **2014**, *53*, 9251–9256.



- (294) Siddiqi, G.; Sun, P. P.; Galvita, V.; Bell, A. T. Catalyst Performance of Novel Pt/Mg(Ga)(Al)O Catalysts for Alkane dehydrogenation. *J. Catal.* **2010**, *274*, 200–206.
- (295) Searles, K.; Chan, K. W.; Mendes Burak, J. A.; Zemlyanov, D.; Safonova, O.; Coperet, C. Highly Productive Propane Dehydrogenation Catalyst Using Silica-Supported Ga-Pt Nanoparticles Generated from Single-Sites. *J. Am. Chem. Soc.* **2018**, *140*, 11674–11679.
- (296) Fajdala, K. L.; Tilley, T. D. Design and Synthesis of Heterogeneous Catalysts: the Thermolytic Molecular Precursor Approach. *J. Catal.* **2003**, *216*, 265–275.
- (297) Redekop, E. A.; Galvita, V. V.; Poelman, H.; Bliznuk, V.; Detavernier, C.; Marin, G. B. Delivering a Modifying Element to Metal Nanoparticles via Support: Pt-Ga Alloying During the Reduction of Pt/Mg(Al,Ga)O<sub>x</sub> Catalysts and Its Effects on Propane Dehydrogenation. *ACS Catal.* **2014**, *4*, 1812–1824.
- (298) Maity, N.; Barman, S.; Minenkov, Y.; Ould-Chikh, S.; Abou-Hamad, E.; Ma, T.; Qureshi, Z. S.; Cavallo, L.; D'Elia, V.; Gates, B. C.; et al. A Silica-Supported Monoalkylated Tungsten Dioxo Complex Catalyst for Olefin Metathesis. *ACS Catal.* **2018**, *8*, 2715–2729.
- (299) Hu, B.; Schweitzer, N. M.; Zhang, G. H.; Kraft, S. J.; Childers, D. J.; Lanci, M. P.; Miller, J. T.; Hock, A. S. Isolated Fe<sup>II</sup> on Silica As a Selective Propane Dehydrogenation Catalyst. *ACS Catal.* **2015**, *5*, 3494–3503.
- (300) Delley, M. F.; Nunez-Zarur, F.; Conley, M. P.; Comas-Vives, A.; Siddiqi, G.; Norsic, S.; Monteil, V.; Safonova, O. V.; Coperet, C. Proton Transfers are Key Elementary Steps in Ethylene Polymerization on Isolated Chromium(III) Silicates. *Proc. Natl. Acad. Sci. U. S. A.* **2014**, *111*, 11624–11629.
- (301) Fridman, V. Z.; Xing, R.; Severance, M. Investigating the CrO<sub>x</sub>/Al<sub>2</sub>O<sub>3</sub> Dehydrogenation Catalyst Model: I. Identification and Stability Evaluation of the Cr Species on the Fresh and Equilibrated Catalysts. *Appl. Catal., A* **2016**, *523*, 39–53.
- (302) Abbot, J. Role of Brønsted and Lewis Acid Sites During Cracking Reactions of Alkanes. *Appl. Catal.* **1989**, *47*, 33–44.
- (303) Hu, B.; Getsoian, A. B.; Schweitzer, N. M.; Das, U.; Kim, H.; Niklas, J.; Poluektov, O.; Curtiss, L. A.; Stair, P. C.; Miller, J. T.; Hock, A. S. Selective Propane Dehydrogenation with Single-Site Co-II on SiO<sub>2</sub> by a Non-Redox Mechanism. *J. Catal.* **2015**, *322*, 24–37.
- (304) Zhao, Z. J.; Wu, T. F.; Xiong, C. Y.; Sun, G. D.; Mu, R. T.; Zeng, L.; Gong, J. L. Hydroxyl-Mediated Non-Oxidative Propane Dehydrogenation over VO<sub>x</sub>/γ-Al<sub>2</sub>O<sub>3</sub> Catalysts with Improved Stability. *Angew. Chem., Int. Ed.* **2018**, *57*, 6791–6795.
- (305) Liu, G.; Zhao, Z. J.; Wu, T. F.; Zeng, L.; Gong, J. L. Nature of the Active Sites of VO<sub>x</sub>/Al<sub>2</sub>O<sub>3</sub> Catalysts for Propane Dehydrogenation. *ACS Catal.* **2016**, *6*, 5207–5214.
- (306) Harlin, M. E.; Niemi, V. M.; Krause, A. O. I. Alumina-Supported Vanadium Oxide in the Dehydrogenation of Butanes. *J. Catal.* **2000**, *195*, 67–78.
- (307) Takahara, I.; Saito, M.; Inaba, M.; Murata, K. Dehydrogenation of Propane Over a Silica-Supported Vanadium Oxide Catalyst. *Catal. Lett.* **2005**, *102*, 201–205.
- (308) Szeto, K. C.; Hardou, L.; Merle, N.; Basset, J. M.; Thivolle-Cazat, J.; Papaioannou, C.; Taoufik, M. Selective Conversion of Butane into Liquid Hydrocarbon Fuels on Alkane Metathesis Catalysts. *Catal. Sci. Technol.* **2012**, *2*, 1336–1339.
- (309) Olsbye, U.; Virnovskaia, A.; Prytz, O.; Tinnemans, S. J.; Weckhuysen, B. M. Mechanistic Insight in the Ethane Dehydrogenation Reaction Over Cr/Al<sub>2</sub>O<sub>3</sub> Catalysts. *Catal. Lett.* **2005**, *103*, 143–148.
- (310) Alexopoulos, K.; Reyniers, M. F.; Marin, G. B. Reaction Path Analysis of Propane Selective Oxidation Over V<sub>2</sub>O<sub>5</sub> and V<sub>2</sub>O<sub>5</sub>/TiO<sub>2</sub>. *J. Catal.* **2012**, *289*, 127–139.
- (311) Gilardoni, F.; Bell, A. T.; Chakraborty, A.; Boulet, P. Density Functional Theory Calculations of the Oxidative Dehydrogenation of Propane on the (010) Surface of V<sub>2</sub>O<sub>5</sub>. *J. Phys. Chem. B* **2000**, *104*, 12250–12255.
- (312) Rozanska, X.; Fortrie, R.; Sauer, J. Oxidative Dehydrogenation of Propane by Monomeric Vanadium Oxide Sites on Silica Support. *J. Phys. Chem. C* **2007**, *111*, 6041–6050.
- (313) Langeslay, R. R.; Kaphan, D. M.; Marshall, C. L.; Stair, P. C.; Sattelberger, A. P.; Delferro, M. Catalytic Applications of Vanadium: A Mechanistic Perspective. *Chem. Rev.* **2019**, *119*, 2128–2191.
- (314) Rossetti, I.; Mancini, G. F.; Ghigna, P.; Scavini, M.; Piumetti, M.; Bonelli, B.; Cavani, F.; Comite, A. Spectroscopic Enlightening of the Local Structure Of VO<sub>x</sub> Active Sites in Catalysts for the Odh of Propane. *J. Phys. Chem. C* **2012**, *116*, 22386–22398.
- (315) Schimmoeller, B.; Jiang, Y. J.; Pratsinis, S. E.; Baiker, A. Structure of Flame-Made Vanadia/Silica and Catalytic Behavior in the Oxidative Dehydrogenation of Propane. *J. Catal.* **2010**, *274*, 64–75.
- (316) Rozanska, X.; Fortrie, R.; Sauer, J. Size-Dependent Catalytic Activity of Supported Vanadium Oxide Species: Oxidative Dehydrogenation of Propane. *J. Am. Chem. Soc.* **2014**, *136*, 7751–7761.
- (317) Carrero, C. A.; Keturakis, C. J.; Orrego, A.; Schomacker, R.; Wachs, I. E. Anomalous Reactivity of Supported V<sub>2</sub>O<sub>5</sub> Nanoparticles for Propane Oxidative Dehydrogenation: Influence of the Vanadium Oxide Precursor. *Dalton Trans* **2013**, *42*, 12644–12653.
- (318) Grant, J. T.; Carrero, C. A.; Love, A. M.; Verel, R.; Hermans, I. Enhanced Two-Dimensional Dispersion of Group V Metal Oxides on Silica. *ACS Catal.* **2015**, *5*, 5787–5793.
- (319) Carrero, C. A.; Schloegl, R.; Wachs, I. E.; Schomaecker, R. Critical Literature Review of the Kinetics for the Oxidative Dehydrogenation of Propane over Well-Defined Supported Vanadium Oxide Catalysts. *ACS Catal.* **2014**, *4*, 3357–3380.
- (320) Cavalleri, M.; Hermann, K.; Knop-Gericke, A.; Hävecker, M.; Herbert, R.; Hess, C.; Oestereich, A.; Döbler, J.; Schlögl, R. Analysis of Silica-Supported Vanadia by X-ray Absorption Spectroscopy: Combined Theoretical and Experimental Studies. *J. Catal.* **2009**, *262*, 215–223.
- (321) Dinse, A.; Wolfram, T.; Carrero, C.; Schloegl, R.; Schomacker, R.; Dinse, K. P. Exploring the Structure of Paramagnetic Centers in SBA-15 Supported Vanadia Catalysts with Pulsed One- and Two-Dimensional Electron Paramagnetic Resonance (EPR) and Electron Nuclear Double Resonance (ENDOR). *J. Phys. Chem. C* **2013**, *117*, 16921–16932.
- (322) Xue, X. L.; Lang, W. Z.; Yan, X.; Guo, Y. J. Dispersed Vanadium in Three-Dimensional Dendritic Mesoporous Silica Nanospheres: Active and Stable Catalysts for the Oxidative Dehydrogenation of Propane in the Presence of CO<sub>2</sub>. *ACS Appl. Mater. Interfaces* **2017**, *9*, 15408–15423.
- (323) Magg, N.; Immaraporn, B.; Giorgi, J. B.; Schroeder, T.; Baumer, M.; Dobler, J.; Wu, Z. L.; Kondratenko, E.; Cherian, M.; Baerns, M.; et al. Vibrational Spectra of Alumina- and Silica-Supported Vanadia Revisited: An Experimental and Theoretical Model Catalyst Study. *J. Catal.* **2004**, *226*, 88–100.
- (324) Luo, Q. X.; Zhang, X. K.; Hou, B. L.; Chen, J. G.; Zhu, C.; Liu, Z. W.; Liu, Z. T.; Lu, J. Catalytic Function of VO<sub>x</sub>/Al<sub>2</sub>O<sub>3</sub> for Oxidative Dehydrogenation of Propane: Support Microstructure-Dependent Mass Transfer and Diffusion. *Catal. Sci. Technol.* **2018**, *8*, 4864–4876.
- (325) Xiong, H. F.; Lin, S.; Goetze, J.; Pletcher, P.; Guo, H.; Kovarik, L.; Artyushkova, K.; Weckhuysen, B. M.; Datye, A. K. Thermally Stable and Regenerable Platinum-Tin Clusters for Propane Dehydrogenation Prepared by Atom Trapping on Ceria. *Angew. Chem., Int. Ed.* **2017**, *56*, 8986–8991.
- (326) Jones, J.; Xiong, H. F.; DeLaRiva, A. T.; Peterson, E. J.; Pham, H.; Challa, S. R.; Qi, G. S.; Oh, S.; Wiebenga, M. H.; Pereira Hernandez, X. I.; Wang, Y.; Datye, A. K. Thermally Stable Single-Atom Platinum-on-Ceria Catalysts via Atom Trapping. *Science* **2016**, *353*, 150–154.
- (327) Cortright, R. D.; Hill, J. M.; Dumesic, J. A. Selective Dehydrogenation of Isobutane Over Supported Pt/Sn Catalysts. *Catal. Today* **2000**, *55*, 213–223.
- (328) Zhu, H. B.; Anjum, D. H.; Wang, Q. X.; Abou-Hamad, E.; Emsley, L.; Dong, H. L.; Laveille, P.; Li, L. D.; Samal, A. K.; Basset, J. M. Sn Surface-Enriched Pt-Sn Bimetallic Nanoparticles as a Selective and Stable Catalyst for Propane Dehydrogenation. *J. Catal.* **2014**, *320*, 52–62.



- (329) Sun, G. D.; Zhao, Z. J.; Mu, R. T.; Zha, S. J.; Li, L. L.; Chen, S.; Zang, K. T.; Luo, J.; Li, Z. L.; Purdy, S. C.; Kropf, A. J.; Miller, J. T.; Zeng, L.; Gong, J. Breaking the Scaling Relationship via Thermally Stable Pt/Cu Single Atom Alloys for Catalytic Dehydrogenation. *Nat. Commun.* **2018**, *9*, 4454.
- (330) Pelzer, K.; Candy, J. P.; Godard, G.; Basset, J. M. Surface Organometallic Chemistry on Metal: Synthesis, Characterization and Application in Catalysis. In *Nanoparticles and Catalysis*; Astruc, D., Ed.; Wiley-VCH Verlag GmbH & Co. KGaA: Weinheim, 2008; Chapter 18, pp 553–620.
- (331) Humblot, F.; Candy, J. P.; Le Peltier, F.; Didillon, B.; Basset, J. M. Surface Organometallic Chemistry on Metals: Selective Dehydrogenation of Isobutane into Isobutene on Bimetallic Catalysts Prepared by Reaction of Tetra n-Butyltin on Silica-Supported Platinum Catalyst. *J. Catal.* **1998**, *179*, 459–468.
- (332) Humblot, F.; Lepeltier, F.; Candy, J. P.; Corker, J.; Clause, O.; Bayard, F.; Basset, J. M. Surface Organometallic Chemistry on Metals: Formation of a Stable  $\text{Sn}(\text{n-C}_4\text{H}_9)$  Fragment as a Precursor of Surface Alloy Obtained by Stepwise Hydrogenolysis of  $\text{Sn}(\text{n-C}_4\text{H}_9)_4$  on a Platinum Particle Supported on Silica. *J. Am. Chem. Soc.* **1998**, *120*, 137–146.
- (333) Leconte, M.; Theolier, A.; Rojas, D.; Basset, J. M. Stoichiometric and Catalytic Homologation of Olefins on the Fischer–Tropsch Catalysts Fe/SiO<sub>2</sub>, Ru/SiO<sub>2</sub>, Os/SiO<sub>2</sub>, and Rh/SiO<sub>2</sub>: Mechanistic Implication in the Mode of C–C Bond Formation. *J. Am. Chem. Soc.* **1984**, *106*, 1141–1142.
- (334) Leconte, M.; Theolier, A.; Basset, J. M. Catalytic Homologation of Olefins to Higher and Lower Olefins - a Metathesis Related Reaction. *J. Mol. Catal.* **1985**, *28*, 217–231.
- (335) Xu, Y. D.; Bao, X. H.; Lin, L. W. Direct Conversion of Methane Under Non-Oxidative Conditions. *J. Catal.* **2003**, *216*, 386–395.
- (336) Schulz, H. Short History and Present Trends of Fischer–Tropsch Synthesis. *Appl. Catal., A* **1999**, *186*, 3–12.
- (337) Dry, M. E. The Fischer–Tropsch Process: 1950–2000. *Catal. Today* **2002**, *71*, 227–241.
- (338) Farrell, B. L.; Igenegbai, V. O.; Linic, S. A Viewpoint on Direct Methane Conversion to Ethane and Ethylene Using Oxidative Coupling on Solid Catalysts. *ACS Catal.* **2016**, *6*, 4340–4346.
- (339) Lunsford, J. H. The Catalytic Oxidative Coupling of Methane. *Angew. Chem., Int. Ed. Engl.* **1995**, *34*, 970–980.
- (340) Kondratenko, E. V.; Peppel, T.; Seeburg, D.; Kondratenko, V. A.; Kalevaru, N.; Martin, A.; Wohlrab, S. Methane Conversion into Different Hydrocarbons or Oxygenates: Current Status and Future Perspectives in Catalyst Development and Reactor Operation. *Catal. Sci. Technol.* **2017**, *7*, 366–381.
- (341) Amin, N. A. S.; Peng, S. E. A Thermodynamic Equilibrium Analysis on Oxidation of Methane to Higher Hydrocarbons. *Z. Phys. Chem.* **2009**, *17*, 363–370.
- (342) Labinger, J. A. Oxidative Coupling of Methane: An Inherent Limit to Selectivity? *Catal. Lett.* **1988**, *1*, 371–375.
- (343) Sun, K. D.; Ginosar, D. M.; He, T.; Zhang, Y. L.; Fan, M. H.; Chen, R. P. Progress in Nonoxidative Dehydroaromatization of Methane in the Last 6 Years. *Ind. Eng. Chem. Res.* **2018**, *57*, 1768–1789.
- (344) Soulivong, D.; Norsic, S.; Taoufik, M.; Coperet, C.; Thivolle-Cazat, J.; Chakka, S.; Basset, J. M. Non-Oxidative Coupling Reaction of Methane to Ethane and Hydrogen Catalyzed by the Silica-Supported Tantalum Hydride:  $(\equiv\text{SiO})_2\text{Ta-H}$ . *J. Am. Chem. Soc.* **2008**, *130*, 5044–5045.
- (345) Szeto, K. C.; Norsic, S.; Hardou, L.; Le Roux, E.; Chakka, S.; Thivolle-Cazat, J.; Baudouin, A.; Papaioannou, C.; Basset, J. M.; Taoufik, M. Non-Oxidative Coupling of Methane Catalysed by Supported Tungsten Hydride onto Alumina and Silica-Alumina in Classical and H<sub>2</sub> Permeable Membrane Fixed-Bed Reactors. *Chem. Commun.* **2010**, *46*, 3985–3987.
- (346) Reddy Enakonda, L.; Zhou, L.; Saih, Y.; Ould-Chikh, S.; Lopatin, S.; Gary, D.; Del-Gallo, P.; Basset, J. M. Methane-Induced Activation Mechanism of Fused Ferric Oxide-Alumina Catalysts During Methane Decomposition. *ChemSusChem* **2016**, *9*, 1911–1915.
- (347) Horn, R.; Schlogl, R. Methane Activation by Heterogeneous Catalysis. *Catal. Lett.* **2015**, *145*, 23–39.
- (348) Schwach, P.; Pan, X. L.; Bao, X. H. Direct Conversion of Methane to Value-Added Chemicals over Heterogeneous Catalysts: Challenges and Prospects. *Chem. Rev.* **2017**, *117*, 8497–8520.
- (349) Hutchings, G. J.; Scurrell, M. S.; Woodhouse, J. R. Oxidative Coupling of Methane Using Oxide Catalysts. *Chem. Soc. Rev.* **1989**, *18*, 251–283.
- (350) Guo, X. G.; Fang, G. Z.; Li, G.; Ma, H.; Fan, H. J.; Yu, L.; Ma, C.; Wu, X.; Deng, D. H.; Wei, M. M.; et al. Direct, Nonoxidative Conversion of Methane to Ethylene, Aromatics, and Hydrogen. *Science* **2014**, *344*, 616–619.
- (351) Tang, P.; Zhu, Q. J.; Wu, Z. X.; Ma, D. Methane Activation: The Past and Future. *Energy Environ. Sci.* **2014**, *7*, 2580–2591.
- (352) Liu, Y.; Li, D. F.; Wang, T. Y.; Liu, Y.; Xu, T.; Zhang, Y. Efficient Conversion of Methane to Aromatics by Coupling Methylation Reaction. *ACS Catal.* **2016**, *6*, 5366–5370.
- (353) Parkinson, G. S. Unravelling Single Atom Catalysis: The Surface Science Approach. *Chin. J. Catal.* **2017**, *38*, 1454–1459.
- (354) Watson, P. L. Methane Exchange-Reactions of Lanthanide and Early-Transition-Metal Methyl Complexes. *J. Am. Chem. Soc.* **1983**, *105*, 6491–6493.
- (355) Quignard, F.; Lecuyer, C.; Choplin, A.; Olivier, D.; Basset, J. M. Surface Organometallic Chemistry of Zirconium - Application to the Stoichiometric Activation of the C–H Bonds of Alkanes and to the Low-Temperature Catalytic Hydrogenolysis of Alkanes. *J. Mol. Catal.* **1992**, *74*, 353–363.
- (356) Thieuleux, C.; Coperet, C.; Dufaud, V.; Marangelli, C.; Kuntz, E.; Basset, J. M. Heterogeneous Well-Defined Catalysts for Metathesis of Inert and not so Inert Bonds. *J. Mol. Catal. A: Chem.* **2004**, *213*, 47–57.
- (357) Thieuleux, C.; Quadrelli, E. A.; Basset, J. M.; Dobler, J.; Sauer, J. Methane Activation by Silica-Supported Zr(IV) Hydrides: the Dihydride  $[(\equiv\text{SiO})_2\text{ZrH}_2]$  is Much Faster than the Monohydride  $[(\equiv\text{SiO})_3\text{ZrH}]$ . *Chem. Commun.* **2004**, 1729–1731.
- (358) Vidal, V.; Theolier, A.; Thivolle-Cazat, J.; Basset, J. M.; Corker, J. Synthesis, Characterization, and Reactivity, in the C–H Bond Activation of Cycloalkanes, of a Silica-Supported Tantalum(III) Monohydride Complex:  $(\equiv\text{SiO})_2\text{Ta}^{\text{III}}\text{-H}$ . *J. Am. Chem. Soc.* **1996**, *118*, 4595–4602.
- (359) Chabanas, M.; Vidal, V.; Coperet, C.; Thivolle-Cazat, J.; Basset, J. M. Low-Temperature Hydrogenolysis of Alkanes Catalyzed by a Silica-Supported Tantalum Hydride Complex, and Evidence for a Mechanistic Switch from Group IV to Group V Metal Surface Hydride Complexes. *Angew. Chem., Int. Ed.* **2000**, *39*, 1962–1965.
- (360) Basset, J. M.; Chakka, S.; Taoufik, M.; Thivolle-Cazat, J. Process for Converting Ethane into Liquid Alkane Mixtures. PCT Patent WO2008152371A1, December 18, 2008.
- (361) Patil, U.; Saih, Y.; Abou-Hamad, E.; Hamieh, A.; Pelletier, J. D. A.; Basset, J. M. Low Temperature Activation of Methane over a Zinc-Exchanged Heteropolyacid as an Entry to its Selective Oxidation to Methanol and Acetic Acid. *Chem. Commun.* **2014**, *50*, 12348–12351.
- (362) Periana, R. A.; Mironov, O.; Taube, D.; Bhalla, G.; Jones, C. J. Catalytic, Oxidative Condensation of CH<sub>4</sub> to CH<sub>3</sub>COOH in one step via CH Activation. *Science* **2003**, *301*, 814–818.
- (363) Periana, R. A.; Taube, D. J.; Evitt, E. R.; Löffler, D. G.; Wentreck, P. R.; Voss, G.; Masuda, T. A Mercury-Catalyzed, High-Yield System for the Oxidation of Methane to Methanol. *Science* **1993**, *259*, 340–343.
- (364) Sun, M.; Abou-Hamad, E.; Rossini, A. J.; Zhang, J. Z.; Lesage, A.; Zhu, H. B.; Pelletier, J.; Emsley, L.; Caps, V.; Basset, J. M. Methane Reacts with Heteropolyacids Chemisorbed on Silica to Produce Acetic Acid under Soft Conditions. *J. Am. Chem. Soc.* **2013**, *135*, 804–810.

- (365) Kobayashi, K.; Kondo, Y. Transition-Metal-Free Carboxylation of Organozinc Reagents Using CO<sub>2</sub> in DMF Solvent. *Org. Lett.* **2009**, *11*, 2035–2037.
- (366) Metzger, A.; Bernhardt, S.; Manolikakes, G.; Knochel, P. MgCl<sub>2</sub>-Accelerated Addition of Functionalized Organozinc Reagents to Aldehydes, Ketones, and Carbon Dioxide. *Angew. Chem., Int. Ed.* **2010**, *49*, 4665–4668.
- (367) Hunger, M. Brønsted Acid Sites in Zeolites Characterized by Multinuclear Solid-State NMR Spectroscopy. *Catal. Rev.: Sci. Eng.* **1997**, *39*, 345–393.
- (368) Shi, D. X.; Feng, Y. Q.; Zhong, S. H. Photocatalytic Conversion of CH<sub>4</sub> and CO<sub>2</sub> to Oxygenated Compounds over Cu/CdS-TiO<sub>2</sub>/SiO<sub>2</sub> Catalyst. *Catal. Today* **2004**, *98*, 505–509.
- (369) Wu, J. F.; Yu, S. M.; Wang, W. D.; Fan, Y. X.; Bai, S.; Zhang, C. W.; Gao, Q.; Huang, J.; Wang, W. Mechanistic Insight into the Formation of Acetic Acid from the Direct Conversion of Methane and Carbon Dioxide on Zinc-Modified H-ZSM-5 Zeolite. *J. Am. Chem. Soc.* **2013**, *135*, 13567–13573.
- (370) Kazansky, V. B.; Serykh, A. I.; Pidko, E. A. DRIFT Study of Molecular and Dissociative Adsorption of Light Paraffins by HZSM-5 Zeolite Modified With Zinc Ions: Methane Adsorption. *J. Catal.* **2004**, *225*, 369–373.
- (371) Kolyagin, Y. G.; Ivanova, I. I.; Ordonsky, V. V.; Gedeon, A.; Pirogov, Y. A. Methane Activation over Zn-Modified MFI Zeolite: NMR Evidence for Zn-Methyl Surface Species Formation. *J. Phys. Chem. C* **2008**, *112*, 20065–20069.
- (372) Kolyagin, Y. G.; Ivanova, I. I.; Pirogov, Y. A. <sup>1</sup>H and <sup>13</sup>C MAS NMR Studies of Light Alkanes Activation Over MFI Zeolite Modified by Zn Vapour. *Solid State Nucl. Magn. Reson.* **2009**, *35*, 104–112.
- (373) Luzgin, M. V.; Rogov, V. A.; Arzumanov, S. S.; Toktarev, A. V.; Stepanov, A. G.; Parmon, V. N. Understanding Methane Aromatization on a Zn-Modified High-Silica Zeolite. *Angew. Chem., Int. Ed.* **2008**, *47*, 4559–4562.
- (374) Luzgin, M. V.; Rogov, V. A.; Arzumanov, S. S.; Toktarev, A. V.; Stepanov, A. G.; Parmon, V. N. Methane Aromatization on Zn-Modified Zeolite in the Presence of a Co-Reactant Higher Alkane: How Does it Occur? *Catal. Today* **2009**, *144*, 265–272.
- (375) Wu, J. F.; Wang, W. D.; Xu, J.; Deng, F.; Wang, W. Reactivity of C-1 Surface Species Formed in Methane Activation on Zn-Modified H-ZSM-5 Zeolite. *Chem. - Eur. J.* **2010**, *16*, 14016–14025.
- (376) Wang, X. M.; Qi, G. D.; Xu, J.; Li, B. J.; Wang, C.; Deng, F. NMR-Spectroscopic Evidence of Intermediate-Dependent Pathways for Acetic Acid Formation from Methane and Carbon Monoxide over a ZnZSM-5 Zeolite Catalyst. *Angew. Chem., Int. Ed.* **2012**, *51*, 3850–3853.
- (377) Xu, J.; Zheng, A. M.; Wang, X. M.; Qi, G. D.; Su, J. H.; Du, J. F.; Gan, Z. H.; Wu, J. F.; Wang, W.; Deng, F. Room Temperature Activation of Methane over Zn Modified H-ZSM-5 Zeolites: Insight from Solid-State NMR and Theoretical Calculations. *Chem. Sci.* **2012**, *3*, 2932–2940.
- (378) Li, L.; Li, G. D.; Yan, C.; Mu, X. Y.; Pan, X. L.; Zou, X. X.; Wang, K. X.; Chen, J. S. Efficient Sunlight-Driven Dehydrogenative Coupling of Methane to Ethane over a Zn+-Modified Zeolite. *Angew. Chem., Int. Ed.* **2011**, *50*, 8299–8303.
- (379) Olivos-Suarez, A. I.; Szecsenyi, A.; Hensen, E. J. M.; Ruiz-Martinez, J.; Pidko, E. A.; Gascon, J. Strategies for the Direct Catalytic Valorization of Methane Using Heterogeneous Catalysis: Challenges and Opportunities. *ACS Catal.* **2016**, *6*, 2965–2981.
- (380) Chin, Y. H.; Buda, C.; Neurock, M.; Iglesia, E. Reactivity of Chemisorbed Oxygen Atoms and Their Catalytic Consequences during CH<sub>4</sub>-O<sub>2</sub> Catalysis on Supported Pt Clusters. *J. Am. Chem. Soc.* **2011**, *133*, 15958–15978.
- (381) Vajda, S.; Pellin, M. J.; Greeley, J. P.; Marshall, C. L.; Curtiss, L. A.; Ballentine, G. A.; Elam, J. W.; Catillon-Mucherie, S.; Redfern, P. C.; Mehmood, F.; et al. Subnanometre Platinum Clusters as Highly Active and Selective Catalysts for the Oxidative Dehydrogenation of Propane. *Nat. Mater.* **2009**, *8*, 213–216.
- (382) Harding, D. J.; Kerpel, C.; Meijer, G.; Fielicke, A. Activated Methane on Small Cationic Platinum Clusters. *Angew. Chem., Int. Ed.* **2012**, *51*, 817–819.
- (383) Yoshinobu, J.; Ogasawara, H.; Kawai, M. Symmetry Controlled Surface Photochemistry of Methane on Pt(111). *Phys. Rev. Lett.* **1995**, *75*, 2176–2179.
- (384) Kim, J.; Kim, W.; Seo, Y.; Kim, J. C.; Ryoo, R. n-Heptane Hydroisomerization over Pt/MFI Zeolite Nanosheets: Effects of Zeolite Crystal Thickness and Platinum Location. *J. Catal.* **2013**, *301*, 187–197.
- (385) Zecevic, J.; van der Eerden, A. M. J.; Friedrich, H.; de Jongh, P. E.; de Jong, K. P. Heterogeneities of the Nanostructure of Platinum/Zeolite Y Catalysts Revealed by Electron Tomography. *ACS Nano* **2013**, *7*, 3698–3705.
- (386) Golinsky, D. V.; Ostanina, N. V.; Ovcharenko, A. I.; Pashkov, V. V.; Udras, I. E.; Belyi, A. S. Adsorption of Methane on the Pt/Al<sub>2</sub>O<sub>3</sub> Catalyst. Studying of Reactionary Activity of the Adsorbed Methane Forms in Reaction of Joint Transformation with N-pentane. *Procedia Eng.* **2015**, *113*, 13–18.
- (387) Fung, V.; Tao, F.; Jiang, D. E. Low-Temperature Activation of Methane on Doped Single Atoms: Descriptor and Prediction. *Phys. Chem. Chem. Phys.* **2018**, *20*, 22909–22914.
- (388) Xie, P. F.; Pu, T. C.; Nie, A. M.; Hwang, S.; Purdy, S. C.; Yu, W. J.; Su, D.; Miller, J. T.; Wang, C. Nanoceria-Supported Single-Atom Platinum Catalysts for Direct Methane Conversion. *ACS Catal.* **2018**, *8*, 4044–4048.
- (389) Marcinkowski, M. D.; Darby, M. T.; Liu, J. L.; Wimple, J. M.; Lucci, F. R.; Lee, S.; Michaelides, A.; Flytzani-Stephanopoulos, M.; Stamatakis, M.; Sykes, E. C. H. Pt/Cu Single-Atom Alloys as Coke-Resistant Catalysts for Efficient C-H Activation. *Nat. Chem.* **2018**, *10*, 325–332.
- (390) Huang, W. X.; Zhang, S. R.; Tang, Y.; Li, Y. T.; Nguyen, L.; Li, Y. Y.; Shan, J. J.; Xiao, D. Q.; Gagne, R.; Frenkel, A. I.; et al. Low-Temperature Transformation of Methane to Methanol on Pd<sub>4</sub>O<sub>4</sub> Single Sites Anchored on the Internal Surface of Microporous Silicate. *Angew. Chem., Int. Ed.* **2016**, *55*, 13441–13445.
- (391) Kwon, Y.; Kim, T. Y.; Kwon, G.; Yi, J.; Lee, H. Selective Activation of Methane on Single-Atom Catalyst of Rhodium Dispersed on Zirconia for Direct Conversion. *J. Am. Chem. Soc.* **2017**, *139*, 17694–17699.
- (392) Tang, Y.; Li, Y. T.; Fung, V.; Jiang, D. E.; Huang, W. X.; Zhang, S. R.; Iwasawa, Y.; Sakata, T.; Nguyen, L.; Zhang, X. Y.; Frenkel, A. I.; Tao, F. Single Rhodium Atoms Anchored in Micropores for Efficient Transformation of Methane Under Mild Conditions. *Nat. Commun.* **2018**, *9*, 1231.
- (393) Shan, J. J.; Li, M. W.; Allard, L. F.; Lee, S. S.; Flytzani-Stephanopoulos, M. Mild Oxidation of Methane to Methanol or Acetic acid on Supported Isolated Rhodium Catalysts. *Nature* **2017**, *551*, 605–608.
- (394) Trens, P.; Durand, R.; Coq, B.; Coutanceau, C.; Rousseau, S.; Lamy, C. Poisoning of Pt/C Catalysts by CO and Its Consequences over the Kinetics of Hydrogen Chemisorption. *Appl. Catal., B* **2009**, *92*, 280–284.
- (395) Nasri, N. S.; Jones, J. M.; Dupont, V. A.; Williams, A. A Comparative Study of Sulfur Poisoning and Regeneration of Precious-Metal Catalysts. *Energy Fuels* **1998**, *12*, 1130–1134.
- (396) Chung, D. Y.; Kim, H. I.; Chung, Y. H.; Lee, M. J.; Yoo, S. J.; Bokare, A. D.; Choi, W.; Sung, Y. E. Inhibition of CO Poisoning on Pt Catalyst Coupled with the Reduction of Toxic Hexavalent Chromium in a Dual-Functional Fuel Cell. *Sci. Rep.* **2015**, *4*, 7450.
- (397) Sahoo, S.; Suib, S. L.; Alpay, S. P. Graphene Supported Single Atom Transition Metal Catalysts for Methane Activation. *ChemCatChem* **2018**, *10*, 3229–3235.
- (398) Pappas, D. K.; Borfecchia, E.; Dyballa, M.; Pankin, I. A.; Lomachenko, K. A.; Martini, A.; Signorile, M.; Teketel, S.; Arstad, B.; Berlier, G.; et al. Methane to Methanol: Structure Activity Relationships for Cu-CHA. *J. Am. Chem. Soc.* **2017**, *139*, 14961–14975.



- (399) Osadchii, D. Y.; Olivos-Suarez, A. I.; Szecsenyi, A.; Li, G. N.; Nasalevich, M. A.; Dugulan, J. A.; Crespo, P. S.; Hensen, E. J. M.; Veber, S. L.; Fedin, M. V.; et al. Isolated Fe Sites in Metal Organic Frameworks Catalyze the Direct Conversion of Methane to Methanol. *ACS Catal.* **2018**, *8*, 5542–5548.
- (400) Zhang, X. Y.; Sun, Z. C.; Wang, B.; Tang, Y.; Nguyen, L.; Li, Y. T.; Tao, F. F. C-C Coupling on Single-Atom-Based Heterogeneous Catalyst. *J. Am. Chem. Soc.* **2018**, *140*, 954–962.
- (401) Cui, X. J.; Li, H. B.; Wang, Y.; Hu, Y. L.; Hua, L.; Li, H. Y.; Han, X. W.; Liu, Q. F.; Yang, F.; He, L. M.; Chen, X. Q.; et al. Room-Temperature Methane Conversion by Graphene-Confined Single Iron Atoms. *Chem.* **2018**, *4*, 1902–1910.
- (402) Yuan, J. Y.; Zhang, W. H.; Li, X. X.; Yang, J. L. A High Performance Catalyst for Methane Conversion to Methanol: Graphene Supported Single Atom Co. *Chem. Commun.* **2018**, *54*, 2284–2287.
- (403) Lustemberg, P. G.; Palomino, R. M.; Gutierrez, R. A.; Grinter, D. C.; Vorokhta, M.; Liu, Z. Y.; Ramirez, P. J.; Matolin, V.; Ganduglia-Pirovano, M. V.; Senanayake, S. D.; et al. Direct Conversion of Methane to Methanol on Ni-Ceria Surfaces: Metal-Support Interactions and Water-Enabled Catalytic Conversion by Site Blocking. *J. Am. Chem. Soc.* **2018**, *140*, 7681–7687.
- (404) Sahoo, S.; Reber, A. C.; Khanna, S. N. Effect of Location and Filling of d-States on Methane Activation in Single Site Fe-based Catalysts. *Chem. Phys. Lett.* **2016**, *660*, 48–54.
- (405) Latimer, A. A.; Kakekhani, A.; Kulkarni, A. R.; Norskov, J. K. Direct Methane to Methanol: The Selectivity-Conversion Limit and Design Strategies. *ACS Catal.* **2018**, *8*, 6894–6907.
- (406) Spivey, J. J.; Hutchings, G. Catalytic Aromatization of Methane. *Chem. Soc. Rev.* **2014**, *43*, 792–803.
- (407) Sakbodin, M.; Wu, Y. Q.; Oh, S. C.; Wachsmann, E. D.; Liu, D. X. Hydrogen-Permeable Tubular Membrane Reactor: Promoting Conversion and Product Selectivity for Non-Oxidative Activation of Methane over an Fe@SiO<sub>2</sub> Catalyst. *Angew. Chem., Int. Ed.* **2016**, *55*, 16149–16152.
- (408) Weckhuysen, B. M.; Wang, D. J.; Rosynek, M. P.; Lunsford, J. H. Conversion of Methane to Benzene over Transition Metal Ion ZSM-5 Zeolites - I. Catalytic Characterization. *J. Catal.* **1998**, *175*, 338–346.
- (409) Weckhuysen, B. M.; Wang, D. J.; Rosynek, M. P.; Lunsford, J. H. Catalytic Conversion of Methane into Aromatic Hydrocarbons over Iron Oxide Loaded ZSM-5 Zeolites. *Angew. Chem., Int. Ed. Engl.* **1997**, *36*, 2374–2376.
- (410) Tan, P. L. Active Phase, Catalytic Activity, and Induction Period of Fe/Zeolite Material in Nonoxidative Aromatization of Methane. *J. Catal.* **2016**, *338*, 21–29.
- (411) Lai, Y.; Vesper, G. The Nature of the Selective Species in Fe-HZSM-5 for Non-Oxidative Methane Dehydroaromatization. *Catal. Sci. Technol.* **2016**, *6*, 5440–5452.
- (412) Achatz, U.; Berg, C.; Joos, S.; Fox, B. S.; Beyer, M. K.; Niedner-Schatteburg, G.; Bondybey, V. E. Methane Activation by Platinum Cluster Ions in the Gas Phase: Effects of Cluster Charge on the Pt<sub>4</sub> Tetramer. *Chem. Phys. Lett.* **2000**, *320*, 53–58.
- (413) Psogogiannakis, G.; St-Amant, A.; Ternan, M. Methane Oxidation Mechanism on Pt(111): A Cluster Model DFT study. *J. Phys. Chem. B* **2006**, *110*, 24593–24605.
- (414) Xiao, L.; Wang, L. C. Methane Activation on Pt and Pt<sub>4</sub>: A Density Functional Theory Study. *J. Phys. Chem. B* **2007**, *111*, 1657–1663.
- (415) Chen, W.; Wang, H.; Mao, L. Q.; Chen, X. P.; Shangguan, W. F. Influence of Loading Pt, RhO<sub>2</sub> Co-Catalysts on Photocatalytic Overall Water Splitting over H<sub>1.9</sub>K<sub>0.3</sub>La<sub>0.5</sub>Bi<sub>0.1</sub>Ta<sub>2</sub>O<sub>7</sub>. *Catal. Commun.* **2014**, *57*, 115–118.
- (416) Kibis, L. S.; Stadnichenko, A. I.; Koscheev, S. V.; Zaikovskii, V. I.; Boronin, A. I. XPS Study of Nanostructured Rhodium Oxide Film Comprising Rh<sup>4+</sup> Species. *J. Phys. Chem. C* **2016**, *120*, 19142–19150.
- (417) WengSieh, Z.; Gronsky, R.; Bell, A. T. Microstructural Evolution of  $\gamma$ -Alumina-Supported Rh upon Aging in Air. *J. Catal.* **1997**, *170*, 62–74.
- (418) Vasquez-Céspedes, S.; Wang, X. M.; Glorius, F. Plausible Rh(V) Intermediates in Catalytic C-H Activation Reactions. *ACS Catal.* **2018**, *8*, 242–257.
- (419) Altinay, G.; Kocak, A.; Silva Daluz, J.; Metz, R. B. Electronic and Vibrational Spectroscopy of Intermediates in Methane-to-Methanol Conversion by CoO<sup>+</sup>. *J. Chem. Phys.* **2011**, *135*, 084311.
- (420) Yoshizawa, K.; Shiota, Y.; Yamabe, T. Methane-Methanol Conversion by MnO<sup>+</sup>, FeO<sup>+</sup>, and CoO<sup>+</sup>: A Theoretical Study of Catalytic Selectivity. *J. Am. Chem. Soc.* **1998**, *120*, 564–572.
- (421) Chen, Y. M.; Clemmer, D. E.; Armentrout, P. B. Conversion of CH<sub>4</sub> to CH<sub>3</sub>OH - Reactions of Co<sup>+</sup> with CH<sub>4</sub> and D<sub>2</sub>, Co<sup>+</sup> with CH<sub>3</sub>OD and D<sub>2</sub>O, and Co<sup>+</sup>(CH<sub>3</sub>OD) with Xe. *J. Am. Chem. Soc.* **1994**, *116*, 7815–7826.
- (422) Woertink, J. S.; Smeets, P. J.; Groothaert, M. H.; Vance, M. A.; Sels, B. F.; Schoonheydt, R. A.; Solomon, E. I. A [Cu<sub>2</sub>O]<sup>(2+)</sup> Core in Cu-ZSM-5, the Active site in the Oxidation of Methane to Methanol. *Proc. Natl. Acad. Sci. U. S. A.* **2009**, *106*, 18908–18913.
- (423) Sushkevich, V. L.; Palagin, D.; Ranocchiar, M.; van Bokhoven, J. A. Selective Anaerobic Oxidation of Methane Enables Direct Synthesis of Methanol. *Science* **2017**, *356*, 523–527.
- (424) Grundner, S.; Markovits, M. A. C.; Li, G.; Tromp, M.; Pidko, E. A.; Hensen, E. J. M.; Jentys, A.; Sanchez-Sanchez, M.; Lercher, J. A. Single-Site Trinuclear Copper Oxygen Clusters in Mordenite for Selective Conversion of Methane to Methanol. *Nat. Commun.* **2015**, *6*, 7546.
- (425) Agarwal, N.; Freakley, S. J.; McVicker, R. U.; Althahban, S. M.; Dimitratos, N.; He, Q.; Morgan, D. J.; Jenkins, R. L.; Willock, D. J.; Taylor, S. H.; et al. Aqueous Au-Pd Colloids Catalyze Selective CH<sub>4</sub> Oxidation to CH<sub>3</sub>OH with O<sub>2</sub> Under Mild Conditions. *Science* **2017**, *358*, 223–226.
- (426) Fella, M. F.; Onal, I. Direct Methane Oxidation to Methanol by N<sub>2</sub>O on Fe- and Co-ZSM-5 Clusters with and without Water: A Density Functional Theory Study. *J. Phys. Chem. C* **2010**, *114*, 3042–3051.
- (427) Yoshizawa, K.; Shiota, Y.; Yumura, T.; Yamabe, T. Direct Methane-Methanol and Benzene-Phenol Conversions on Fe-ZSM-5 Zeolite: Theoretical Predictions on the Reaction Pathways and Energetics. *J. Phys. Chem. B* **2000**, *104*, 734–740.
- (428) Impeng, S.; Khongpracha, P.; Warakulwit, C.; Jansang, B.; Sirirajarensre, J.; Ehara, M.; Limtrakul, J. Direct Oxidation of Methane to Methanol on Fe-O Modified Graphene. *RSC Adv.* **2014**, *4*, 12572–12578.
- (429) Impeng, S.; Khongpracha, P.; Sirirajarensre, J.; Jansang, B.; Ehara, M.; Limtrakul, J. Methane Activation on Fe- and FeO-Embedded Graphene and Boron Nitride Sheet: Role of Atomic Defects in Catalytic Activities. *RSC Adv.* **2015**, *5*, 97918–97927.
- (430) Kalamaras, C.; Palomas, D.; Bos, R.; Horton, A.; Crimmin, M.; Hellgardt, K. Selective Oxidation of Methane to Methanol Over Cu- and Fe-Exchanged Zeolites: The Effect of Si/Al Molar Ratio. *Catal. Lett.* **2016**, *146*, 483–492.
- (431) Hammond, C.; Forde, M. M.; Ab Rahim, M. H.; Thetford, A.; He, Q.; Jenkins, R. L.; Dimitratos, N.; Lopez-Sanchez, J. A.; Dummer, N. F.; Murphy, D. M.; et al. Direct Catalytic Conversion of Methane to Methanol in an Aqueous Medium by using Copper-Promoted Fe-ZSM-5. *Angew. Chem., Int. Ed.* **2012**, *51*, 5129–5133.
- (432) Tinberg, C. E.; Lippard, S. J. Dioxygen Activation in Soluble Methane Monooxygenase. *Acc. Chem. Res.* **2011**, *44*, 280–288.
- (433) Groothaert, M. H.; Smeets, P. J.; Sels, B. F.; Jacobs, P. A.; Schoonheydt, R. A. Selective Oxidation of Methane by the bis( $\mu$ -oxo)dicopper Core Stabilized on ZSM-5 and Mordenite Zeolites. *J. Am. Chem. Soc.* **2005**, *127*, 1394–1395.
- (434) Alayon, E. M. C.; Nachtegaal, M.; Kleymentov, E.; van Bokhoven, J. A. Determination of the Electronic and Geometric Structure of Cu Sites During Methane Conversion over Cu-MOR with X-ray Absorption Spectroscopy. *Microporous Mesoporous Mater.* **2013**, *166*, 131–136.
- (435) Beznis, N. V.; Weckhuysen, B. M.; Bitter, J. H. Cu-ZSM-5 Zeolites for the Formation of Methanol from Methane and Oxygen:



Probing the Active Sites and Spectator Species. *Catal. Lett.* **2010**, *138*, 14–22.

(436) Wulfers, M. J.; Teketel, S.; Ipek, B.; Lobo, R. F. Conversion of Methane to Methanol on Copper-Containing Small-Pore Zeolites and Zeotypes. *Chem. Commun.* **2015**, *51*, 4447–4450.

(437) Tomkins, P.; Ranocchiari, M.; van Bokhoven, J. A. Direct Conversion of Methane to Methanol under Mild Conditions over Cu-Zeolites and beyond. *Acc. Chem. Res.* **2017**, *50*, 418–425.

(438) Shan, J. J.; Huang, W. X.; Nguyen, L.; Yu, Y.; Zhang, S. R.; Li, Y. Y.; Frenkel, A. I.; Tao, F. Conversion of Methane to Methanol with a Bent Mono( $\mu$ -oxo)dinickel Anchored on the Internal Surfaces of Micropores. *Langmuir* **2014**, *30*, 8558–8569.

(439) Krisnandi, Y. K.; Putra, B. A. P.; Bahtiar, M.; Zahara; Abdullah, I.; Howe, R. F. Partial Oxidation of Methane to Methanol over Heterogeneous Catalyst Co/ZSM-5. *Procedia Chem.* **2015**, *14*, 508–515.

(440) Ingold, C. K.; Piggott, H. A. The Mobility of Symmetrical Triad Systems. Part I. The Conditions Relating to Systems Terminated by Phenyl Groups. *J. Chem. Soc., Trans.* **1922**, *121*, 2381–2389.

(441) Merle, N.; Le Quemener, F.; Bouhoute, Y.; Szeto, K. C.; De Mallmann, A.; Barman, S.; Samantaray, M. K.; Delevoye, L.; Gauvin, R. M.; Taoufik, M.; et al. Well-Defined Molybdenum Oxo Alkyl Complex Supported on Silica by Surface Organometallic Chemistry: A Highly Active Olefin Metathesis Precatalyst. *J. Am. Chem. Soc.* **2017**, *139*, 2144–2147.

(442) Meyer, K. E.; Walsh, P. J.; Bergman, R. G. Zirconium-Mediated Imine Metathesis - Synthesis of 2,4-Diaza-1-Zirconiacyclobutanes and the Mechanism of Their Reactions with Imines and Alkynes. *J. Am. Chem. Soc.* **1994**, *116*, 2669–2670.

(443) Barman, S.; Merle, N.; Minenkov, Y.; De Mallmann, A.; Samantaray, M. K.; Le Quemener, F.; Szeto, K. C.; Abou-Hamad, E.; Cavallo, L.; Taoufik, M.; et al. Well-Defined Silica Grafted Molybdenum Bis(imido) Catalysts for Imine Metathesis Reactions. *Organometallics* **2017**, *36*, 1550–1556.

(444) Keith, J. A.; Henry, P. M. The Mechanism of the Wacker Reaction: A Tale of Two Hydroxypalladations. *Angew. Chem., Int. Ed.* **2009**, *48*, 9038–9049.

(445) Roundtable Discussion Held on February 18, 2016; Sustainable Ammonia Synthesis—Exploring the Scientific Challenges Associated with Discovering Alternative, Sustainable Processes for Ammonia Production; ; U. S. Department of Energy, Office of Science, Feb 18, 2016; <https://www.osti.gov/biblio/1283146-sustainable-ammonia-synthesis-exploring-scientific-challenges-associated-discovering-alternative-sustainable-processes-ammonia-production> (accessed September 11, 2019).

(446) Milton, R. D.; Cai, R.; Abdellaoui, S.; Leech, D.; De Lacey, A. L.; Pita, M.; Minter, S. D. Bioelectrochemical Haber-Bosch Process: An Ammonia-Producing  $H_2/N_2$  Fuel Cell. *Angew. Chem., Int. Ed.* **2017**, *56*, 2680–2683.

(447) Olivier, J. G. J.; Janssens-Maenhout, G.; Muntean, M.; Peters, J. A. H. W. *Trends in Global CO<sub>2</sub> Emissions: 2015 Report*; PBL Netherlands Environmental Assessment Agency: The Hague, 2015.

(448) Haber, F.; Le Rossignol, R. The Technical Demonstration of Ammonia in the Elements. *Z. Elektrochem. Angew.* **1913**, *19*, 53–72.

(449) Kandemir, T.; Schuster, M. E.; Senyshyn, A.; Behrens, M.; Schlögl, R. The Haber-Bosch Process Revisited: On the Real Structure and Stability of "Ammonia Iron" under Working Conditions. *Angew. Chem., Int. Ed.* **2013**, *52*, 12723–12726.

(450) Liu, H. Z. Ammonia Synthesis Catalyst 100 years: Practice, Enlightenment and Challenge. *Chin. J. Catal.* **2014**, *35*, 1619–1640.

(451) Kitano, M.; Kanbara, S.; Inoue, Y.; Kuganathan, N.; Sushko, P. V.; Yokoyama, T.; Hara, M.; Hosono, H. Electride Support Boosts Nitrogen Dissociation over Ruthenium Catalyst and Shifts the Bottleneck in Ammonia Synthesis. *Nat. Commun.* **2015**, *6*, 6731.

(452) Somorjai, G. A.; Materer, N. Surface Structures in Ammonia Synthesis. *Top. Catal.* **1994**, *1*, 215–231.

(453) Li, J.; Li, S. H. Energetics and Mechanism of Dinitrogen Cleavage at a Mononuclear Surface Tantalum Center: A New Way of Dinitrogen Reduction. *Angew. Chem., Int. Ed.* **2008**, *47*, 8040–8043.

(454) Hellman, A.; Honkala, K.; Remediakis, I. N.; Logadottir, A.; Carlsson, A.; Dahl, S.; Christensen, C. H.; Norskov, J. K. Insights into Ammonia Synthesis from First-Principles. *Surf. Sci.* **2006**, *600*, 4264–4268.

(455) Avenier, P.; Taoufik, M.; Lesage, A.; Solans-Monfort, X.; Baudouin, A.; de Mallmann, A.; Veyre, L.; Basset, J. M.; Eisenstein, O.; Emsley, L.; et al. Dinitrogen Dissociation on an Isolated Surface Tantalum Atom. *Science* **2007**, *317*, 1056–1060.

(456) Solans-Monfort, X.; Chow, C.; Goure, E.; Kaya, Y.; Basset, J. M.; Taoufik, M.; Quadrelli, E. A.; Eisenstein, O. Successive Heterolytic Cleavages of  $H_2$  Achieve  $N_2$  Splitting on Silica-Supported Tantalum Hydrides: A DFT Proposed Mechanism. *Inorg. Chem.* **2012**, *51*, 7237–7249.

(457) Tanaka, H.; Arashiba, K.; Kuriyama, S.; Sasada, A.; Nakajima, K.; Yoshizawa, K.; Nishibayashi, Y. Unique Behaviour of Dinitrogen-Bridged Dimolybdenum Complexes Bearing Pincer Ligand Towards Catalytic Formation of Ammonia. *Nat. Commun.* **2014**, *5*, 3737.

(458) Medford, A. J.; Vojvodic, A.; Hummelshøj, J. S.; Voss, J.; Abild-Pedersen, F.; Studt, F.; Bligaard, T.; Nilsson, A.; Norskov, J. K. From the Sabatier Principle to a Predictive Theory of Transition-Metal Heterogeneous Catalysis. *J. Catal.* **2015**, *328*, 36–42.

(459) Honkala, K.; Hellman, A.; Remediakis, I. N.; Logadottir, A.; Carlsson, A.; Dahl, S.; Christensen, C. H.; Norskov, J. K. Ammonia Synthesis from First-Principles Calculations. *Science* **2005**, *307*, 555–558.

(460) Ertl, G.; Lee, S. B.; Weiss, M. Kinetics of Nitrogen Adsorption on Fe(111). *Surf. Sci.* **1982**, *114*, 515–526.

(461) Bozso, F.; Ertl, G.; Grunze, M.; Weiss, M. Interaction of Nitrogen with Iron Surfaces 0.1. Fe(100) and Fe(111). *J. Catal.* **1977**, *49*, 18–41.

(462) Bligaard, T.; Norskov, J. K.; Dahl, S.; Matthiesen, J.; Christensen, C. H.; Sehested, J. The Brønsted-Evans-Polanyi Relation and the Volcano Curve in Heterogeneous Catalysis. *J. Catal.* **2004**, *224*, 206–217.

(463) Vojvodic, A.; Medford, A. J.; Studt, F.; Abild-Pedersen, F.; Khan, T. S.; Bligaard, T.; Norskov, J. K. Exploring the Limits: A Low-Pressure, Low-Temperature Haber-Bosch Process. *Chem. Phys. Lett.* **2014**, *598*, 108–112.

(464) Dahl, S.; Logadottir, A.; Jacobsen, C. J. H.; Norskov, J. K. Electronic Factors in Catalysis: the Volcano Curve and the Effect of Promotion in Catalytic Ammonia Synthesis. *Appl. Catal., A* **2001**, *222*, 19–29.

(465) Zhang, S. R.; Nguyen, L.; Liang, J. X.; Shan, J. J.; Liu, J. Y.; Frenkel, A. I.; Patlolla, A.; Huang, W. X.; Li, J.; Tao, F. Catalysis on Singly Dispersed Bimetallic Sites. *Nat. Commun.* **2015**, *6*, 7938.

(466) Zhang, B.; Zheng, X. L.; Voznyy, O.; Comin, R.; Bajdich, M.; Garcia-Melchor, M.; Han, L. L.; Xu, J. X.; Liu, M.; Zheng, L. R.; et al. Homogeneously Dispersed Multimetal Oxygen-Evolving Catalysts. *Science* **2016**, *352*, 333–337.

(467) Ma, X. L.; Liu, J. C.; Xiao, H.; Li, J. Surface Single-Cluster Catalyst for  $N_2$ -to- $NH_3$  Thermal Conversion. *J. Am. Chem. Soc.* **2018**, *140*, 46–49.

(468) van der Ham, C. J. M.; Koper, M. T. M.; Hetterscheid, D. G. H. Challenges in Reduction of Dinitrogen by Proton and Electron Transfer. *Chem. Soc. Rev.* **2014**, *43*, 5183–5191.

(469) Anderson, J. S.; Rittle, J.; Peters, J. C. Catalytic Conversion of Nitrogen to Ammonia by an Iron Model Complex. *Nature* **2013**, *501*, 84–87.

(470) Hoffman, B. M.; Lukoyanov, D.; Yang, Z. Y.; Dean, D. R.; Seefeldt, L. C. Mechanism of Nitrogen Fixation by Nitrogenase: The Next Stage. *Chem. Rev.* **2014**, *114*, 4041–4062.

(471) Rodriguez, M. M.; Bill, E.; Brennessel, W. W.; Holland, P. L.  $N_2$  Reduction and Hydrogenation to Ammonia by a Molecular Iron-Potassium Complex. *Science* **2011**, *334*, 780–783.

- (472) McWilliams, S. F.; Holland, P. L. Dinitrogen Binding and Cleavage by Multinuclear Iron Complexes. *Acc. Chem. Res.* **2015**, *48*, 2059–2065.
- (473) Liu, J.-C.; Ma, X.-L.; Li, Y.; Wang, Y.-G.; Xiao, H.; Li, J. Heterogeneous Fe<sub>3</sub> Single-Cluster Catalyst for Ammonia Synthesis via an Associative Mechanism. *Nat. Commun.* **2018**, *9*, 1610.
- (474) Deka, U.; Lezcano-Gonzalez, I.; Weckhuysen, B. M.; Beale, A. M. Local Environment and Nature of Cu Active Sites in Zeolite-Based Catalysts for the Selective Catalytic Reduction of NO<sub>x</sub>. *ACS Catal.* **2013**, *3*, 413–427.
- (475) Artz, J.; Müller, T. E.; Thenert, K.; Kleinekorte, J.; Meys, R.; Sternberg, A.; Bardow, A.; Leitner, W. Sustainable Conversion of Carbon Dioxide: An Integrated Review of Catalysis and Life Cycle Assessment. *Chem. Rev.* **2018**, *118*, 434–504.
- (476) Tappe, N. A.; Reich, R. M.; D'Elia, V.; Kühn, F. E. Current Advances in the Catalytic Conversion of Carbon Dioxide by Molecular Catalysts: An Update. *Dalton Trans.* **2018**, *47*, 13281–13313.
- (477) Song, Q.-W.; Zhou, Z.-H.; He, L.-N. Efficient, Selective and Sustainable Catalysis of Carbon Dioxide. *Green Chem.* **2017**, *19*, 3707–3728.
- (478) Porosoff, M. D.; Yan, B.; Chen, J. G. Catalytic Reduction of CO<sub>2</sub> by H<sub>2</sub> for Synthesis of CO, Methanol and Hydrocarbons: Challenges and Opportunities. *Energy Environ. Sci.* **2016**, *9*, 62–73.
- (479) Li, W.; Wang, H.; Jiang, X.; Zhu, J.; Liu, Z.; Guo, X.; Song, C. A Short Review of Recent Advances in CO<sub>2</sub> Hydrogenation to Hydrocarbons over Heterogeneous Catalysts. *RSC Adv.* **2018**, *8*, 7651–7669.
- (480) Goeppert, A.; Czaun, M.; Jones, J.-P.; Surya Prakash, G. K.; Olah, G. A. Recycling of Carbon Dioxide to Methanol and Derived Products – Closing the Loop. *Chem. Soc. Rev.* **2014**, *43*, 7995–8048.
- (481) Klankermayer, J.; Wesselbaum, S.; Beydoun, K.; Leitner, W. Selective Catalytic Synthesis Using the Combination of Carbon Dioxide and Hydrogen: Catalytic Chess at the Interface of Energy and Chemistry. *Angew. Chem., Int. Ed.* **2016**, *55*, 7296–7343.
- (482) Tlili, A.; Blondiaux, E.; Frogneux, X.; Cantat, T. Reductive Functionalization of CO<sub>2</sub> with Amines: An Entry to Formamide, Formamidine and Methylamine Derivatives. *Green Chem.* **2015**, *17*, 157–168.
- (483) Kleij, A. W.; North, M.; Urakawa, A. CO<sub>2</sub> Catalysis. *ChemSusChem* **2017**, *10*, 1036–1038.
- (484) Yingcharoen, P.; Kongtes, C.; Arayachukiat, S.; Suvarnapunya, K.; Vummaleti, S. V. C.; Wannakao, S.; Cavallo, L.; Poater, A.; D'Elia, V. Assessing the pK<sub>a</sub>-Dependent Activity of Hydroxyl Hydrogen Bond Donors in the Organocatalyzed Cycloaddition of Carbon Dioxide to Epoxides: Experimental and Theoretical Study. *Adv. Synth. Catal.* **2019**, *361*, 366–373.
- (485) Arayachukiat, S.; Kongtes, C.; Barthel, A.; Vummaleti, S. V. C.; Poater, A.; Wannakao, S.; Cavallo, L.; D'Elia, V. Ascorbic Acid as a Bifunctional Hydrogen Bond Donor for the Synthesis of Cyclic Carbonates from CO<sub>2</sub> under Ambient Conditions. *ACS Sustainable Chem. Eng.* **2017**, *5*, 6392–6397.
- (486) Martín, C.; Fiorani, G.; Kleij, A. W. Recent Advances in the Catalytic Preparation of Cyclic Organic Carbonates. *ACS Catal.* **2015**, *5*, 1353–1370.
- (487) Comerford, J. W.; Ingram, I. D. V.; North, M.; Wu, X. Sustainable Metal-Based Catalysts for the Synthesis of Cyclic Carbonates Containing Five-Membered Rings. *Green Chem.* **2015**, *17*, 1966–1987.
- (488) Shaikh, R. R.; Pornpraprom, S.; D'Elia, V. Catalytic Strategies for the Cycloaddition of Pure, Diluted, and Waste CO<sub>2</sub> to Epoxides under Ambient Conditions. *ACS Catal.* **2018**, *8*, 419–450.
- (489) Arayachukiat, S.; Yingcharoen, P.; Vummaleti, S. V. C.; Cavallo, L.; Poater, A.; D'Elia, V. Cycloaddition of CO<sub>2</sub> to Challenging N-tosyl Aziridines Using a Halogen-Free Niobium Complex: Catalytic Activity and Mechanistic Insights. *Mol. Catal.* **2017**, *443*, 280–285.
- (490) Martin, R.; Tortajada, A.; Juliá-Hernández, F.; Borjesson, M.; Moragas, T. Transition Metal-Catalyzed Carboxylation Reactions with Carbon Dioxide. *Angew. Chem., Int. Ed.* **2018**, *57*, 15948–15982.
- (491) Lee, S. Y. T.; Ghani, A. A.; D'Elia, V.; Cokoja, M.; Herrmann, W. A.; Basset, J.-M.; Kühn, F. E. Liberation of Methyl Acrylate from Metallalactone Complexes via M–O ring Opening (M = Ni, Pd) with Methylation Agents. *New J. Chem.* **2013**, *37*, 3512–3517.
- (492) Li, L.; Abou-Hamad, E.; Anjum, D. H.; Zhou, L.; Laveille, P. V.; Emsley, L.; Basset, J.-M. Well-Defined Mono( $\eta^3$ -allyl)nickel complex  $\equiv\text{MONi}(\eta^3\text{-C}_3\text{H}_5)$  (M = Si or Al) Grafted onto Silica or Alumina: A Molecularly Dispersed Nickel Precursor for Syntheses of Supported Small Size Nickel Nanoparticles. *Chem. Commun.* **2014**, *50*, 7716–7719.
- (493) Li, L.; Zhou, L.; Ould-Chikh, S.; Anjum, D. H.; Kanoun, M. B.; Scaranto, J.; Hedhili, M. N.; Khalid, S.; Laveille, P. V.; D'Souza, L.; et al. Controlled Surface Segregation Leads to Efficient Coke-Resistant Nickel/Platinum Bimetallic Catalysts for the Dry Reforming of Methane. *ChemCatChem* **2015**, *7*, 819–829.
- (494) Larmier, K.; Liao, W.-C.; Tada, S.; Lam, E.; Verel, R.; Bansode, A.; Urakawa, A.; Comas-Vives, A.; Copéret, C. CO<sub>2</sub>-to-Methanol Hydrogenation on Zirconia-Supported Copper Nanoparticles: Reaction Intermediates and the Role of the Metal-Support Interface. *Angew. Chem., Int. Ed.* **2017**, *56*, 2318–2323.
- (495) Lam, E.; Larmier, K.; Wolf, P.; Tada, S.; Safonova, O. V.; Copéret, C. Isolated Zr Surface Sites on Silica Promote Hydrogenation of CO<sub>2</sub> to CH<sub>3</sub>OH in Supported Cu Catalysts. *J. Am. Chem. Soc.* **2018**, *140*, 10530–10535.
- (496) Zheng, T.; Jiang, K.; Ta, N.; Hu, Y.; Zeng, J.; Liu, J.; Wang, H. Large-Scale and Highly Selective CO<sub>2</sub> Electrocatalytic Reduction on Nickel Single-Atom Catalyst. *Joule* **2019**, *3*, 265–278.
- (497) Millet, M.-M.; Algara-Siller, G.; Wrabetz, S.; Mazheika, A.; Girgsdies, F.; Teschner, D.; Seitz, F.; Tarasov, A.; Levchenko, S. V.; Schlögl, R.; et al. Ni Single Atom Catalysts for CO<sub>2</sub> Activation. *J. Am. Chem. Soc.* **2019**, *141*, 2451–2461.
- (498) Su, X.; Yang, X.-F.; Huang, Y.; Liu, B.; Zhang, T. Single-Atom Catalysis toward Efficient CO<sub>2</sub> Conversion to CO and Formate Products. *Acc. Chem. Res.* **2019**, *52*, 656–664.
- (499) Guo, Y.; Mei, S.; Yuan, K.; Wang, D.-J.; Liu, H.-C.; Yan, C.-H.; Zhang, Y.-W. Low-Temperature CO<sub>2</sub> Methanation over CeO<sub>2</sub>-Supported Ru Single Atoms, Nanoclusters, and Nanoparticles Competitively Tuned by Strong Metal–Support Interactions and H-Spillover Effect. *ACS Catal.* **2018**, *8*, 6203–6215.
- (500) Kalhor, M. P.; Wischert, R.; Copéret, C.; Chermette, H. Reactivity of Silica Supported Zirconium Hydride Towards N<sub>2</sub>O and CO<sub>2</sub> Probe Molecules: A Computational Point of View. *New J. Chem.* **2014**, *38*, 3717–3721.
- (501) Pasha, F. A.; Bendjeriou-Sedjerari, A.; Abou-Hamad, E.; Huang, K.-W.; Basset, J.-M. CO<sub>2</sub> Activation Through Silylimido and Silylamido Zirconium Hydrides Supported on N-donor Chelating SBA15 Surface Ligands. *Chem. Commun.* **2016**, *52*, 2577–2580.
- (502) Kelly, M. J.; Barthel, A.; Maheu, C.; Sodpiban, O.; Dega, F.-B.; Vummaleti, S. V. C.; Abou-Hamad, E.; Pelletier, J. D. A.; Cavallo, L.; D'Elia, V.; Basset, J.-M. Conversion of actual flue gas CO<sub>2</sub> via cycloaddition to propylene oxide catalyzed by a single-site, recyclable zirconium catalyst. *J. CO<sub>2</sub> Util.* **2017**, *20*, 243–252.
- (503) Fukuoka, S.; Kawamura, M.; Komiya, K.; Tojo, M.; Hachiya, H.; Hasegawa, K.; Aminaka, M.; Okamoto, H.; Fukawa, I.; Konno, S. A Novel Non-Phosgene Polycarbonate Production Process Using By-Product CO<sub>2</sub> as Starting Material. *Green Chem.* **2003**, *5*, 497–507.
- (504) Zhao, D.; Chen, Z.; Yang, W.; Liu, S.; Zhang, X.; Yu, Y.; Cheong, W.-C.; Zheng, L.; Ren, F.; Ying, G.; et al. MXene (Ti<sub>3</sub>C<sub>2</sub>) Vacancy-Confined Single-Atom Catalyst for Efficient Functionalization of CO<sub>2</sub>. *J. Am. Chem. Soc.* **2019**, *141*, 4086–4093.
- (505) North, M.; Pasquale, R.; Young, C. Synthesis of Cyclic Carbonates from Epoxides and CO<sub>2</sub>. *Green Chem.* **2010**, *12*, 1514–1539.
- (506) Fiorani, G.; Guo, W.; Kleij, A. W. Sustainable Conversion of Carbon Dioxide: The Advent of Organocatalysis. *Green Chem.* **2015**, *17*, 1375–1389.

- (507) D'Elia, V.; Pelletier, J. D. A.; Basset, J.-M. Cycloadditions to Epoxides Catalyzed by Group III-V Transition-Metal Complexes. *ChemCatChem* **2015**, *7*, 1906–1917.
- (508) Whiteoak, C. J.; Martin, E.; Belmonte, M. M.; Benet-Buchholz, J.; Kleij, A. W. An Efficient Iron Catalyst for the Synthesis of Five- and Six-Membered Organic Carbonates under Mild Conditions. *Adv. Synth. Catal.* **2012**, *354*, 469–476.
- (509) Dutta, B.; Sofack-Kreutzer, J.; Ghani, A. A.; D'Elia, V.; Pelletier, J. D. A.; Cokoja, M.; Kühn, F. E.; Basset, J.-M. Nucleophile-Directed Selectivity Towards Linear Carbonates in the Niobium Pentaethoxide-Catalysed Cycloaddition of CO<sub>2</sub> and Propylene Oxide. *Catal. Sci. Technol.* **2014**, *4*, 1534–1538.
- (510) Maisonneuve, L.; Lamarzelle, O.; Rix, E.; Grau, E.; Cramail, H. Isocyanate-Free Routes to Polyurethanes and Poly(hydroxy Urethane)s. *Chem. Rev.* **2015**, *115*, 12407–12439.
- (511) Yadav, N.; Seidi, F.; Crespy, D.; D'Elia, V. Polymers Based on Cyclic Carbonates as *Trait d'Union* Between Polymer Chemistry and Sustainable CO<sub>2</sub> Utilization. *ChemSusChem* **2019**, *12*, 724–754.
- (512) Schäffner, B.; Schäffner, F.; Verevkin, S. P.; Börner, A. Organic Carbonates as Solvents in Synthesis and Catalysis. *Chem. Rev.* **2010**, *110*, 4554–4581.
- (513) Lawrenson, S. B.; Arav, R.; North, M. The Greening of Peptide Synthesis. *Green Chem.* **2017**, *19*, 1685–1691.
- (514) Beyzavi, M. H.; Klet, R. C.; Tussupbayev, S.; Borycz, J.; Vermeulen, N. A.; Cramer, C. J.; Stoddart, J. F.; Hupp, J. T.; Farha, O. K. A Hafnium-Based Metal–Organic Framework as an Efficient and Multifunctional Catalyst for Facile CO<sub>2</sub> Fixation and Regioselective and Enantioselective Epoxide Activation. *J. Am. Chem. Soc.* **2014**, *136*, 15861–15864.
- (515) Guillermin, V.; Weseliński, E. J.; Belmabkhout, Y.; Cairns, A. J.; D'Elia, V.; Wojtas, L.; Adil, K.; Eddaoudi, M. Discovery and Introduction of a (3,18)-Connected Net as an Ideal Blueprint for the Design of Metal–Organic Frameworks. *Nat. Chem.* **2014**, *6*, 673–680.
- (516) Beyzavi, M. H.; Stephenson, C. J.; Liu, Y.; Karagiari, O.; Hupp, J. T.; Farha, O. K. Metal–Organic Framework-Based Catalysts: Chemical Fixation of CO<sub>2</sub> with Epoxides Leading to Cyclic Organic Carbonates. *Front. Energy Res.* **2015**, *2*, 63.
- (517) Carvalho, P.; Comerford, J.; Lamb, K.; North, M.; Reiss, P. Influence of Mesoporous Silica Properties on Cyclic Carbonate Synthesis Catalysed by Supported Aluminium(salen) Complexes. *Adv. Synth. Catal.* **2019**, *361*, 345–354.
- (518) Wang, S.; Song, K.; Zhang, C.; Shu, Y.; Li, T.; Tan, B. A Novel Metalporphyrin-Based Microporous Organic Polymer with High CO<sub>2</sub> Uptake and Efficient Chemical Conversion of CO<sub>2</sub> Under Ambient Conditions. *J. Mater. Chem. A* **2017**, *5*, 1509–1515.
- (519) Huang, K.; Zhang, J.-Y.; Liu, F.; Dai, S. Synthesis of Porous Polymeric Catalysts for the Conversion of Carbon Dioxide. *ACS Catal.* **2018**, *8*, 9079–9102.
- (520) Wang, C.; Song, Q.; Zhang, K.; Liu, P.; Wang, J.; Wang, J.; Zhang, H.; Wang, J. Atomic Zinc Dispersed on Graphene Synthesized for Active CO<sub>2</sub> Fixation to Cyclic Carbonates. *Chem. Commun.* **2019**, *55*, 1299–1302.
- (521) Xie, Y.; Wang, T.-T.; Liu, X.-H.; Zou, K.; Deng, W.-Q. Capture and Conversion of CO<sub>2</sub> at Ambient Conditions by a Conjugated Microporous Polymer. *Nat. Commun.* **2013**, *4*, 1960.
- (522) Wang, W.; Li, C.; Jin, J.; Yan, L.; Ding, Y. Mg–Porphyrin Complex Doped Divinylbenzene Based Porous Organic Polymers (POPs) as Highly Efficient Heterogeneous Catalysts for the Conversion of CO<sub>2</sub> to Cyclic Carbonates. *Dalton Trans* **2018**, *47*, 13135–13141.
- (523) Sopeña, S.; Martin, E.; Escudero-Adán, E. C.; Kleij, A. W. Pushing the Limits with Squaramide-Based Organocatalysts in Cyclic Carbonate Synthesis. *ACS Catal.* **2017**, *7*, 3532–3539.
- (524) D'Elia, V.; Ghani, A. A.; Monassier, A.; Sofack-Kreutzer, J.; Pelletier, J. D. A.; Drees, M.; Vummaleti, S. V. C.; Poater, A.; Cavallo, L.; Cokoja, M.; et al. Dynamics of the NbCl<sub>5</sub>-Catalyzed Cycloaddition of Propylene Oxide and CO<sub>2</sub>: Assessing the Dual Role of the Nucleophilic Co-Catalysts. *Chem. - Eur. J.* **2014**, *20*, 11870–11882.
- (525) Yang, Q.; Yang, C.-C.; Lin, C.-H.; Jiang, H.-L. Metal–Organic–Framework-Derived Hollow N-Doped Porous Carbon with Ultrahigh Concentrations of Single Zn Atoms for Efficient Carbon Dioxide Conversion. *Angew. Chem., Int. Ed.* **2019**, *58*, 3511–3515.
- (526) Clegg, W.; Harrington, R. W.; North, M.; Pasquale, R. Cyclic Carbonate Synthesis Catalysed by Bimetallic Aluminium–Salen Complexes. *Chem. - Eur. J.* **2010**, *16*, 6828–6843.
- (527) Yang, Y.; Lee, J.-W. Toward Ideal Carbon Dioxide Functionalization. *Chem. Sci.* **2019**, *10*, 3905–3926.
- (528) Cvetanovic, R. J.; Baranski, A. Low-Temperature Hydrogenation of Ethylene on Zinc Oxide by Temperature-Programmed Desorption. *J. Phys. Chem.* **1971**, *75*, 208–220.
- (529) Lucci, F. R.; Darby, M. T.; Mattera, M. F. G.; Ivimey, C. J.; Therrien, A. J.; Michaelides, A.; Stamatakis, M.; Sykes, E. C. H. Controlling Hydrogen Activation, Spillover, and Desorption with Pd–Au Single-Atom Alloys. *J. Phys. Chem. Lett.* **2016**, *7*, 480–485.
- (530) Han, L.; Liu, X.; Chen, J.; Lin, R.; Liu, H.; Lü, F.; Bak, S.; Liang, Z.; Zhao, S.; Stavitski, E.; Luo, J.; Adzic, R. R.; Xin, H. L. Atomically Dispersed Molybdenum Catalysts for Efficient Ambient Nitrogen Fixation. *Angew. Chem., Int. Ed.* **2019**, *58*, 2321–2325.
- (531) Ling, C.; Bai, X.; Ouyang, Y.; Du, A.; Wang, J. Single Molybdenum Atom Anchored on N-Doped Carbon as a Promising Electrocatalyst for Nitrogen Reduction into Ammonia at Ambient Conditions. *J. Phys. Chem. C* **2018**, *122*, 16842–16847.
- (532) Yan, J.; Kong, L.; Ji, Y.; White, J.; Li, Y.; Zhang, J.; An, P.; Liu, S.; Lee, S.-T.; Ma, T. Single Atom Tungsten Doped Ultrathin  $\alpha$ -Ni(OH)<sub>2</sub> for Enhanced Electrocatalytic Water Oxidation. *Nat. Commun.* **2019**, *10*, 2149.
- (533) Chen, W.; Pei, J.; He, C.-T.; Wan, J.; Ren, H.; Wang, Y.; Dong, J.; Wu, K.; Cheong, W.-C.; Mao, J.; Zheng, X.; Yan, W.; Zhuang, Z.; Chen, C.; Peng, Q.; Wang, D.; Li, Y. Single Tungsten Atoms Supported on MOF-Derived N-Doped Carbon for Robust Electrochemical Hydrogen Evolution. *Adv. Mater.* **2018**, *30*, 1800396.
- (534) Fechet, I.; Idriss, H.; Hutchings, G.; Bond, G.; Garin, F. Catalytic Reactivity of Surfaces: in Recognition of François Gault. *Catal. Sci. Technol.* **2017**, *7*, 5181.